

Internalisation of Biophotonic Techniques:

Transfection, Injection and Thermometry

William Tulloch Ramsay

Submitted for the degree of Doctor of Philosophy

Heriot-Watt University

Institute of Biological Chemistry, Biophysics and Bioengineering

May 2018

The copyright in this thesis is owned by the author. Any quotation from the thesis or use of any of the information contained in it must acknowledge this thesis as the source of the quotation or information.

Abstract

Single cell manipulation can offer great insights into the whole of an organism, the rapidly growing -omics fields are illustrating the heterogeneity that can be found within cell populations and where these subtle differences may be exploited, from fundamental knowledge to diagnostics and therapeutics. The cutting edge of this single cell work requires the application of interdisciplinary research to fully exploit the boundaries being pushed. Biophotonics is one such body of interdisciplinary research, employing light to manipulate biological samples. This work seeks to make use biophotonic techniques as analogues for conventional biological methods. High throughput raster scan photoporation is utilised for attempted transfection, multiple trap optical tweezers are used in an attempt to optically drive mechanical injection of cells and the thermal impact of these optical tweezers, which require high energy densities to confine particles, is tested, via the exploitation of the temperature sensitive emission of quantum dot nanoparticles.

For my family

Acknowledgements

It almost goes without saying that this work would not have been possible without the support of a great many people. This is a page I never thought I would get around to writing, and without doubt, this will only scratch the surface of debt of gratitude I owe to so many.

Firstly, I owe an insurmountable debt of thanks to Dr Lynn Paterson and Prof Ajoy K. Kar, without their support, mentorship and endless patience, this work could never have come to fruition. Thank you for giving me this fantastic opportunity to work with you, and for always pushing me.

From time to explanations to lab space and equipment, I owe a great deal to a great many members of the scientific community at Heriot-Watt University. Dr Nik Willoughby and Dr Fiona Dempsey for their help and access to cell culture and flow cytometry facilities. Dr Helinor Johnston and Dr David Brown for their support with toxicological work. Dr Alison Dun for the help with confocal microscopy. Dr. Bill MacPherson for providing so many opportunities to be involved in public engagement. Dr Debaditya Choudhury for the coffee breaks, the company in the lab, late nights and weekends!

Beyond Heriot-Watt, I must also thank Prof Daniel Jaque, Dr Laura Maestro and Dr Patricia Haro from the Universidad Autónoma de Madrid for their contribution to the nanothermometry work and boundless enthusiasm. Dr Mohammed Elhassan and Prof Carragher's group at the University of Edinburgh for cells and plasmids for the photoporation work. Shonna Johnston from the University of Edinburgh for her support and providing the flexible environment that allowed me to complete this writing.

Lastly, I must thank my family, for with their support through absolutely everything (even with the quips on being an eternal student) and Heather for suffering me during this process!

ACADEMIC REGISTRY

Research Thesis Submission

Name:	William Tulloch Ramsay		
School:	Engineering & Physical Sciences; Institute of Biological Chemistry, Biophysics and Bioengineering		
Version: <i>(i.e. First, Resubmission, Final)</i>	Final	Degree Sought:	Doctor of Philosophy

Declaration

In accordance with the appropriate regulations I hereby submit my thesis and I declare that:

- 1) the thesis embodies the results of my own work and has been composed by myself
- 2) where appropriate, I have made acknowledgement of the work of others and have made reference to work carried out in collaboration with other persons
- 3) the thesis is the correct version of the thesis for submission and is the same version as any electronic versions submitted*.
- 4) my thesis for the award referred to, deposited in the Heriot-Watt University Library, should be made available for loan or photocopying and be available via the Institutional Repository, subject to such conditions as the Librarian may require
- 5) I understand that as a student of the University I am required to abide by the Regulations of the University and to conform to its discipline.
- 6) I confirm that the thesis has been verified against plagiarism via an approved plagiarism detection application e.g. Turnitin.

* Please note that it is the responsibility of the candidate to ensure that the correct version of the thesis is submitted.

Signature of Candidate:		Date:	
-------------------------	--	-------	--

Submission

Submitted By <i>(name in capitals)</i> :	
Signature of Individual Submitting:	
Date Submitted:	

For Completion in the Student Service Centre (SSC)

Received in the SSC by <i>(name in capitals)</i> :			
Method of Submission <i>(Handed in to SSC; posted through internal/external mail):</i>			
E-thesis Submitted (mandatory for final theses)			
Signature:		Date:	

Table of Contents

<i>Table of Contents</i>	<i>i</i>
<i>List of Tables</i>	<i>vii</i>
<i>List of Figures</i>	<i>viii</i>
<i>Glossary</i>	<i>xii</i>
<i>Publications</i>	<i>xiv</i>

1 Introduction: Life at the microscopic – single cell biology	1
1.1 Synopsis.....	1
1.2 Motivation.....	2
1.3 The cell	3
1.4 Single cell analysis	6
1.4.1 Genomics	7
1.4.2 Transcriptomics.....	7
1.4.3 Proteomics	8
1.5 Microfluidics.....	8
1.6 Photonic tools.....	9
1.6.1 Microscopy	9
1.6.2 Cytometry	11
1.7 Biophotonics	11
2 Laser driven transfection of pancreatic cells with activated <i>KRAS</i>.....	13
2.1 Introduction.....	13
2.2 Background.....	14
2.2.1 Cancer.....	14

2.2.2 Pancreatic cancer.....	17
2.2.2.1 <i>KRAS</i>	19
2.2.3 Transfection	21
2.2.3.1 Transfection techniques.....	22
2.2.3.2 Photoporation.....	23
2.3 Experimental methods	26
2.3.1 Optical design	26
2.3.2 Computer control	29
2.3.3 Cell culture.....	29
2.3.3.1 CHO-K1 cell culture	30
2.3.3.2 HPDE4 cell culture.....	31
2.3.4 Microscopy	32
2.3.5 Glass etching.....	32
2.3.6 Sample preparation.....	33
2.3.7 Photoporation.....	34
2.3.7.1 Photoporation optimisation.....	35
2.3.7.2 Optical transfection	36
2.4 Results	36
2.4.1 Photoporation optimisation – 5 kHz pulsed laser	36
2.4.2 Photoporation optimisation – 1 MHz pulsed laser	38
2.4.2.1 Point exposure; viability and efficiency	38
2.4.2.2 Raster scanning; viability and efficiency	41
2.4.3 GFP transfection.....	43
2.4.4 Transfection of activated <i>KRAS</i>	44
2.5 Discussion.....	47
2.6 Conclusions.....	49

3 Optical manipulation of hollow cylinders; towards microinjection	51
3.1 Introduction	51
3.2 Background	52
3.2.1 Optical tweezers	52
3.2.1.1 Spherical trapping	53
3.2.1.2 Non-spherical trapping	56
3.2.1.3 Multiple beam optical trapping	60
3.2.1.4 Ronchi ruling	63
3.2.2 Microinjection	64
3.3 Experimental methods	66
3.3.1 Optical design	66
3.3.2 Microneedle fabrication	69
3.3.2.1 Pulled borosilicate capillaries	69
3.3.2.2 Rolled SiO / SiO ₂ microneedles	70
3.3.2.3 Laser inscribed microneedles	72
3.3.3 Cell culture	73
3.3.3.1 HL-60 cell culture	74
3.3.4 Sample preparation	74
3.4 Results	75
3.4.1 Calibration of optical tweezers	75
3.4.1.1 Power and spacing of multiple beam optical tweezers	76
3.4.2 Optical tweezing of hollow microcylinders	79
3.4.2.1 Optical tweezing of pulled borosilicate capillaries	79
3.4.2.2 Single beam optical tweezing of rolled hollow cylinders	80
3.4.2.3 Multiple beam optical tweezing of rolled hollow cylinders	81
3.4.3 Construction of optically controlled microsyringe	83

3.4.4 Cell isolation using microneedles	86
3.5 Discussion.....	87
3.6 Conclusions.....	88
4 Quantum dot luminescence nanothermometry in optical tweezers.....	89
4.1 Introduction	89
4.2 Background	90
4.2.1 Temperature and biology.....	91
4.2.2 Heatshock	92
4.2.3 Temperature on the small scale.....	92
4.2.4 Fluorescence methods	94
4.2.5 Quantum dots	96
4.2.6 Thermal loading with optical devices	100
4.2.6.1 Thermal properties of optical tweezers	100
4.2.6.2 Thermal influences in optofluidic devices.....	102
4.3 Experimental methods	103
4.3.1 Thermal calibration methodology	103
4.3.1.1 Calibration setup	104
4.3.1.2 Temperature control acquisition	105
4.3.2 Thermal flux from optical tweezers	105
4.3.2.1 Optical design	106
4.3.3 Sample preparation.....	109
4.3.4 Spectroscopic acquisition and processing	110
4.3.5 Aqueous environments	112
4.3.6 Cell culture.....	112
4.3.7 Toxicity.....	113

4.3.7.1 Lactate dehydrogenase assay	113
4.3.7.2 Resazurin assay	116
4.3.8 Confocal imaging of internalised quantum dots	117
4.4 Results	117
4.4.1 Quantum dot calibration	118
4.4.2 Laser power measurements	120
4.4.3 Nanothermometry of optical tweezers	122
4.4.3.1 CdSe quantum dots	122
4.4.3.2 CdTe quantum dots	123
4.4.3.3 Improved nanothermometry system	128
4.4.3 Nanothermometry in biological environments	131
4.4.4.1 Phosphate-buffered saline	131
4.4.4.2 pH	133
4.4.4.3 Cell culture media	135
4.4.5 Toxicity	136
4.4.5.1 CdTe toxicity	137
4.4.7 Confocal imaging	139
4.4.8 Optofluidics	140
4.5 Discussion	
141 4.6 Conclusions	143
5 Summary	145
5.1 A close	145
5.2 Summary of thesis	145
5.3 Future work	149
5.4 Closing remarks	150

Appendix A – Published papers	152
A1 Quantum Dot-Based Thermal Spectroscopy and Imaging of Optically Trapped Microspheres and Single Cells.....	153
A2 Quantum dot enabled thermal imaging of optofluidic devices.....	163
A3 A 3D mammalian cell separator biochip	171
A4 Triple beam optical trap for microsyringe construction.....	178
 References	 188

List of Tables

2 Laser driven transfection of pancreatic cells with activated *KRAS*

2.1	Photoporation parameter space.....	46
-----	------------------------------------	----

4 Quantum dot luminescence nanothermometry in optical tweezers

4.1	LDH standard curve concentrations.....	115
4.2	Summary of CdTe quantum dots in optical tweezers	126

List of Figures

1 Introduction: Life at the microscopic – single cell biology

1.1	The eukaryotic cell.....	4
1.2	The compound microscope.....	10

2 Laser driven transfection of pancreatic cells with activated *KRAS*

2.1	Cancer progression.....	16
2.2	The pancreas	18
2.3	RAS switching	20
2.4	<i>KRAS</i> activity.....	21
2.5	Schematic diagram of the photoporation apparatus.....	27
2.6	Stitched images of laser-written markings on glass.....	33
2.7	Scanning photoporation.....	35
2.8	Photoporation with Ti:Sapph laser.....	37
2.9	Photoporation of CHO-K1 cell in the presence of trypan blue	39
2.10	Single shot photoporation efficiency and viability using a 1 MHz source	40
2.11	CHO-K1 viability after exposure to a 1MHz, 1064 nm laser.....	42
2.12	Scanning photoporation efficiency and viability using a 1 MHz source	42
2.13	Attempted GFP transfection utilising photoporation	43
2.14	Attempted <i>KRAS</i> transfection utilising photoporation.....	45

3 Optical manipulation of hollow cylinders; towards microinjection

3.1	Ray optics description for optical trapping of solid spheres	54
3.2	Ray optics description for optical trapping of hollow spheres	55
3.3	Optical tweezing solid cylinders.....	57

3.4	Probes designed for optical trapping.....	58
3.5	Time sharing optical tweezers	61
3.6	Optical trap pattern produced using static DOE	62
3.7	iTweezers.....	63
3.8	Image projection of interference pattern from grating.....	63
3.9	Microinjection of mouse embryo.....	65
3.10	Optical tweezer with Ronchi ruling	67
3.11	Drawing borosilicate capillaries	69
3.12	Microscopy of diced, pulled borosilicate capillaries.....	70
3.13	Fabrication of rolled microneedles	71
3.14	Rolled microneedle	72
3.15	ULI fabrication.....	73
3.16	Triple beam optical tweezing of microspheres.....	76
3.17	Optical trap forces.....	77
3.18	Triple beam optical tweezer spacing.....	78
3.19	Optical tweezing of a pulled capillary.....	80
3.20	Optical tweezing of rolled microneedle	81
3.21	Triple beam optical trapping of rolled microneedles	82
3.22	Pushing a rolled microneedle.....	83
3.23	Optical tweezing inside a rolled microneedle.....	84
3.24	Optically controlled microinjection illustration.....	85
3.25	Isolation of cyanobacteria.....	86

4 Quantum dot driven luminescence nanothermometry in optical tweezers

4.1	Gallium nanothermometer.....	93
4.2	Jablonski diagram of QD fluorescence	97

4.3	Temperature dependent wavelength shift in quantum dots.....	98
4.4	Jablonski diagram of upconversion fluorescence	99
4.5	Emission spectra of CdTe and CdSe quantum dots	104
4.6	Fluorescence spectroscopy of test samples on a heated stage	104
4.7	Optical tweezers with integrated fluorescent spectroscopy capabilities	107
4.8	Absorption spectrum of water.....	109
4.9	Fitted curve using GaussMod function	111
4.10	Emission peak shift	111
4.11	Interconversion process of pyruvate and lactate as mediated by LDH.....	114
4.12	Standard curve for LDH assay.....	115
4.13	Conversion of resazurin to resorufin.....	116
4.14	CdTe quantum dot calibration	118
4.15	CdSe quantum dot calibration.....	119
4.16	Summary quantum dot calibration.....	119
4.17	Laser power loss through apparatus, 980 nm	121
4.18	Laser power loss through apparatus, 1064 nm	121
4.19	CdSe spectral shift as power of optical tweezing beam increases	122
4.20	CdTe QDs with 980 nm, x40 microscope objective, optical tweezing	123
4.21	CdTe QDs with 980 nm, x100 microscope objective, optical tweezing	124
4.22	CdTe QDs with 1064 nm, x40 microscope objective, optical tweezing	124
4.23	CdTe QDs with 1064 nm, x100 microscope objective, optical tweezing	124
4.24	CdTe spectra shift as power of optical tweezing beam increases.....	125
4.25	CdTe spectra shift in high power optical tweezing.....	126
4.26	CdTe emission gradient in optical tweezers	127
4.27	Temperature shift with different optical tweezing wavelengths.....	129
4.28	Wavelength dependent heating of water by optical tweezers.....	130

4.29	Optimal optical tweezer wavelengths	131
4.30	Fluorescence emission of CdSe QDs in PBS	132
4.31	Temperature induced emission shift of CdSe QDs in PBS	132
4.32	Fluorescence emission of CdSe QDs at various pH levels.....	133
4.33	Temperature induced emission shift of CdSe QDs at different pH levels	134
4.34	Summary of temperature dependent CdSe emission shift rates at pH 3-pH 7	134
4.35	Temperature induced peak emission shifts of CdSe QDs in cell media	135
4.36	Summary of temperature dependent CdSe emission shift rates in cell media	136
4.37	LDH assay, CdTe toxicity	137
4.38	Resazurin assay, CdTe toxicity.....	138
4.39	CdSe quantum dots in macrophages	139
4.40	Optofluidic device.....	140
4.41	Optofluidic device imaging and spectroscopy.....	141

Glossary

$\lambda/2$	-	Half-wave
$\lambda/4$	-	Quarter-wave
ADP	-	Adenosine Diphosphate
AFM	-	Atomic Force Microscopy
AOD	-	Acousto-Optic Deflector
ATP	-	Adenosine Triphosphate
CCD	-	Charge-Coupled Device
CdSe	-	Cadmium Selenide
CdTe	-	Cadmium Telluride
CHO-K1	-	Chinese Hamster Ovary
CNT	-	Carbon Nanotube
CRISPR	-	Clustered Regularly Interspaced Short Palindromic Repeats
DC	-	Dichroic Mirror
DNA	-	Deoxyribonucleic Acid
DOE	-	Diffractive Optical Element
DPBS	-	Dulbecco's Phosphate-buffered Saline
eco gtp	-	<i>Escherichia coli</i> Glutamic Pyruvic Transaminase
EGF	-	Epidermal Growth Factor
FCS	-	Foetal Calf Serum
FGF	-	Fibroblast Growth Factor
FIR	-	Far Infrared
FR	-	Far Red
GAP	-	GTPase Activating Proteins
GDP	-	Guanosine Diphosphate
GEF	-	Guanine Nucleotide Exchange Factor
GFP	-	Green Fluorescent Protein
GTP	-	Guanosine Triphosphate
HAZ	-	Heat Affected Zone
HL-60	-	Human Leukaemia cell line
HPDE4	-	Human Pancreatic Duct Epithelial
HSF	-	Heatshock Transcription Factor
HSP	-	Heatshock Protein
HWU	-	Heriot-Watt University

KRAS	-	V-Ki-ras2 Kirsten rat sarcoma viral oncogene homolog
LDH	-	Lactate dehydrogenase
LED	-	Light Emitting Diode
LOC	-	Lab-On-a-Chip
MO	-	Microscope Objective
NA	-	Numerical Aperture
NAD ⁺	-	Nicotinamide adenine dinucleotide (oxidized)
NADH	-	Nicotinamide adenine dinucleotide (reduced)
ND	-	Neutral Density
Nd:YAG	-	Neodymium doped Yttrium Aluminium Garnet
NIR	-	Near Infrared
PBS	-	Phosphate-buffered Saline
PBSC	-	Polarised Beam Splitting Cube
QD	-	Quantum Dot
RNA	-	Ribonucleic Acid
SAGE	-	Serial Analysis of Gene Expression
SLM	-	Spatial Light Modulator
STED	-	Stimulated Emission Depletion Microscopy
TEM	-	Transverse Electromagnetic Mode
Ti:Sapph	-	Titanium-sapphire
UAM	-	Universidad Autónoma de Madrid
UV	-	Ultraviolet

Publications

Haro-Gonzalez, P., Ramsay, W. T., Maestro, L. M., Rosal, B., Santacruz-Gomez, K., Cruz, M. C. I., Sanz-Rodriguez, S., Bettinelli, M., Choudhury, D., Kar, A. J., Sole, J. G., Jaque, D. & Paterson, L. “Quantum dot-based thermal spectroscopy and imaging of optically trapped microspheres and single cells” *Small* **9(12)**, 2162-2170 (2013).

Choudhury, D., Jaque, D., Rodenas, A., Ramsay, W. T., Paterson, L. & Kar, A. J. “Quantum dot enabled thermal imaging of optofluidic devices” *Lab Chip* **12(13)**, 2414-2420 (2012).

Choudhury, D., Ramsay, W. T., Kiss, R., Willoughby, N. A., Paterson, L. & Kar, A. K. “A 3D mammalian cell separator biochip” *Lab Chip* **12(5)**, 948-953 (2012).

Ramsay, W. T., Bechu, M., Quinones, V. A. B., Mei, Y., Schmidt, O. G. & Paterson, L. “Triple beam optical trap for microsyringe construction” *Proc. SPIE 8097 Optical Trapping and Optical Micromanipulation VIII*, 809708 (2011).

Chapter 1

Introduction: Life at the microscopic - single cell biology

1.1 Synopsis

This thesis encapsulates a body of research used to study the application of various photonic techniques for interacting with single biological cells; biophotonics. As the body of work presented herein crosses the 'borders' of the classical scientific fields, this chapter aims to primarily serve as an introduction covering the broader fundamentals of the relevant work. This introduction will be followed by three experimental chapters that are, to an extent, self-contained. Each providing an introduction and review of the principles and existing literature, applied methodologies and results. A closing chapter summarises and ties the experimental work, with final conclusions and thoughts on the future direction of this research.

In chapter one I aim to briefly explain the fundamental background to cell biology, why and how the single cell is studied. Conventional techniques are discussed, and advanced tools and methods introduced. Chapter two explores the development of a new iteration of photoporation instrumentation; a device where pulsed laser light is focused onto a cell in order to create a transient pore in the cell membrane, and the refinements required to maximize the efficiency of pore formation while minimizing damage. Different modes of operation in the system, point and scanning exposure, are compared in terms of efficiency and viability. A common mammalian cell line is utilised as an initial model and control baseline before advancing to a human pancreatic cell line, seeking to study issues resulting from the unregulated expression of the gene *KRAS*, with a view to cell line generation to assist the understanding and modelling of pancreatic cancer progression. Chapter three discusses the first example of optically confined hollow cylinders and the potential applications in cell biology which arise. The application of both single and multiple beam optical tweezers are explored to optimize the confinement of the cylinders. A series of manufacturing techniques are applied for the production of the hollow cylinders to maximize uniformity and optimise parameters for optical trapping with which they are confined. Chapter four addresses the issue of localized heating caused by high density irradiance. The temperature sensitive emission of quantum dot nanocrystals is exploited to allow the optimisation of conventional optical tweezers and optofluidic devices. Chapter five summarises and draws conclusions on this body of research, including the potential applications and implications. The direction of future work is discussed and closing thoughts on this thesis are presented.

1.2 Motivation

This work aims to employ and develop photonic techniques in the study and manipulation of single cells. Cross-discipline methods are used to facilitate effects that are not feasible with conventional biological techniques which often require large numbers of cells. Methods to optimise biophotonic techniques are explored and biophotonic analogues for conventional techniques are used, such as transfection (Chapter 2), microinjection (Chapter 3) and thermometry (Chapter 4).

1.3 The cell

Biological research can be viewed from a number of different scales and perspectives, from submicron organelles to entire environments. This body of work is primarily focused on biology at the cellular level, studying and manipulating single cells in isolation. Every organism is comprised of cells, from the simplest single cell bacterium to large mammals with trillions of cells in several hundred varieties. The cell is the basic building block of an organism, a microscopic, organic machine, able to sustain itself within the correct environment and, within multicellular organisms, providing a specialized function for the organism as a whole.

The discovery of the cell is attributed to Robert Hooke, during 1665, in his seminal publication on microscopy, *Micrographia* [1]. Hooke noted the compartmented structures he saw in plant tissue samples as bearing a similarity to small rooms in which a monk would abide, a cell. While his discovery was of immense importance, and it was not long until other scientists noted life on the microscopic scale, it was not until 1839 when Theodor Schwann, a physiologist, and Matthias Jakob Schleiden, a botanist, claimed these cells to be the basic building blocks of all life, in essence founding cell theory and the modern field of cell biology.

In the study of the cell, the classification of cell must be considered, it is important to note the taxonomic domain of the cells. In taxonomy, the domain is the first major separation of organism definition, from which all will be either Eukaryotic or Prokaryotic. There are a few key differences between Eukaryotes and Prokaryotes, however, the primary defining difference is that Eukaryotic cells have genetic information stored within a nuclear membrane, Prokaryotes do not. The organisms which fall under the Prokaryote domain are the single cell Eubacterium and Archaea whereas the domain of Eukaryotes consists of microscopic protists, plants, fungi and animals. Here we will focus on Eukaryotes, primarily from the animal kingdoms, using cell lines which are on the order of $\sim 10\text{ }\mu\text{m}$ in diameter. A schematic of a eukaryotic cell and the significant internal structures is shown in Figure 1.1.

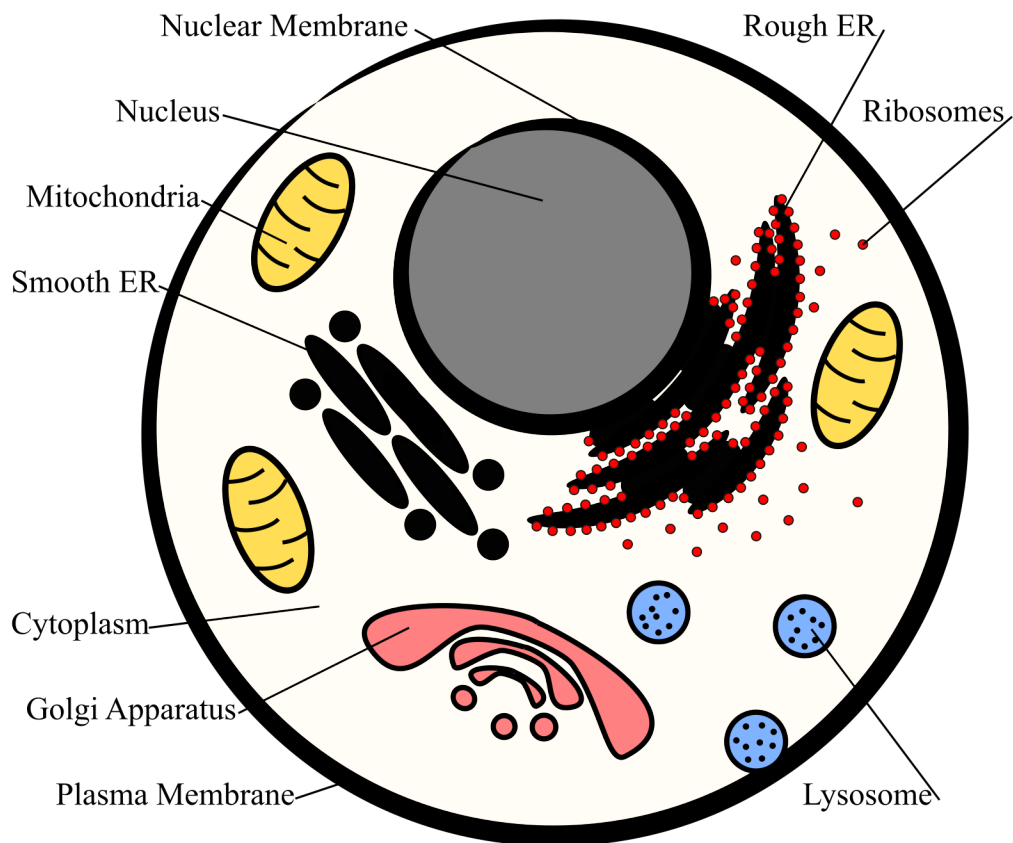


Figure 1.1 – The eukaryotic cell. The plasma membrane is both the barrier between the intra- and extracellular environments, and a structure which can support protein structures used to interact with the surrounding environment.

The variety in form and function of cells is simply staggering, yet they share the same basic construction. The outermost anatomy of a cell is the plasma membrane, a boundary between the intracellular space and the surrounding environment. Long chain lipids with a hydrophilic head and hydrophobic tail form a bilayer where the hydrophobic tails are energetically suited to being in contact, end to end, leaving the hydrophilic heads in contact with the intra- and extracellular environments. This fluid, lipid bilayer allows the cell to maintain a chemical potential differential between the cell and the surrounding environment. It is not solely used as a boundary, it is also functional as a foundation which supports numerous different structures, namely proteins, both on the surface and transmembrane. These proteins serve many different functions, from signalling and recognition to balancing intracellular ion concentrations. Lipid production within the cell is mediated by the smooth endoplasmic reticulum. The cell is capable of producing several types of vesicle, small lipid bilayer bubbles, each with specialised functions.

These are formed from the cell membrane and can be used to consume material from the environment (endocytosis) or transport material out of the cell (exocytosis). The function of a vesicle can be determined by the contents it holds and the manner in which it is controlled by the cell. Lysosomes are a form of vesicle that contain enzymes for digestion and are used to by the cell to consume material from the extracellular environment or dispose of damaged or unnecessary internal components. The separation of internal and external environments makes the plasma membrane a key area of interest to scientists looking to study how the cell interacts with the surrounding environment, or a delicate hurdle when introducing new materials into the cell. The barrier must be overcome, but not permanently damaged, as the loss of this boundary will cause the catastrophic loss of internal chemistry regulation, which would prove fatal to the cell.

The volume within the cell membrane is the cytoplasm. In this region, all of the internal components of the cell are supported in an aqueous gel, cytosol. This acts as an optimal environment within which to hold, transport and allow the intracellular chemistry, the working of the cell. Within the cell are a number of discrete components that perform specific functions for the cell as a whole, these are called organelles, in analogy to the organs of a full organism.

In the eukaryotic cell, the most prominent internal feature an observer will notice is the nucleus, an organelle which is clearly definable as a separate region within the cell. This contains the genetic blueprint of the organism, the long molecules of deoxyribonucleic acid, well known as DNA. It is from this genetic blueprint that the form and function of the cell is created and maintained, generating instructions for the production of proteins – the large molecules which are the molecular machinery of the cell; this overarching process is known as the Central Dogma of molecular biology. The DNA is encapsulated separately from the remainder of the cell by the nuclear membrane. Similar to the cell membrane, this is a separation formed by lipids. However, the nuclear membrane consists of two porous lipid bilayers that also facilitate transport of macromolecules. In order to produce proteins, a region of the cellular instruction set (DNA) is transcribed to produce a similar molecule chain, but in this instance, it is ribonucleic acid (RNA).

The RNA is transferred from the nuclear membrane into the cytoplasm of the cell where organelles, ribosomes, translate the RNA chain to produce the instructed protein. While ribosomes may be freely available within the cytoplasm, they can be attached to the rough

endoplasmic reticulum, a structure which is transiently bound to numerous ribosomes, facilitating protein translation. Proteins which are destined to be membrane bound will be transferred, via transport vesicles, to the Golgi apparatus – the organelle which facilitates the membrane binding of proteins. All of these specialised internal structures are responsible for creating the aforementioned molecular machinery, maintaining the cell and providing its functions.

To maintain function, the cell requires energy, this is produced via the process of respiration. Within eukaryotic cells, respiration is primarily a function of organelles called mitochondria. While capable of a wide range of processes, many of which owing to mitochondria containing their own genome, the single most significant process is the Krebs cycle. This biochemical process happens within the mitochondria and acts to add inorganic phosphate to adenosine diphosphate (ADP), creating adenosine triphosphate (ATP). At required sites, the ATP may then be hydrolysed to ADP by the cell – releasing energy stored in the ATP chemical bonds. The mitochondria is also a valuable indicator of cell health, and issues with mitochondria are related to numerous diseases.

Understanding the biology of the cell, the function of internal chemistry and the manner in which they work together is the foundation of the life sciences. The mechanisms of cell regulation, the genetics and protein machinery of a cell, are a key interest. These variables control growth, malfunction (disease), repair and attributes used widely throughout society from medicine to agriculture to energy production. It is the intricate complexity of these systems that also drives the need for techniques which induce minimal stress upon the cell, be that from the chemical stress of toxic particles to physical damage from mechanical or thermal stress.

1.4 Single cell analysis

Techniques for the study and manipulation of cells are common throughout biological laboratories. Cells contain a wealth of information that can be recorded in numerous manners. While cells of a population may appear near identical, they may still act in different manners. Studying the heterogeneities of a population, at the single cell level, can help in our deeper understanding of all biological functions, their reactions to environmental perturbations and expand our appreciation of the complexities of this

foundation level of life [2]. Practically, this can lead to greater understanding of genetic predispositions and disease progressions [3]. A great amount of this information is studied in the various ‘omics’ fields, covering the breadth of cellular functions. These include; genomics – the study of genome (DNA), transcriptomics – the study of the transcriptome (RNA) & proteomics – the study of proteins [4, 5]. Our understanding of processes at this scale can then be extrapolated to better understand the manner in which the biological pathways function and interact, in the field of systems biology [6, 7]. A variety of biological, chemical and physical techniques may be employed in the exploration of this information, from interaction with other cells to gel electrophoresis for visualisation of DNA fragments and atomic force microscopy (AFM) that allows for the imaging of materials on the atomic level. The tools are numerous, but the focus of this work will be placed primarily on a few specific examples of single cell analysis.

1.4.1 Genomics

The genome is the entirety of an organisms’ genetic material, the molecular blueprints that form the basis of each component of the cell. This scales to the attributes of a whole organism, defining physical traits and even disease. Genes provide the entire instruction set for protein production and even minor alterations in a gene can have a potentially fatal outcome for the cell or even an entire organism. This can provide an insight to genetic disorders and predispositions to diseases, such as cancer [8]. Mapping the human genome in the Human Genome Project was one of the largest biological experiments of recent years, taking nearly 20 years in total, from initial planning to fruition. This provided an unprecedented understanding of human genetics while also garnering significant media attention and public interest. It also saw the technology used in genetic study advance rapidly. Beyond the DNA, the genetic composition of a cell, the activity of the genes may then be unveiled by study of the RNA, the transcriptome, in the field of transcriptomics.

1.4.2 Transcriptomics

The transcriptome is the encompassing term for the RNA within a cell. Where the genome tells us the entirety of genetic information within a cell, the transcriptome allows us to understand the activity of the cell, which components of the genome are being transcribed and what final impact this has on the cell. This can highlight regions

of under- or over-expression and the effects this may have on the cell, whether it be a routine heterogeneity within the population or regulatory issues which may indicate disease. There are a range of techniques, from the earlier Serial Analysis of Gene Expression (SAGE) [9] and RNA microarrays [3] to the current hot-topic technique of RNA-Seq [10]. The miniscule quantities of material required means that techniques such as RNA-Seq are capable of analysing individual single cells [11]. This advancing range of high throughput devices allows for the rapid screening of thousands of cells, resulting in the generation of extensive bioinformatics data. This can be used to cluster sub-populations, aiding our understanding of biological systems and advancing research from cancer precursors to drug discovery [12]. The next logical step in this cellular study is that of proteomics, viewing the product of the transcriptome.

1.4.3 Proteomics

The entirety of protein within the cell is referred to as the proteome. While transcriptomics indicates the genes that are being transcribed from the genome, and the corresponding rates of expression, this doesn't necessarily correlate with the relative protein content within a cell. RNA is not uniformly translated to protein and beyond the production of protein, numerous subsequent cellular processes may alter or remove the proteins. Proteomic analysis can allow us a greater understanding of cellular processes and cellular reactions, leading to advances and novelties in applications, for instance, in clinical diagnostics; allowing for new biomarker targeting and increased sensitivity, towards objectives such as earlier disease detection [13].

1.5 Microfluidics

Classically, biological experimentation may use relatively significant volumes of reagents and samples, often on the scale of millilitres, while also requiring large scale and expensive equipment. The requirement for larger sample volumes, generally owing to a lack of sensitivity with a technique, may mask small heterogeneities within a population. These systems may also result in significant capital and consumable costs.

Counter to this, microfluidic devices operate on a significantly smaller scale, these devices allow miniaturisation of many laboratory processes, operating with volumes on the order of microliters or lower, on to a single physical structure [14 - 17]. These are

often referred to as a “Lab-On-a-Chip” (LOC). These devices can be extremely sensitive and capable of accurate use at minute test volumes [18], such as for single cell [19, 20] or single molecule [21] study. This low volume environment may also be used to monitor and test rapid physical changes, such as temperature shifts [22]. Using a LOC, the efficiency of processes may be increased with time and cost requirements reduced, this also allows improvements to be easily implemented in terms of parallel processing. The microfluidic architectures are not solely restricted to conventional analysis, allowing the design of novel methods to exploit cell morphology, such as cell sorting based on deformability [23]. Specificity and speed of use are of prime interest for medical application of LOCs, where it may become possible to generate immediate results for a patient without the requirement of offsite processing [24]. Alongside techniques developing advanced microfluidic devices, there is also an interest in exploiting the cost minimisation for medical devices in impoverished areas, such as the work by Whitesides and colleagues in producing ‘zero cost’ microfluidics [25]. Microfluidic devices are tools with a truly multidisciplinary scope and are implemented in a broad range of applications, many of which having transitioned from the laboratory bench into the general consumer market. These devices offer a host of applications to biological research and beyond.

1.6 Photonic tools

Light is arguably the most powerful physical property for biological study on the microscopic scale. It is intrinsically non-invasive, the manipulation of light allows for the imaging of structures that could not be resolved by the naked eye – a feat which may be performed while maintaining cells in their optimal environments, without sacrificing sterility. Fluorescence can also be employed to study properties that would otherwise not produce a visible effect, by use of probes, dyes or fluorescence protein generation.

1.6.1 Microscopy

The microscope is one of the most influential tools available for biological study, allowing the user, by manipulation of light, to magnify their view of a sample and observe greater detail than possible with the naked eye. The history of microscopy is vast, with primitive forms of magnification being attributed to numerous ancient groups. However, the origins of the modern compound microscope arise towards the end of the 16th, and into the 17th century [26].

Microscopes typically consisted of two lenses, requiring an objective lens, to focus on the sample of interest, and an eyepiece lens, which focuses the image generated from the objective lens, into the eyes of the user, this is illustrated in Figure 1.2.

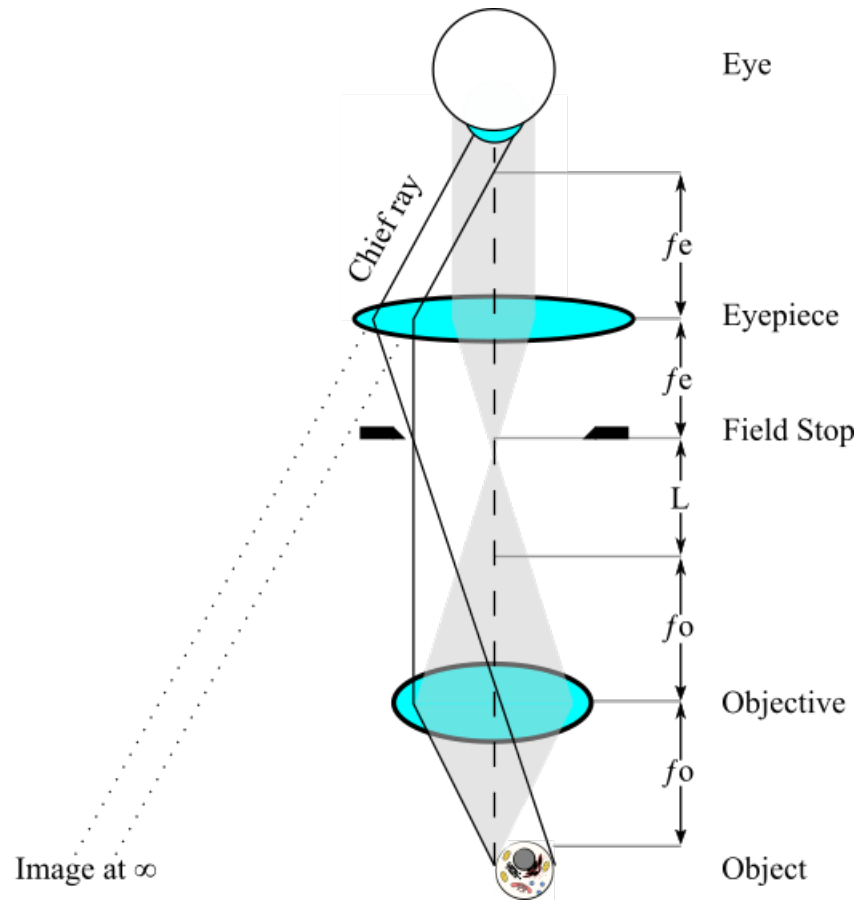


Figure 1.2 – The compound microscope. The objective lens focuses on a target object at the focal length of f_o . An eyepiece lens, with a focal length f_e , acting as a magnifier, forms an enlarged image of the object (Image at ∞) for the viewer. The objective lens is separated by a fixed tube length (L) from the eyepiece lens with the field of view limited by the field stop. Based on Figure 5.98, Hecht (1987) [27].

Advances in optical design and manufacture has allowed the production of multiple component objective lenses, reducing optical and chromatic aberrations, increasing the image quality and spectral bandwidth. A growing range of laser emission wavelengths and optical filters has driven the advance of powerful microscopes for the detection of fluorescence. The rise of digital light sensors has revolutionised the capture of microscope images and allowed incredibly low-light image capture with the most advanced sensors capable of detecting single photons. Coupled with modern

computational power this has also allowed numerous benefits, such as signal tracking and the generation of three dimensionally mapped images. These factors have seen the development of many specialised forms of microscopy, for instance, the maturation of confocal microscopy, which allows the generation of images with narrow focal depth, significantly reducing blur caused by out of focus light.

1.6.2 Cytometry

Cytometric analysis embodies a range of techniques that are designed to quantitatively measure characteristics and variables of a cell. The data that can be harvested from a single cell is extensive.

The most common cytometry technique is flow cytometry. This technique takes cells in suspension and using hydrodynamic focusing, produces a laminar flow of cells that are interrogated individually – allowing for the generation of analytical data or to physically isolate cell populations of interest, by use of specialist cell sorting instruments. Interrogation is carried out using a laser, or multiple lasers, focused on fixed point that the cells pass through. The light that is scattered from the cell, and any fluorescence generated, is captured by photodetectors that allow multiple parameters to be viewed simultaneously. The data from these detectors may be used to optimise instrument settings, recorded for analysis or used to define populations for cell sorting.

These techniques are used to view differences in cell populations. Cell populations can be identified by surface markers, morphological properties may be determined by light scatter, and staining techniques can define parameters such as the cell cycle stage or viability of cells [23]. Commercial devices are now entering the market which allow imaging to be produced simultaneously with this flow cytometry data, in essence combining flow cytometry with microscopy, in what are called imaging cytometers.

1.7 Biophotonics

Photonics is the branch of physics which encompasses the understanding and exploitation of photons, the quanta of light. While light is of key importance to life, primarily via the process of photosynthesis, the understanding of light itself is often neglected by purer biological studies. Today this artefact is founded at the early stages

of secondary education, where the study of hard sciences is partitioned into the fields of biology, chemistry and physics and the intertwined features of the sciences are typically not a point of focus. While this separation is maintained, to a degree, in tertiary education, the options for cross disciplinary study become more apparent with fields such as physical chemistry and biochemistry. However, the interface of biology and physics often remains a neglected facet of scientific study. Classically, the study of natural philosophy encompassed a significantly broader realm than the niches typically occupied in modern science, such as Newton's descriptions of the optical functionality of the anatomy of the eye [28]. However, while the rise of the humble microscope was pivotal to the birth of the field of cell biology, it took later technical advances to develop techniques which further exploited light, in order to influence the cell.

The latter half of the 20th century saw the rise of the laser and the photonic revolution began. The biological and medical sciences were among the many fields benefitting from the expansive advance in techniques and applications afforded, primarily, by the inventions of the laser and detector. Allowing distinct fields to fuse, this gave rise to the now growing field of biophotonics, photonics driven techniques with biological applications. An early example was shown by Bessis et. al, in 1962. By using focused laser light, they were able to show an example of the power, application and impact of these new light-emitting devices could have in the life sciences when they produced the first laser scalpel [29]. A photonic device that used the ruby lasers of the day to crudely ablate tissue. With the maturity of the classic fields of scientific study, it is the interface of these fields that is yielding some of the most exciting advances in science and technology.

While the range of photonic techniques applicable to the life sciences is phenomenal, from novel photodynamic therapies in medicine [30, 31] to advanced imaging techniques [32, 33], or the incorporation of micro- [14-25] and nanoscale [34] experimentation with lab-on-a-chip devices, the following body of work will focus on a few specific techniques. In particular, the techniques utilizing highly focused beams of laser light for applications on single cells: photoporation and optical tweezers.

Chapter 2

Laser driven transfection of pancreatic cells with activated *KRAS*

2.1. Introduction

Cancer is one of the largest causes of mortality in the developed world. Research into understanding, preventing and treating cancer is one of the largest fields of medical study. Cancer Research UK alone, spends in the region of £400m per year on cancer research, of which approximately 33 % is focused on studying the biology of cancer [35]. As the traditional fields of scientific study mature, there is a greater onus on the development and implementation of new technologies stemming from interdisciplinary collaboration, to further our understanding of cancers [36]. The focus of this chapter is to investigate the use of laser assisted transfection in the study of cancer.

Tightly focused pulses of light are used to punch transient holes in cell membranes, a technique called photoporation, this allows for the insertion of exogenous genetic materials into the cell [37]. This emerging optical transfection technique is used in order to facilitate the genetic modification of cells key to the progression of pancreatic cancer. Modification, in this instance, seeks to introduce an activated gene that is present in a high proportion of incidents of pancreatic cancer – with the goal of creating a stable cell line which expresses the *KRAS* gene. Photoporation is used to facilitate this genetic modification, using high-energy pulses of laser light to induce a transient pore in the plasma membrane of a cell. This temporarily overcomes the barrier that encases the cell and allows the transfer of material, in this instance, nucleic acids, from the extracellular environment to the intracellular.

2.2 Background

In this subsection the topics and literature relevant to this course of research are reviewed. The biology of cancer is introduced, including the principles of genetics and the implications of genetic instability. The broader societal impact of the disease in developed nations is briefly explored. A particular focus is shone on pancreatic cancer and its specific oncology. General techniques used to study the genetics of such diseases are reviewed and summarised. Laser driven devices that can be applied to the research of genetic disease are introduced with the different applicable techniques of photoporation reviewed.

2.2.1 Cancer

Few medical diagnoses permeate the zeitgeist, eliciting such a powerful emotional response, as that of cancer. While the term embodies a significant number of different diseases, they all hold the common element that the disease is caused by uncontrolled growth, not of a foreign pathogen, but of the sufferer's own cells. Cancer can be said to be a disease of dysregulated proliferation [38]. The societal impact of cancer in the UK is significant. Cancerous disease accounts for approximately 162,000 of the 550,000 deaths per year in the UK, almost 30 % of all mortality [39 - 41], with recent approximations now placing the lifetime risk of cancer at 53.5 % for men and 47.5 % for women in the UK [42].

Cancer itself is a broad term used to describe the development of malignant neoplasms. These are new tissue growths that occur when there is a loss in cellular regulation and cells which should not be able to, generate the capacity to spread to new tissues. Simply, these uncontrolled growths of tissue impede the normal function of tissues, eventually proving fatal to the sufferer. While the term cancer is applicable to a broad range of individual diseases – dependent on location, cell type and pathology of the cancer – Hanahan and Weinberg describe the generalised requisite traits as the ‘Hallmarks of Cancer’: resisting cell death; sustaining proliferative signalling; enabling replicative immortality; evading growth suppressors; inducing angiogenesis; and activating invasion and metastasis [43, 44].

In the human body, as with most multicellular organisms, it is important that individual cells maintain a degree of self-regulation. The genetic instructions, genes, in the cell define the on-going protein production and manner of response the cell will take to various stimuli. Mutations in some genes generate errors in these instructions that can then cause a suppression or upregulation of critical responses. When such a gene has the potential to contribute to the formation of a neoplasm, it is said to be an oncogene. A key factor of self-regulation is the ability of the cell to self-sacrifice in order to maintain the greater organism. When there is a radical change in normal response from the cell there is an upregulation of the genes responsible for apoptosis – programmed cell death. A prime example is one of the main factors in this response pathway, p53. This gene induces apoptosis in response to DNA damage and is found to be damaged or suppressed in > 50 % of malignant neoplasms [45 - 47].

There are several factors that can induce oncogene modification. These can be attributed to proof reading errors in genetic replication or a number of environmental stimuli. Healthy genes will mutate during a person’s life. If these mutations occur as a result of an error during replication, these will typically be detected and repaired by the DNA polymerase enzymes that are responsible for facilitating the replication. A spontaneously generated mutation should result in the upregulation of apoptosis, inducing programmed cell death to sacrifice the cell, in order to maintain the genetic integrity of the organism. In many forms of the disease there may also be an inherited genetic pre-disposition, this can dramatically increase the likelihood of developing a related cancer.

While it is simple to note that mutation can lead to the development of cancer, the diseases are typically not limited to a single mutation. Typically, a cell will lose a degree of regulation and continue dividing as normal, with subsequent mutations appearing in tissues that become increasingly closer to presenting all of the aforementioned hallmarks of cancer. This is represented in the illustration in Figure 2.1.

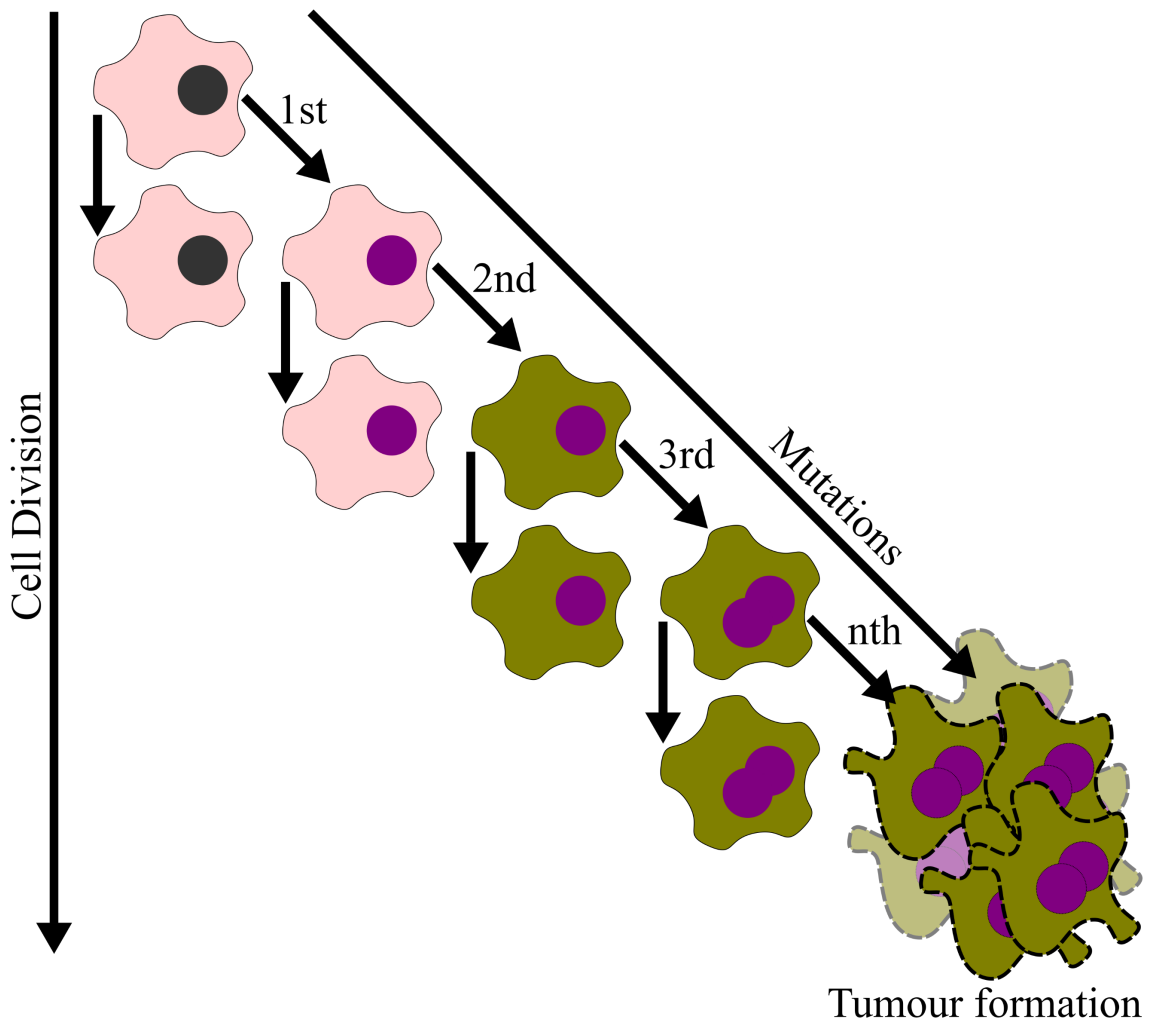


Figure 2.1 – Cancer progression. An illustration visualising the stacking effect of mutations that can lead to the development of cancer. As a mutation – that does not result in cell death – occurs (1st), it persists through cell division. The integrity of the cells in a tissue is compromised and this may result in increased susceptibility – often due to loss of regulatory control – to subsequent mutations through time (2nd, 3rd, nth). Subsequent mutations may also persist through cell division and result in tumour formation.

While different types of mammalian cell will present various specialised functions, their general facilities are common. With such commonalities it is possible for any cell type, capable of proliferation, to become malignant. Therefore, it is possible for cancer to arise in any tissue within the body. However, as there are several different stimuli that can increase the chances of a cancer arising, it is to be expected that cancers do not present equally throughout all tissues; similarly, the prognosis of each type of cancer is not equal. Of the regularly occurring cancers, it is cancer of the pancreas that has the lowest survival rate and where we now apply photoporation methods to try to further understand the disease [48].

2.2.2 Pancreatic cancer

Where all cancers are life threatening, to varying degrees, it is cancer of the pancreas that is the most damning diagnosis. The pancreas is a tadpole shaped glandular organ with dual exocrine and endocrine function and is largely regulatory in purpose. The exocrine function is responsible for the release of an alkali secretion of digestive enzymes, via the pancreatic duct, into the small intestine in order to assist digestion. Endocrine function is in the form of hormone production, where the pancreas is responsible for the production and release of several hormones, such as insulin and glucagon, into the bloodstream.

Organs consist of a heterogeneous compliment of cell types in a structurally significant arrangement. Anatomically, the pancreas has three separate regions: the head; the body; and the tail, illustrated in Figure 2.2. The composition of the pancreas consists of multiple specialist cell types clustered in defined structures. Interspersed throughout the pancreatic tissue are the islets of Langerhans, these islets are clusters of cells responsible for the endocrine function of the pancreas and as such are connected to the blood supply. The largest population of cell cluster structures are the pancreatic acini which provide the exocrine function, producing and releasing enzymes into the ductile network which leads to the main pancreatic duct which in turn leads to release into the small intestine via the major duodenal papilla. A lining of epithelial cells produces the duct structure, which facilitates the secreted enzymes within the pancreas.

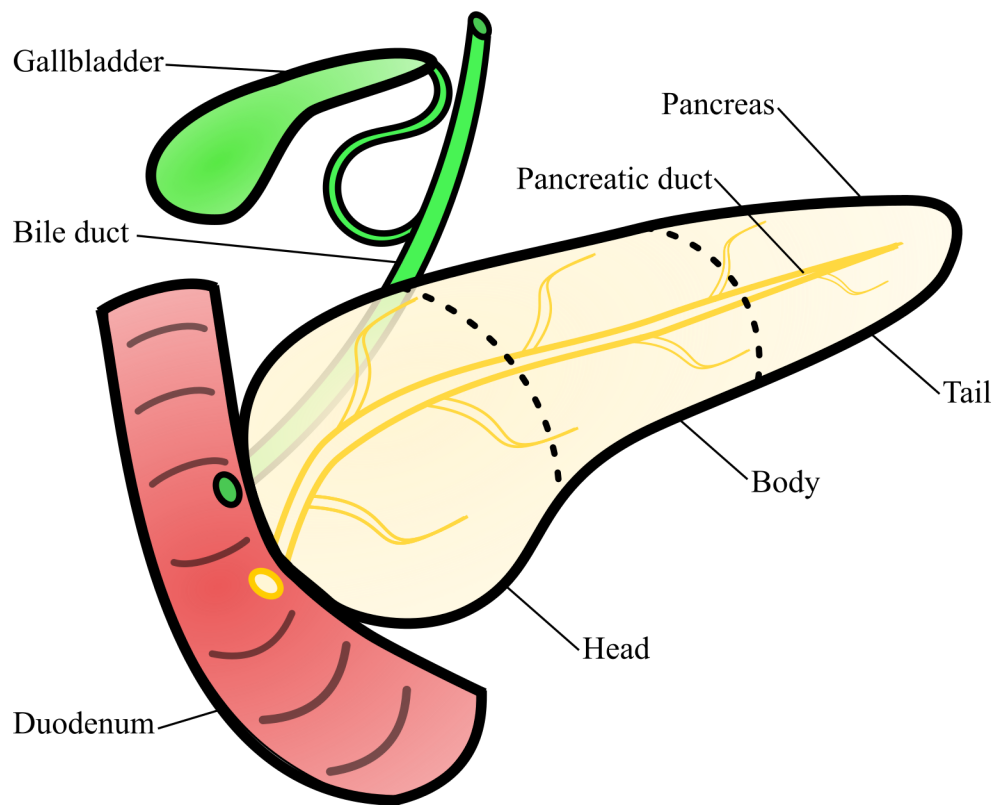


Figure 2.2 – The pancreas. The main body regions: head, body & tail are denoted, separated by dashed lines. The pancreatic duct traverses the length of the pancreas, connecting to the duodenum.

Cancerous growths can potentially rise in any region and from any cell type within the pancreas. However, while there are various forms of pancreatic cancer, they occur primarily in the head region of the pancreas, where ~85 % of pancreatic tumours are found. There, the most common type of tumour is the ductal adenocarcinoma, which is formed in the epithelial lining of the pancreatic duct, accounting for ~90 % of the tumours in this region [49 - 51]. These tumours are thought to originate and develop initially in the epithelial cells that form the lining of the pancreatic duct. There is, however, some evidence that some of these tumours may be initiated in the exocrine clusters of the pancreatic tissue [52]. While the ductal connection to the small intestine and gallbladder can act as a point of connection for tumour progression, the vascularity of the pancreatic endocrine system provides the capacity to spread widely throughout the body. It is usually only when the cancer has metastasised that it becomes symptomatic. The resultant late diagnosis is one of the greatest issues with pancreatic cancer prognosis and is one of the reasons that it has such a high mortality rate. In the UK, the one-year survival rate of pancreatic cancer is 22 % with the five-year survival rate dropping to 4 % [53].

The high rate of mortality is one of the key motivators of pancreatic cancer research. The main objectives of this research are to improve the diagnosis time and to provide drastically improved treatments. Considering ductal adenocarcinoma, as this is the most common form of pancreatic cancer, one of the most common mutations is found in the loss in regulation of the *KRAS* oncogene. This oncogene and the regulation of it becomes a significant component in the understanding of most pancreatic cancers [54, 55].

2.2.2.1 KRAS

Cell responses are mediated by a variety of chemical signals and pathways. While signalling can occur in a number of ways, cell-signalling pathways are typically performed by proteins. Proteins provide a high degree of binding specificity, this is important as it significantly reduces the risk of misbinding, which could induce a detrimental outcome to the cell or organism. The high binding specificity of proteins comes from the tertiary structure of the protein, the shape of the molecule dictating the molecules with which the protein interacts, not unlike a key in a lock.

This work focuses on the V-Ki-ras2 Kirsten rat sarcoma viral oncogene homolog protein, also known as *KRAS*. This protein is coded by the oncogene *KRAS*, which is a member of the broader family of *RAS* genes [56]. *KRAS* proteins are membrane bound and crucial for the regulation of a range of processes within the cell. The regulatory function is that of a molecular switch. The “off” state *KRAS* is bound to a guanosine diphosphate (GDP) molecule. External stimulus by cytokines, growth factors and hormones - or specific internal Guanine Nucleotide Exchange Factors (GEFs) can induce the addition of a phosphate to GDP, converting GDP to guanosine triphosphate (GTP), resulting in the activation of *KRAS*. Once activated, *KRAS* acts as a node that promotes several downstream pathways that are responsible for cellular proliferation and transformation. In healthy operation, feedback signalling causes several GTPase Activating Proteins (GAPs) to induce GTPase enzymes to hydrolyse the *KRAS* bound GTP to GDP, thus inactivating the *KRAS* [55]. This activation-inactivation molecular cycle is illustrated in Figure 2.3. However, problems can arise with even a single point mutation in the encoded *KRAS*.

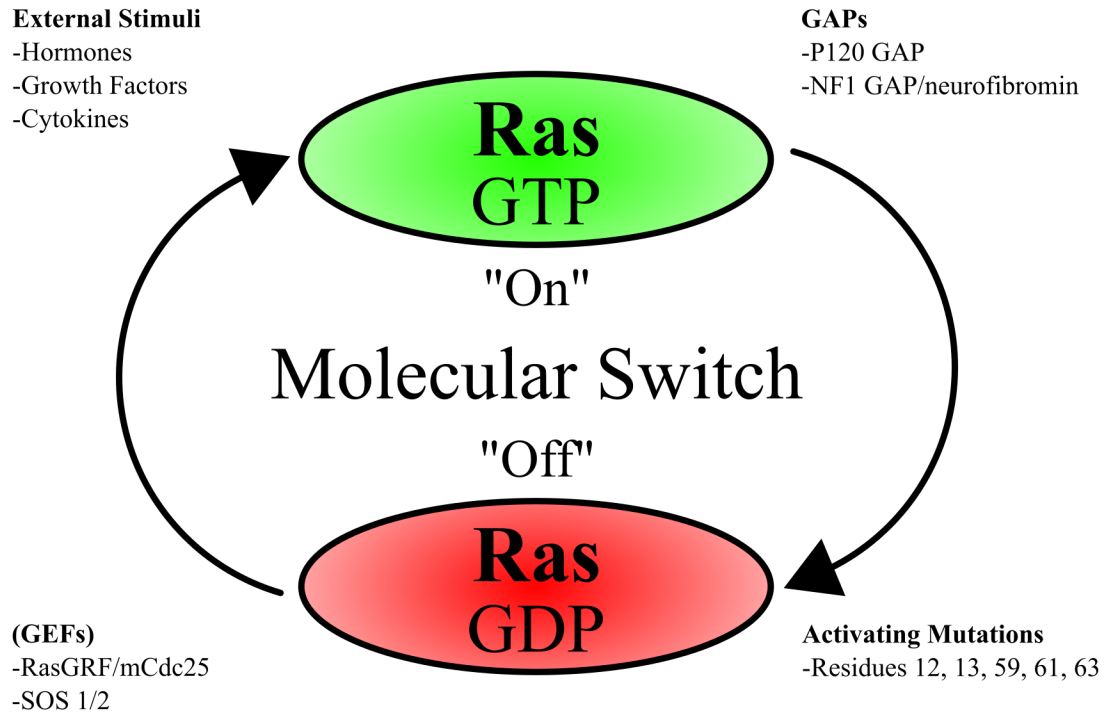


Figure 2.3 – RAS switching. The cycle of activation and inactivation of the RAS family of proteins. Molecular switch state depends on the bound GDP (inactive) or GTP (active). Stimuli induce the addition of a phosphate group, binding to the GDP to form GTP, activating the protein. Feedback signalling uses GAPs to recruit GTPase which hydrolyses GTP to GDP, inactivating the protein. Based on Figure 1, Ellis & Clark (2000) [55].

Mutations in the *KRAS* gene have the potential to arise throughout the gene but are generally found to be present at a limited number of specific areas. These hotspots for mutation are reported to be the 12th, 32nd, 33rd and 61st codons [55]. The frequent occurrence of mutations at these specific codons provide specific mutations of interest. The primary effect on the *KRAS* proteins produced after these genetic mutations, is that they become desensitised to GAPs. Stimuli will then cause the activation of *KRAS*, however, the feedback pathways that revert *KRAS* to the inactive state cease to work, leaving *KRAS* locked in the active state. While stuck in the active stage, *KRAS* will continue to promote the upregulation of proliferative and transformative signal pathways in an uncontrolled manner [57 - 61], this is illustrated in Figure 2.4.

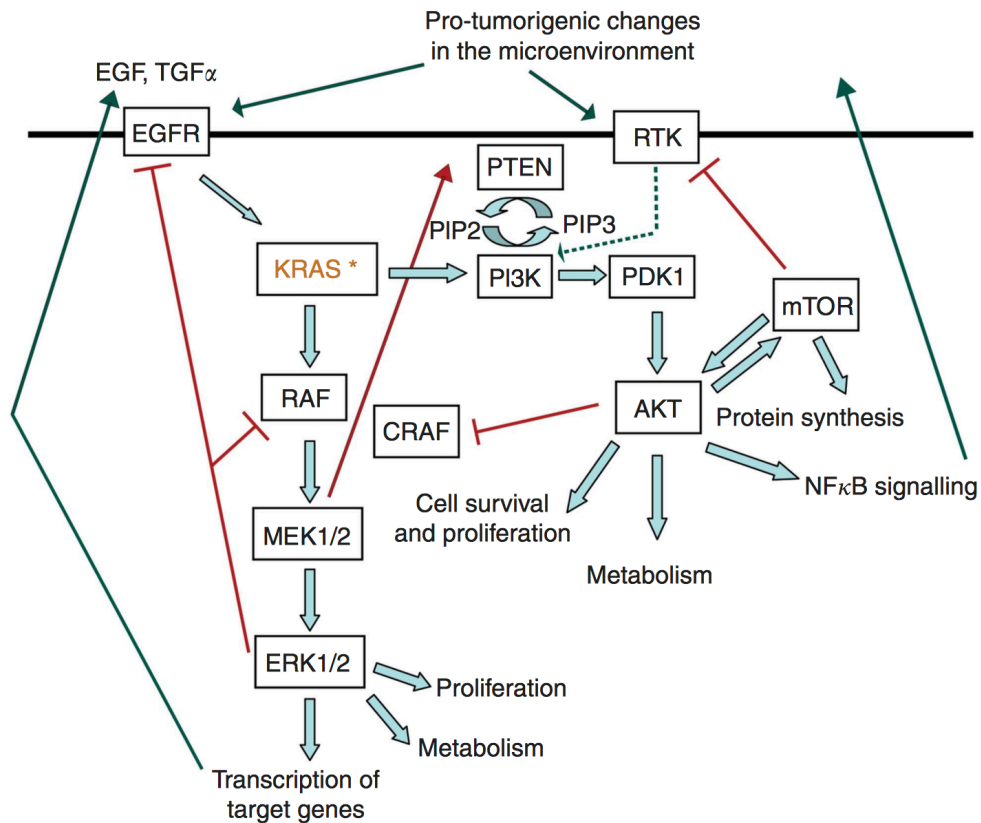


Figure 2.4 – *KRAS* activity. The numerous interactions of *KRAS* with key pathways of metabolism, proliferation and cell survival. Where mutation causes a loss of regulation, these cellular processes contribute towards the previously defined ‘Hallmarks of Cancer’. Taken from Figure 1, Eser *et al.* (2014) [61].

Due to its frequent presence, to the point of near ubiquity in some neoplasms, *KRAS* is widely viewed as a key target for early detection, treatment and even pre-treatment of cancers. Creating a cell line which intrinsically presents a mutated form of *KRAS* would provide a powerful biological tool for the continued study and pursuit of treatments [62 - 65].

2.2.3 Transfection

One of the most powerful advances in the past century of biological research has been the discovery and subsequent decoding of the genome. Studying the mechanisms of the genome, particularly where there are issues, allows the progression of genetic diseases to be understood on the biochemical level. With the growing knowledge around

the genome there have been many advances in the techniques that can be used to manipulate the genome. Through genetic manipulation it is possible to add or modify genes, inducing genetic disorders or incorporating beneficial traits. Genetic additions are typically added via a vector, such as a plasmid, that is independently functional, outside of a chromosome. When applied to eukaryotic cells, the addition of external genetic material is called transfection.

2.2.3.1 Transfection techniques

There is a broad range of transfection techniques in the toolbox of biological methodology. The techniques share the common goal of overcoming the physical barrier of the cell membrane temporarily, allowing the insertion of genetic material from an external source, while maintaining the viability of the cell. Transfection techniques are multidisciplinary with established techniques based on biological, chemical and physical processes.

The biological approach to transfection is transduction, this exploits the naturally occurring processes used by various types of virus. The virion, the distinct virus particle, is a biological particle but does not constitute a living entity; viruses can be said to be found at the boundary of life. These particles do not have the capability to replicate, requiring a host cell in which to hijack the sequencing mechanics and generate new viral particles. While these vary widely in structure, they all contain the genetic instructions required to create clone virions and a surrounding shell, the capsid. For genetic modification it is possible to fabricate modified viral particles, taking an existing mechanism for inserting genetic material and tailor the genetic contents as desired [66].

It is possible to manipulate the chemistry of the cell membrane in order to insert genes of interest into the cell. Liposomes can be fabricated which contain a specific gene. Liposomes are a form of vesicle, a bubble of phospholipids that contain the additional genes of interest. As these are created using phospholipids, the same material that forms the cell membrane, these can merge with a cell membrane and release the genetic material into the cell [67]. Genetic material may also be bound in a calcium phosphate precipitate. This precipitate is then added to a cell culture and is absorbed by the cells within the culture [68].

Physical and mechanical techniques may also be used to facilitate transfection. Techniques such as microinjection [69, 70] or impalefection [71] use mechanical force to pierce the cell membrane and introduce genetic material into a target cell. A similar effect may also be produced using particle delivery systems, such as magnet assisted transfection, which uses magnetic fields to drive particles with bound genetic material into cells within a sample [69, 72] or ‘gene guns’ which ballistically launch microparticles of materials such as gold or tungsten, which are similarly coated in genetic material, into a target organism – which is particularly useful in plant sciences where the microparticles must overcome the thick cell walls present around plant cells [73, 74]. Pores may be generated in cell membranes by the use of short bursts of high intensity electrical fields or ultrasonic waves, in electroporation and sonoporation respectively [69, 72]. Recent work at MIT has also reported the potential of transfection via cell squeezing in microfluidic devices. The reported device mechanically deformed cells through a narrowing with a smaller diameter than that of the cells. The compressive and shear forces on the cell resulted in the formation of transient holes in the cell membrane, allowing material from the extracellular environment to enter the cytoplasm of the cell [75].

With different efficiencies and potential drawbacks, these methods are all capable of overcoming the cell membrane and allowing transfection to occur. However, there is a common attribute to most of these that may be detrimental to the goals of the research, and that is the lack of specificity. Barring an invasive, mechanical intrusion into the sample, these techniques will affect all of the cells in the sample or within a target range. In some instances, it may be of interest to target a single cell or specific cells of interest within a sample. To attain this while also maintaining a closed, sterile, sample chamber we look to the light. More specifically, laser sources, in the technique known as photoporation.

2.2.3.2 Photoporation

The importance of light manipulation in biological research was introduced earlier, with the microscope. While light-based techniques generally use light in an observational role, with minimal impact on biological samples, photoporation is one of the biophotonic techniques that make use of light in a more active manner, directly affecting cells of interest.

Photoporation creates transient submicron pores in the membrane of cell, allowing a brief window of time for membrane-impermeable molecules from the extracellular environment to enter the cell [37]. While the use of a laser to generate micropunctures in cells was first reported at the dawn of the ruby laser in the early 1960s [76], it was Tsukakoshi et. al. who first reported example of photoporation as a transfection mechanism in 1984 [77]. The authors produced 5 ns pulses of light from the third harmonic of a neodymium doped yttrium aluminium garnet (Nd:YAG) laser (355 nm) and coupled this into an Olympus BHT-NE microscope. The light was focused onto the membrane of rat kidney cells using a 32x Zeiss Ultrafluar microscope objective to induce a submicron pore and allow an exogenous *Escherichia coli* gene for glutamic pyruvic transaminase (*eco gtp*) to enter and be expressed by the target cell. Systems in this regime were used to great effect in the early development of what is now referred to as photoporation. These approaches used a relatively low magnification microscope objective, which, when coupled with the high pulse energy of these nanosecond laser sources generated a broader area effect than that found in later photoporation techniques.

A great facilitator of photoporation was the development of the stable, ultrafast, self-mode-locking Titanium Sapphire (Ti:Sapph) lasers in 1991 [78]. These systems allowed the stable generation of femtosecond pulses of 800 nm laser light. Beneficially, these systems proved to provide pulses in an energy range and with a wavelength of light with reduced phototoxic effects, compared to the 355 nm source used in the earlier work [77, 79]. The first work in producing this photoporation effect was reported by Tirlapur and König in 2002, using a Ti:Sapph laser which was emitting 800 nm at 80 MHz, with an average power of 50-100 mW [80]. The primary focus of these studies tends to be on mammalian cells [80 - 85]. However, this technique has also been shown to be functional for plant cells [86, 87]. This is owing to the similar physiology of all cells, but shows particular effectiveness considering plant cells contain the additional barrier of the cell wall. Ultrafast photoporation has also been facilitated by use of fibre lasers, and a number of different source wavelengths [88, 89].

The focusing of collimated, coherent light from a femtosecond laser source through a high numerical aperture (NA) microscope objective lens will create a very small focal volume with an incredibly high density of photons. When this high-energy pulse of light is focused onto a cell membrane, a multiphoton effect occurs. This creates a low density free-electron plasma within the molecular structure of the membrane, creating a transient,

submicron diameter pore [83, 90]. During the brief existence of this pore, a volume, on the order of femtolitres, is transferred from the exogenous environment around the target cell, into the intracellular environment, while the cell remains viable [91].

Research into the application of photoporation has been modified and advanced through the introduction of additional optical elements. Notably, a non-diffracting Bessel beam can be generated in order to overcome the small focal depth produced when a beam is tightly focused using a conventional microscope objective. This technique was reported by Tsampoula et. al. in 2007 [92]. Overcoming the shallow depth of focus is ideal for applications involving biological samples. While the reality of these beams presents a finite distance through which diffraction is limited, they still provide a greater focal depth than conventional microscope objectives. As individual cells to be targeted for photoporation are not uniform in size and shape, a larger focal depth increases the likelihood of striking the cell membrane with sufficient energy.

Inducing transient pores in the cell membrane is not limited to the use of pulsed lasers; sources that generate short, intense pulses of light that are in the region of nanoseconds to hundreds of femtoseconds long. Successful attempts at the photoporation of a variety of cell types have also been reported using violet (405 nm) continuous wave laser sources [93]. While these techniques increase concern of wavelength dependent phototoxic effects, they are beneficial in that it significantly decreases the cost of implementation of photoporation, using laser sources which are a fraction of the price of ultrafast Ti:Sapph or fibre laser systems.

The addition of dyes and particles have been used to induce photoporation effects with sources that otherwise would not be capable. A number of dyes, such as indocyanine green and phenol red, have been used to increase the absorption of light to facilitate photoporation [94, 95], making photoporation feasible with a 488 nm laser source [95]. Approaches involving gold nanoparticles [96], which may be conjugated to antibodies in order to increase specificity [97], being used to permeabilise the cell membrane due to photothermal effects caused by the absorption of visible light (561 nm [96] & 532 nm [97]).

The lack of commercial systems leads to the requirement of laboratories to produce their own photoporation systems to accomplish the required effect. Owing to issues in

attempting to introduce a faulty *KRAS* gene into pancreatic duct epithelial cells with conventional transfection techniques, the work in this chapter was to investigate the feasibility of using photoporation to transfect pancreatic cells to create stable cells lines for cancer research. This required the design, building and testing of a photoporation system, the design of which is outlined in the following section.

2.3 Experimental methods

This section describes the experimental methods applied for the optical transfection of *KRAS* into HPDE4 cells. The optical design and computer controlled nature of the photoporation instrument is presented. Culture techniques required for maintaining the relevant cells and sample preparation are described. The application of the photoporation apparatus is then described, including techniques to etching glass microscope slides and photoporation of target cells. Fluorescent microscopy, used in recording the effects of transfection, is also described.

2.3.1 Optical design

The photoporation system, designed to transfect cells, was constructed to accept the input from one of two laser systems to be tested for their use in transfection experiments. Both of the laser systems used were ultrafast sources that generated sub-picosecond pulses of light. These were a Spectra Physics Hurricane Titanium: Sapphire (Ti:Sapph) laser system and a Fianium FemtoPower HE1060-fs fibre laser system.

The Spectra Physics Hurricane is a system which houses a pump laser, seed laser, regenerative amplifier and pulse compressor in an integrated device. This unit was tuned to generate $\lambda = 800$ nm light in >130 fs pulses. These pulses were >0.25 mJ, linear horizontal (parallel) polarised and generated at 5 kHz. The output of the laser was TEM_{00} with a 6 mm beam diameter. The Fianium FemtoPower system generated $\lambda = 1064$ nm light in 430 fs pulses. These pulses were 1.1 μ J, TEM_{00} , linear vertical (perpendicular) polarised and generated at 1 MHz. This system used an additional collimator and beam expander to bring the beam diameter to 6 mm and a half-wave ($\lambda/2$) plate was used to adjust the output polarisation from linear vertical to linear horizontal polarisation. The output of these systems was guided by silver mirrors into the photoporation apparatus. One of the mirrors was mounted on a flip stand which allowed that mirror to be removed

from, or added to, the beam path in order to select the laser system which was being used in these experiments. A schematic of the optical layout is displayed in Figure 2.5, this is followed by a detailed description of the system.

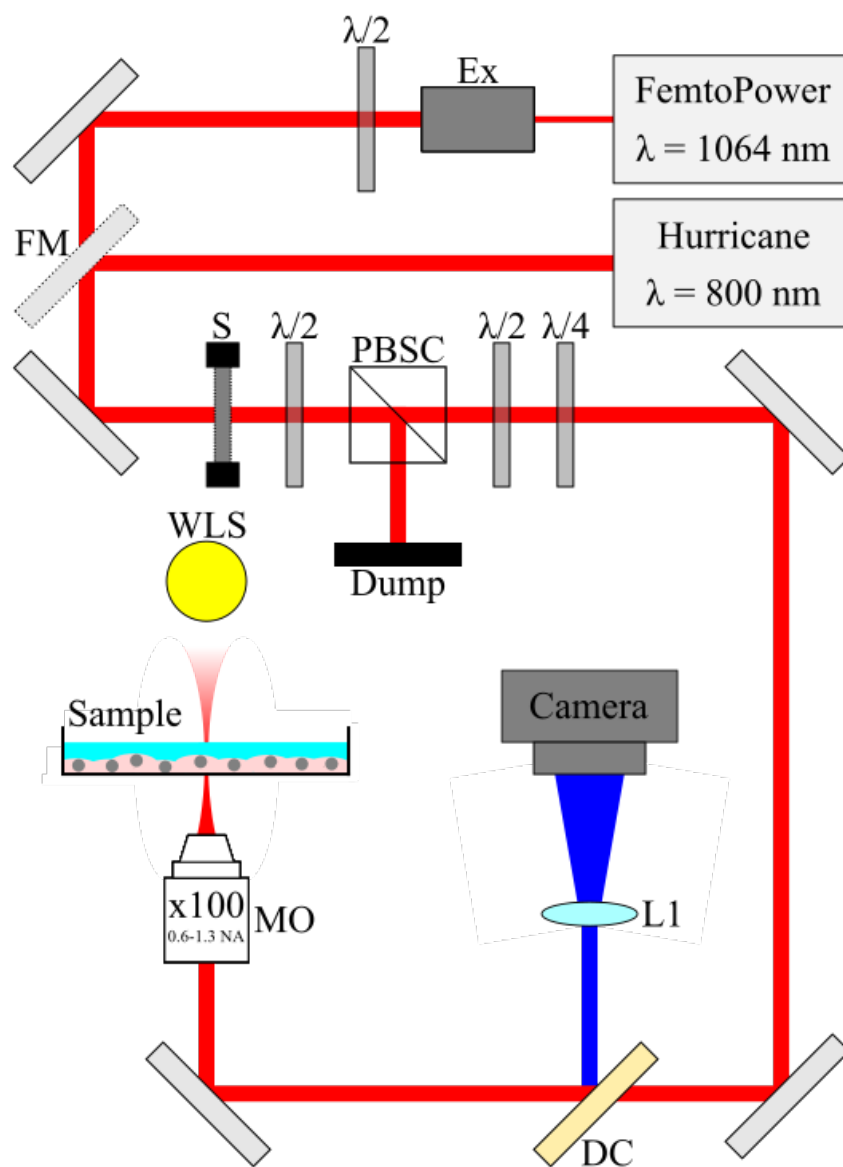


Figure 2.5 – Schematic diagram of the photoporation apparatus. The red line indicates the beam path from the denoted laser sources, guided by mirrors. A beam expander (Ex) was required to increase the beam diameter from the Fianium FemtoPower ($\lambda = 1064$ nm) and an additional flip mount mirror (FM) was used for introducing the Spectra Physics Hurricane ($\lambda = 800$ nm) beam. The beam is restricted by use of a shutter (S) and attenuated by use of a polarised beam splitting cube (PBSC), and half-wave ($\lambda/2$) and quarter-wave ($\lambda/4$) plates. A microscope objective (MO) is used to focus the beam onto the sample. A white light source (WLS) is used to illuminate the sample, with the blue line indicating the path of the gathered image as it is redirected by the dichroic mirror (DC) and imaged onto a camera via a pseudo-eyepiece lens (L1).

The beams were directed into a section that allowed fine power, polarisation and exposure control. The first stage of the section was an electronically triggered shutter (ThorLabs, SH05) capable of limiting exposure time within the system to 100 ms with the available controller (ThorLabs, TSC001). The beam then passes a $\lambda/2$ plate in a perpendicular rotary mount and a fixed polarised beam splitting cube. The rotational position of the $\lambda/2$ plate alters the polarisation of light that has entered the system. The PBSC splits the light depending on polarisation state. Parallel polarised light passes through the PBSC unaffected, perpendicularly polarised light is reflected at 90° into a beam blocker. This allows the power of the laser light entering the system to be adjusted. The light then passes through another $\lambda/2$ plate and a quarter-wave ($\lambda/4$) plate, each in independent rotary mounts. This configuration allows the polarisation of the light entering the system to be adjusted to linear and circular modes. Additional power reduction – described later - was used in testing the 5 kHz, $\lambda = 800$ nm laser system, as power levels were found to require additional attenuation. This was attempted using fixed and variable (rotary) neutral density filters. Beam steering using silver mirrors in kinematic mounts guided light into the photoporation and imaging section of the system.

Photoporation and imaging was achieved in the next, and final, section of the system. The beam was directed through a fixed position mount, held at 45° to beam propagation, which held a dichroic mirror (DC). A 567 nm longpass DC was used with the $\lambda = 800$ nm laser system. However, when using the $\lambda = 1064$ nm laser system, this DC mirror was found to reflect a notable proportion of the laser light, saturating the camera and rendering it ineffective. Therefore a 932 nm longpass DC was used with this system. Using a final silver mirror, the beam was directed vertically, upwards into the rear aperture of a 100x oil immersion microscope object (MO), variable NA 0.55-1.3 (Olympus Plan Fluorite, ThorLabs, RMS100X-PFO). The microscope objective was used to focus the laser light into the sample. An image of the sample was gathered utilising the same 100x oil immersion MO and a white light emitting diode (LED) suspended above the sample surface, comparable to an inverted microscope configuration. This MO is infinity corrected, so image divergence is negligible over the path lengths present in this apparatus. The image is transmitted counter to the path of the laser and reflected by the longpass DC mirror. The image is then focused using a $f = 50$ lens into a CCD camera (ThorLabs, DCU223C) which is connected to a computer. Given the open nature of this apparatus, it was possible to take power measurements (ThorLabs, S302C head with ThorLabs, PM100D meter) at multiple points within the system.

A custom mount held 35 mm diameter sample chambers. The mount was suspended using three linear actuators (ThorLabs, MTS50-Z8) mounted in a three-dimensional array (ThorLabs, MTS50C-Z8). Each actuator had an independent control unit (ThorLabs, TDC001) connected to a computer. These allowed for programmed movement of the sample through the focal point of the laser beam. Two actuators provided movement across a plane, perpendicular to the beam path. The third actuator provided movement in the direction of beam propagation, effectively as a focus control.

2.3.2 Computer control

Photoporation requires precision irradiation of target cells, so to make the exposure conditions as consistent as possible the motorised stages and shutter were controlled using a custom build computer interface.

A control program was produced using National Instruments' LabVIEW software. This allowed for quantified actuation of the electronically controlled mechanical components in the photoporation system. This was designed specifically to move the stages in a raster pattern. This patterned approach was initially adopted to increase throughput of the system, exposing a larger number of cells in a shorter timeframe. The raster pattern was repeated along the Y-axis, the number of cycles that set in the software. The control parameters for each stage were maximum acceleration, maximum velocity and distance travelled. Each length of the raster cycle was manually set, these were labelled as x_1 , x_2 , y_1 and y_2 . A repeating raster pattern required the fulfilment of two rules; $x_2 = -x_1$ & $y_1 = y_2$. Stage position in the Z-axis remained fixed during the operation of a program and was adjusted manually for focusing purposes only. The shutter controller allowed independent open and close times to be set in the software. The shutter was programmed to expose the sample in a 200 ms cycle (100 ms open, 100 ms close) when etching glass. During photoporation, the shutter was set to remain open for the duration of the program.

2.3.3 Cell culture

Two cell lines were used in this project. A Chinese Hamster Ovary (CHO-K1) cell line was used in the calibration and configuration of the photoporation device. However, the ultimate goal was to induce the expression of *KRAS* in Human Pancreatic Duct Epithelial (HPDE4) cells.

2.3.3.1 CHO-K1 cell culture

These cells must be maintained in an incubator at 37 °C with 5 % CO₂ to mimic the physiological environment. The local environment for the cells was a solution of Ham's F-12 culture medium with 10 % Foetal Calf Serum (FCS) and the addition of PenStrep, a common solution that supplemented the solution with the antibiotics Penicillin (at 100 U/ml) and Streptomycin (at 100 µg/ml).

These cells are adherent, requiring a surface on which to grow. The cells were grown in a volume of 5 ml culture media, on a 25 cm² tissue culture flask (Nunc). To prevent overpopulation – which would result in cell death and potential physiological changes – the cells were passaged once they reached approximately 80 % confluence. This provided approximately 2x10⁶ cells per 25 cm² tissue culture flask.

Passaging is the process by which a population of cells are reseeded in fresh growth media, at a lower concentration, to allow continued growth. Once the cells reached approximately 80 % confluence, the cells would be moved to and handled within a class II biosafety cabinet. The growth medium is aspirated from the tissue culture flask and the cells washed twice with PBS pre-heated to 37 °C, this step is to remove serum and dead cells from the sample. As the cells are adherent, the bonds to the surface of the tissue culture flask must be broken with minimal trauma to the cells. One of the safest methods of cell dissociation is by using the enzyme trypsin, which digests the proteins that cause surface adhesion. 1 ml of the trypsin analogue TrypLE Express (Invitrogen) – also pre-heated to 37 °C – was added to the flask and made to cover the entire surface. The tissue culture flask is then returned to the incubator for approximately 90 seconds. After this time the tissue culture flask is viewed under a wide field microscope and the flask is gently tapped to remove the CHO-K1 cells from the surface of the flask. At this stage 5 ml of fresh complete growth medium, pre-heated to 37 °C, is added to the flask and the resulting suspension of cells is pipetted into a 15 ml falcon tube. This tube is then centrifuged at 500 g for 5 minutes, to remove the TrypLE Express, causing the cells to form a pellet at the base of the tube. The supernatant is carefully aspirated and the cells are resuspended by gentle pipetting in 5 ml of fresh complete growth medium. 0.5 ml of the resulting solution, 10 % of the original cell population, excluding losses, is then added to a tissue culture flask with an additional 4.5 ml of fresh complete growth medium. This freshly passaged tissue culture flask is then returned to the incubator.

The initial sample was removed from LN₂ storage and seeded onto a 25 cm² tissue culture flask with 5 ml of fresh, pre-heated, growth media and incubated for 12 to 18 hours. The supernatant is then aspirated and fresh growth medium added before checking confluence. The short incubation period allows the cells to attach, but the sample must be quickly rinsed to remove the high proportion of dead cells – resulting from the cryogenic process – and the additional cryopreservatives that are added prior to freezing, in this instance, DMSO.

2.3.3.2 HPDE4 cell culture

HPDE4 cells are an adherent cell line. Stocks were grown on 25 cm² tissue culture flasks (Nunc) in 5 ml of Keratinocyte serum-free media (Invitrogen), supplemented with 10 % FCS (Invitrogen). Samples were incubated at 37 °C in a 5 % CO₂ atmosphere. Cells were passaged at approximately 80 % confluence to prevent overpopulation. Due to the slow growth of this cell line, stock flasks were seeded at 40 % confluence.

Passaging of this cell line differed from the protocol used for the CHO-K1 cell line. At 80 % confluence the growth media was aspirated from the tissue culture flask. The cells were washed twice with 5 ml of Dulbecco's phosphate-buffered saline (DPBS) without calcium or magnesium (Invitrogen) at 37 °C. 1 ml of pre-heated 0.05 % Trypsin EDTA (Invitrogen) was then added to the tissue culture flask and the flask was returned to the incubator for 5 minutes. The flask was imaged using an inverted microscope to confirm dissociation of cells from the flask surface and additional incubation time was used as required. Upon dissociation from the flask surface, 1 ml of soybean trypsin inhibitor (Invitrogen) was washed over the cells. 3 ml of complete growth media was then added to the tissue culture flask and the total volume (5 ml) was pipetted into a 15 ml falcon tube. The sample was then centrifuged at 500 g for 5 minutes to pellet the cells. The supernatant was carefully aspirated and the cells were resuspended in 10 ml of complete growth media. Half of this volume was used to seed a new stock tissue culture flask and the remaining 5 ml was available for photoporation experiments or for stock expansion in an additional tissue culture flask. The growth media in the stock tissue culture flasks was replenished after 48 hours.

Stock HPDE4 cells were provided by collaborators, Prof. Neil Carragher's group at the MRC Institute of Genetics & Molecular Medicine, University of Edinburgh.

2.3.4 Microscopy

The samples used in this experiment were grown in glass-bottomed fluorodishes. To maintain sterility of the samples, the dishes must be kept closed outside of a tissue culture hood. As these dishes hold a volume of growth medium and must be kept sterile, conventional upright microscopy is not possible. The thin glass bottom of the fluorodishes is designed to be comparable in function to a cover glass on a microscope slide, allowing imaging through this bottom surface with most microscope objectives. Therefore, all images of the fluorodishes were recorded with an inverted microscope. As the monitoring of green fluorescent protein (GFP) expression was necessary for some aspects of this work, a fluorescent microscope was required. A Nikon Eclipse with a Nikon DS-Fi1c camera was employed for this function. Typically, the 40x microscope objective was used to record images of the fluorodishes after etching, after seeding and at several time points after photoporation.

2.3.5 Glass etching

Cell samples for photoporation were grown on 35 mm glass bottomed fluorodishes. The preparation of these dishes was integral to experimental tracking and management, allowing visualization of defined regions for separate controls and exposure parameters. These dishes are provided in sterile single packages, so to minimise contamination the dishes were opened and labelled immediately prior to etching.

The dishes were placed on the stage mount in the photoporation apparatus and an alignment mark was made, typically using the Fianium FemtoPower laser. Etching required focusing of the laser beam onto the glass base of these dishes. The femtosecond fibre laser was used and the power attenuated to ~400 mW. Bursts of light indicated plasma formation, providing a visible confirmation of the etching process. As this system uses an oil immersion microscope objective, the index matching oil was added before opening the shutter. The stage would be actuated to the point that the glass surface came into contact with the oil. The laser shutter was then left open while the stage was driven through the Z-axis until plasma formation was visible on the camera feed, confirming the ideal position in the Z-axis to mark the glass.

The first etching step involved manually scanning a rough cross pattern over an area of approximately $50\ \mu\text{m}^2$. The initial etch provides an origin and orientation. A pre-set program for producing a raster pattern with dashed lines was then initialised to write a pattern of markings on the dish. The pattern was repeated along the Y-axis with a repetition of width of $250\ \mu\text{m}$ for a set number of cycles and a length that was adjusted depending on the sample, though these tended to vary between $250\ \mu\text{m}$ and $1\ \text{mm}$. An example of this etching pattern is shown in Figure 2.6.

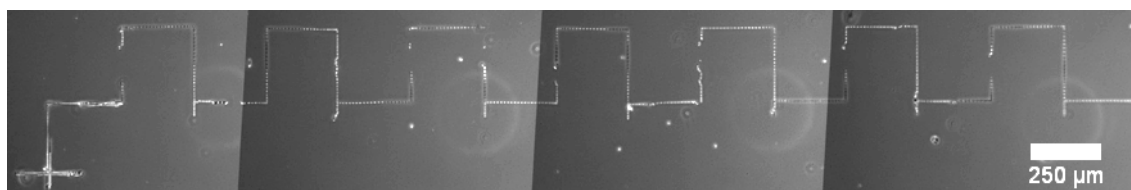


Figure 2.6 – Stitched images of laser-written markings on glass. 7 cycles writing at $250\ \mu\text{m}$ in both X and Y. Inconsistent background is a result of uneven illumination from the microscope, particularly noticeable in the stitched images.

Etched dishes were kept closed and the external glass surface was wiped to remove residual index matching oil. Dishes were transported in a petri dish, sealed with Parafilm, to cell culture facilities for seeding.

2.3.6 Sample preparation

Biological samples for laser exposure in the photoporation apparatus were prepared in 35 mm glass bottomed fluorodishes. Etched dishes were used for seeding purposes. Cells for photoporation were taken when the stock was passaged. 10 - 50 % of the stock cells are used to maintain stock, depending on cell line, and the remaining cells could be used for experimental samples. The dishes were filled with 1 ml of growth media and $\sim 1 \times 10^5$ cells. The cells required several hours to adhere to the surface of the dish after seeding. To assure complete adhesion of viable cells, freshly seeded dishes were provided with a minimum of 24 hours incubation time. Prior to exposure the growth media in the dish was aspirated and replenished, reducing the risk of dehydration and removing non-viable cells. Micrographs of each dish were recorded immediately prior to each photoporation test as $t = 0$ hours.

2.3.7 Photoporation

A prepared sample with adherent cells was placed in the photoporation apparatus and aligned using the alignment mark made during etching. A drop of index matching oil was added to the microscope objective and the z-axis actuator is used to lower the sample towards the microscope objective. The sample was brought into focus and the alignment was fine-tuned, in terms of starting cross and rotational position of the dish. The required laser power was set and a test exposure was carried out on a cell outside of the etched area.

These experiments were performed in one of two actuation modes, single shot exposure and raster scanning exposure. Single shot operation consisted of positioning a cell then exposing it to a pulse of focused laser light. This provided the benefit of selecting and targeting specific individual cells, however the minimum exposure time in the setup was ≥ 100 ms and the correct position of the beam focus with respect to the cell membrane was difficult to judge owing to the non-uniform height of the cells. Scanning exposure moved the sample in a defined raster pattern with the beam on, and the focus fixed onto the sample so that cavitation bubbles were witnessed. This allowed for greater area coverage, allowing faster photoporation of numerous cells. Concerns regarding exposure are also reduced, as the beam is not dwelling on the same area for >100 ms, but continually hitting new areas of the cell. This also increases the likelihood of the focused beam interacting with the membrane as the beam was scanned across the whole cell. As illustrated in Figure 2.7.

For single shot operation, the x-axis and y-axis actuator are moved manually and the shutter is triggered independently. In scanning operation, once focus and alignment are confirmed, the actuators were operated using the LabVIEW script. Dishes were kept closed during the photoporation process. After photoporation, residual index matching oil was removed and the dishes were transported in a closed petri dish, wrapped in Parafilm, to the tissue culture facility. The dishes were immediately removed from the transport petri dish and placed in an incubator.

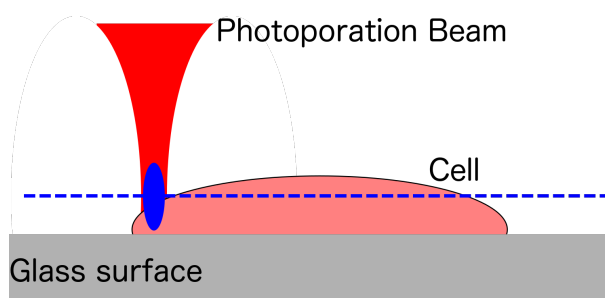


Figure 2.7 – Scanning photoporation. Illustration of the scanning mode photoporation, the dashed blue line denoting the travel of a hypothetical focal volume which induces photoporation on a surface (cell) that is not uniform in height.

2.3.7.1 Photoporation optimisation

Optimisation was performed with a view to minimize cell damage while maximising the rate at which pore formation occurs. This was performed with similar, but separate, experiments to measure viability and photoporation efficiency. Each of these required slight modifications to the photoporation process.

The viability of the biological samples is of key importance in these projects. For a cell to express additional genetic content, the cell must be viable. CHO-K1 cells were used in the first instance to test the viability and efficiency of photoporation in mammalian cells. They were seeded and allowed to adhere to pre-etched sample dishes. Images of these dishes were recorded immediately prior to photoporation. Using both single shot and scanning operation, on different sample sets, each section of the etched dish was exposed to a different level of laser power with an unexposed control group used as a growth baseline. Samples were rinsed, fresh media was added, and they were then incubated. Images of the sample dishes were recorded at $t = 18$ hours. A comparative cell count between the pre-photoporation and 18 hours post-photoporation images of the samples were used to chart cell survival. Efficiency of photoporation was determined by using a membrane impermeable dye, trypan blue. To measure efficiency, CHO-K1 cells were seeded and allowed to adhere to a pre-etched sample dishes. Microscopy images of the samples were taken prior to photoporation. Trypan blue was added to the sample, creating a 0.1 % final concentration. Following the approach used with the viability optimisation, each section of the plate was exposed to a different laser power. If a pore was formed in a cell membrane, trypan blue is expected to enter the cell, an effect visible when viewed under the microscope [81]. Images of the dishes were recorded for counting purposes, prior to and immediately following photoporation.

2.3.7.2 Optical transfection

Transfection techniques require the addition of the vector of genetic material that is to be inserted into target cells. Cells of interest were seeded and allowed to adhere to pre-etched sample dishes. Images of the sample were taken prior to photoporation. Immediately before photoporation 5 μ g GFP vector or *KRAS*-GFP was added. Photoporation was carried out in scanning operation and samples were returned to the incubator immediately after photoporation. Fluorescence and bright-field images of the samples were recorded after 24 hours and up to 96 hours for analysis.

2.4 Results

The etching and photoporation experimental results are presented in this section. Initially the results using the 5 kHz Ti:Sapph system are described and the reasons for ceasing use of this system, in this application, are reviewed. The viability of CHO-K1 cells and effectiveness of pore formation, monitored through use of Trypan Blue is then presented. Photoporation via exposure of a single point is compared to exposure while the sample stage is moving in a raster pattern. Final optimisation of photoporation using a GFP plasmid and CHO-K1 cells is attempted prior to the attempts at *KRAS* transfection in HPDE4 cells.

2.4.1 Photoporation optimisation - 5 kHz pulsed laser

The Spectra Physics Hurricane laser system operated at 5 kHz and generated up to 700 mW of (average) continual power. Power adjustment was attempted using the half wave plate and the finest adjustment would transition from no evidence of photoporation to catastrophic cell destruction. In an attempt to reduce the power further, with the goal to provide a more usable range of power adjustment for reaching the threshold of free-electron plasma formation, a ND4 filter and continuously variable OD0 - OD4 filter were added to the beam path. With these additions and the photoporation device operating in raster scanning mode, a functional region for photoporation between sub-threshold and catastrophic cell death could not be found. An example of this is illustrated in Figure 2.8.

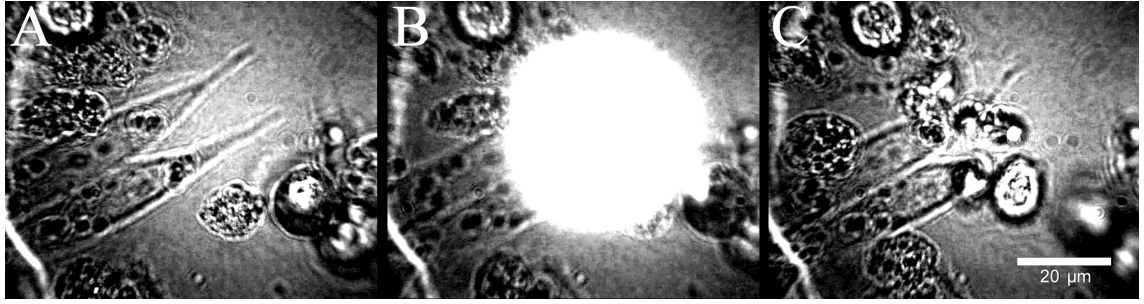


Figure 2.8 – Photoporation with Ti:Sapph laser. (A) CHO-K1 cells viewed on the photoporation apparatus, alignment of the system places the focal point of the laser in the centre of the field of view. (B) Plasma formation at the focal point during a single 100 ms exposure of 60 mW (average) from the 5 kHz Ti:Sapph laser source. (C) Significant debris from the target cell, and an adjacent cell, indicating catastrophic damage.

In single shot operation, the minimal shot time of 100 ms, at 60 mW, resulted in an exposure of 6 mJ on the sample. This contrasts to the lower reported exposure times in other high NA objective systems, which is typically lower, around 16 ms [70], which comparatively, would yield an exposure of 0.96 mJ. Overcoming the issue of exposure time, by scanning the beam across the sample, the beam still too destructive for viable photoporation.

Lower repetition rates result in a higher individual pulse energy, and typically a higher peak power. If the pulse energy imparted on a cell is too high, the damage is catastrophic. A lower repetition rate typically indicates a greater dwell time between pulses. Increasing the dwell time reduces the cumulative effects of a pulsed system, whereby a free-electron plasma may not be generated. The 5 kHz repetition rate, with a 130 fs pulse length, results in peak powers of 92.3 MW, compared to 5.77 kW in an 80 MHz system, which is typically employed in photoporation systems using a high NA objective [70], with similar pulse length. Given the extent of damage across all ranges with this laser system, the individual peak pulse energies appear too high for viable photoporation. Ongoing experimentation focused of using the Fianium 1 MHz laser.

2.4.2 Photoporation optimisation – 1 MHz pulsed laser

The Fianium FemtoPower HE1060-fs fibre laser system produces 1.1 μJ , 430 fs pulses of light at $\lambda = 1064 \text{ nm}$ at a rate of 1 MHz, for an average power of 1.1 Watts. Compared to the 5 kHz system, the specifications of this system are closer to the 80 MHz lasers used in other high NA objective photoporation setups, and provided significantly more positive results in terms of feasibility [70]. The following sections cover the experimental results which arose from the point and scanning exposure methods.

2.4.2.1 Point exposure; viability and efficiency

The original intention of this experiment was to attempt point exposure photoporation, using a short exposure time on a stationary target cell to induce pore formation. CHO-K1 cells were seeded and allowed to adhere on glass-bottomed fluorodishes that had previously been etched. Images of the dishes were recorded, using a Nikon Eclipse microscope, prior to photoporation for cell counting. Marked regions on the etched dish were exposed to powers from 50 mW to 75 mW in 5 mW increments and a final section was left unexposed as a control. The shutter controller was set to the shortest exposure time possible; 100 ms. Following photoporation, these samples were washed, imaged and returned to the incubator. Further images were recorded 18 hours post photoporation. Comparative counts of the cells, exposed to different photoporation laser powers, were recorded to produce a viability trend. To allow for cell division, the growth in the unexposed control section was used as a comparative reference of 100 % viability. The change in cell number was normalized against the test sections.

Photoporation efficiency experiments were treated in a similar manner to viability experiments, with the addition of trypan blue immediately prior to photoporation and the counting of cells immediately following exposure. Effectiveness of photoporation was recorded using the membrane impermeable dye, trypan blue. The cell becomes significantly darker once this dye has entered, a change that is easily observed using a microscope and indicates compromise of the cell membrane and therefore indicative of pore formation. An example of this effect is shown below in Figure 2.9.

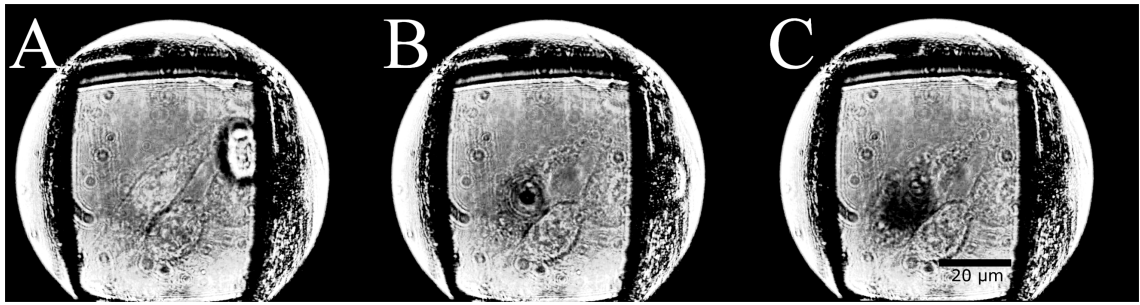


Figure 2.9 – Photoporation of CHO-K1 cell in the presence of trypan blue. (A) Target CHO-K1 cell (centre of field of view) is visualised and focused in photoporation apparatus. (B) Cell exposed to focused laser light, point of exposure visible as dark spot on cell. (C) Cell darkens, indicating that trypan blue has entered the intracellular environment. This is only possible if the cell membrane has been compromised, indicating that a pore has been formed.

To determine viability, cells in each marked region were counted at $t = 0$ hours, prior to photoporation and compared to counts at $t = 18$ hours after photoporation. As there will be some growth in the cells between these time points, a growth rate was determined by comparing the cell counts of an unexposed region on the sample at $t = 0$ and $t = 18$ hours, which was then applied across all test regions. The seeding concentration of $\sim 1 \times 10^5$ cells/ml yielded initial counts of approximately 40 to 80 cells per etched region. Poration efficiency was determined by comparing the number of cells in each region at $t = 0$ hours, to the number of cells which were stained with trypan blue immediately following photoporation. Plates were replicated in triplicate. At higher powers, cells were often completely ruptured or ablated from the glass surface, cells lost in this manner were not counted as being successfully photoporated. Pore formation was only counted where the cell was still visible. Low photoporation efficiency is primarily due to the excessive damage experienced by the cells and the difficulty focusing on the cell membrane. Data of photoporation viability and efficiency using the Fianium FemtoPower laser at different average powers have been plotted in a graph which shows a crossover area, indicating the power range that can be used for maximum photoporation efficiency while maintaining viability. This is shown in Figure 2.10.

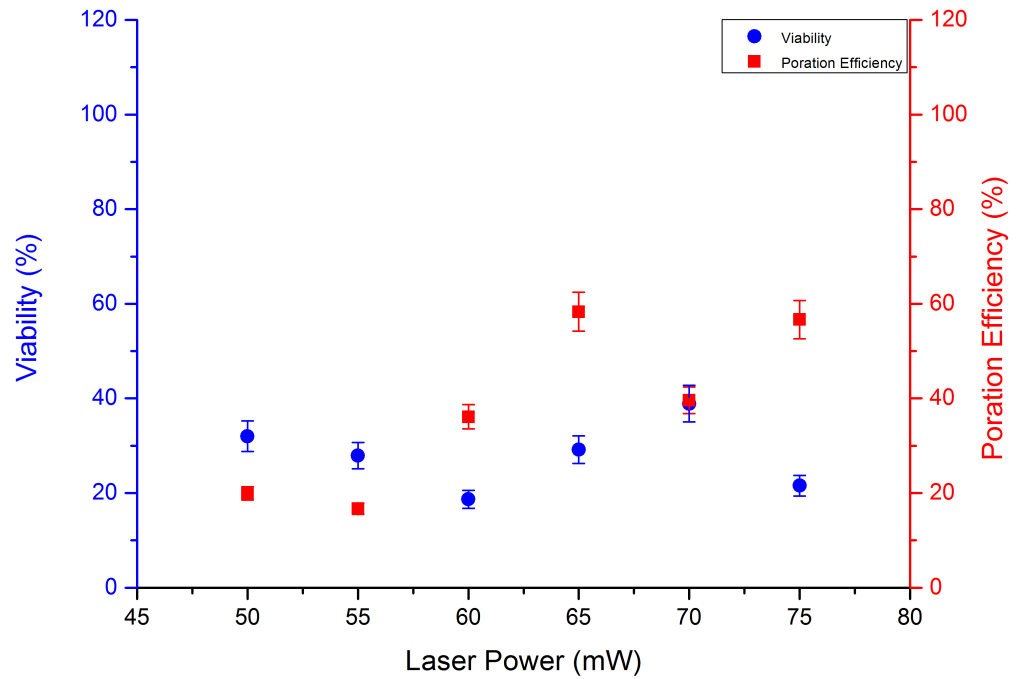


Figure 2.10 – Single shot photoporation efficiency and viability using a 1 MHz source. Photoporation with Fianium FemtoPower HE1060-fs laser system. This data indicates that 58 mW is the point at which viability is reduced below photoporation efficiency.

The point exposure method of photoporation was found to cause significant cell destruction with both laser sources. The Ti:Sapph source was completely destructive, as outlined in Section 2.4.1 and displayed in Figure 2.8 and the viable number of cells after fibre laser photoporation – in single shot operation – was poor.

The minimum exposure time used in these experiments (100 ms) is significantly higher than what has been reported in many ultrafast photoporation systems (~10 ms) [70, 71, 72, 75, 81]. As reported with the 5 kHz Ti:Sapph operation, this leads to significantly higher energy exposure on the target sample. While, as stated early, reported systems are using exposures in the region of 1 mJ [70], this system would provide a 5 mJ – 7.5 mJ in the measured regimes. The peak power produced by this system is also higher than those typically reported. A typical 80 MHz Ti:Sapph, generating pulses in the range of 130 fs and using average powers of 50 mW to 75 mW will have peak powers of 4.81 kW to 7.2 kW, respectively. While the higher peak powers in this lower repetition range, 1 MHz, system are slightly offset by a longer pulse duration (430 fs), a comparable average power range will generate peak powers of 116 kW to 174 kW. The extended exposure time, coupled with higher peak energy, is the likely cause of the significant cell damage that was recorded, in place of the desired transient pore formation.

Due to the ineffectiveness of the single shot experiments for creating a large proportion of viable, photoporated cells we move on to experiments whereupon the cells in a sample are scanned with respect to the laser beam, rather than holding the beam in a stationary position over a single cell. The reason for this is that scanning exposure spreads the laser exposure over an extended area of the cell. As subsequent pulses are not hitting the same area of the cell, the risk of overexposure damage should be reduced. Using this approach, photoporation was attempted, where viability and efficiency data were measured for different average laser powers.

2.4.2.2 Raster scanning; viability and efficiency

In comparison to photoporation systems reported in the literature, the minimum exposure time in this system was much longer and thought a potential issue in regards to cell viability. To alleviate the excess exposure on any single location, the sample plane was moved linearly in both the x and y axis, while maintaining a fixed z (focus). The stage moved at a maximum velocity of 0.08 mms^{-1} along the x and y-axis, with an acceleration of 0.08 mms^{-2} . This was found to be the highest speed at which the stages would operate stably within the submillimetre range of travel used in these experiments. Sample setup in these experiments was similar to that used in the previous section for point exposure. However, in place of manual exposures on individual cells, a scanning raster pattern was used to expose all cells within the target regions. An example of this is shown below in Figure 2.11. In the same manner as the point exposure experiments, viability data and photoporation efficiency were plotted to compare these in relation to laser power. This is shown in Figure 2.12.

As expected, and experienced in the point exposure experiments, the likelihood of pore formation increases with laser power, while the viability decreases. The data also indicates a clear increase in the likelihood of pore formation, when compared to single point exposure, this is likely due to the scanning pattern moving at a fixed focus, which is more likely to correctly strike the variable height of the cell membrane. Viability also increased under this regime, following the hypothesis on minimising localised exposure by moving the sample stage. Following this optimisation work, experiments progressed to applying the optimised parameters; scanning a beam of 58 mW across the sample at 0.08 mms^{-1} , to transfection of a GFP plasmid.

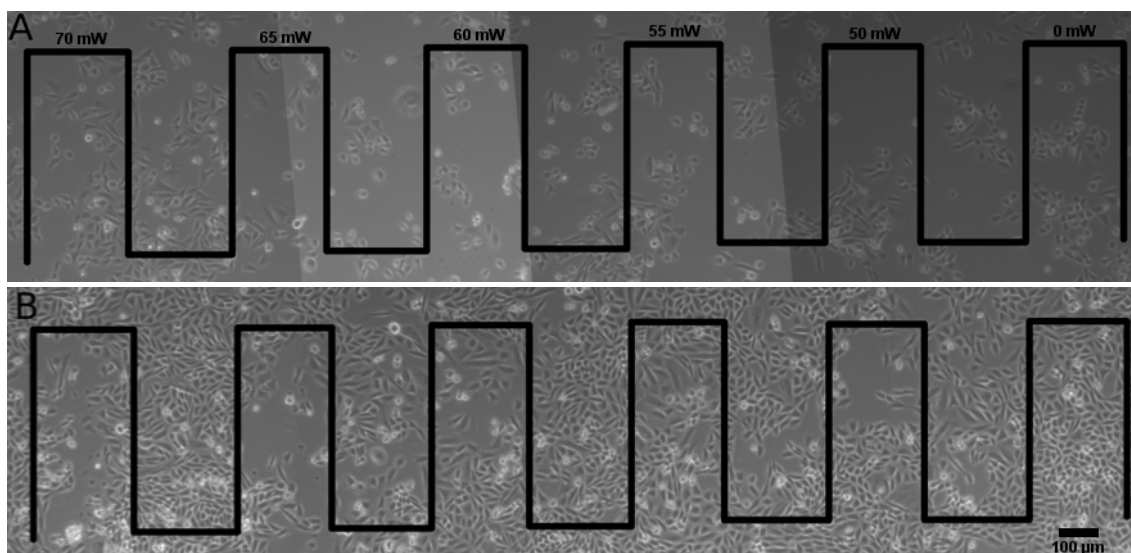


Figure 2.11 – CHO-K1 viability after exposure to a 1 MHz, 1064 nm laser. (A) CHO-K1 cells prior to photoporation, $t = 0$ h. (B) CHO-K1 cells at $t = 18$ h after photoporation with the Fianium FemtoPower laser. This example held six $250\ \mu\text{m} \times 500\ \mu\text{m}$ sampling regions (illustration superimposed due to faint presence on images), from left to right, these were exposed to 70 mW, 65 mW, 60 mW, 55 mW, 50 mW & 0 mW (control). Inconsistent background is a result of uneven illumination from the microscope.

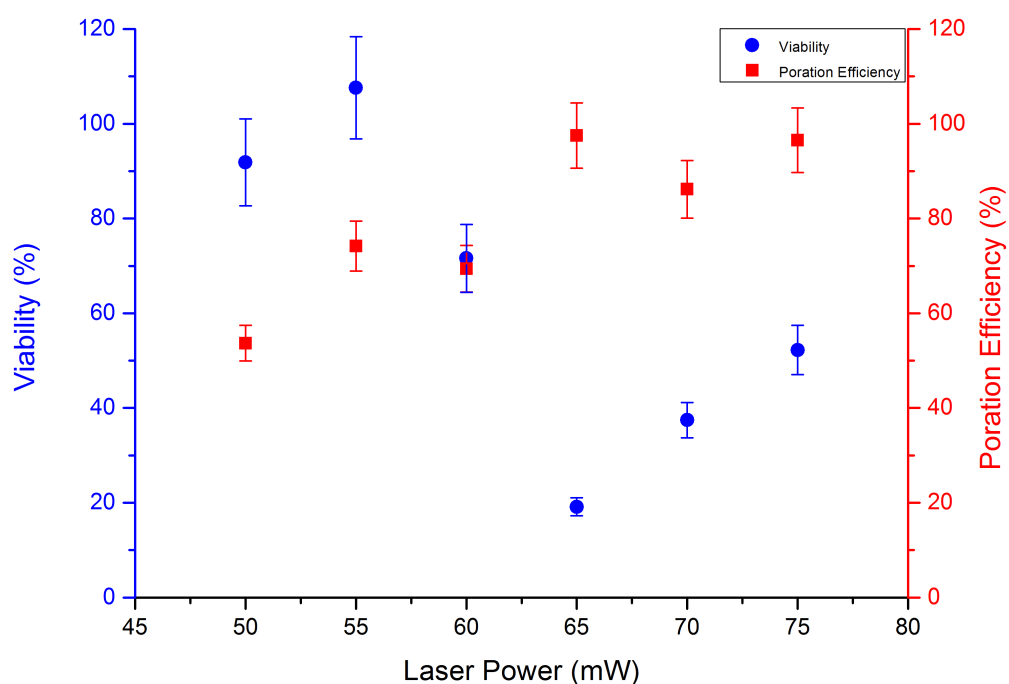


Figure 2.12 – Scanning photoporation efficiency and viability using a 1 MHz source. Photoporation with Fianium FemtoPower HE1060-fs laser system. This data indicates that 58 mW is the point at which viability is reduced below photoporation efficiency. This can be applied beyond the simple use of the crossover point. It is also possible to tailor specific experiments to viability requirements.

2.4.3 GFP transfection

Initial transfection experimentation sought to introduce a plasmid for GFP expression into target mammalian cells (CHO-K1 or HPDE4). Cells underwent photoporation at 58 mW using the $\lambda = 1064$ nm, 430 fs laser source and scanning operation based upon the best prior tested parameters, in initial tests using CHO-K1 cells and trypan blue staining, described in Section 2.4.2.2. Images were recorded before photoporation and at 18 hours after photoporation. An example of this process is shown in Figure 2.13.

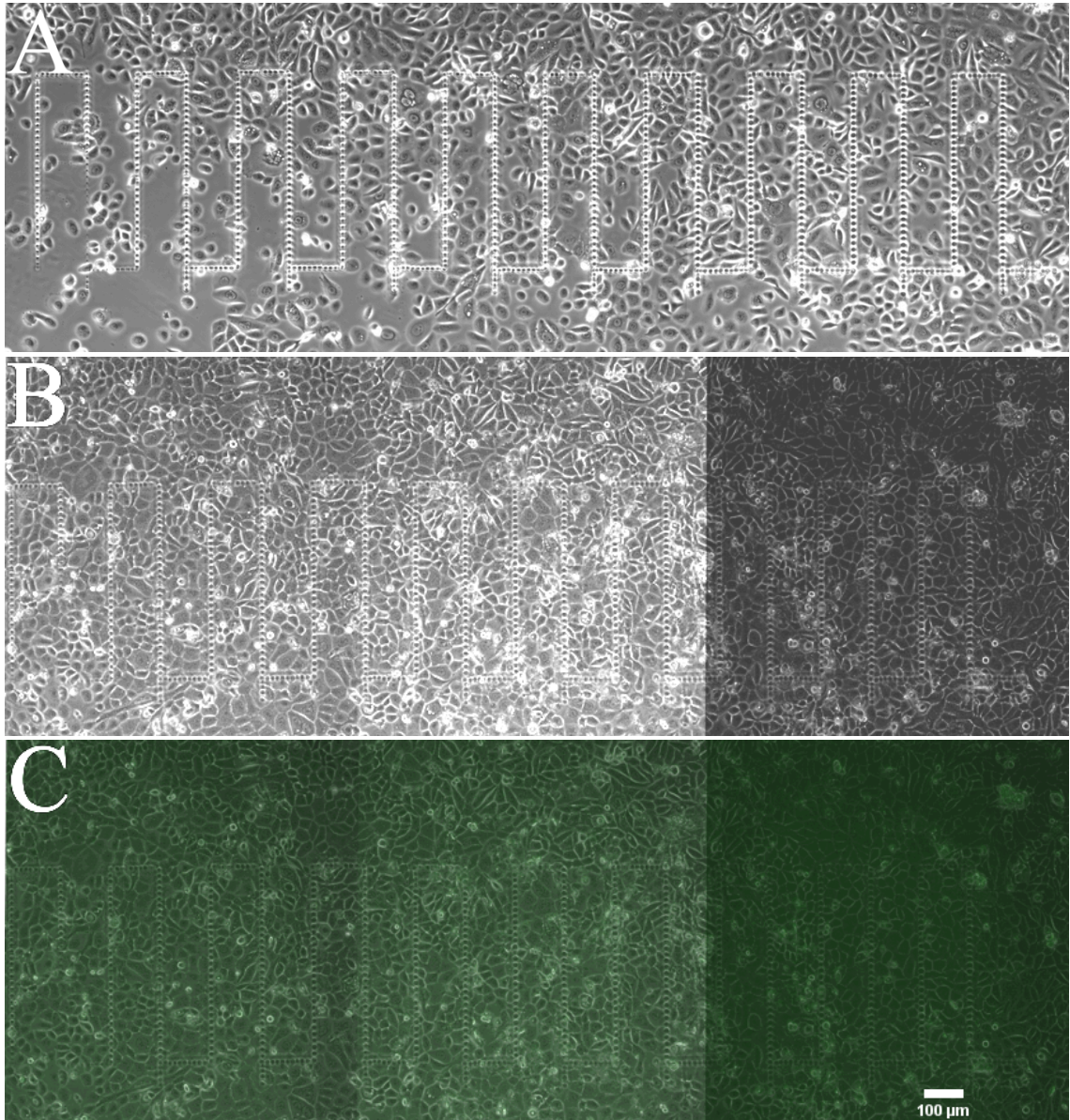


Figure 2.13 – Attempted GFP transfection utilising photoporation. (A) CHO-K1 cells attached to a glass-bottomed dish with 125 μm x 500 μm etched pattern on glass, prior to photoporation, $t = 0$ h. (B) CHO-K1 cells at $t = 18$ h after photoporation with GFP vector. Dark region due to camera setting error. (C) CHO-K1 cells 18 hours after photoporation with GFP vector with superimposed fluorescence channel. No fluorescence recorded.

Initial experiments attempted broad coverage of the target area in the sample, using an average power of 58 mW scanned at 0.08 mms^{-1} , the parameters determined in the optimisation step. Multiple etched regions were kept in order to aid cell counting. Unfortunately, GFP fluorescence, and therefore expression, was not witnessed in samples of CHO-K1 or HPDE4 cells after several repetitions.

The GFP plasmid concentration was increased from $5 \mu\text{g ml}^{-1}$ to $2\times (10 \mu\text{g ml}^{-1})$ and $10\times (50 \mu\text{g ml}^{-1})$, but yielded no improvement. Attempts across a range of exposure powers also yielded no improvement in results. Photoporation with trypan blue provides a very clear indication of pore formation. Comparatively, plasmid uptake is difficult to determine as it cannot be directly visualised. If poration occurred and the plasmid entered the cell, it may be possible that the plasmid was damaged prior to, or during the photoporation. While cells appeared viable, it may be possible that stress from exposure may have hindered expression of internalised plasmids, or the plasmid uptake was so small that expression could not be detected by our microscope. In parallel with the experiments to transfect CHO-K1 cells with a GFP plasmid, photoporation experiments to incorporate activated KRAS-GFP plasmids into HPDE4 cells was attempted.

2.4.4 Transfection of activated *KRAS*

A series of experiments designed to insert vectors for the production of activated *KRAS* and GFP in HPDE4 cells was attempted. These are introduced on a single plasmid as the activated *KRAS* alone does not present a significant visual change in the cell, however the expression of GFP reporter can be easily detected on a fluorescent microscope. HPDE4 cells were seeded on etched fluorodishes and allowed to adhere. The photoporation apparatus was configured to use the $\lambda = 1064 \text{ nm}$, 430 fs laser source and set to run in raster scanning operation. Initially the samples were exposed to 58 mW (average), selected from the earlier viability optimisation. No fluorescence was observed 48 hours after photoporation. Following this, attempts were made using a range of different average laser powers, from 40 to 100 mW, and increased plasmid concentrations. Increased incubation time, up to 240 hours, was also attempted. An example of the modified HPDE4 photoporation experiments is shown in Figure 2.14.

As experienced with the GFP plasmid in the previous set of results (2.4.3), no fluorescence was observed following the photoporation with 58 mW average power scanned at 0.08 mms^{-1} , the parameters described in the optimisation step. The

experimental parameters were broadened in an attempt to induce photoporation driven transfection. A range of exposures, from 40 mW to 100 mW (average), and increased plasmid concentrations from 5 $\mu\text{g ml}^{-1}$ to 50 $\mu\text{g ml}^{-1}$ were attempted. A sample set which was exposed to a range of powers was monitored over a prolonged incubation period of 10 days. This also yielded no fluorescence. The parameter space explored through these experiments is presented in Table 2.1.

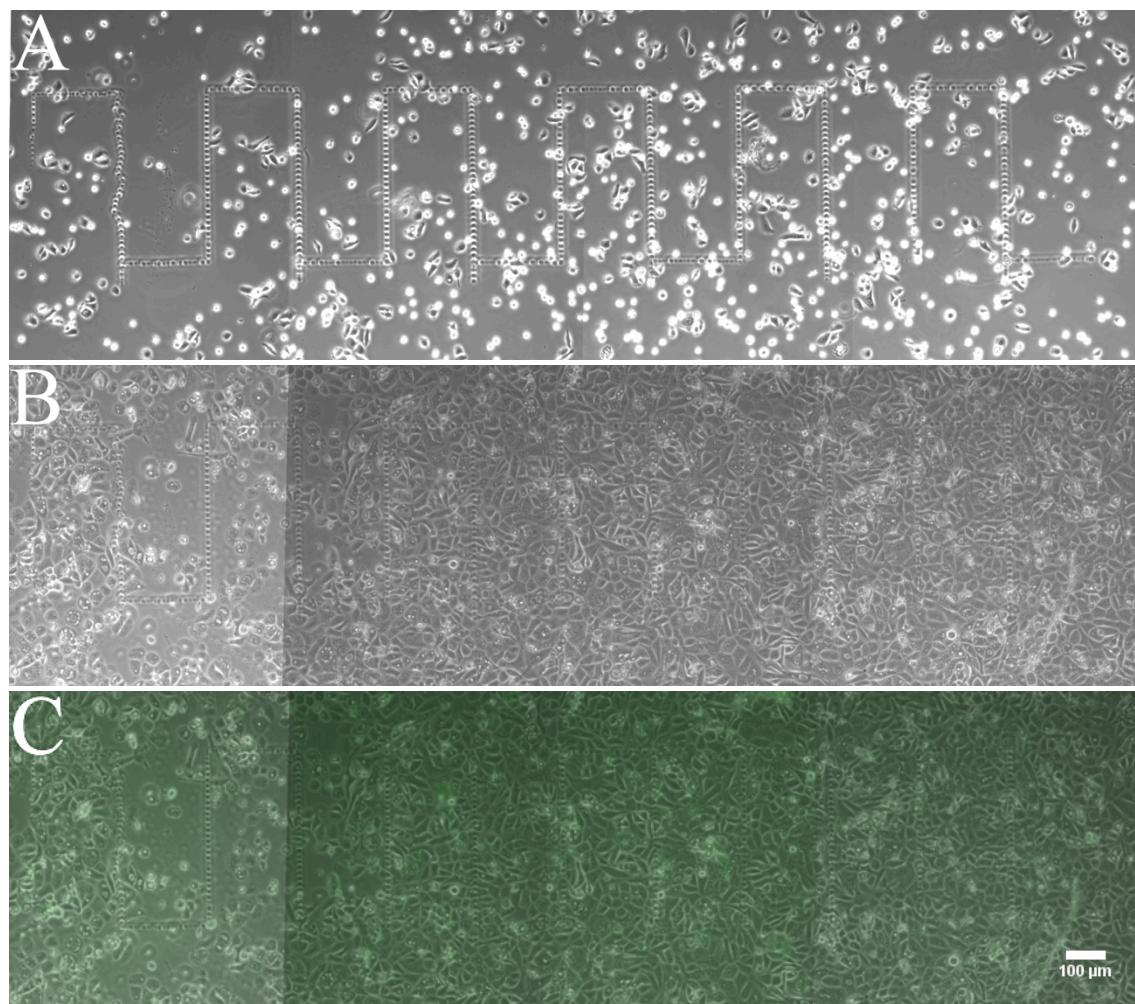


Figure 2.14 – Attempted *KRAS* transfection utilizing photoporation. (A) HPDE4 cells attached to a glass-bottomed dish with 250 $\mu\text{m} \times 500 \mu\text{m}$ etched pattern on glass. (B) HPDE4 cells 240 hours after photoporation with *KRAS* vector. (C) HPDE4 cells 240 hours after photoporation with *KRAS* vector with superimposed fluorescence channel.

The following section will provide a discussion on this body of photoporation work, including the success at using scanning mode photoporation to porate a large number of cells quickly and efficiently, allowing trypan blue dye to enter the cells, paving the way for rapid delivery of extracellular material into adherent cells and the reasons we believe we were unsuccessful in demonstrating transfection of HPDE4 cells with *KRAS* using the photoporation technique.

Table 2.1 – Photoporation parameter space. A summary of the range of parameters explored with the photoporation apparatus used within this work.

Laser	Wavelength	Repetition Rate	Power (average)	Cell Type	Point Exposure Time	Scan Speed	Plasmid Concentration	
							GFP	GFP- <i>KRAS</i>
Spectra- Physics Hurricane	800 nm	5 kHz	0 – 100 mW	CHO-K1	100 ms	-	-	-
Spectra Physics Hurricane	800 nm	5 kHz	0 – 100 mW	CHO-K1	-	0.08 mms ⁻¹	-	-
Fianium FemtoPower	1064 nm	1 MHz	0 – 100 mW	CHO-K1	100 ms	-	-	-
Fianium FemtoPower	1064 nm	1 MHz	0 – 100 mW	CHO-K1	-	0.08 mms ⁻¹	5, 10 & 50 µg ml ⁻¹	-
Fianium FemtoPower	1064 nm	1 MHz	0 – 100 mW	HPDE4	-	0.08 mms ⁻¹	5, 10 & 50 µg ml ⁻¹	5, 10 & 50 µg ml ⁻¹

2.5 Discussion

An optical system for cell photoporation was designed and built around the use of two pulsed laser sources, a Ti:Sapph operating at 5 kHz (Spectra Physics Hurricane) and a fibre laser operating at 1 MHz (Fianium FemtoPower). Experiments performed on the CHO-K1 cells, using trypan blue dye, demonstrated the capability of the system to allow a membrane impermeable dye to enter cells, as the laser created a pore, or pores in the target cell membrane (Figure 2.7). Cell membrane disruption, from pore formation to significant membrane destruction, was experienced using average laser powers ≥ 50 mW. Viability studies showed that using the Fianium FemtoPower laser, within a range of laser powers, from 50 mW to 75 mW, while scanning the sample at 0.08 mms^{-1} , $> 60\%$ of the exposed cells survived. This shows that, while a pore is created, it is temporal and produced minimal damage. However, no evidence of expression from transfection was witnessed during this body of work, implying a failure of transfection to occur in either the CHO-K1 or HPDE cell lines. While photoporation is a well-reported transfection technique, there was no evidence of transfection in this body of work.

The initial laser system used in this experiment was a Ti:Sapph operating at 5 kHz. Published photoporation experiments using Ti:Sapph laser systems are typically operating at approximately 80 MHz [70, 71, 75, 81, 82]. Given the significantly higher repetition rate, over four orders of magnitude higher, the individual pulse powers used in 80 MHz work — when operated at equivalent average powers — will be several orders of magnitude lower. In my work, the choice of using equivalent average power of the reported 80 MHz photoporation systems, resulted in the individual pulses from this particular Ti:Sapph laser system being too energetic. Additional attempts to attenuate the power of reaching the sample were implemented, however, this resulted in a transition between no recorded effect and catastrophic cell damage. This is likely due to the lower repetition rate resulting in a significantly higher dwell time, resulting in the loss of the cumulative effect which produced the free-electron plasma. The outcome of this being a severe regime change that resulted in a free-electron plasma formation which was too energetic, or not plasma formation at all. Implementing a fibre laser which operates at a repetition rate of 1 MHz, the energy per pulse was significantly lower than that emitted by the 5 kHz system, and closer in magnitude to the pulse energies presented in the literature.

Single shot point exposure operation was not practical with this photoporation system. The high peak energies produced by the Ti:Sapph and fibre lasers used in this work produced issues, however, for single shot operation, it was primarily that the exposure time was found to be too long. While the Thorlabs SH05 optical beam shutter is reported as capable of a 27 ms minimum open time with the Thorlabs SC10 controller, the controller available for this body of work was a Thorlabs TSC001, which has a minimum cycle time of 100 ms and therefor an operating time >100 ms. This exposure duration was also found to be significantly higher than those typically reported in the literature, which are on the order of ~10 ms [70, 71, 75, 81]. This combination of high pulse energies and the inability to reduce the time which cells were exposed to the beam, due to the restrictions in available equipment, meant that cells in the single shot regime were always exposed to energies that would destroy the cell.

Issues regarding exposure time were overcome, to a certain degree, by the introduction of sample scanning. This reduced the exposure time on any given location of a cell and resulted in significantly higher cell viability. Due to the variable height of the cell membrane, relative to the base of the culture plate, scanning should increase the likelihood of the membrane passing the beam focus (as illustrated in Figure 2.7). Most importantly, however, this scanning mode allows for significantly higher throughput over what is possible in single shot operation. At confluence, adhesive cells have a surface density of approximately 1×10^5 cells per cm^2 . Operating at the scanning parameters described in this chapter, 0.08 mm/s and using an interscan spacing of 12.5 μm , an area of 1 cm^2 could be scanned in approximately 28 hours. Photoporating approximately 1 cell per second. It is worth noting that the scan speed here was restricted to stop overshoot issues over the distances monitored, this would be less of an issue over greater distances, so it may be possible to increase scan speed, and thus throughput time. Increased scan speed would also reduce individual cell exposure, potentially increasing viability.

The relatively slow growth of HPDE4 cells resulted in a greater time requirement for experiments in terms of iterations and performance of repetitions, human pancreatic duct epithelial cell lines are reported as having a doubling time of approximately 30 hours [98, 99]. As such, HPDE4 work also relied on parameter ranges defined by optimisation using the CHO-K1 cell line. The slower growth time did, however, allow for a greater post-exposure time until the cells reached confluence, providing a greater time window of observation in which to monitor for GFP presentation.

Transfection was not witnessed during this body of work. It is not possible to state the cause of this with certainty. The HPDE4 cell line is not widely used and the tandem *KRAS* and GFP vector was not provided from a commercial source. Transduction of a different human pancreatic duct epithelial cell line — HPDE - E6E7 — with *KRAS* has been reported [100]. However, there is no reported success in the HPDE4 cell line or with the plasmid used in the work presented here. It is possible that *KRAS* expression occurred and the cell may have lost adhesion, as *KRAS* has been shown to downregulate genes associated with adhesion [101]. CHO-K1 cells, however, are widely used and their use has been reported in several transfection experiments [71, 72, 82, 83]. Where the incompatibility is potentially more likely with the HPDE4 cells and *KRAS* it is certainly unlikely to have been the issue in both instances. Apoptosis, and thus loss of adhesion, initiated by the vector uptake may be possible [102].

The primary shared effect on both cell lines was from the photoporation apparatus. It is possible that a high proportion of cells which experienced pore formation became apoptotic or necrotic, and the cells which were exposed in the system but did not experience pore formation were those that remained viable. However, as it was possible to maintain viability while also forming a pore in the membrane, this appears to be an unlikely candidate. This may be further studied at the single cell level by tracking vector uptake and viability of individual cells, rather than looking at ensembles and making observations on large numbers at given time points.

2.6 Conclusions

Photoporation has a proven track record as a transfection technique; published instances have reported successful transfection of a range of different cells using a number of different laser sources; 355 nm [77], 405 nm [93], 488 nm [95], 532 nm [103], 800 nm [80], 1064 nm [82], 1554 nm [89]. The technique has been shown capable, depending on the optical configuration, of a targeted specificity that is almost unrivalled. Compared to mechanical techniques that do provide a comparable specificity, photoporation can also provide a significantly higher throughput with scanning operation, while reducing sterility concerns. Higher throughput systems have also been reported, utilising microfluidics to direct cells in suspension through a focused beam for photoporation [104].

The optimisation steps in this body of work highlighted the requirement for fine power control and exposure time in these systems as well as the importance of individual pulse energies. While the literature has shown the prevalence of Ti:Sapph laser systems, these are typically operated in the region of 80 MHz, the available systems for this work operated at 5 KHz or 1 Mhz. With this reduction in repetition rate the individual pulse energies increase significantly, to the detriment of feasible photoporation. A shortcoming that was overcome with scanning operation. Where there were concerns discussed about the vectors, it is difficult to categorically state where the main issue arose.

The wealth of literature reporting functional photoporation devices speaks volumes to the use of the technique, one that will surely start to garner support in the conventional biology laboratory. The study of *KRAS* activation, working towards early detection and potential treatments will continue to be a key goal in pancreatic cancer research. Emerging techniques that bridge numerous fields of research can create opportunities not afforded by the conventional, historical, realms of science. In the drive of such an evocative subject, particularly one with such expansive funding, the multidisciplinary approach must continue to be exploited in cancer research.

Chapter 3

Optical manipulation of hollow cylinders; towards microinjection

3.1. Introduction

The controlled permeabilization of the plasma membrane allows for substantial modification and internal monitoring of a single cell. Crossing this physical barrier provides the opportunity to apply techniques with a broad range of biological and medical applications. Direct photon induced permeabilization was illustrated and discussed in Chapter 2, utilizing the technique of photoporation. In this chapter, a novel approach to indirect, light-driven permeabilization is attempted. Using the technique of optical tweezing, light is used to impart force onto microneedles, which are used as microscopic tools with the aim of interacting with single cells in various applications. This chapter describes a method to controllably translate and rotate hollow glass cylinders, microtubes, in the x-y plane of a sample, using multi beam optical tweezers with an aim to ultimately apply the technique to single cell biology studies.

3.2 Background

This section reviews the background literature and ongoing research that is relevant to using customised optical tweezers to trap rod shaped particles and applications, such as their use in microinjection. The concept and principles of optical tweezers are introduced. The relevant theory for these studies is included. Conventional microinjection is introduced to provide familiarity with the tool that this project seeks to improve upon.

3.2.1 Optical tweezers

Optical tweezers are a photonic tool capable of generating three-dimensional optical confinement using a single laser beam. The precursor to this effect was first reported by Ashkin in his seminal 1970 paper which noted the observation of scattering and gradient forces on micron scaled particles [105]. This work led to the later publication, in 1986, which described the full three-dimensional confinement and coined the phrase “Optical Tweezers” [106]. While this thesis will consider optical tweezers with biological applications, the technique laid the foundations for a broad range of studies using optical forces, including single atom confinement and ‘cold atom’ research, which was awarded the 1997 Nobel Prize in Physics.

Optical tweezers are most suited to manipulating particles on the scale of microns, so they are an ideal tool for working on single cells [107 - 110]. They have also been applied in the manipulation of smaller particles [111], including the manipulation of intracellular components [112]. Beyond simple manipulation, these devices have also been used to measure forces on a molecular level, tweezing and stretching DNA *in vitro* [113]. That optical tweezers allow the exertion of force without mechanical interaction is also favourable for biological study, allowing sterility to be maintained while manipulation can be carried out in a closed volume. Particularly useful for, biological researchers is the ability of optical tweezers to be adapted to some conventional microscope configurations.

In these experiments, a method for manipulating microscopic hollow cylinders, and microspheres within them, is attempted. The goal is to construct, and operate, an-optically controlled microsyringe - with the potential to controllably dispense femtolitres of material. Other applications of the manipulation of hollow microneedles are also considered and discussed.

3.2.1.1 Spherical trapping

Since inception, optical tweezers have been known to work ideally with spherical particles. The symmetry provided by a spherical particle offers a uniform distribution of forces and an easily described degree of autocorrection that keeps the particle in the central region of the optical trap. There are a number of ways in which the effect of an optical trap on a spherical particle can be described. If particles significantly smaller than the emission wavelength of the laser are used, the optical traps can be described in terms of the electromagnetic field. If particles are larger than the emission wavelength, the ray-optics approach can be implemented, as described in further detail below. There are also special considerations for scenarios where particularly high or low refractive index particles are trapped [114, 115].

This project uses particles that are greater in dimension than the emission wavelength of the source laser; as such, the ray-optic approximation is a suitable descriptor for optical tweezers in this function. In this we consider three general physical principles; momentum, refraction and Newton's third law of motion. A ray of light is composed of individual packets of energy, photons. These photons carry a momentum (p) which can be described using Plank's constant (h) and the wavelength (λ) of the photon, as expressed in equation 3.1. A material through which light can travel through will be described as having a refractive index, this property describes the speed which light travels through that material. When light transitions from one refractive index to another, unless the angle is 0° to the normal, the angle of the path changes - refraction. In these optical tweezing experiments the particles of interest have a higher refractive index than the surrounding aqueous environment so the beam of light will shift towards the normal. Newton's third law of motion states that for every action there is an equal and opposite reaction [114, 115].

$$p = \frac{h}{\lambda} \tag{3.1}$$

Implementing these principles, it is possible to infer the behaviour of a wave of light as it passes through a solid spherical object that has a higher refractive index than the surrounding environment. The light will be refracted within the sphere and exit in the direction opposite to the side that the wave entered. This change in momentum requires

an equal reaction in the opposite direction, causing the sphere to deflect away from the direction that the wave exited. When using a laser that has a Gaussian beam profile (TEM_{00}), the density of photons is significantly higher towards the centre of the beam. In this case, a sphere that drifts from the centre of the beam will experience a denser volume of photons refracting on the side that remains closer to the centre. This in turn causes the sphere to move towards the centre. The resulting effect is a form of lateral self-correction, causing a spherical particle to return to the photon dense centre of the beam. When a particle is laterally stable, due to the self-correction effects, and held within a tightly focused beam, the reactionary force is in line but opposite to that of the beam axis, the gradient force. This force will then reach an equilibrium with the scattering forces generated by the beam upon the sphere, holding the sphere at a position just below the beam waist. This results in a three-dimensional optical trap, where axial and lateral confinement occur. These behaviours are illustrated in Figure 3.1.

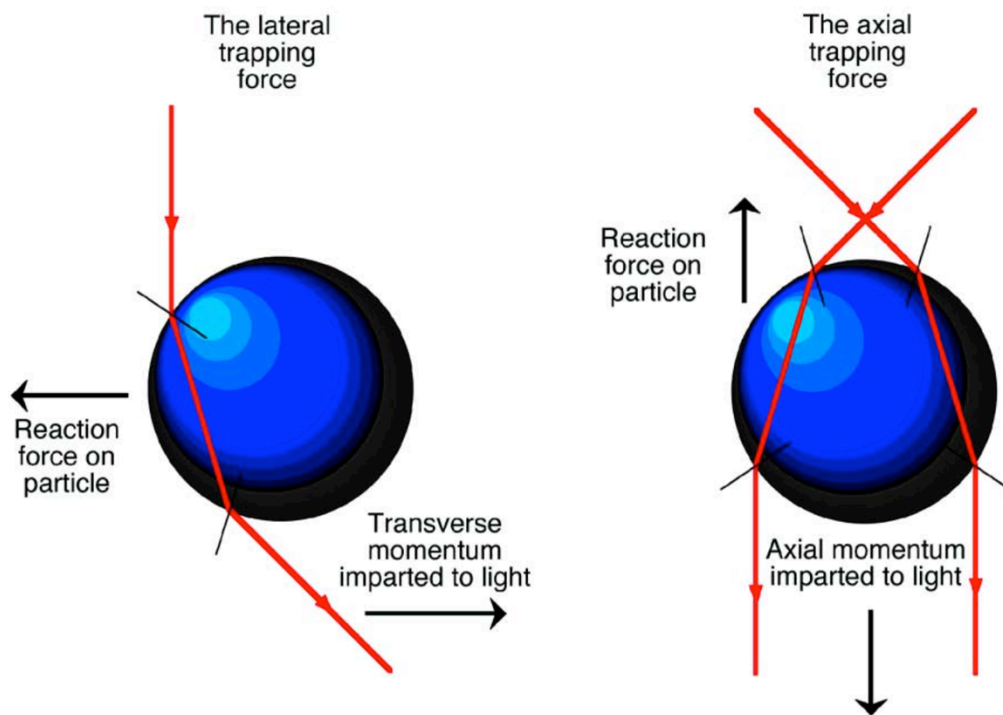


Figure 3.1 – Ray optics description for optical trapping of solid spheres. Taken from Figure 1, Molloy & Padgett (2002) [114].

While the use of solid spheres is commonplace with the work of optical tweezers, the use of hollow structures must also be considered. As a hollow microsphere will have an additional series of refractive index changes which the beam of light must travel through. In addition, the thickness of the sphere wall becomes a significant variable. Spheres which present a thicker wall may present total internal reflection, drastically altering the

beam path and spheres with a thinner wall may not present a significant volume of refractive index change, resulting in minimal force generation due to momentum change, as illustrated in Figure 3.2. The transverse momentum change occurs in the opposite direction to that experienced by solid spheres, this results in a loss of the self-centring properties experienced with solid sphere optical trapping and increases the likelihood of the sphere being ejected from the optical trap. However, the properties of such structures may introduce novel benefits, such as functioning as micromirrors [116].

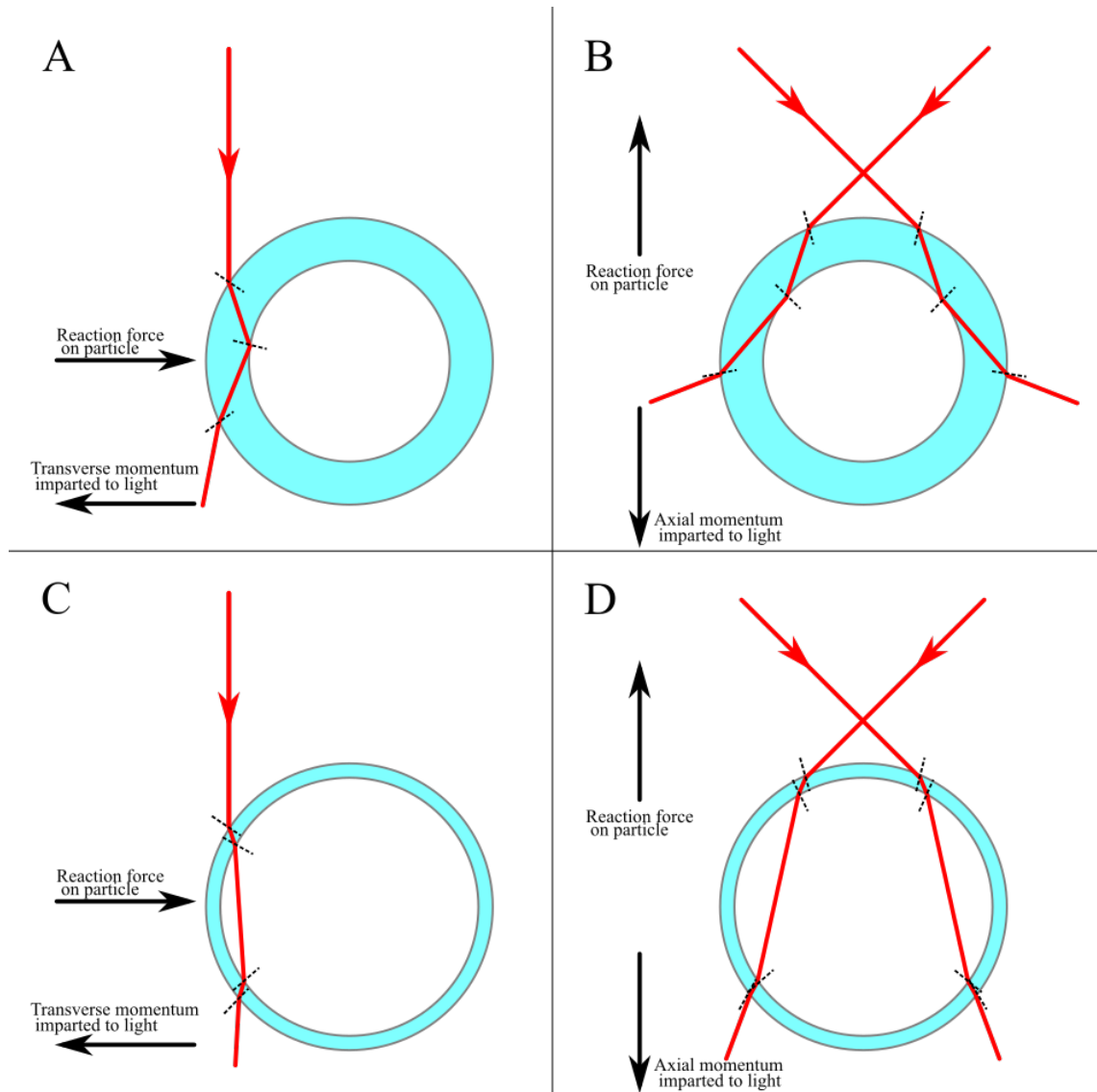


Figure 3.2 – Ray optics description for optical trapping of hollow spheres. The blue circle represents the cross section of a hollow sphere with the rays denoted by red lines, normal indicated by a dashed line at refractive index changes in the ray path and the sum forces are shown by black arrows. (A) Lateral trapping forces on a thick walled, hollow sphere. (B) Axial trapping forces on a thick walled, hollow sphere. (C) Lateral trapping forces on a thin walled, hollow sphere. (D) Axial trapping forces on a thin walled, hollow sphere.

This degree of symmetry present when using a spherical particle allows for relatively simple theoretical calculations to determine the trapping, or confinement force, F_{trap} , with which a particle is held in an optical trap. Due to their small size, microspheres in an aqueous environment will produce negligible turbulence as they move in the environment, as such they can be said to generally have a low Reynolds numbers. A low Reynolds number means that it is possible to apply Stokes' law (3.2) to this scenario [114]. This law is used to calculate the drag force, F_d , of a sphere moving at constant velocity in a viscous environment and requires knowledge of the fluid viscosity (μ), sphere radius (r) and sphere velocity (v).

$$F_d = 6\pi\mu r v \quad (3.2)$$

Using this approach, it is possible to quantify the force of laser confinement at the velocity point prior to failure (critical velocity), which occurs when the drag force, F_d overcomes the confinement force, F_{trap} .

If we apply these forces to particles with a volume on the order of femtolitres, it follows that their manipulation within a confined space, such as a hollow cylinder that has the same inner diameter as the particle diameter, it may be used to displace similarly small volumes, and this may in turn lead to the ability to further miniaturise microfluidics, where one might wish to manipulate femtolitres of chemicals using the optical manipulation of mechanical pumps and valves.

3.2.1.2 Non-spherical trapping

The majority of optical trapping experiments and theoretical simulations use spherical particles. This is because trapping of spherical particles is stable and the forces acting on a sphere can be modelled relatively easily due to well established, accurate theory for symmetrical systems. However, throughout the last 20 years, non-spherical particles have also been optically manipulated and a range of methods have been developed to produce different shapes and patterns of optical traps: methods such as using higher order laser modes [117], Ronchi rulings [114], interference of two trapping beams [118] and spatial light modulators [119] have been used to create confinement in fringes, grid-like patterns and allow for additional control, such as rotation. As these technologies

become more widely used, interest in modelling the optical trapping forces and torques on particles with less than spherical symmetry, in particular cylindrical particles (microrods), has also grown [120 - 124]. An example of cylindrical particles being manipulated by optical tweezer is shown in Figure 3.3.

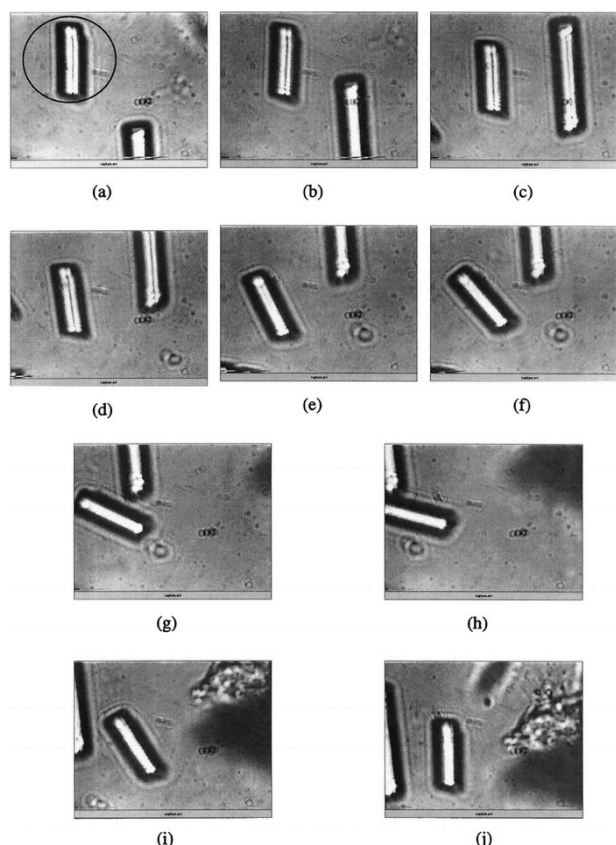


Figure 3.3 – Optical tweezing solid cylinders. A 5 μm long glass cylinder is manipulated around a stationary cylinder. Taken from Figure 4, Gauthier et al. (1999) [120].

Complicated structures have also been produced for use as mechanical probes. Examples of probes have been produced using direct laser writing, these can be designed with a number of specific component shapes. Tapered points are used as the contact point of the probe with spherical or cylindrical regions providing handles for optimised optical trapping and computer tracking [124]. The picoNewton force generated by optical tweezers allows for gentle mechanical probing of biological samples while high sensitivity allows a fine degree of accuracy in tracking. An example of this probe technology is shown in Figure 3.4. Micron scaled shapes and tools which mimic life-sized counterparts have also been produced, these ‘light robots’ have varying degrees of functionally, including transport of microspheres [125].

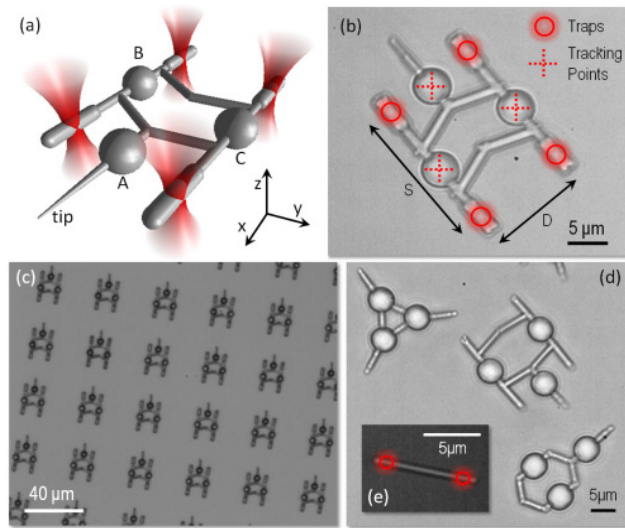


Figure 3.4 – Probes designed for optical trapping. A complex 3D structure used as a surface probe, cylindrical regions are handles for the optical tweezers, spherical regions are for tracking. Taken from Figure 1, Phillips et al. (2012) [126].

The work in this chapter focuses on the optical trapping of microcylinders (or microrods), in particular, hollow microcylinders (or microneedles) and their applications [127]. The very nature of hollow structures creates additional variables in regard to optical trapping. The additional refractive index changes experienced by light traversing the material introduce additional momentum changes. As we can take the two-dimensional cross section of a hollow sphere to present similarly to that of a hollow cylinder, the issues illustrated in Figure 3.2 will also apply to hollow cylinders, where axial trapping force is diminished and lateral repulsion from an optical trap is a feasible outcome. It also stands that the behaviour of forces on a cylinder within a viscous environment will differ from those on a sphere. For optically driven microinjection applications, it is useful to quantify the tweezing force thus the potential penetration force that can be exerted by a microneedle. For example, injecting a mammalian cell (in this instance, HEK-293) with an AFM tip requires 1-2 nN [128, 129] to > 100 nN [130], where conventional microinjection on an embryo is > 400 μ N [131]. In order to calculate the force that may be imparted by a microcylinder held in an optical trap, the force with which that optical trap holds a microcylinder must be determined. While there are accurate methods of calculating the drag force on a sphere confined by optical tweezers, no such solutions are present for the drag force on a hollow cylinder, however, there are methods which may be employed to make an approximation.

An approximation for the drag force on a hollow cylinder was proposed by Roger & Weidman in 1998 [132]. This model used a Beads-on-a-Shell technique to simulate the Stokes drag on a hollow cylinder. However, this methodology required isolation from boundaries by assuming, for the purposes of calculations, that the fluid environment extends infinity in all directions, removing any boundary effects. A method for calculating the drag force on microtubules, by kinesin molecules, was proposed by Hunt *et al.* in 1994 [133]. This model accounts for the close proximity of a surface boundary, which is more representative of the experimental approach used in this chapter, where a hollow cylinder is on the bottom a sample chamber. Tweezing in a direction parallel to the microneedle's long axis generates a drag force parallel to the microneedle's axis, and assuming a solid cylinder, the drag force can be calculated as shown in equation (3.3).

$$\langle F_D \rangle = C_{II} \mu L \langle v \rangle \quad (3.3)$$

Where F_D is the drag force on the cylinder, $\langle v \rangle$ is the average velocity of the cylinder, μ is the fluid viscosity and L is the length of the cylinder. C_{II} is the dimensionless drag coefficient (drag per unit length per unit viscosity) which is calculated using (3.4) where h is the height from the surface of the wall to the axis of the cylinder and r is the radius of the cylinder [133].

$$C_{II} = \frac{2\pi}{\text{arccosh}\left(\frac{h}{r}\right)} \quad (3.4)$$

There are a number of caveats regarding the use of this model. It requires that the cylinder is in close proximity to a wall, given the microcylinders are located at the base of the sample chamber, and, generally, there was no noticeable lift, the distance between the surface and the cylinder was estimated to be approximately 100 nm. This model also required that the length of the cylinder is greater than the radius $\therefore L/h > 1$. The cylinders with the highest uniformity in this work were rolled microtubes, described later in Section 3.3.2. These were produced with a length of 50 μm and a 4 μm diameter. Taking the 100 nm boundary distance estimation, this gives an h value of 2.1 μm , giving $L/h = 23.8$, meeting this requirement. This model also presumes the laminar flow in regard to the fluid drag, requiring a low Reynolds number, Hunt *et al.* presumes $\sim 1 \times 10^{-5}$ [133]. Using the rolled microtube in an aqueous solution and assuming

a velocity range of $1 - 10 \mu\text{m/s}$, this achieves a Reynolds number of 5.6×10^{-6} to 5.6×10^{-5} , respectively. As the potential velocity of the trapped microtubes in this work is very low, significantly lower than $10 \mu\text{m/s}$, this criteria is also met.

3.2.1.3 Multiple beam optical trapping

The ability to generate a localised optical force with which particles can be manipulated is a valuable tool. However, using a single optical trap is also limited in application. Through the proliferation of optical tweezing techniques - and advances in computational power - a wide range of approaches have been developed which allow the manipulation of light in order to generate several locations of optical confinement, allowing separate objects to be confined, simultaneously, at different three-dimensional positions.

One of the simplest ways in which to produce multiple optical tweezers, in principle, is by the use of multiple laser sources. The steering of a laser beam – while the sources are isolated – allows multiple optical traps to be generated at different spatial locations within the sample [114]. However, in practice this method introduces difficulties in stability and motion control. While often used in differing circumstances to free space optical traps, it is possible to use multiple optical fibres to generate multiple regions of confinement [134]. These systems are more often found in microfluidic devices where beam delivery to the sample may be problematic with high NA microscope objectives.

The relatively high viscous forces experienced by particles on the micron scale makes it possible for a particle to be held in localised position by periodic confinement using an optical trap. This phenomenon allows the use of rapidly attenuated mirrors, such as galvanometer mounted or acousto-optic deflectors, to be used to generate optical traps in several locations, using a single laser source [135], an example of this is shown in Figure 3.5. This periodic confinement is maintained by providing a brief dwell time over set regions or particles, maintaining the spatial position of a particle and this function will maintain the particle position as long as the diffusion of the particle – which is mostly associated with Brownian motion on this scale – is lower than the volume within which the optical trap corrects and centres particles during its dwell time. These methods may all be computer controlled which allows significant improvements in accuracy and timing of the optical traps.

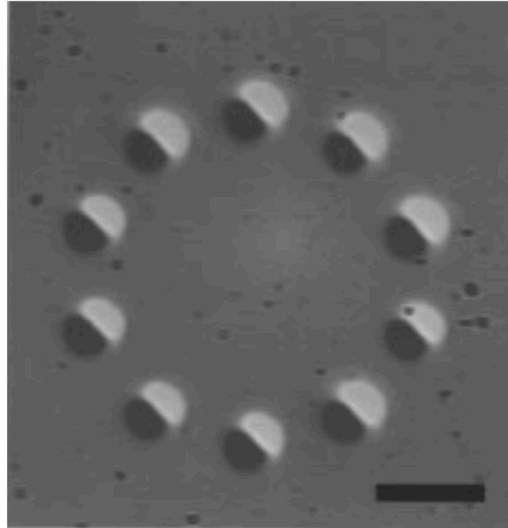


Figure 3.5 – Time sharing optical tweezers. Incorporating rapidly moving acousto-optical deflectors (AOD) providing consistent redirection between different positions, allowing ten silica beads to be confined by a single beam. The scale bar represents 2 μm . Taken from Figure 2, Visscher et al. (1996) [135].

The aforementioned methods introduce multiple optical traps with a fixed beam profile, adding laser sources or via beam sharing. However, modern techniques for multiple optical tweezer generation generally lean towards the manipulation of the beam profile, producing multiple optical traps through the physical alteration of the cross-section of the laser beam. The beam profile can be manipulated by using multiple sources or inducing interference patterns by blocking regions of the beam and allowing the wave-like nature of light, from a coherent source, to generate a stable pattern on the target sample [136, 137]. It is also possible to introduce diffraction patterns by introducing a static diffractive optical element (DOE) into the beam path or by use of a dynamic, reconfigurable spatial light modulator (SLM) [114]. A holographic plate allows for the patterned modulation of the phase of the optical tweezing beam, generating multiple optical traps that are static [138], allowing only some adjustment in scaling. An example of holographic optical tweezing is shown below in Figure 3.6.

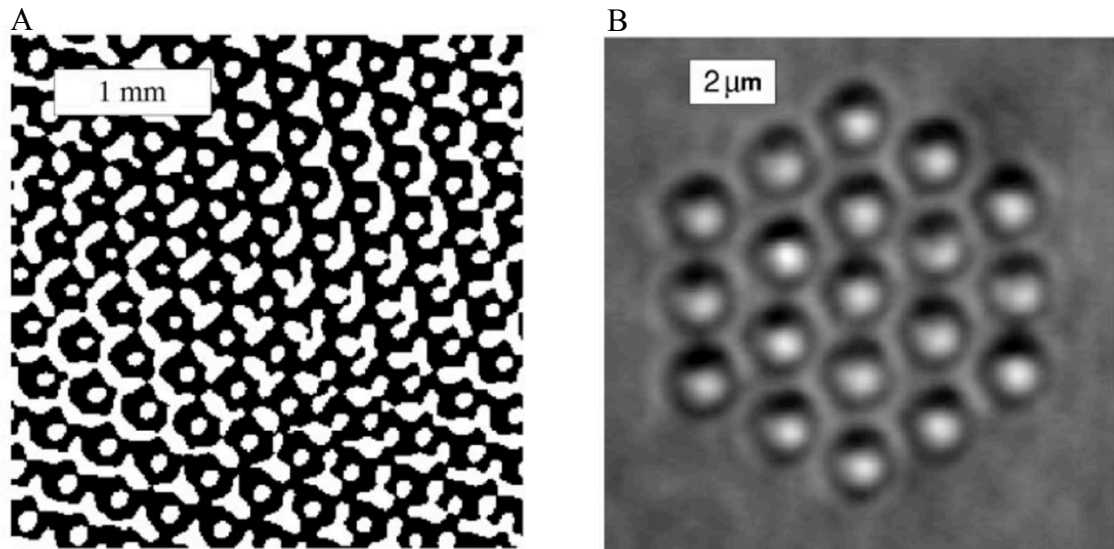


Figure 3.6 – Optical trap pattern produced using a static DOE. (A) Patterning of the DOE. (B) Optical trapping pattern of 1 μm silica beads. Taken from Figure 1, Dufresne et al. (2001) [138].

Holographic plates have been used widely and can be produced in a great range of patterns, projecting any desired pattern into the sample – they are still limited by being static. Pattern adjustment of a fixed plate is generally limited to magnification or scaling of that pattern. However, this is not an issue for the SLM. The SLM is generally a computer controlled device which modulates either the phase or intensity of a beam of light [114]. For optical tweezers configurations, phase modulators are the most commonly found form of SLM. When used as a component of an optical tweezer device, this allows for the generation of multiple optical traps within a sample, by adjusting the pattern generation with a rapidly responding SLM it is possible to create dynamic optical traps with full three-dimensional separation. This configuration also has the potential for generating the greatest range of spatial control within the sample. The advancing levels of computing, particularly portable computing, has allowed the production of touch screen SLM controller software. This has opened the functionality of optical tweezers to other scientists and can be applied as an exciting tool in public engagement [139], as shown in Figure 3.7.



Figure 3.7 – iTweezers. Software for touch-screen devices, allowing the generation of responsive holographic patterns for a SLM, producing multiple optical tweezers that are easily controlled in three dimensions. Taken from Figure 1, Bowman et al. (2011) [139].

While there is a range of options available for attempting multiple beam optical tweezing, this project focuses on the applications using conventional single beam optical tweezers and simple diffraction pattern, multiple beam, optical tweezers in order to manipulate microneedles.

3.2.1.4 Ronchi ruling

A simple manner in which to generate an interference pattern is with the use of a Ronchi ruling. The Ronchi ruling is an optical element which has a constantly spaced pattern of parallel lines deposited on a transparent substrate. This functions to block half of a cross-section of a laser beam, projecting linear fringes on the image plane. A focusing Gaussian beam transmitted through a Ronchi grating will generate an interference pattern in the axis perpendicular to the lines of the grating [114], an example of this is illustrated in Figure 3.8.

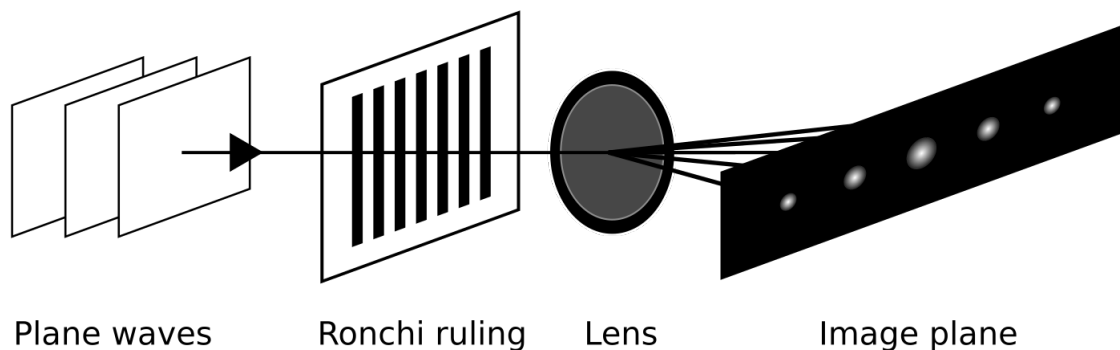


Figure 3.8 – Image projection of interference pattern from grating. Illustration based on image from Hecht (1987), Figure 14.3(a) [27]

In optical tweezers, the addition of Ronchi ruling generates a number of high and low intensity regions in the sample, these interference fringes act as multiple optical traps arranged in a linear array [114]. The size and spacing of these fringes is dependent on the focusing optics, wavelength of the source and the position and spacing of the Ronchi ruling used in the system. Increased line density on a Ronchi ruling will increase the number of slits through which the beam travels and thus increase the number of fringes generated. Optical tweezers that integrate a Ronchi ruling for interference generation have been shown to be capable of trapping microspheres [137]. In the first reported use of a Ronchi ruling in an optical tweezer device, the authors describe the expansion of this technique as potential tool for the simultaneous optical confinement of multiple particles or rod-shaped structures [137].

While proven to work well in optical tweezer apparatus, the implementation of a Ronchi ruling suffers the same limitation as holographic plates in that the pattern generation is static beyond optical scaling or rotation of the plate. In addition, the Ronchi ruling also causes additional power losses due to the blocked laser light during image generation. This chapter investigates the application of multiple beam optical trapping to confine microcylinders, microneedles, and the potential functions of such apparatus. The application of focus, in this instance, is the generation of an optically driven microinjection device. The following section outlines the history and operation of conventional, mechanical, microinjection.

3.2.2 Microinjection

Microinjection is typically an *in vitro* process whereby minute volumes of liquid are injected into a target biological sample. This process was initially developed by Barber in 1911 [140, 141], however, it was not until towards the end of the 20th century that the technique began to be more widely adopted. The original technique has been widely developed and is used in numerous branches of biological research. Microinjection has been used to introduce a wide range of materials into a host of different cells [142].

The technique is generally carried out by inserting two sterile, micrometre controlled, pipettes into the sample environment. One of these pipettes has a fine pointed tip, while the other has a larger flatter tip. The larger tip is used to apply gentle suction to the sample

and acts to temporarily clamp the cell. The finer tip is used to inject the required liquid [143], as displayed in Figure 3.9. The technique has also been used on adherent cells, without the requirement of a clamping pipette [144].

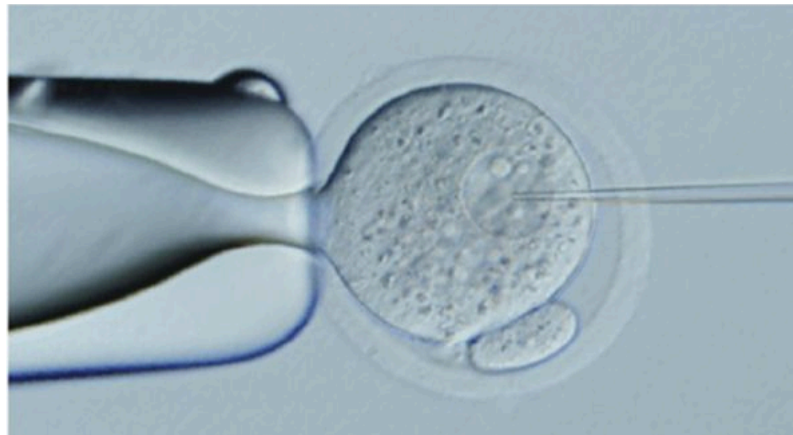


Figure 3.9 – Microinjection of mouse embryo. Microinjection is used to introduce GENIE-3 plasmids directly into the nucleus of a single cell mouse embryo. Taken from Figure 2(5) of Marh et al. (2012) [143].

These techniques have been used with a wide range of materials and target cell types. Early examples of microinjection attempted to introduce bacterial into cells [140]. The technique has also been used with a focus on simple chemistry, such as addition of ionic compounds into the intracellular environment [145]. However later attempts have seen the addition of biological materials such as enzymes and whole organelles [146]. The technology saw a surge in interest during the 1990's as it became an invaluable technique for the direct delivery of genetic material in transfection experiments and saw wide use in cloning studies where it has been used with a range of mammalian [147, 148], fish [149] and plant species [150, 151]. Scaled up microinjection has also been used widely in artificial insemination where the technique can be applied for the intracytoplasmic injection of a sperm cell into a donor egg [152]. Recently, microinjection has also been utilised in the application of gene editing of a human embryo, using clustered regularly interspaced short palindromic repeats, commonly referred to as CRISPR, in CRISPR-Cas9 genome editing. This was carried out in order to correct a mutated copy of the MYBPC3 gene, as mutations on this gene account for approximately 40 % of instances of hypertrophic cardiomyopathy [153].

The ability to use optical forces in order to overcome a cell membrane and insert material into a cell was outlined in the previous chapter. An all optical solution provides numerous benefits, from maintaining a sterile environment to extremely high precision. The photoporation work presented was capable of creating pores in cell membranes and while there was no expression of reporter genes witnessed, it did allow material, in this case trypan blue, to enter the cell. An approach to addressing this issue would be to create an optically controlled needle and syringe-like device, capable of dispensing a greater volume into the cell. To this end, we approach the construction of a microsyringe, using a variety of hollow microcylinders and microspheres, controlled by optical tweezers, to manipulate femtolitres of material into cells.

3.3 Experimental methods

In this section the design and reasoning of the experiments are introduced. These experiments introduce a novel, light driven alternative to conventional, mechanical microinjection techniques. The broad range of cross-discipline techniques are introduced in a number of subsections. Methods used to produce and quantify optical tweezers for the confinement of spherical and non-spherical – in this instance, hollow cylindrical – particles are described. Modification of the optical tweezers, to generate multiple points of optical confinement, are detailed. The methods utilised to fabricate the hollow cylinders and the applicable cell culture protocols are described.

3.3.1 Optical design

The construction of an instrument to generate optical tweezers was central to this series of experiments. To generate the optical tweezing effect, collimated light must be tightly focused. The device in these experiments, illustrated in Figure 3.10, was constructed around a diode pumped Nd:YAG laser, emitting in the NIR (Laser Ventus, 1064 nm, 3000 mW, TEM₀₀). In these experiments, biological samples were suspended in aqueous solutions (PBS or growth media). As water exhibits significantly higher absorption coefficients in the ultraviolet (UV) and far infrared (FIR) ranges of the spectrum, these ranges are avoided to minimise thermal damage to the sample. Unfortunately, biological samples generally have high absorption coefficients within the visible range of the spectrum and more energetic wavelengths induce photochemical reactions within the samples. Hence, the far red (FR) and near infrared (NIR) wavelength

ranges are deemed the most suitable for working in biophotonic research - due to the relative safety when used with biological samples. While this laser was capable of relatively high powers, optical confinement can be achieved with significantly lower laser powers.

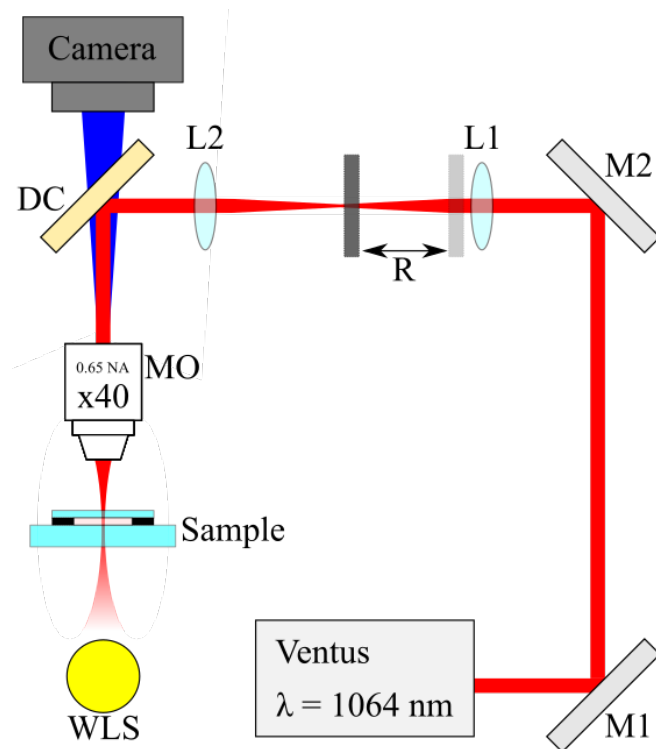


Figure 3.10 – Optical tweezer with Ronchi ruling. The beam from a NIR Nd:YAG source is guided into the system using mirrors M1 and M2. Lenses L1 and L2 act as a Keplerian telescope which is adjusted to manipulate the beam diameter, collimation of beam at MO, to adjust trapping focal position, and also act as an image relay so that tilting of the beam at M2 results in tilting of the beam at the back aperture of MO. A dichroic mirror, DC, is used to guide the beam into the rear of the microscope objective MO. A Ronchi ruling, R, is mounted in the middle of the telescope. The location of R between L1 and its focal point has the effect of widening or narrowing the interference pattern on the image plane.

The laser light is guided by a pair of steering mirrors (Thor Labs, E03) in a periscope arrangement – allowing complete redirection and isolation from the source path – into a 1 : 1 $f = 100$ mm Keplerian telescope (Thor Labs). The beam was directed downwards at 90 °, by a 1037 nm shortpass dichroic mirror (Y1-1037-45UNP, CVI) into the back aperture of a 40x, 0.65 NA microscope objective (Newport, M-40X). The microscope

objective focuses onto a sample slide that is held on a platform mounted to a three-dimension linear translation stage (Newport, M-562-XYZ). This allowed the sample to be moved relative to the fixed microscope objective, so it should be noted that this was also used to allow focusing of the system. One of the micrometres responsible for actuation of the stage orthogonally to the propagation axis of the beam was replaced with a computer-controlled stepper motor. This allowed for controlled acceleration and stable velocity of the stage – critical for accurate measurement of translation velocity which is used to calculate drag force. Stages of the experiment that used biological samples included the placement of a heated stage (P-1000, PeCon), which maintained a temperature at 37 °C, this was to extend the viability of the cells in the samples. A white light LED was suspended below the sample plane to provide illumination for wide field imaging. The image plane was captured using the optical trapping microscope objective and a CCD camera with a removable NIR filter in front of the sensor. Images were recorded using a USB capture card (UTV2820, Techgear) connected to the camera and a desktop workstation.

One of the primary modifications to this system was to integrate a Ronchi ruling (B56-596, Edmund Optics) into the Keplerian telescope region of the system. The Ronchi ruling was supported in a rotary mount that allowed the Ronchi ruling to be turned in the plane perpendicular to beam propagation. This addition projected the Ronchi ruling on the image plane which produced a linear array of optical traps.

At stages of this experiment an inverted setup was used, to record the effects of additional lift from the scattering force. This was comparable in design to an inverted microscope where the microscope objective is held beneath the sample. In the inverted setup the laser was directed upwards by the dichroic mirror, so the scattering force from the optical trap was in the opposing direction to gravity. The imaging components of the system were also adjusted to accommodate this change in orientation.

To record the most accurate measurements of laser power at the sample and account for losses in the system, power measurements were taken after the microscope objective. When the Ronchi ruling was used, an aperture was utilised to carefully isolate the diffraction orders, to approximate the power of each individual trap.

3.3.2 Microneedle fabrication

Microneedles is the term hereto used describe the hollow microscopic cylinders used in large parts of this chapter. As the ease of which a material is held in optical tweezers is determined by the refractive index difference between the sample of interest and the environment surrounding it, a number of different fabrication techniques were tested in an attempt to optimise the confinement of hollow cylinders.

3.3.2.1 Pulled borosilicate capillaries

Microneedles were fabricated by pulling borosilicate capillaries using a micropipette puller (P-97, Sutter Instruments). The borosilicate capillaries used in this experiment had an internal filament – providing greater structural support once pulled – and were 1 cm in length with an outer diameter of 1.0 mm and inner diameter of 0.5 mm (BF-100-50-10, Sutter Instruments). The micropipette puller was programmed to use a temperature of 289 (RAMP), a pull of 30, velocity of 120 and a delay of 200. This process is shown in Figure 3.11. After the pulling process two strands of extremely fine borosilicate were cut from the relatively unchanged main mass of the capillary. These fine ends exhibited a minimal taper, which ranged from an inner diameter of 4 μm to 10 μm and an outer diameter of 6 μm to 14 μm over approximately 15 mm. To reduce the length of these strands, so they were suitable for optical trapping, the strands were diced, using a scalpel blade, in a small volume of water on a microscope slide. An example of the resulting structures is illustrated below in Figure 3.12.

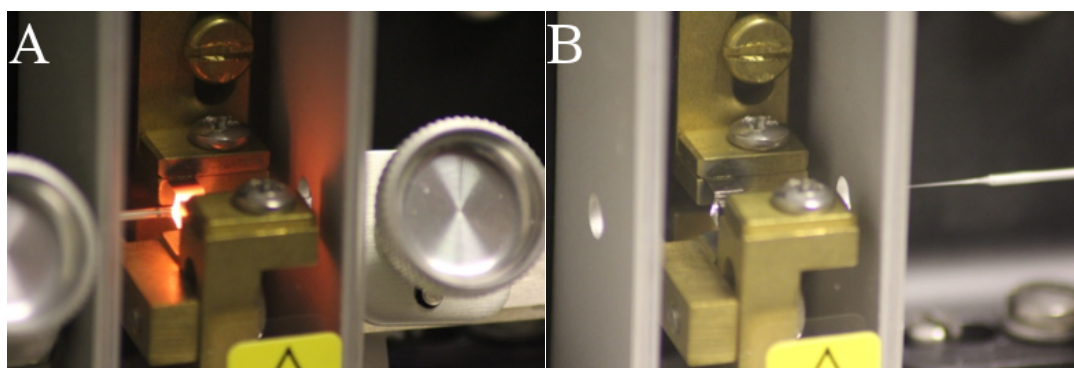


Figure 3.11 – Drawing borosilicate capillaries. (A) A borosilicate capillary is clamped and heated in the P-97 micropipette puller. (B) Upon the programmed temperature and time being met, the capillary is separated with the set force. This results in the formation of two ultrafine pipettes.

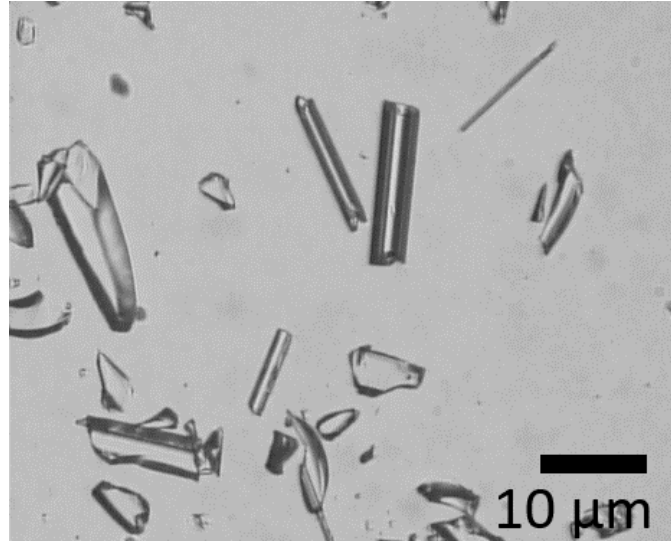


Figure 3.12 – Microscopy of diced, pulled borosilicate capillaries. The methods used to reduce the length of the capillaries all resulted in a significant amount of debris.

3.3.2.2 Rolled SiO / SiO₂ microneedles

Microneedles formed by stress-induced rolling of heterogenous layers were also used in these experiments. These microtubes were provided as part of a collaboration with the Institute for Integrative Nanosciences, IFW Dresden and were produced by the deposition of SiO and SiO₂ layers on a substrate with patterned photoresist. After deposition the sample is exposed to UV light to remove the photoresist. This results in regions of the SiO / SiO₂ bilayers being freed from the substrate, where the stress of the mismatched layers causes the suspended region to roll over on itself. The sample is then coated with a layer of Al₂O₃. The samples are then sonicated in an aqueous solution to dislodge the rolled microtubes from the main substrate. The details of this process are described by Huang et al. [154] and illustrated in Figure 3.13. These samples are shown in Figure 3.14.

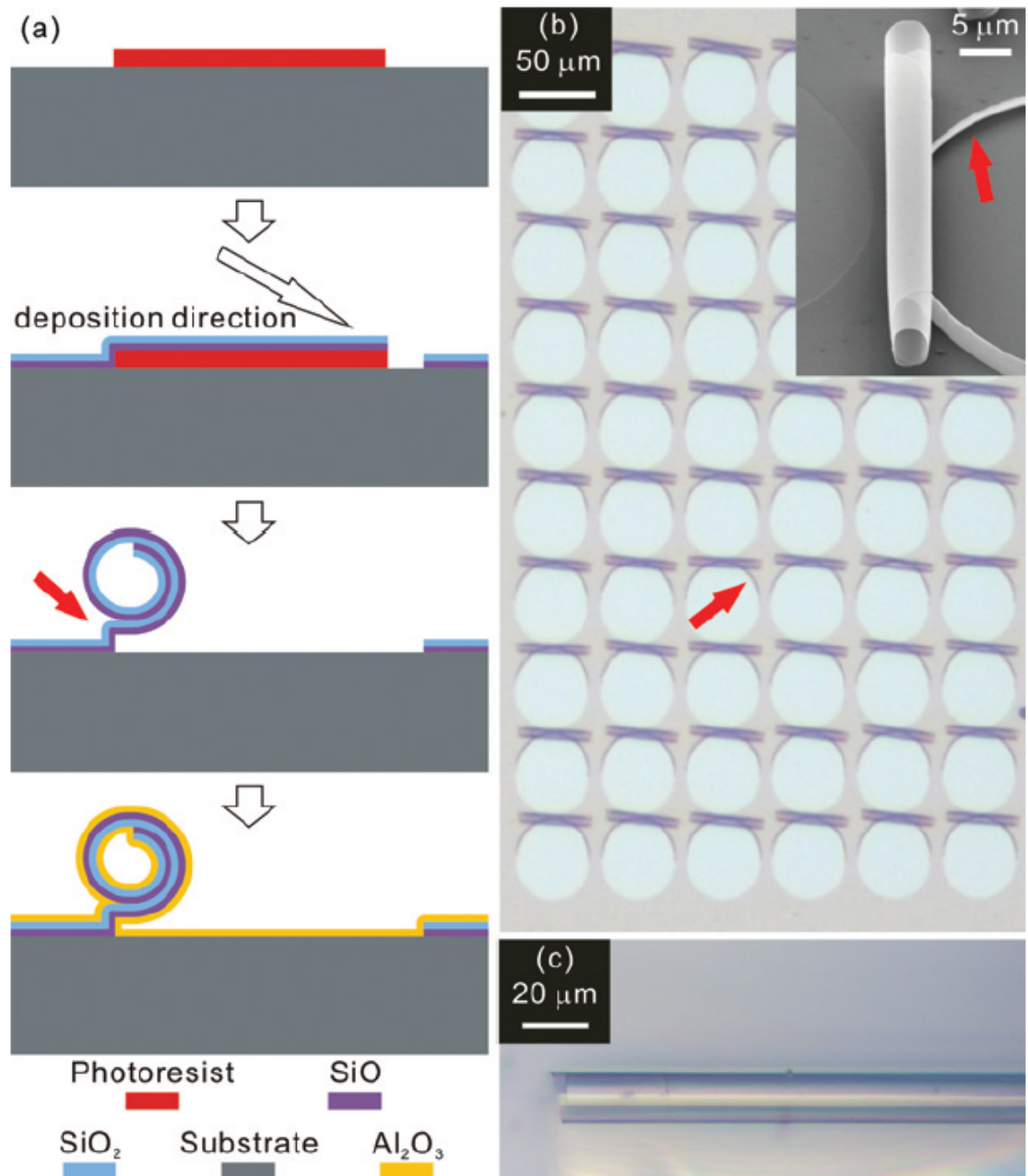


Figure 3.13 – Fabrication of rolled microneedles. (A) The layer-by-layer deposition and etching process. (B) Image of a substrate on which many of these structures have been produced. (C) Image of a single rolled microneedle. Taken from Figure 1, Huang *et. al.* (2009) [154].



Figure 3.14 – Rolled microneedle. A thin-walled, rolled microneedle as viewed through the microscope objective of the system for optical tweezing that was presented in Figure 3.10.

3.3.2.3 Laser inscribed microneedles

Ultrafast laser inscription (ULI) is a process that uses focused high energy pulses of laser light to modify a material. This technique can be used to induce a change in refractive index, producing waveguides in a solid substrate [155, 156], and to cause a conformational change which increases the susceptibility of a localised area to chemical etching [155, 156]. The process is dependent on the chemistry of the target material, but is generally caused by induced ionisation and thermal shock within the focal volume of the laser beam. In this project the use of ULI as a selective etching technique was considered for the fabrication of hollow cylinders. This provides the opportunity for novel use of this technique to accurately control the characteristics of the fabricated hollow cylinders, where the inner diameter, outer diameter and length could be decided in advance. Control over these variables provides the potential to overcome the consistency and supply issues presented with the alternative methods of hollow cylinder fabrication.

ULI with potassium hydroxide etching was used to attempt fabrication of hollow cylinders on a fused silica substrate. These initial hollow cylinders were chosen to be

25 μm in length with a 5 μm inner diameter and a 2.5 μm wall thickness. The resultant structures are shown in Figure 3.15. Unfortunately, these structures proved problematic to release from the substrate and could not be recovered. A more intense etching with hydrofluoric acid was considered, however safety issues regarding removal of the hydrofluoric acid etching solution stopped the advancement of this fabrication method.

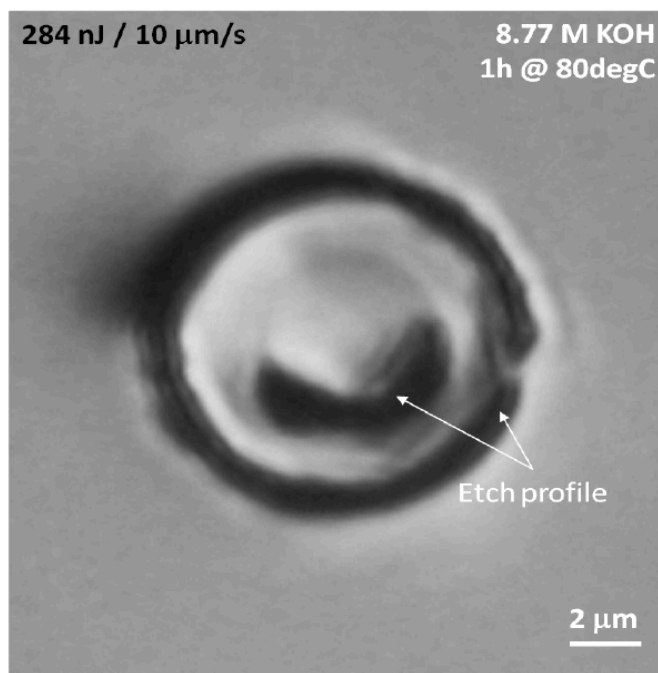


Figure 3.15 – ULI fabrication. End-on view of hollow cylindrical structures etched on borosilicate substrate. Image courtesy of Debaditya Choudhury.

3.3.3 Cell culture

The aim of microneedle manipulation was to apply the technique to single cell biology, for example cell microinjection. For these studies the CHO-K1 cell line was used to provide an adherent test sample. This mammalian cell line is derived from a Chinese Hamster ovary with an epithelial-like morphology. The culture techniques for this cell line are listed in Chapter 2 (2.3.3.1). This work also used cells in suspension for easier optical tweezing. The HL-60 cell line was used here.

3.3.3.1 HL-60 cell culture

The HL-60 cell line is a widely used and stable culture of human promyelocytic leukaemia cells. Unlike many other cells used in this thesis, they do not adhere and grow on surfaces, instead remaining in suspension within the growth medium. Cells were maintained at a concentration between 1×10^5 and 1×10^6 cells/ml in an incubator at 37 °C with 5 % CO₂. Cells were grown in 25 cm² tissue culture flasks (Nunc) containing 5 ml of DMEM (Invitrogen), supplemented with 20 % FCS (Invitrogen) and 100U/ml PenStrep (Invitrogen). Cells were passaged every 48 to 72 hours to avoid overpopulation and renew growth media.

Passaging the cells involved transferring the 5 ml cell suspension to a 15 ml falcon tube. This volume was then supplemented with an additional 5 ml of fresh, growth media at 37 °C. The tube was centrifuged at 500 g for 5 minutes. The supernatant was removed and the cell pellet resuspended in 5 ml of fresh growth media at 37 °C. 1 ml of this cell suspension would be added to a new 25 cm² tissue culture flask and supplemented with 4 ml of fresh growth media in order to maintain the cell line. The remaining 4 ml of cell suspension could be used in experimentation or to bulk the cell line.

3.3.4 Sample preparation

Samples that contained no cells were prepared on glass microscope slides with glass cover slips. To provide a working volume which would allow for optical tweezing, a vinyl spacer was used which was 100 µm thick with a circular space of radius 10 mm. These samples use a maximum sample volume of 20 µl, containing microneedles and/or microspheres, in water. Two varieties of microsphere were used in these experiments, 3 µm diameter latex spheres (17134, Polysciences) and 7 µm diameter polystyrene spheres (64100, Polysciences).

Samples containing biological samples were prepared with either cells in suspension or adherent to a surface. To produce samples with HL-60 cells in suspension, the cells were diluted in a volume of fresh growth medium or PBS, from which an aliquot would be taken and pipetted onto a slide, in the manner listed above.

CHO-K1 cells that had adhered to a surface were used in some cases. In these experiments 35 mm FluoroDishes (WPI) were used to hold the sample. These tissue

culture dishes have a rim that accommodates coverslip glass and a glass base that is comparable in thickness to a coverslip – allowing use in both standard and inverted setups. For these samples and aliquot of cells was seeded 24 hours before the experiment. Microneedles and, or microspheres would be added as required in the moments before attempting optical tweezing.

3.4 Results

The optical tweezers are calibrated in the first instance with a single beam and then with the addition of the Ronchi ruling, which is used to create a triple beam trap for manipulation of microneedles or multiple spheres. The manipulation of different types of microneedle is quantified and finally the manipulation of microneedles is used to attempt to microinject cells. The data generated by the body of experimental work, in this chapter, is presented within this section. Calibration results are presented first, followed by the data for single beam optical tweezer experiments and multiple beam optical tweezing. For each configuration of optical tweezers, the data shows the resultant confinement of microspheres and microtubes. Additional results show the manipulation of single cells for the purposes of isolation by utilizing these systems and the microscopic constructs contained within the sample environment. This is followed by discussion and conclusions.

3.4.1 Calibration of optical tweezers

The simplest structures to confine in an optical trap are spherical. The force generated by an optical trap to confine spherical particles is also simple to express. In these experiments the optical trap remained stationary while the sample stage moved, therefore the optical trap acted to confine particles against the viscous forces of the surrounding environment as it is flowed past the trapped particle.

Polymer and latex microspheres suspended in an aqueous environment were used to visualise the effect of the optical trap and align the beam angle to be perpendicular to the sample. Controlled linear actuation over a range of 20 mm with a low acceleration, 1 mms^{-2} , was used to slowly increase maximum velocity of the sample thus introducing a steadily increasing lateral force on the confined particle. The velocity at which the particle was dislodged from the optical trap is extrapolated as the point at which the

viscous forces of the sample overcome the confinement force of the optical trap, this was repeated in triplicate and instances where the particle was dislodged by collision with another particle were discounted.

3.4.1.1 Power and spacing of multiple beam optical tweezers

Modification of the optical tweezer apparatus to include a Ronchi ruling with a 50 μm period into the telescopic relay generated a diffraction pattern in the profile of the laser beam. This pattern, when focused using a microscope objective formed three usable optical traps, the central – and most powerful – trap is the 0th order of the diffraction pattern which was flanked by weaker – approximately equal – 1st order points. The orientation of the three optical traps could be adjusted by use of a rotary mount within which the Ronchi ruling was held. The Ronchi ruling could be moved in the direction of propagation in the telescopic relay to alter the spacing of the diffraction pattern. This modified optical tweezer arrangement was used to confine 3 μm polymer microspheres, as shown below in Figure 3.16.

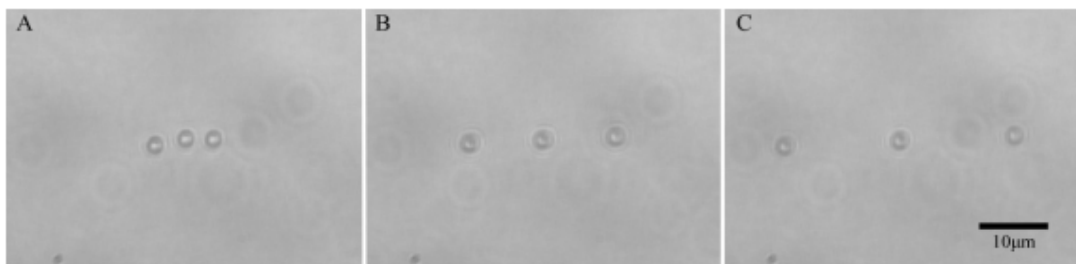


Figure 3.16 – Triple beam optical tweezing of microspheres. 3 μm diameter, polymer, microspheres were confined in each optical trap in this triple beam configuration. The spacing of the traps were adjusted by moving the Ronchi ruling within the focusing region of the telescope in the apparatus. These images were taken as the Ronchi ruling was approximately (A) 20 mm (B) 60 mm and (C) 90 mm from the focus in the telescope, towards L1.

When optically confining polymer microspheres of $r = 1.5 \mu\text{m}$ suspended in an aqueous environment, with a dynamic viscosity of $\sim 1 \times 10^{-3} \text{ Nsm}^{-2}$ at room temperature, it is possible, by noting the maximum velocity prior to the failure of confinement, to apply these values to the Stokes' drag formula, equation (3.1), in order to calculate the force

experienced by the particle, giving the force of the optical trap on the particle prior to failure. This measurement was repeated for the optical tweezer apparatus in both single beam and three beam operation, noting the confinement forces in the 0th and 1st orders in the later instance. The results of these measurements are presented in Figure 3.17.

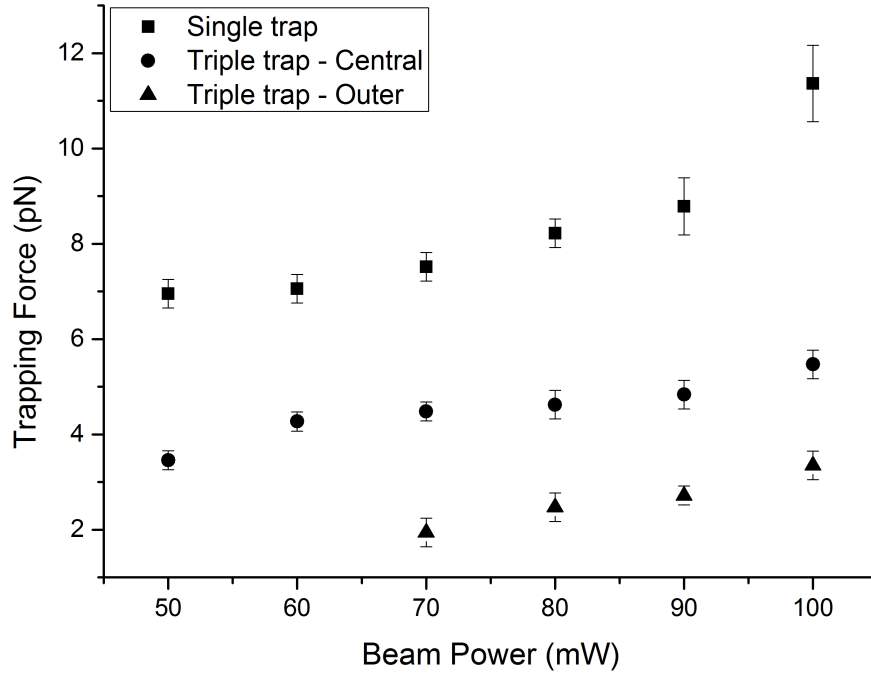


Figure 3.17 – Optical trap forces. Trapping force experienced by 3 μm diameter microspheres in single and triple beam optical tweezers, repeated in triplicate. Power range of 50 mW to 100 mW (measured at rear aperture of microscope objective), single beam optical tweezers denoted by squares. 0th order of triple beam optical trap denoted by circles, 1st order of triple beam optical trap denoted by triangles.

The measurements of critical velocity were used to calculate the force exerted on 3 μm microspheres. With a laser power of 100 mW, the single beam optical tweezers exerted a force of 11.3 pN (± 0.85 pN). The triple beam optical tweezers exerted a force of 5.5 pN (± 0.3 pN) at the central trap (zeroth order) and 3.3 pN (± 0.3 pN) in the peripheral traps (first order). The increased trapping power at the zeroth order is expected owing to the pattern of wave-interference introduced by the Ronchi ruling, whereby the amplitude of the constructive interference decreases across increasing orders.

Still using the 40x, 0.65 NA MO, images of these spheres were recorded and used to produce an accurate measurement of scale, possible through the high degree of tolerance of the spheres (5 % coefficient of variance). Spacing between the optical traps was then recorded as the Ronchi ruling was shifted between the first lens, L1, and the focal point of the telescopic relay. The results of these observations are presented below in Figure 3.18.

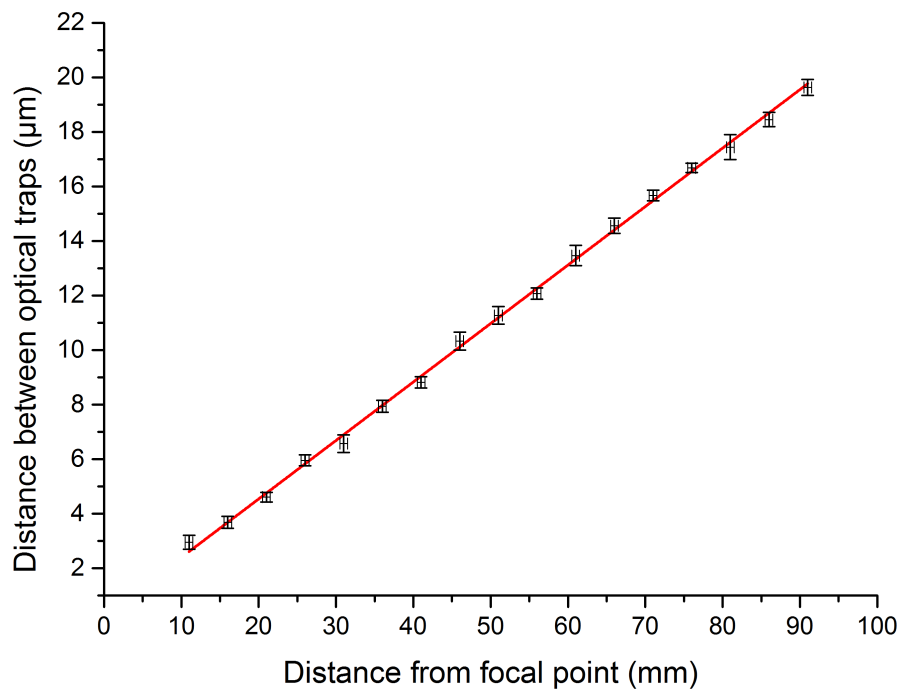


Figure 3.18 – Triple beam optical tweezer spacing. In moving the Ronchi ruling in the focusing region of the telescope, the spatial separation of the optical traps increases as it moves from the focal point. Measurements taken in triplicate.

This information was used to determine where to place the Ronchi ruling in the system, to create the appropriate traps for manipulation of different sized microneedles or multiple spheres, as required.

3.4.2 Optical tweezing of hollow microcylinders

Samples which contained microscopic hollow cylinders were introduced to the optical tweezer apparatus. As this shape presents a higher surface area and lower volume, these structures were expected to be more difficult to confine than microspheres when using optical tweezers. The higher surface area increases the area of interaction and therefore friction between the particle and the environment while the reduced volume of material decreases the force which can be generated on the particles. Differences in confinement force between type of hollow microcylinder and the application of single beam and multiple beam optical tweezers is noted in the following sections.

3.4.2.1 Optical tweezing of pulled borosilicate capillaries

The single beam optical tweezer configuration was used to manipulate pulled borosilicate capillaries. Negligible confinement was noted in the conventional optical tweezer configuration with no measurable movement parallel or perpendicular to the long axis of the capillary being achieved. In the inverted optical tweezer configuration it was possible, using laser powers greater than 1,000 mW, to manipulate the pulled borosilicate hollow microcylinders in the direction parallel to the long axis of the cylinders, this is shown in Figure 3.19. A capillary of $\sim 150\ \mu\text{m}$ in length and $9\ \mu\text{m}$ in diameter was dragged laterally, parallel to the long axis of the capillary, within the sample at a velocity of $7\ \mu\text{m/s}$ ($\pm 1\ \mu\text{m/s}$). Utilizing equations (3.3) and (3.4), it is calculated that $10\ \text{pN}$ ($\pm 1\ \text{pN}$) of force was generated on this capillary. The scattering force of the optical tweezers caused the confined end of the capillary to be lifted slightly from the slide surface in this process. The lifting effect was exaggerated as laser power was increased, while no improvement in lateral movement were noted. Short capillary fragments were witnessed aligning vertically in the direction of beam propagation, when using the inverted optical tweezer setup.

Due to the minimal changes in the profile which the tweezing beam encounters as it is actuated along the length of the capillary there was no noticeable manipulation outside of interaction at the ends of the capillary. It was not possible to generate any notable manipulation of the pulled borosilicate capillaries with the multiple beam optical tweezer configuration.

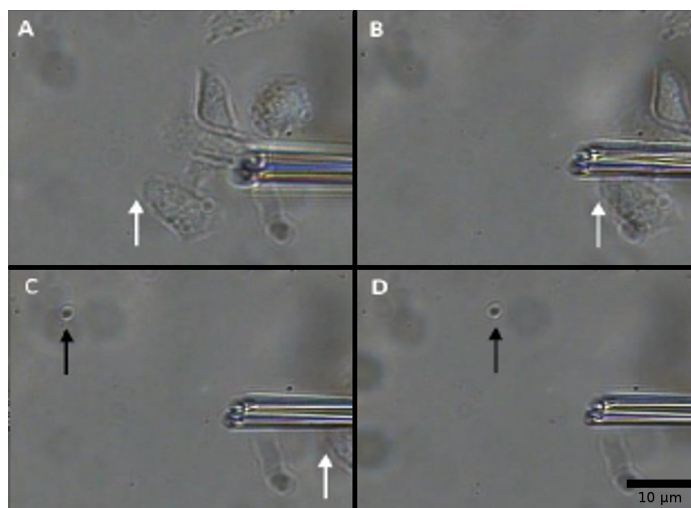


Figure 3.19 – Optical tweezing of a pulled capillary. Using 1,000 mW from the optical tweezing laser, the hollow cylinder is held in place while the surrounding environment is moved (A-D). Frames show this movement by highlighting surrounding debris in the field of view with a white and black arrow.

Initial test samples contained traces of solid borosilicate that were approximately cylindrical in shape. These fragments were present as the remnants of a supporting filament that is present in the first type of borosilicate capillary used in these experiments. Solid cylinders present a greater volume of refractive index change and were significantly easier to confine and manipulate with each optical tweezer configuration. This observation is comparable to the literature where there are examples of solid cylinders and nanowires being manipulated using optical tweezers [123].

3.4.2.2 Single beam optical tweezing of rolled hollow cylinders

Manipulation of the rolled SiO / SiO₂ microneedles was attempted using the inverted single beam configuration of the optical tweezer apparatus. Using this configuration, it was not possible to manipulate the microneedle in the direction parallel to the long axis. This effect, or lack thereof, is thought to be due to the lack of refractive index change when actuated in this direction. This coincides with the observations utilising the pulled capillaries, particularly when trapping forces are expected to be weaker with the rolled microneedles due to the decrease in wall thickness.

Manipulation approximately perpendicular to the long axis of the rolled cylinder was only possible at the ends of the microneedle. Mid-length confinement did not generate enough force to allow movement, regardless of available laser power. Using a beam of 2,800 mW, confinement at the end of the capillary was possible. This resulted in a slight lift of the confined end, via which the capillary could then be rotated. This is illustrated below in Figure 3.20. While this allowed some manipulation, the ultimate requirement is relocation of a capillary while maintaining control over its orientation.

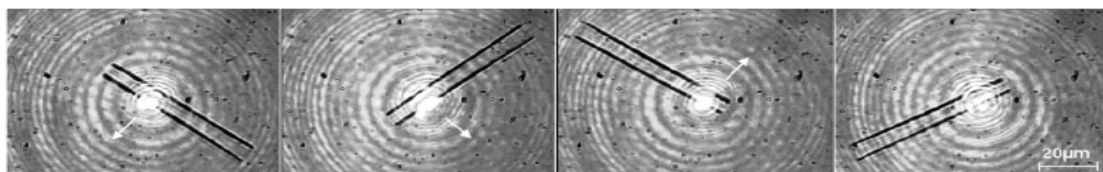


Figure 3.20 – Optical tweezing of a rolled microneedle. Optical tweezers confine the end of a rolled microneedle and rotate the microneedle on axis, direction indicated with white arrow.

3.4.2.3 Multiple beam optical tweezing of rolled hollow cylinders

The multiple beam optical tweezer configuration was used to confine and manipulate these SiO / SiO₂ (~120 nm wall thickness) rolled microtubes. Similarly, to the single beam configuration, the forces generated upon these structures were extremely weak, even at higher laser powers.

Manipulation of the microtube parallel to the long axis was not possible. It is feasible that with a significantly increased power, the rotational effect noted in Figure 3.18 would be possible. However, due to the loss in power caused by both the Ronchi ruling itself, and the spread of power in the resultant diffraction pattern, it was not possible to generate a confinement force in the sample which was comparable to that used in the rotary example.

It was possible to confine and manipulate the rolled microtube perpendicular to the long axis. However, this tweezing was extremely weak. The microtube could be seen to become confined, but it could only be gently rocked, it was not possible to create continuous motion — with motorised or manual actuation — as such, accurate force

measurements could not be produced in this instance. It is interesting to note that the microtube does not align parallel to the array of multiple optical traps. The effect observed was for the microtube to align with the central beam over the centre of the structure while opposing walls aligned with the outer beams. This is shown below in Figure 3.21.

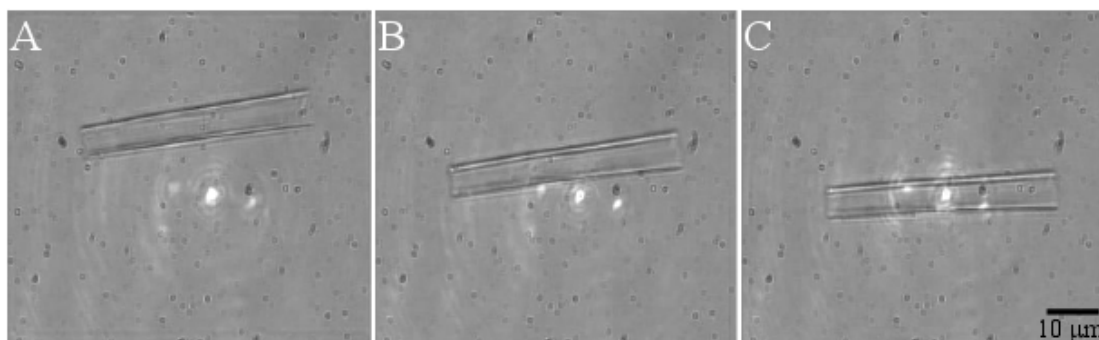


Figure 3.21 – Triple beam optical trapping of rolled microneedles. Weak confinement and off axis alignment of the cylinder. (A) The three-beam optical tweezer is turned on with a suitable rolled microtube in the field of view. (B) The rolled microtube is moved towards the optical trap. (C) In extremely close proximity to the optical trap, the rolled microtube ‘snaps’ into the trap and is weakly confined, aligning walls with the outer optical traps.

The alignment and manner in which the microneedle is pulled into array of optical traps is likely due to the manner in which hollow structures react in an optical trap. A combination of forces attracting and repelling the microneedle create a well in which it is contained, with the central beam producing a primarily repulsive force and the lateral traps providing a weak attractive force. The net axial force is relatively weak, resulting in an inability to manoeuvre the microneedle in the axial direction. In the experiments presented it became apparent that this optical tweezer system was not capable of adequately manipulating these hollow microcylinders. To continue approaching this issue, with the materials available, the additional manipulation of microspheres was required to use as handles which would allow the hollow microcylinders to be manipulated indirectly within the optical tweezer system.

3.4.3 Construction of optically controlled microsyringe

To address the intrinsic difficulties of directly manipulating hollow cylinders when using optical tweezers, an alternative approach was considered. Utilising the known strong confinement of spherical particles, these spheres were considered as handles with which to control the hollow cylinders. Many groups have presented work where microscopic structures have been manipulated by fabricating them with the addition of spherical handles [126]. However, this work attempts full construction of a microdevice and its novel application within the sample chamber.

In this experiment 7 μm diameter polymer microspheres were used in the sample as handles with which to manipulate microcapillaries. As these spheres were larger in diameter than most of the microcapillaries, once confined by an optical trap at 240 mW, they were used to push on the end of the microcapillaries within the sample. This is illustrated in Figure 3.22. As this method imparts force on the microcapillary from one side there was no control over the orientation of the microcapillary, which could slowly rotate around the sphere, away from the direction of movement imparted microsphere. These erratic movements proved problematic when attempting to reproduce and, due to deflection from surfaces with which the microcapillary came into contact, it was not suitable for penetrating a cell membrane. When in close proximity to the walls of the capillary the microspheres would regularly become attached and were generally not removable using the optical tweezers. Using this effect, it was possible to use these microsphere handles to pull the capillaries. However, this regime also proved ineffective for the purposes of cellular penetration.

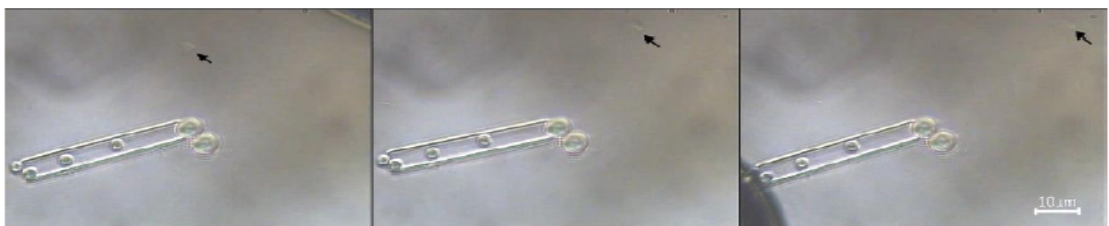


Figure 3.22 – Pushing a rolled microneedle. A 7 μm microsphere is optically trapped and used as a handle to manoeuvre a rolled microneedle. Arrow notes stationary debris in environment.

Utilizing the ease with which relatively small, 3 μm , latex microspheres can be confined using optical tweezers, at 100 mW, these microspheres were manipulated into and controlled within hollow capillaries. This is illustrated below in Figure 3.23. Microspheres were also noted to stick to capillaries when they were brought into contact. This effect was significantly more prevalent with microspheres that were within the capillary and increasing optical tweezer powers were unable to dislodge them, once stuck. This binding could allow additional trapping control of the capillaries, overcoming the rotational issue discussed when the microcapillaries were being pushed by a microsphere.



Figure 3.23 – Optical tweezing inside a rolled microneedle. A 3 μm microsphere is manipulated using a single beam optical tweezer and loaded into a rolled microneedle.

The ultimate aim of this was to utilize a pair of optically trapped microspheres to manipulate a hollow microcylinder. One microsphere, with a diameter greater than the inner diameter of the hollow cylinder, is held in the zeroth order of the three beam optical tweezers. The other microsphere must be smaller, but close to, the inner diameter of the hollow cylinder and held within a peripheral trap from the three beam optical tweezers. To construct the device, the larger microsphere would be moved into direct contact with one of the open ends of the hollow microcylinder. The larger microsphere would primarily act to exert force on the hollow microcylinder, moving it towards and piercing the membrane of the target cell, as per Figure 3.22. The smaller microsphere would be aligned and manoeuvred into a hollow microcylinder, as per Figure 3.23. The smaller microsphere serves two purposes. When manoeuvring the hollow microcylinder, it would assist in maintaining the alignment of the hollow microcylinder by reducing the opportunity for it to rotate around the larger sphere. Once the target cell has been pierced, the smaller microsphere could then be manipulated by adjusting the position of the Ronchi ruling, resulting in the syringe-like expulsion of material held within the microcylinder, into the cell, as illustrated in Figure 3.24.

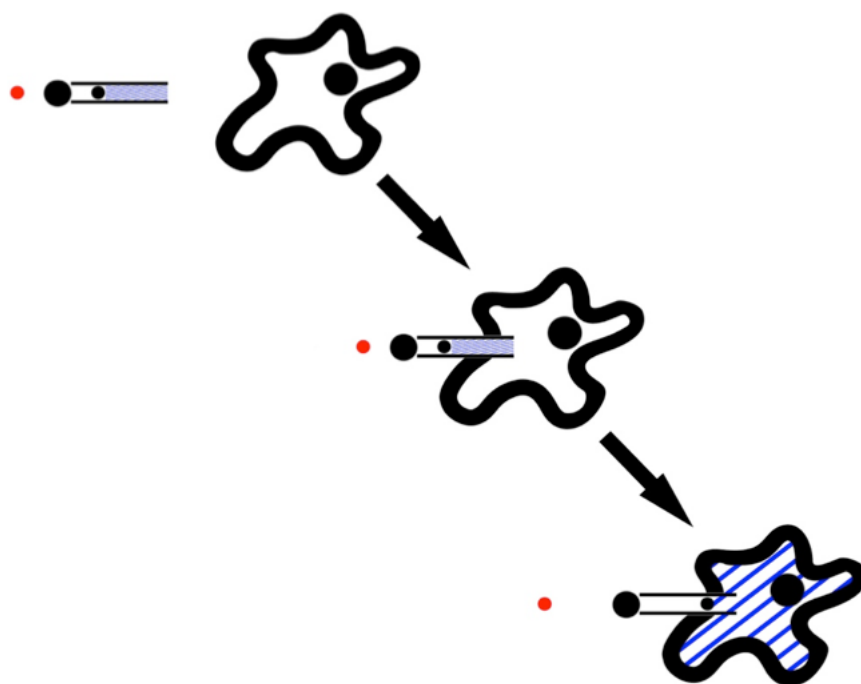


Figure 3.24 – Optically controlled microinjection illustration. Idealised illustration of optical tweezing of a hollow cylinder, by proxy. Large microsphere used as a handle, smaller microsphere inside the hollow cylinder used for trapping stability and to dispense material into a target cell. Red point indicating unused 1st order trap.

When these structures were created and confined within samples which contained cells, it was not possible, in the present configuration, to penetrate the cell membrane. Cells could not be adequately confined while also using the optical tweezers to maintain the microcapillary structure; when they were brought together, the cell was simply dislodged from the optical trap. The experiment was slightly modified and attempted using adherent cells, so the optical tweezers would only be required to control the microsyringe apparatus. However, using these adherent cells, the capillary was deflected from the surface of the cell. In the conformation used in these experiments, where penetration of the cell is attempted parallel to any rigid surface, the soft cytoplasmic body of the cell allows greater deformation of the cell membrane, hence greater forces are required to penetrate the membrane [157]. Physical and chemical methods of increasing permeability of the cell membrane exist, which may allow future success in such experiments, these are discussed later in this chapter.

3.4.4 Cell isolation using microneedles

The ease with which particles could be confined within capillaries was used as the basis for another attempt at utilising these hollow structures with optical tweezers. These cylinders were used to attempt transport of an individual cell from a large sample into an isolated environment. A culture of cyanobacteria, provided by Charles Cockel of the University of Edinburgh, was viewed under the optical tweezer setup. A pulled capillary, which was not dissected, was fixed to the stage with the pulled end in the sample. Using the optical tweezers it was possible to confine a single cyanobacteria cell from the colony and manipulate that cell into the pulled capillary, as shown in Figure 3.25.

The tip of the capillary was then broken into an Eppendorf tube containing growth medium. While cultures developed, it was not possible to say with certainty that this was from the optically tweezed cell. It may have resulted from contamination of other cells from the target sample, either sticking to the external surfaces of the capillary or extra cell suspension being drawn into the capillary as it was removed from the sample. Issues which may be alleviated by the use of smaller, optically confined microcapillaries. And incorporating this technique with a microfluidic device capable of selectively isolating cells [158].

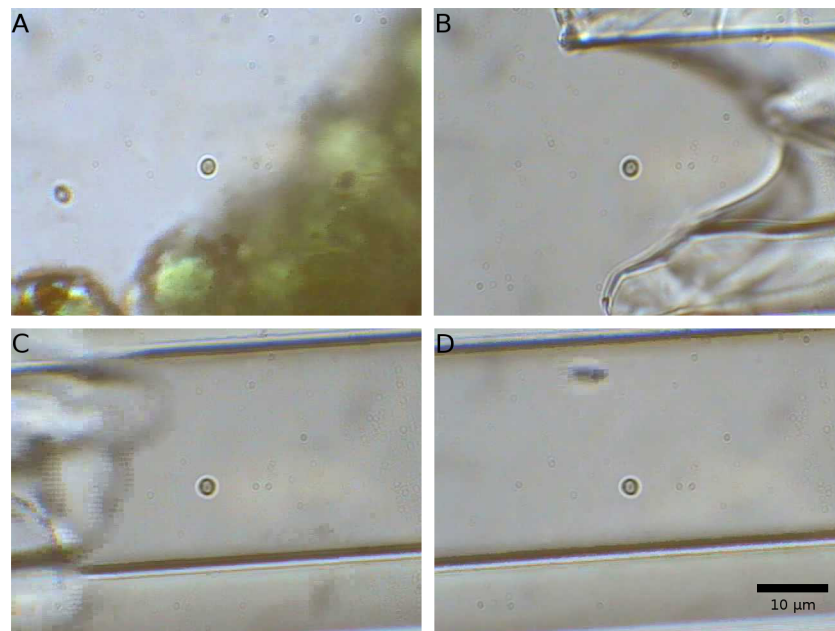


Figure 3.25 – Isolation of cyanobacteria. (A) A single cell is manipulated using the optical tweezers isolated. (B) The cell is brought to the opening of the pulled borosilicate micropipette. (C) The cell is pulled into the micropipette. (D) The cell is taken 100s of microns into the capillary.

3.5 Discussion

Summarising the results; it was feasible to optically trap microcapillaries in a limited capacity, under certain conditions. At the time of presentation and publication this was the first reported instance of hollow cylindrical structures being confined and manipulated using optical tweezers [139]. In the presented format, utilizing these structures in this manner of optical tweezing, it was not possible to generate a system analogous to those used for conventional microinjection. However, the results still provide some promise.

Limitation in optical trapping could be overcome by the use of specifically designed two-dimensional diffraction gratings or the implementation of a spatial light modulator to allow adaptive control of the optical traps. This would allow for the optimisation of all optical tweezing, allowing controlled optical trap formation at desired locations and the capability for multiple equally powered optical traps which could be manoeuvred dynamically, and not restricted to a single direction, as per the Ronchi ruling. The use of an adaptive element would also allow for an optimisation of the optical trap patterns when directly tweezing hollow cylinders. These techniques have been used widely and, particularly in the case of spatial light modulators, are becoming more commonplace.

The issue of lateral force generation will persist with cylindrical particles. Moving an optical trap along the long axis of a cylindrical particle will not yield a change in refractive index and there will be minimal force generation in that axis. This would prompt problems in trying to pierce a cell membrane, in biological experimentation. Other work has utilised AFM technology to track the force required to penetrate a cell membrane, but found the required forces ranging from ~ 1 nN [129, 130] to >100 nN [157]. Due to the fluid nature of the cell membrane and cytoplasm, the thickness of the cell at point of penetration was found to increase the force required to pierce the membrane [157].

Modification of the experimental procedure — to align and move the optically trapped microcylinder perpendicular to a rigid surface, such as the growth substrate — would minimise the degree of cell membrane deformation and thus reduce the force required for penetration. Attempts at modification of the surface chemistry of the piercing device have yielded no discernible improvement in penetration [129]. Adjustments in temperature influence the permeability of cell membranes [130] and there are a range of chemical methods which increase the permeability of the cell membrane for other

biological techniques [159, 160]. It is possible that utilising solutions containing tris or EDTA may increase the likelihood of successfully piercing a cell membrane with an optically trapped microcylinder.

The greatest issue with this project was the availability of microcapillaries. In the case of the pulled borosilicate capillaries it was an inability to produce regular and debris-free samples. With the resources at hand, the extent at which their production could have progressed, was limited. The rolled microtubes suffered from lack of raw supply with quality dropping latterly. Attempts were made towards novel manufacturing techniques using ultrafast laser inscription followed by selective chemical etching, but these never came to fruition. However, the use of ULI would have provided the ability to produce, in house, hollow microcylinders that could be tailored specifically to requirements, in attempts to provide a uniform source of microcylinder.

There also were no commercial sources of suitable microneedles, however the technique of two photon polymerisation might be worth pursuing in future. Further optimisation may be possible by combining ultrafast laser inscription techniques, or two photon polymerisation for microneedle production and combining this with the technique of including spherical handles as part of the fabrication process, as per Philips et al., 2012 [126].

3.6 Conclusions

This body of work was not able to display an alternative to conventional microinjection. However, there does appear to be potential for optical tweezing of structures with the intention of compromising the mammalian cell membrane, with the aforementioned optimisations. The fundamental manipulation of hollow cylindrical structures is in itself an interesting validation. This also produced the interesting application for sample isolation using the optical tweezers to load hollow capillaries. Additional applications utilising these techniques are undoubtedly possible. The development of techniques from the optics bench to a clinical environment is rarely a rapid one. The footsteps of research carried out within this chapter will hopefully build towards the applications of optical tweezers outside the physics laboratory.

Chapter 4

Quantum dot luminescence nanothermometry in optical tweezers

4.1 Introduction

Temperature is a vital variable that must be carefully controlled in many bodies of physical research. At 0.01 °C, and a vapour pressure of 4.58 mm Hg, water can be a solid, a liquid or a gas, this temperature representing the phenomena known as the triple point of water [161]. Water is a significant resource in chemistry and biologically, it is a requirement for life, yet the physical properties of this highly abundant and critical compound vary drastically depending on temperature. This is true across chemistry, where chemical reactions will only occur within a certain temperature range, and by extension, this is also true for biological systems, which rely on reactions, often with large, temperature sensitive molecules, to function. Regarding biology, the simple viability of an organism may only be maintained within a relatively narrow thermal window, with even small fluctuations still capable of inducing changes in cellular behaviour.

Biophotonic techniques, such as photoporation and optical tweezing, often use tens to hundreds of milliwatts of laser power, and beyond, tightly focused into small volumes. These could be to generate pores in a cell membrane, optically trap a cell, affect volumes within a microcapillary or provide function in a microfluidic device. However, the density of energy from such highly focused light can also generate significant local temperature increases if photon absorption occurs. If the photon density is high enough, as with optical tweezers – but more frequently when using instruments that utilise femtosecond pulses, as per Chapter 2 – two photon absorption can occur [162], transferring energy to the cell that may break chemical bonds, induce DNA damage or generate free radicals. Attempts to measure such local temperature changes, particularly intracellularly, are limited due the scale and sensitivity required. To approach this, nanoparticles are considered as probes for use in temperature measurement within biological environments, particularly those within biophotonic applications.

This chapter introduces the application of quantum dot nanocrystals as a means of measuring temperature change, initially within the confinement volume of an optical tweezer. While optical tweezers provide an excellent tool for biological study, the thermal impact of this high photon density must be considered. Where source wavelength may be chosen to minimise phototoxicity, it should also be considered as an unwanted heat source. This effect may be minimised by employing a source with minimal absorption in the target environment.

4.2 Background

The following subsection of this chapter will open with the effects of temperature on biological samples and the inherent importance of temperature regulation over a relatively narrow thermal range, leading into aspects of single cell biology and biochemistry. The issues with recording temperatures in microscopic environments will be discussed and a variety of techniques, which can be exploited to measure temperature, introduced. The concept of luminescent nanothermometry is discussed and the exploitation of semiconductor quantum dots for this application, particularly in biological samples, is reviewed. Heat generation resulting directly from the operation of photonic tools, for example optical tweezers, is examined.

4.2.1 Temperature and biology

All organisms are sensitive to a wide range of physical effects and generally constrained to a narrow range of parameters, temperature is a variable that is particularly important in biological studies.

On the scale of a large multicellular organism, there are several mechanisms that act to maintain a relatively narrow temperature range. In cold weather, hairs are raised to trap an insulating layer of air and blood vessels in the extremities constrict to preserve the temperature around the vital organs. In the heat, skin may produce sweat, which evaporates in the air, lowering the surface temperature of the skin and blood vessels dilate, increasing blood flow to the extremities and increasing the heat transfer from the core of the body, again protecting the vital organs. The human body operates typically at 36 °C to 37 °C, an increase over 37.5 °C is deemed to be developing a fever, hyperthermia, and increases over 40 °C are life threatening. Conversely, a core body temperature below 35 °C is considered hypothermic. However, when considering the single cell, these macro mechanisms are not present. As the single cell is orders of magnitude smaller, it has a significantly larger surface to volume ratio, owing to the square-cube law, making it more susceptible to even relatively minor temperature fluctuations in the exogenous environment.

We are fundamentally aware that temperature is important. The question is, why? To answer this, we must consider the foundations of biology. We take the cell, the smallest and most basic biological unit that conforms to our definitions of life. The cell contains a variety of complex structures and relies on a host of biochemical processes that control everything from energy generation and waste management to cell division or cell death; in effect, a phenomenally complex chemical reaction. Many cellular processes are regulated by proteins, large biological molecules that rely on a robust tertiary structure in order to function. In chapter 2, some of the effects of changes in protein structure were discussed. The case described there was a change introduced by a genetic change or error; the proteins were incorrect from production. However, protein shape and thus function can be inhibited once formed, where it is said to be denatured. In these instances, the cell may be able to rectify the issue via internal regulation mechanisms. If the cell is unable to recover the damaged pathways, this can induce the cell to become apoptotic, or necrotic, depending on the extent of the damage. Proteins are often extremely sensitive to environmental variables, temperature in particular.

Proteins are generally formed by number of secondary structures; helixes and sheets. These structures are formed by thousands of chemical bonds, the bond angles of which define the shape of the structure, where even a slight change in temperature has the potential to cause a protein to be denatured. A denatured protein can have an inhibited, or completely lost, functionality. However, while temperature changes are damaging to cells, many species have evolved biochemical mediators that respond to these environmental changes.

4.2.2 Heatshock

Exposure to a change in temperature that is even slightly out with the ideal range of the cell can result in catastrophic damage. This form of environmental insult will result in the cell upregulating factors to manage the stress; this is the heatshock response. The factors involved are the heat shock proteins (HSP) [163].

The response of HSPs is regulated by a complex that is formed between the HSPs and the heat shock transcription factors (HSF). There are a broad range of HSPs and HSFs, but in healthy cell operation, the HSPs and HSFs are inactive. However, in response to denatured proteins in the cellular environment, the HSP binds to the denatured proteins, separating from the HSFs. The release of the HSFs promote the production of more HSPs to respond to more denatured proteins. The HSPs which bind to denatured proteins can then attempt to refold the proteins to the correct shape or remove them from the cell [163]. While required in function, these factors have also been reported as contributory, or being present, in the disease of mammals [164 - 166]. They are of particular interest in oncology [167, 168], including pancreatic cancers [169], and have also been discovered to have function related to the cardiovascular system [170]. These factors are found widely throughout biology, further highlighting their importance.

4.2.3 Temperature on the small scale

The temperature sensitivity of the cell is a primary variable in biological work. Biological research is often performed on a bulk scale, where macroscopic processes can be used to regulate temperature, such as via an incubator. However, a growing body of work focuses on the single cell, and while this may often be maintained at a macroscopic level, techniques using tools such as optical tweezers, may introduce highly localised

temperature changes, which only significantly effect an individual, or small number, of cells. These effects may be so localised as to not be detected on a macroscopic level, such as with the conventional temperature probes of an incubator. When exploring these processes on single cells, such as with optical tweezing, we must concern ourselves with the effects, such as thermal loading, which can be burdened upon the individual cell – with a view to minimise any unintentional physiological insult. The issue then falls on the problem of detecting temperatures at the cell level, the micro- or nanoscale. In addition to the size requirements, detection speed must also be considered, owing to the likelihood of rapid temperature changes in a minute volume, as must accurate measurement at physiological temperatures, owing to the narrow range of temperatures over which cells are functional. A number of temperature detecting tools are presented in the literature, which reside within the nanoscale realm (typically 1 – 100 nm). This range of devices, particles and dyes can be classified as nanothermometers.

While a nanothermometer, following the classic design style of a mercury-in-glass thermometer has been produced, utilizing liquid gallium in a carbon nanotube and read using an electron microscope [171], as shown in Figure 4.1, this approach, while elegant, is clearly not practical for applications monitoring live cells within viable environments. Instead, we look at the applications of light-based technologies as tools for measuring temperature and how these technologies can be applied for the purpose of monitoring the environment surrounding single cells or even the temperature of single cells themselves.

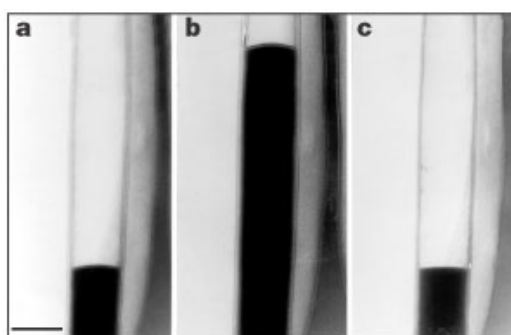


Figure 4.1 – Gallium nanothermometer. The level of gallium shift as the temperature is adjusted from (A) 58 °C, to (B) 490 °C and (C) 45 °C. Scale bar denotes 75 nm. Taken from Figure 1, Gao & Bando (2002) [171].

A wide array of methods exist which can be implemented for monitoring the thermal properties of single cells and other biological samples. The implementation of temperature sensing of biological samples, on a cellular level, will generally rely on the use of particles or pigments in a sample as fluorescent probes. There are also a broad range of non-fluorescence techniques which have been used for the acquisition of temperature data from a sample [172].

Raman spectroscopy does not require fluorescence from the sample, instead the Raman scattering relies on inelastic scattering of photons from the sample. From this inelastic scattering, it is possible to calculate temperature generation by the ratiometric comparison of the Stokes and anti-Stokes shift. However, this tends to require a strong Raman signal, and yields a relatively low accuracy, with the literature often citing a range of ± 10 °C, which is not useful for the resolution required in single cell thermometry or biological research in general [173, 174].

Similarly, without the use of a fluorescence emission, it is potentially possible to use infrared thermography to monitor the temperature within a system [172]. Thermography is the measurement of the black body infrared radiation released from a target sample, generally in the mid to long-wavelength regime. However, as with Raman scattering, the technique would not be ideal for use with biological samples at the cellular and sub-cellular level. In this instance, the thermal sensitivity is not an issue, long wavelengths of light are employed, and these techniques have a spatial resolution which is Rayleigh limited, thus it is not suitable for applications that require a high spatial resolution [172]. When fluorescence emission is considered as an approach for measuring temperature, there is a broad range of materials and properties that can be exploited.

4.2.4 Fluorescent methods

Fluorescence is the backbone of a range of incredibly powerful analytical tools. The exploitation of light is the foundation of many of the greatest tools for life science research. In biological research, fluorescence techniques are already widely exploited for labelling biomarkers and providing observable evidence of genetic modification. However, the fluorescence properties are dependent on variables within the physical environment of the material, such as temperature.

A range of fluorescence sources may be used to allow the measurement of temperature change within a sample. These offer a practical solution for measuring temperature in microscopic volumes, allowing access to the cell, the extracellular environment or microfluidic devices. The properties of fluorescence can be recorded in a number of manners, two of the most common methods are to measure the intensity of the fluorescence and the spectral shift of the fluorescence. The fluorescence lifetime and bandwidth of emission may also be recorded and interpreted to calculate fluctuations in temperature [175].

The varying intensity of a fluorescence is temperature dependent [175]. However, the intensity of fluorescence is also affected by a wide range of variables. The fluorescence intensity of a marker will be sensitive to photobleaching [176], pH changes [175] and possibly chemical reaction [175]. Therefore, monitoring changes in intensity becomes problematic, especially within the variable biological environment. As with intensity, fluorescence lifetime presents issues with environmental impact [177], this technique also typically requires several minutes to generate an adequate signal, limiting the effectiveness for use with live cells [177]. We therefore look towards temperature dependent shifts in emission spectrum.

The fluorescence of dyes may be monitored to record changes in temperature. Rhodamine is a family of fluorescent dyes with a broad range of uses, including tracking flow within fluidic systems [178] and as stains in microscopy [179, 180], flow cytometry [181] and histology [182]. Some members of this family of dyes are also noted to exhibit temperature sensitivity in a number of ways, such as a decrease in the emission intensity as temperature increases [183] or a measurable decrease in fluorescence lifetime [175]. However, the spectral properties become problematic, owing to the broadband nature of the fluorescence from rhodamine dyes, so we look towards the narrow fluorescence spectrum typically exhibited by uniformed particle-like probes. Thermometric properties of lanthanide based compounds have been reported [184, 185] as an option for thermometry, however, availability is limited and these exotic structures are often generated in-house by research groups. Here we place focus on the widely available and broadly used quantum dot nanoparticles, for which the literature indicates they have also been used to great effect in this application [175].

4.2.5 Quantum dots

A range of materials can be applied to the quantitative study of temperature changes. Within systems where the information is gathered via fluorescence, additional material will generally be added to either the cells, or the environment within which they are suspended. These are typically in the form of fluorescent proteins, dyes or distinct particles. When probing a biological sample, it is important to maintain the viability of the cells and limit the introduction of materials which induce physiological changes and damage, to this end, a great deal of interest in thermometric particles has been focused on quantum dots (QDs) [175, 186, 187].

Semiconductor nanocrystals, such as QDs, exhibit quantum confinement in three dimensions. This results in a greater distinction of the available energy levels, which causes the fluorescent light emitted to be of a highly uniform wavelength. These have been produced using a range of materials in several different structures. Though quantum dots are available in a range of sizes, they are typically <10 nm in diameter and can often be easily dispersed in solution [188, 189].

Quantum dots are semiconductors. Upon absorbing a photon, an electron may be excited from the ground state to a higher energy state, moving from the valence band to the conduction band, becoming an exciton. The difference in energy between these bands is the bandgap. The electron will, typically, rapidly relax back to the ground state with the energy from the exciton being released as a photon, fluorescence [190, 191]. This process can be illustrated by use of a Jablonski diagram, as shown in Figure 4.2. The fluorescent properties of a QD are defined by the bandgap properties. The bandgap of a QD depends on the chemical composition, but in QDs, it is also heavily influenced by the QD size. As QD structures become larger, the bandgap decreases [190], impacting the energy of the photon released upon relaxation to ground state. Simply, the larger a QD, the longer the wavelength of the emission photon. This allows for the specific design of fluorescent properties of QDs, as such, the range of commercially available quantum dots, particularly those tailored for biological study is growing.

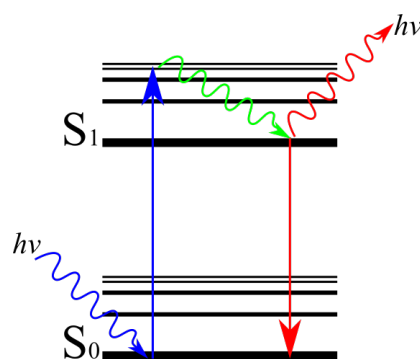


Figure 4.2 – Jablonski diagram of QD fluorescence. A photon ($h\nu$) is absorbed, exciting an electron from the ground state, S_0 , to an excited state, S_1 (blue arrow). There is a loss in energy due to internal conversion and vibrational relaxation (green), before the electron relaxes back to the ground state (red arrow), emitting a red-shifted photon.

The first reported biological applications of QDs were for labelling in fluorescent microscopy [192, 193], in 1998. Since these initial works, the range of applications has broadened significantly, incorporating QDs into numerous biological experiments [194], from immunoassays [195] to drug delivery [196] and thermometry [175].

The fluorescence emission of a quantum dot is determined by the bandgap, a physical characteristic that is determined by a variety of factors, such as the chemical composition, structural composition and size. While these changes can have significant effect on the emission properties of a quantum dot, as evident by the broad range commercially available, these are not the only factors. The bandgap of semi-conductor materials has been shown to exhibit a temperature dependence, with the bandgap decreasing as temperature increases [197]. This translates to a reduction in the energy of photon released, a red-shift in emission wavelength released as temperature increases. Exploiting this temperature sensitive property, for thermometry, has been reported in the literature [22, 198 – 207]. An example of which is shown in Figure 4.3. A number of quantum dot types have been reported, most commonly Cadmium Selenide (CdSe) [199 – 204] and Cadmium Telluride (CdTe) [22, 205 – 207]. The use of these particles as temperature probes with biological specimens has been reported, with a range of applications, from monitoring the general environment [200] or specific biological events, such as calcium flux [201], to tracking the impact of localised heating induced by the high absorbance coefficients of gold nanoparticles [202] or carbon nanotubes [22]. There is also another form of nanocrystals which may be used for these applications, upconverting nanocrystals.

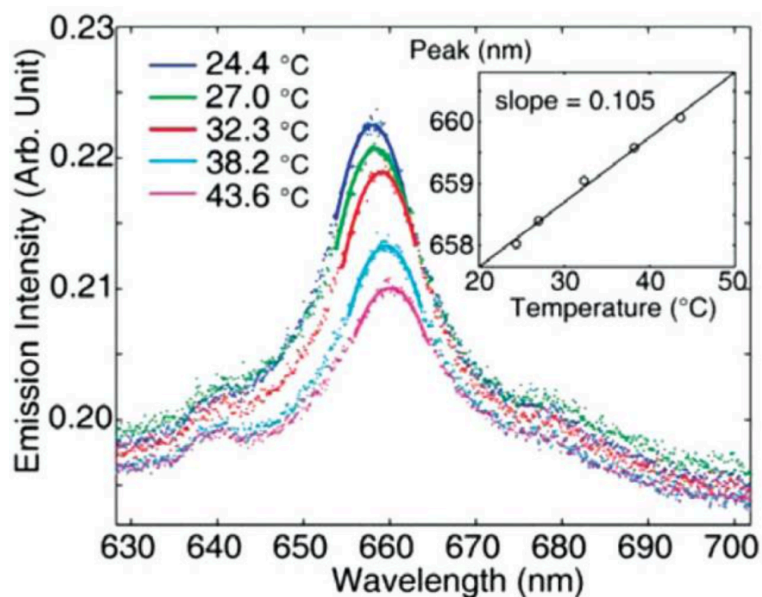


Figure 4.3 – Temperature dependent wavelength shift in quantum dots. The temperature dependent shift of CdSe quantum dots. Taken from Figure 2a, Yue et al (2012) [204].

Upconverting nanocrystals share many properties with standard quantum dots, however, these particles are often larger and are typically lanthanide based compounds [208]. The difference with upconverting nanoparticles is that they may emit photons of a higher energy than the excitation source, an anti-Stokes shift. This can happen in a number of manners, such as intermediate energy states with slower decay times or via forms of cooperative luminescence, such as that reported in triplet-triplet annihilation, which uses two molecules within the compound, a triplet sensitizer and a triplet acceptor. Upon interaction with an excitation photon, the triplet sensitizer creates a triplet exciton. This higher state triplet sensitizer molecule will transfer energy to a triplet acceptor molecule in the ground state, exciting it via Dexter energy transfer. The interaction of two acceptor molecules in the excited state will cause triplet-triplet annihilation, this results in an energy transfer, exciting an acceptor molecule to the excited singlet state, followed by rapid relaxation and release of a photon which is of a higher energy than the individual excitation photons [209]. This is illustrated in the Jablonski diagram in Figure 4.4. These particles are beneficial for biological study as express two-photon functionality, so longer wavelength sources may be used, without the typical requirement for pulsed sources, reducing the peak energy exposure on the sample. However, as with QDs, these particles may offer benefits beyond that of a simple fluorescence probe, with many compositions reported as displaying measurable thermal sensitivities [210].

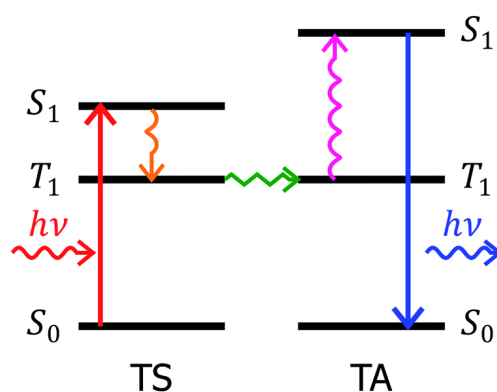


Figure 4.4 – Jablonski diagram of upconversion fluorescence. Triplet sensitizer (TS) absorbs a photon ($h\nu$) and is excited to S_1 , rapidly decaying to create a triplet exciton, T_1 , which is transferred to the triplet acceptor (TA). The collision of two excited TA molecules causes triplet-triplet annihilation and the excitation to the excited singlet state, which rapidly decays, releasing a photon. Taken from Figure 1, Aulin *et al.* [209].

If nanoparticles are incubated with cells prior to experimental study, they may be internalised, by the process of endocytosis. In this process, the cell membrane engulfs material in the extracellular environment, fully encapsulating the material in a spherical parcel of plasma membrane — a vesicle. Once within the cell, it is possible to use these particles as intracellular point probes. This allows for accurate temperature measurement within the cell. A major benefit of using particles, in place of discrete molecules, is the relative ease with which their surface chemistry can be modified to allow the binding of relatively large biological molecules, from sugars to antibodies. These molecules allow targeting towards specific areas on or within a cell. Hydrophilic particles have the additional potential for use, in a non-localised manner, to determine the temperature gradient over a wide area in a homogeneous aqueous solution, similar to the effects of using a dye [175].

A major issue that arises with QDs is the toxicity associated with the particles. These nanocrystals are often composed of materials that are highly toxic to biological samples, such as cadmium [211]. With the large growth in application of QDs in biological research applications, there has also been a significant body of research studying the toxicology of QDs [212, 213], focusing on specific constructs and coatings, including CdSe [214, 215] and CdTe [216, 217] QDs.

4.2.6 Thermal loading with optical devices

The exploitation of light has yielded many of the most important tools in biological research, a theme that has continued with the growth of the biophotonics field. However, where light techniques were primarily passive in nature, with little direct impact on the cell itself, some techniques require a large number of photons to interact with the single cell, for example in optical trapping, or some imaging modalities — such as confocal or stimulated emission depletion (STED) microscopy. In many of these techniques the samples are exposed to a significantly higher irradiance, introducing significantly more energy into the system and increasing the likelihood of unintended transformative effects on the biological samples and surrounding environment.

4.2.6.1 Thermal properties of optical tweezers

The development of optical tweezers has proven valuable to a number of avenues for microscopic particle manipulation, providing a tool that has no functional comparison. Specifically, this has shown to be an excellent tool for single cell study. However, there are concerns regarding the use of high volumes of light energy on biological samples.

Light may cause damage to biological samples in a number of manners. Ultraviolet and visible wavelengths of light are especially likely to provoke phototoxic effects in biological specimens. The toxicity is generated by photochemical interactions that may break chemical bonds and increase oxidative stress on a sample, causing extensive damage to DNA and increasing mutagenesis, therefore impacting the viability of the sample [218 – 220]. Photothermal effects generally relate to the sample heating induced by the wavelength dependent absorption of materials. While optical tweezers use relatively low powers, typically 10s - 100s mW, the tight focusing of the laser creates a spot size which is only micrometres in size, resulting in power densities as large as several MW/cm².

Heating effects can have a significant impact on the properties of samples being manipulated by optical tweezers. Elevations in temperature can result in fluid currents induced by temperature related pressure differences. In such cases, the radiation pressure from the optical tweezer is no longer the only force being imparted on the sample. This can lead to the effect of photothermal trapping [221 – 223]. Even materials with a relatively low absorption coefficient, at the wavelength of the optical tweezer, can

experience incidental heating from any residual absorption. Relatively minor changes in temperature can have a significant impact on a biological specimen, interfering with the cytoskeleton or altering gene expression [224, 225] and potentially induce apoptosis or necrosis [226, 227]. It is therefore imperative that the impacts of thermal loading in optical tweezers is considered when designing a system.

Owing to the wide range of applications of optical tweezers in the study of biological specimens, the effects of heating when using these devices, has been reported on in a number of instances. Liu *et al.* reported the temperature measurement of an optical trap by use of the temperature dependent dye Laurdan, bound to the membrane of a micron scale vesicle. Using a 1064 nm trapping laser, focused using a 1.3 NA microscope objective, they reported heating of approximately 15 °CW⁻¹ in the 0 to 300 mW regime [221]. Experiments used to determine the temperature change of optical tweezers, using Brownian motion, similarly with a 1064 nm trapping laser and 1.3 NA microscope objective, Peterman *et al.* reported a temperature change of 12 °CW⁻¹ [222]. Comparatively, with a lower wavelength of optical tweezer laser, 985 nm, and a 1.25 NA microscope objective, Celliers *et al.* determined temperature changes using refractive index changes, determining a heating rate of approximately 73 °CW⁻¹, significantly higher than those recorded with the 1064 nm sources [223]. In design of deliberate heating, Mao *et al.* described the use of a 975 nm source to controllably heat a sample in a dual beam optical tweezer setup, within this system a heating rate of 56 °CW⁻¹ was noted [228]. Mao *et al.* proposed a model for analysis of heating within these systems, in order to explain the noted differences in heating.

The high energy density generated by an optical trap has the potential to increase the temperature of a sample, introducing a number of drawbacks, from creating issues with sample measurements to compromising the functionality of a target cell. This high density is due to microscope objectives tightly focusing light upon a small area. To calculate this area, when using a fixed focus objective, the beam radius (ω_l) may be calculated using the wavelength of light (λ) and the numerical aperture (NA) of the microscope objective are applied as given in equation (4.1), this diameter may then be used to determine the spot size.

$$\omega_l = \frac{0.6 \cdot \lambda_{trap}}{NA} \quad (4.1)$$

The model proposed by Mao *et al.* states that the heating induced by optical tweezers (ΔT_{trap}) is dependent on the absorption coefficient (at the wavelength of the laser used) ($\alpha_{abs}(\lambda_{trap})$) and thermal diffusivity of the sample (K), the thickness of the chamber holding the sample (D) and the laser power (P_l) and spot size (ω_l) of the optical tweezers interacting with it. This is presented in equation (4.2).

$$\Delta T_{trap} = \frac{\alpha_{abs}(\lambda_{trap}) \cdot P_l}{2 \cdot \pi \cdot K} \cdot \ln \left[\frac{D \cdot NA}{\omega_l} \right] \quad (4.2)$$

It is then possible to determine the heating rate of the trap (β_{trap}) by taking the induced heating by optical tweezers divided by the laser power, of the optical tweezers, (4.3).

$$\beta_{trap} = \frac{\Delta T_{trap}}{P_l} \quad (4.3)$$

Photothermal effects may often be overlooked as a major concern in modern applications of optical tweezers, which are predominantly produced using NIR sources, such as Nd:YAG. However, it should be noted that thermal generation due to environmental absorption of light should still be a consideration when using optical tweezers. In terms of physical effects, localised heating will increase thermal motion and potentially generate convection currents within the sample, an additional force on an optically confined particle that may be non-negligible. Increasing the temperature of a sample will also tend to decrease the viscosity of a liquid environment, a particular problem when optical tweezing forces are often determined via Stokes' Law, for which viscosity is a variable. As previously discussed, this localised heating may also have an effect on the single cell, leading to an undesired change in function or, at worst, apoptosis or necrosis.

4.2.6.2 Thermal influences in optofluidic devices

Growth in the capabilities of microfluidic devices has shown an increase in the integration of additional features. Devices have been produced which incorporate electrodes and mechanical components. However, for biological research, the versatility and ubiquity of light-based methods makes these, arguably, the most important tools for microfluidic integration — optofluidics. These may allow imaging owing to transparency

or may implement modifications in refractive index to produce light guides [22]. As with optical tweezers, these devices face temperature issues in the aqueous environment. Complications arise with the introduction of light energy into a confined, microscopic volume, where localised heating may also be maintained, potentially to the detriment of the system. An enclosed environment is highly susceptible to temperature changes, so the inclusion of submicron temperature detection can be highly beneficial [229].

4.3 Experimental methods

The overarching premise of these experiments is to quantitatively measure changes in thermal activity, within an aqueous sample, by utilizing the temperature dependent peak emission from colloidal quantum dots. The impact on viability of biological samples, primarily mammalian cell lines, is considered, both from the exposure to heating, via optical tweezers and the toxic effects of nanoparticles used in these experiments

4.3.1 Thermal calibration methodology

The temperature dependent peak emission wavelength shift ($\Delta\lambda_{\text{peak}}$) associated with colloidal quantum dots is seen to vary depending on their size and chemical composition. Two types of quantum dot were used in these experiments; Cadmium Selenide (CdSe) quantum dots which are 6 nm in diameter, with an emission peak at 655 nm (Invitrogen) and Cadmium Telluride (CdTe) quantum dots which are 2.3 nm in diameter and have an emission peak at 540 nm (PlasmaChem). CdSe quantum dots are one of the most ubiquitous nanocrystals used in biological research [230 - 232], given the wide use of this composition of quantum dot, it was clear that this would be an ideal test material. The emission spectra for these quantum dots, at 25 °C, is presented in Figure 4.5.

CdTe quantum dots are less commonly used in biological research, however, they have been shown to produce larger shifts in peak emission wavelength than CdSe [233], with the 2.3 nm CdTe QDs reported as exhibiting a peak emission shift of 0.6 nm/°C [233], compared to 0.16 nm/°C reported with the 6 nm CdSe QDs [203]. Initially, calibration curves for the temperature and emission wavelength of the quantum dots are generated for each type, size and batch. The protocol for this is outlaid in the following subsections.

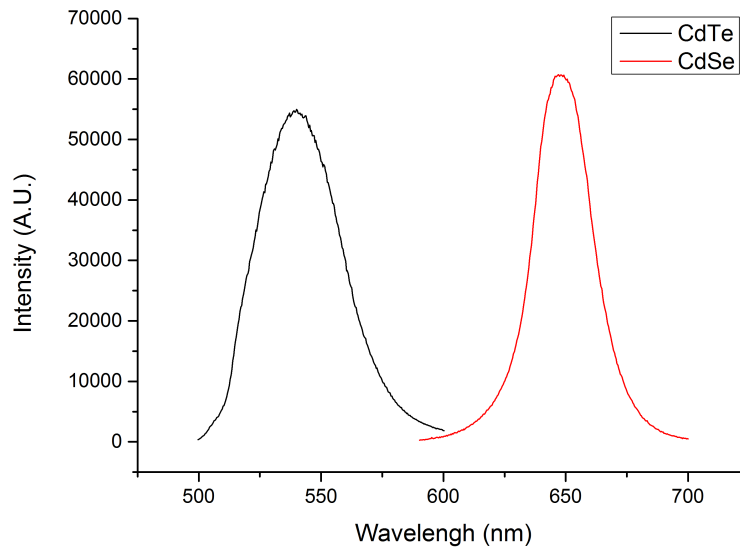


Figure 4.5 – Emission spectra of CdTe and CdSe quantum dots. The emission spectra of 2.3 nm CdTe and 6 nm CdSe quantum dots, excited by a 488 nm source with fluorescence collected by an Ocean Optics USB2000+ ER spectrometer.

4.3.1.1 Calibration setup

The setup for quantum dot $\Delta\lambda_{\text{peak}}$ calibration experiments required a controlled heat source and the ability to excite and probe fluorescence emission from a test sample, illustrated in Figure 4.6.

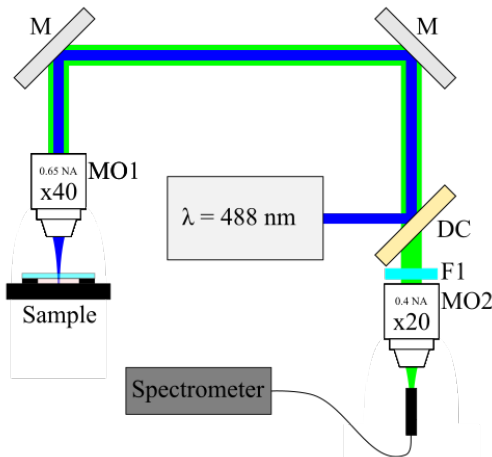


Figure 4.6 – Fluorescence spectroscopy of test samples on a heated stage. 488 nm light, from an argon ion laser, acts as an excitation source. A 500 nm longpass dichroic mirror (DC) and gold-coated mirrors (M), steer the beam into a 0.65 NA, x40 microscope objective (MO1) which is focused on a test sample, held on a heated stage. Fluorescence emitted from the sample is collected by MO1, counterpropagating to DC where the fluorescent light is transmitted. A 488 nm narrowband filter (F1) removes residual 488 nm light, fluorescent light collected by a 0.4 NA, x20 microscope objective (MO2), and focused into an optical fibre, coupled to a spectrometer.

Samples were placed on a heated stage (Tempcontrol 37-2 digital controller with Heating Insert P) which was mounted on a micrometer controlled, three axis precision stage (M-562-XYZ, Newport). An Argon-Ion laser, $\lambda = 488$ nm (Laser Technologies), was used as the excitation source. The beam was directed using a longpass dichroic mirror, which reflected visible wavelengths below 500 nm, and gold-coated mirrors into the back aperture of a NA 0.65, x40 microscope objective that was suspended approximately 3 mm from the sample surface.

Fluorescence emission from the sample was collected using the NA 0.65, x40 microscope objective, the emitted light travelled along a collinear path to the excitation light, reflected by the gold-coated mirrors. Emitted wavelengths, being lower energy than the excitation source, were transmitted by the dichroic mirror. A 488 nm narrowband filter was added beyond the dichroic mirror to reduce any residual excitation light. Emitted light was directed into the rear aperture of a x20, 0.4 NA microscope objective that coupled the light into an optical fibre patch cord, connected to a fibre-coupled spectrometer capable of detecting wavelengths of 339 nm to 1028 nm, with a resolution of ~ 0.28 nm (USB2000+ ER, Ocean Optics).

4.3.1.2 Temperature control acquisition

Quantum dot samples were diluted 1:10 with dH₂O to mimic experimental procedure. 20 μ L samples were held in a vinyl well between two slides of coverslip glass. Samples were placed on the heated stage. The heated stage was set to 20 °C, with the sample being given 120 seconds to acclimatise to the stage temperature once the set temperature was reached. Sample was then exposed to the 3 mW, 488 nm excitation source and the emission spectrum was recorded by the spectrometer in triplicate. This approach was repeated for temperatures from 20 °C to 60 °C at 5 °C intervals. A linear fit of the peak emission wavelengths in relation to sample temperature was generated; the gradient was used to extrapolate the rate of emission peak shift.

4.3.2 Thermal flux from optical tweezers

The temperature dependent shift in peak emission wavelength from the quantum dots was applied to measuring temperature change in optical tweezers experiments. One reason the optical tweezers have not found widespread use in the life sciences community

is the concern regarding the high energy exposure, with the potential for photochemical damage or localised heating of the samples by the trapping laser.

Photochemical damage associated with higher energy photons, such as DNA damage, can be avoided by careful selection of laser source [234]. However, lower energy photons in the NIR range are absorbed by water, this can result in the localised heating of a cell and the surrounding aqueous environment. Tens of milliwatts focused into a region of several square microns produces a relatively high energy dose over a small area, for example: using equation (4.1), a beam of 1064 nm laser light focused through a 1.25 NA objective will create a focus with a radius of 0.51 μm , a spot size of 2.57 μm^2 , assuming a Gaussian beam profile. Using a 10 mW source, and calculating as a lossless system, an irradiance of $3.89 \times 10^8 \text{ W/m}^2$ would be imparted on the focal area. Were a cell to be held in this beam for 10 seconds, it will have been exposed to an energy of 1.95 GJ / m^2 . This is a significant dose of energy onto the sample, which, if absorbed, will cause localised temperature increases. This series of experiments looks to apply quantum dot nanothermometers for use with optical tweezers, monitoring temperature change within the sample.

4.3.2.1 Optical design

The overarching goal of this experiment was to measure the influence of optical tweezers on temperature in an aqueous environment while verifying the validity of quantum dot nanoparticles as temperature sensors. As such, the experiment was designed around a conventional optical tweezer system, similar to that used in chapter 3, with the inclusion of a number of modifications. The experimental setup produced for this system is shown in Figure 4.7.

To compare the differences in temperature increase between wavelength, a 400 mW fibre coupled laser diode emitting at $\lambda = 980 \text{ nm}$ and a 3500 mW Nd:YAG laser (Laser Quantum, Ventus IR) emitting at $\lambda = 1064 \text{ nm}$ were used as sources for the optical tweezers. A collimator and Keplerian telescope were used directly after the 980 nm source to match the beam diameter of the 1064 nm source. A pair of E03 mirrors (Thor Labs), on flip mounts, were used to isolate and guide a beam from the desired source into the device.

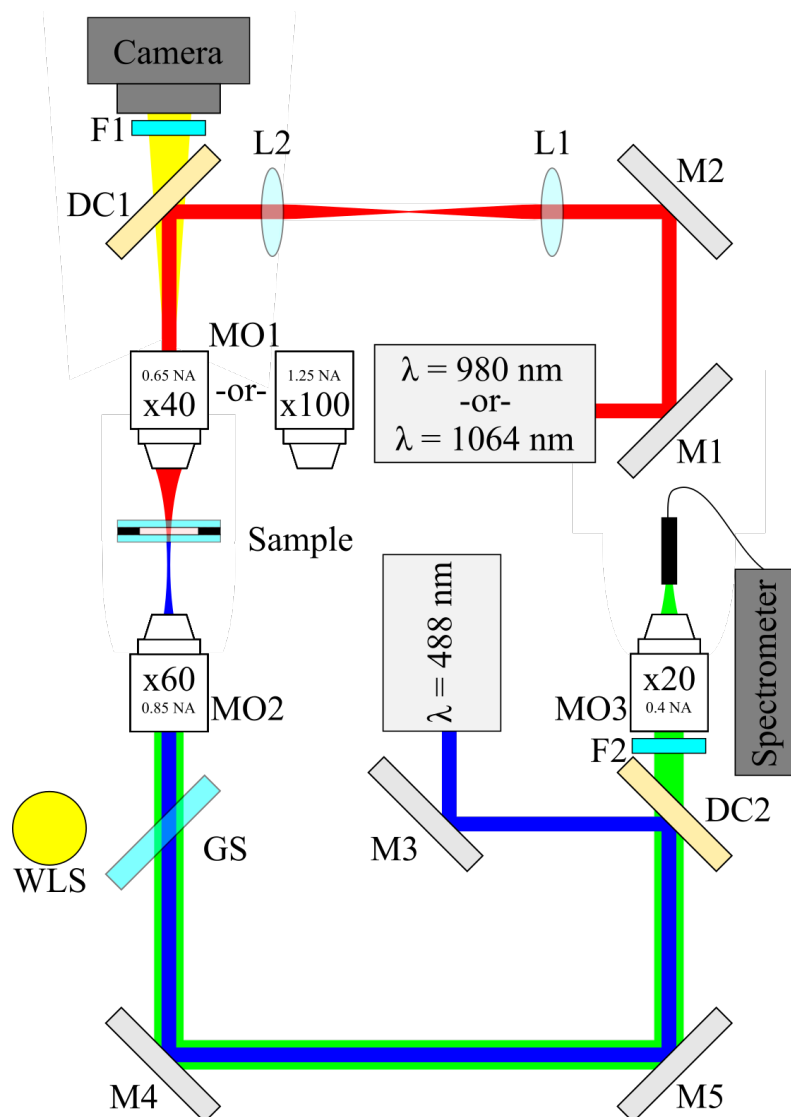


Figure 4.7 – Optical tweezers with integrated fluorescent spectroscopy capabilities. Optical tweezers driven by a $\lambda = 980 \text{ nm}$ or $\lambda = 1064 \text{ nm}$ laser, the beam is steered using a combination of EO3 mirrors (M1, M2) into a telescopic array with two $f = 100 \text{ mm}$ lenses (L1, L2). Using a shortpass dichroic mirror (DC1), the beam is guided into either a 0.65 NA, x40, or 1.25 NA x100 microscope objective (MO1), which is focused onto the sample. Sample is excited by light from a $\lambda = 488 \text{ nm}$ laser, guided using EO3 mirrors (M3, M4, M5) and a longpass dichroic mirror (DC2), into a 0.85 NA, x60 microscope objective (MO2). Emitted fluorescence is gathered by MO2 and counter propagates through the system, passing through DC2 and a longpass 495 nm filter (F2), removing residual excitation light. A 0.4 NA, x20 microscope objective (MO3) then focuses the light into an optical fibre, connected to a spectrometer. A glass microscope slide (GS) is used to guide light from a white light LED (WLS) into MO2, to provide illumination. Imaging via MO1, with visible light passing through DC1 for detection with a camera held at the tube length of MO1. A NIR filter (F1) was positioned before the camera to remove residual reflections from the optical tweezer beam.

The tweezing beam was finely directed within the device, using a second pair of E03 mirrors (Thor Labs) in a periscope arrangement. The beam was then expanded using a second pair of $f = 100$ mm lenses as a Keplerian telescope. The beam is guided at 90° , using a shortpass dichroic mirror (Thor Labs) mounted at 45° to the direction of propagation, into the rear aperture of a microscope objective used for optical tweezing, which is focused into the sample. To monitor the impact of different light densities on the sample, either a x40, 0.65 NA (Newport, M-40X) or a x100, 1.25 NA (Leitz Wetzlar, EF100) microscope objective was employed for the optical tweezers.

The sample is held on a custom plate which is attached to a micrometer stage with axial control in three dimensions (Newport M-562). Control of this stage in the direction of beam propagation was used to control focus, by adjusting the sample relative to the focal point of MO1.

The device required the excitation of fluorescent particles within the sample and recording the spectral information of the emitted fluorescence. The excitation source in this application was a 3 mW Argon-Ion laser emitting at 488 nm. This source was isolated and guided into the device using a gold mirror (M3) and a 500 nm longpass dichroic mirror (DC2). Beam was translated 90° using a second gold mirror (M4), mounted at 45° into the rear aperture of a x60, 0.85 NA microscope objective (Newport, M-60X) (MO2). MO2 was mounted on a single axis translator (Thor Labs), in the direction of beam propagation as a focus control. At this stage, the optical tweezing beam (980 nm or 1064 nm) is collinear and counter propagating to the excitation beam (488nm).

Fluorescence emission was collected by MO2 and transmitted through DC2. A 495 nm longpass filter (Thor labs) (F2) blocked excess 488 nm excitation light that passed through DC2. The light is directed into a x20, 0.4 NA microscope objective (Newport, M-20X) (MO3) which focuses the light into a connectorized optical fibre. F2, MO3 and an optical fibre mount are held in a cage system, which is mounted on a stage with translation control in three dimensions, this allows fine alignment to optimise coupling of emitted light from the quantum dots into the optical fibre. Within this system, MO3 was mounted on an independent translation mount to control the focus, optimising focal coupling to the optical fibre. A fibre-coupled spectrometer (Ocean Optics) was connected to the optical fibre to record the emission spectra of the fluorescence.

Imaging is attained using the first microscope objective (MO1) and a CCD camera that is placed behind the dichroic mirror (DC1), at the image plane of MO1. A near infra-red filter (F1) was introduced between DC1 and the CCD camera to reduce aberrant transmitted reflections from the optical tweezer beam. Illumination is generated by a white LED that is directed into the rear of MO2 using a glass slide.

The optical tweezing wavelengths used here, 980 nm and 1064 nm, are commonly used as optical trapping sources, at least in part, as they are relatively inexpensive (compared to Ti:Sapph lasers at 800 nm). The absorption coefficients of water are well defined [235], a Shimadzu UV160 spectrophotometer was used to record the absorption coefficients, shown in Figure 4.8, the wavelengths of the lasers used in this work are then highlighted.

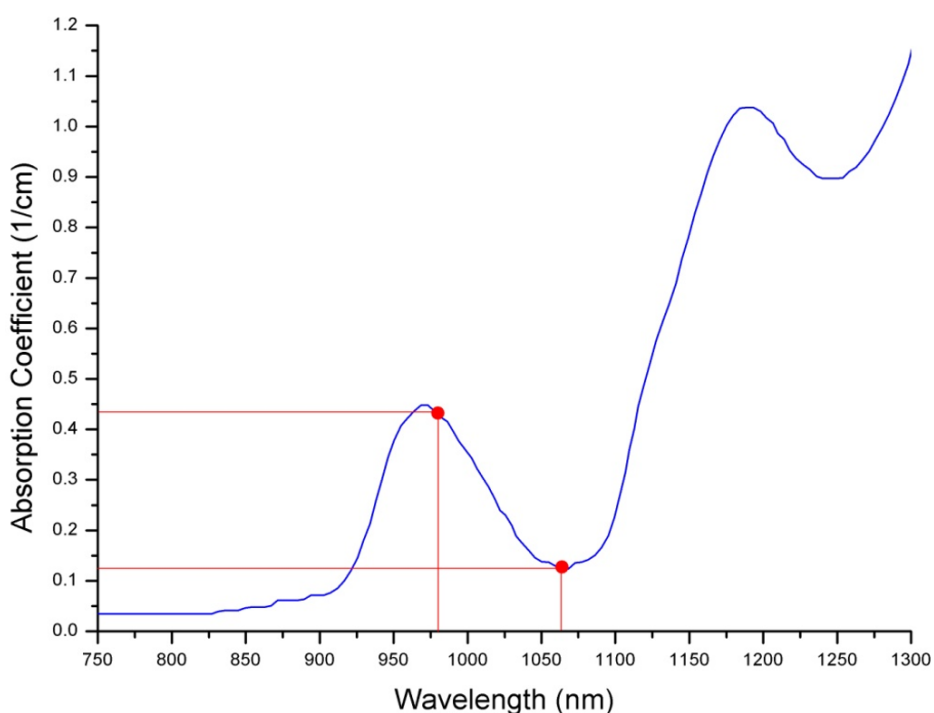


Figure 4.8 – Absorption spectrum of water. Absorption spectrum denoted by blue line and annotated with red points to highlight the wavelength of lasers used for optical tweezing ($\lambda = 980$ nm & $\lambda = 1064$ nm) and the corresponding absorption coefficients.

4.3.3 Sample preparation

In order to make full use of the abilities of optical tweezers, a sample depth greater than that granted by a simple cover slip on a microscope slide was required. To achieve a greater sample depth, a vinyl cut-out was used as a spacer, producing a well 10 mm in diameter and 0.08 mm deep, for a volume of 6.3 μ L.

The inclusion of counter propagating microscope objectives on the target sample resulted in a very narrow working distance. Therefore, it was not possible to use standard microscope slides for sample preparation. One of the aforementioned vinyl cut-outs was applied to a 22 mm x 50 mm x 0.2 mm microscope cover slip glass, 10 μ L of the required sample was added to the well and a 22 mm x 22 mm x 0.2 mm cover slip was placed over the well.

Samples contained 20 μ M of CdTe quantum dots (PlasmaChem) or 800 nM of CdSe quantum dots (Invitrogen). At these concentrations, the focal volume of the 0.85NA, x60 microscope objective will record a great number of quantum dots simultaneously. Owing to the relatively low sensitivity of the available apparatus, lower concentrations of quantum dots yielded inadequate fluorescence intensity. Low concentrations of 3 μ m polymer microspheres (PolySciences) were initially used to allow clear visualisation of their optical trapping during measurements.

4.3.4 Spectroscopic acquisition and processing

The fluorescence information in this series of experiments was captured using compact fibre coupled spectrometers. Three spectrometers were used throughout the duration of the project; all of which were produced by Ocean Optics and followed the Czerny-Turner design. A common interface software (SpectraSuite) was shared amongst them. Initially an Ocean Optics USB2000+ was used. This was first replaced with a higher resolution Ocean Optics HR4000 spectrometer. Ultimately an Ocean Optics USB2000+ ER spectrometer was used in this application.

An initial recording of ambient spectral data is taken prior to each experimental run. This background is then removed using the SpectraSuite software. The integration time used by the software was varied between 100 ms and 1,000 ms; this was to account for variations in intensity from the sample and necessary to capture the clearest possible emission curve. The software was set to record spectral data that was averaged over three scans. Data collection was repeated three times. Raw data was fitted to a GaussMod curve in Origin 9.0.0 (OriginLabs Co), to produce the cleanest possible peak, as shown in Figure 4.9. This allowed for emission peaks shift to be recorded, an example of this, where the fluorescence of 2.3 nm CdTe QDs was measured with and without the influence of heating from an optical trapping beam is shown in Figure 4.10.

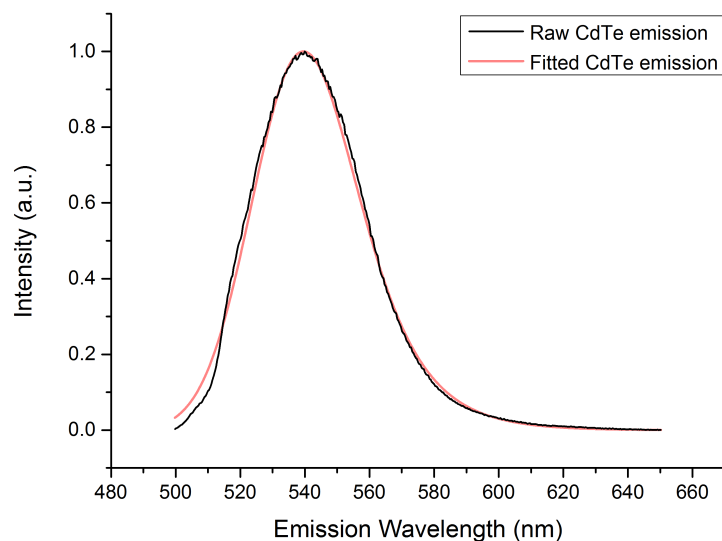


Figure 4.9 – Fitted curve using GaussMod function. The fluorescence emission of 2.3 nm CdTe quantum dots, excited by a 488 nm source, was recorded using an Ocean Optics USB2000+ ER spectrometer. The raw emission curve (black) from was processed using the GaussMod curve function in Origin to generate a best fit, in order to produce distinct peak from the curve.

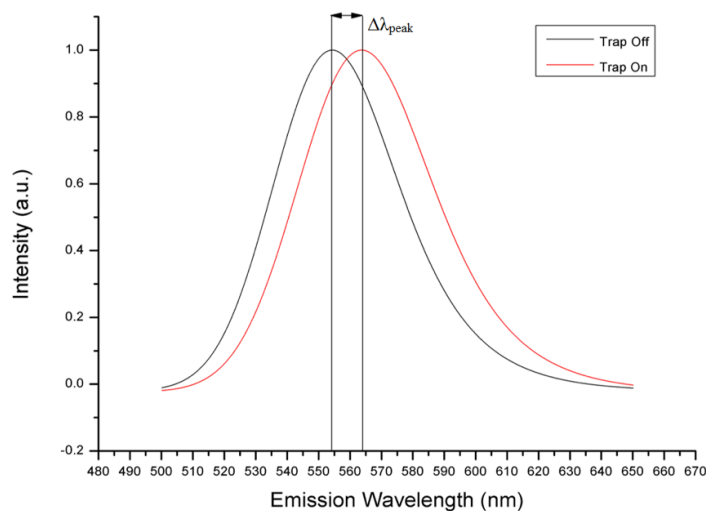


Figure 4.10 – Emission peak shift. The emission from 2.3 nm CdTe quantum dots with no optical tweezing (black) and optical tweezing (red), with a x40, 0.65 NA objective and 2,125 mW of power from a $\lambda = 1064$ nm laser. Using the processing illustrated in Figure 4.5, the two curves are compared and the shift in peak wavelength ($\Delta\lambda_{\text{peak}}$) is produced.

This initial experimentation showed a distinct red-shift in the λ_{em} of the CdTe quantum dots, indicating an increase in local temperature, when exposed to optical tweezers. A 3,500 mW beam of $\lambda = 1064$ nm light, focused through a x40, 0.65 NA microscope objective, exposing $9.8 \mu\text{m}^2$ of a 20 μM aqueous solution of CdTe quantum dots to 2,125 mW of $\lambda = 1064$ nm photons. Applying a fitted curve to the recorded λ_{em} spectra indicated λ_{em} peaks of 554.4 nm (trap off) and 563.3 nm (trap on), indicating a shift of 8.9 nm resulting from the energy added to the system by the optical tweezers.

4.3.5 Aqueous environments

A number of environments were tested to monitor the effectiveness of the quantum dots as nanothermometers. These included a variety of growth media, pH levels and salt concentrations. While it is key to understand the properties of these nanoparticles in a variety of environments, the aim is to eventually test these with biological specimens, and in the future use them as intracellular thermometers. A dye-based staining process, to infer temperature from fluorescence in mitochondria, has since been reported [236].

4.3.6 Cell culture

One of the ultimate targets of these experiments is to assess the viability of these quantum dots as nanothermometers for use in biological systems. This work includes some experimentation with cell lines in order to determine the viability of working with these nanoparticles while minimally impacting biological samples. J774 cells are an established cell line of mouse macrophages. These are a semi-adherent cell line which were grown on 75 cm^2 Nunc tissue culture flasks with 15 ml of DMEM (Invitrogen), supplemented with 10 % FCS (Invitrogen) and 100 U/ml PenStrep (Invitrogen). The adherent properties of this cell line are diminished if the population approaches confluence, so the cells were passaged when the population reached approximately 80 %. Cells were maintained in an incubator at 37 °C with 5 % CO_2 .

Passaging of the J774 cells was performed in a class II biosafety cabinet. The culture medium was aspirated and the cells were washed with 15 ml of PBS pre-heated to 37 °C. PBS was aspirated, leaving approximately 2-3 ml of residual PBS. Cells were gently removed from the surface of the flask with a cell scraper. The cells, now in suspension with the residual PBS were pipetted into a 15 ml falcon tube, which was filled to 10 ml

with growth media and centrifuged at 500 g for 5 minutes. Growth media was aspirated and the cell pellet was resuspended in 10 ml of growth media at 37 °C. Subsequent flasks were seeded with 2.5 ml of the cell suspension and an additional 12.5 ml of fresh growth media. The remaining cell suspension was used in toxicity experiments.

4.3.7 Toxicity

While the range of nanotechnologies applied to the biological sciences is vast, there is a great concern regarding the toxic effects of such particles, even when applied in relatively low concentrations, to quote Paracelsus “All things are poison, and nothing is without poison; only the dose permits something not to be poisonous”. While there are a massive number of toxicological studies regarding quantum dots [212 - 216], the toxicity varies depending on a number of factors, such as the quantum dot size, chemical composition and surface chemistry. It was therefore important to quantify the toxicity of the specific quantum dots within this experiment in order to maintain validity of these particles as nanothermometers with mammalian cells.

Two standard toxicity assays were used to produce a broad view of the toxic effects of these nanoparticles. These are the Lactate Dehydrogenase (LDH) assay [237] and the Resazurin assay [238]. The LDH assay is used to quantify damage to the cell membrane whereas the Resazurin assay is used to quantify the metabolic activity of the cells. Both assays were performed on the J774 (mouse macrophage) cell line. This line was deemed appropriate for toxicological assessment due to the nature of macrophages, which broadly consume particles within their environment and are used widely in the literature [213].

4.3.7.1 Lactate dehydrogenase assay

Cadmium based quantum dots are known to stress cell membranes [239], therefore, the ability to test a large sample of cells and record the cell membrane damage is a prime method in determining the viability of the population. LDH is an intracellular enzyme used to mediate the interchange of lactate and pyruvate and is located within the cytosol of the cell. The chemical conversion is illustrated in Figure 4.11. If the cell membrane is compromised, LDH is released into the surrounding environment. This can occur from cell death or damage to the membrane. Therefore, one approach to monitoring toxicity is to quantify and compare the levels of LDH within the environment.

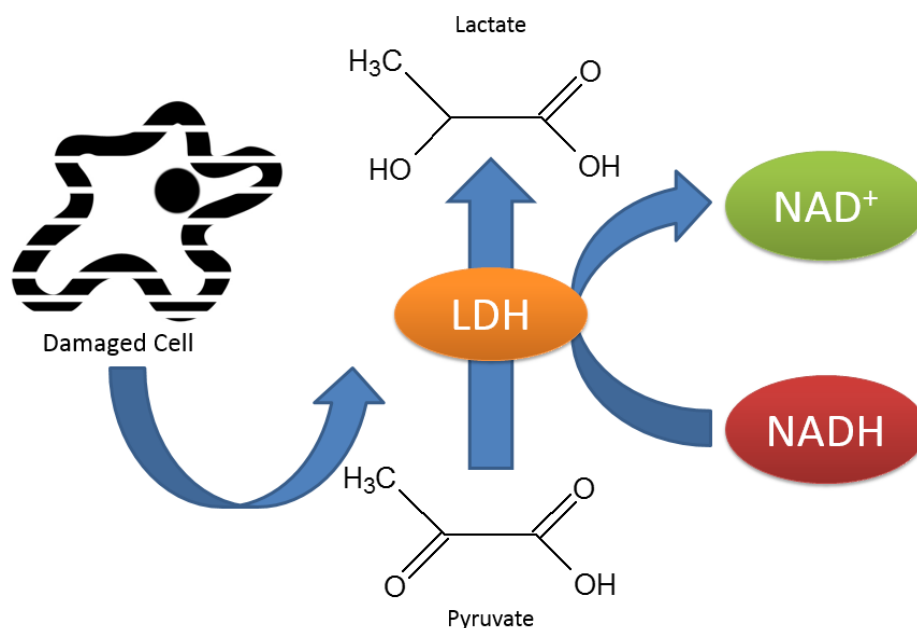


Figure 4.11 – Interconversion process of pyruvate and lactate as mediated by LDH. A damaged cell membrane releases LDH into the surrounding environment. LDH catalyses supplemental pyruvate to lactate via nicotinamide adenine dinucleotide oxidization, converting from NADH to NAD⁺. Pyruvate remaining in solution reacts with 2,4-dinitrophenylhydrazine, the product of which can then be colorimetrically measured to determine the degree of LDH released and thus the extent of membrane damage throughout a population.

The assay uses a colorimetric method for determining the levels of LDH present within the environment. This is determined by the conversion of supplemental pyruvate to lactate in the presence of NADH. The less LDH released, then less pyruvate is converted to lactate. Residual pyruvate reacts with supplemental 2,4-dinitrophenylhydrazine and the product is measured colorimetrically. The experimental results are then compared to a standard curve of pyruvate concentration vs colour intensity, in order to determine LDH activity.

A stock of J774 cells (murine macrophages) was diluted to $\sim 10^4$ cells per ml. 100 μ L of cell suspension was pipetted into 54 wells of a 96 well plate. This allowed for positive and negative controls as well as 16 variations of concentration. Each test value is run in triplicate. The cells were then incubated at 37 °C with 5 % CO₂ for 24 hours. After this time, the standard growth media was replaced with growth media which incorporated CdTe quantum dots at a range of concentrations from 40 nM to 40 μ M. The cells were then incubated for a further 24 hours.

The reaction solution was created by adding 1 mg/ml of the reduced form of nicotinamide adenine dinucleotide (NADH) to 0.75 mM sodium pyruvate in dH₂O. A standard curve was obtained by creating dilutions of the stock reaction solution. For these experiments a series of six dilutions, shown in Table 4.1, were used to generate the standard curve, shown in Figure 4.12.

Table 4.1 – LDH standard curve concentrations

NADH volume (μ L)	0.75 nM pyruvate volume (μ L)	Comparative LDH activity (units/ml)
500	50	0
400	150	280
300	250	640
200	350	1040
100	450	1530
50	500	2000

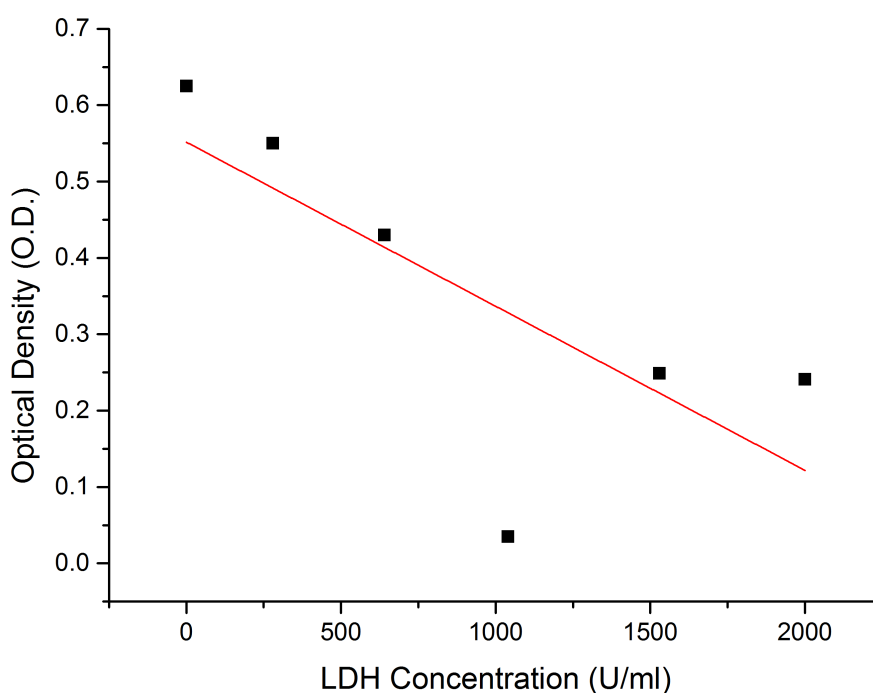


Figure 4.12 – Standard curve for LDH assay. Standard curve generated using concentrations defined in Table 4.1.

Each standard curve concentration was added, at 60 μL per well, in triplicate to a 96 well plate. 10 μL of the supernatant from each toxicological sample was transferred to the new 96 well plate and supplemented with a 50 μL of the reaction solution. The plate is then incubated at 37 $^{\circ}\text{C}$ for 30 minutes to allow the enzymatic reaction to occur. 50 μL of 2,4-dinitrophenylhydrazine is added to each well and the plate is left to sit for 20 minutes at room temperature. This is followed by the addition of 4M sodium hydroxide, which inactivates the LDH, and a further resting period of 5 minutes to stop the reaction.

The 96 well plate is then scanned on a plate reader, measuring absorbance at 540 nm to determine the lactate concentration, and hence the LDH activity, within the sample. These readings are compared to the standard curve to determine the quantity of LDH within a sample. In this experiment heightened LDH activity indicates serious damage to the cell membrane.

4.3.7.2 Resazurin assay

Cellular damage may be present which is not directly quantifiable by the pure distinction between live and dead cells. Cadmium based quantum dots are known to induce stress in the metabolic activity of the cell [238]. Therefore, the study of the mitochondrial activity was deemed a useful tool to compliment the LDH assay.

As with the LDH assay, the resazurin assay is also colorimetric in nature. However, unlike the LDH assay, the coloration does not require additional supplementation to the probing molecule. In this instance, the resazurin, which is a non-fluorescent dye is converted by the mitochondria to resorufin, which emits fluorescence at ~ 590 nm. This process is illustrated below in Figure 4.13. The brightness of the fluorescence is used to comparatively express the mitochondrial activity of the experimental cells.

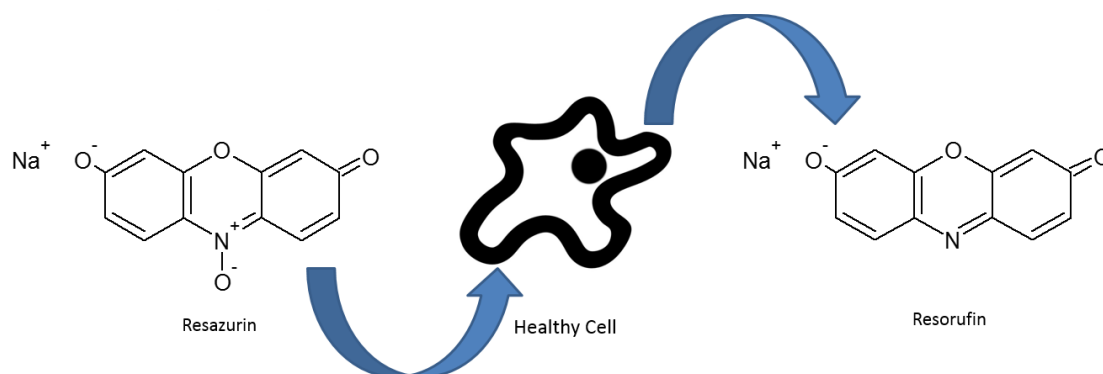


Figure 4.13 – Conversion of resazurin to resorufin.

To maintain comparable results, the resazurin assay was approached in a similar manner to the LDH assay. 100 μ L, containing $\sim 10^4$ cells were added to 54 wells of a 96 well plate, again allowing for 16 variations in concentration with positive and negative controls, repeated in triplicate.

The 96 well plates were incubated at 37 °C with 5 % CO₂ for 24 hours, the growth media was then replaced with fresh media that contained a series of concentrations of CdTe quantum dots (ranging from 40 nM to 40 μ M). The positive control received fresh growth media with no quantum dots and the negative control was washed with Triton X-100, a powerful detergent which kills the cells in these wells. After a further 24 hours of incubation, the samples were washed twice with phosphate buffered saline (PBS) and a mixture of fresh growth media and 10 % resazurin (AlamarBlue, Invitrogen) was added. The plate was returned to the incubator. The plate was scanned in a plate reader at $\lambda_{\text{excitation}} = 570$ nm after 18 hours. Fluorescence emission at 590 nm from the sample indicated conversion of resazurin, showing metabolic activity. When plotted between the positive and negative controls, the test samples show the impact of certain quantum dot concentrations on the cell metabolic rate.

4.3.8 Confocal imaging of internalised quantum dots

Confocal microscopy was employed to record quantum dots that have been incubated with J774 macrophages. This was used in order to track the position of the quantum dots and image any internalisation of the quantum dots. Images of cells containing phagocytosed quantum dots were recorded using a Leica SP5 confocal microscope. Approximately 10^5 cells were seeded in 35 mm glass-bottomed fluorodishes and left in an incubator at 37 °C with 5 % CO₂ for 18 hours. Quantum dots were added and the cells were returned to the incubator for 4 hours prior to microscopy.

4.4 Results

Temperature sensitive responses of quantum dots, as nanothermometers, in optical tweezing experiments are shown in this section. Firstly, the calibration and laser power measurements are provided. Monitoring of the thermal characteristics of quantum dots in optical tweezers are then presented. Additional experiments determine the biological validity of these particles as thermometers were also carried out. This included

the effects of various biological environments, from PBS and growth media to pH. Toxicological analysis of the quantum dots is also performed. Imaging of the particles upon internalisation is also attempted and applications within microfluidic devices reviewed. A discussion and conclusion follow the results presented here.

4.4.1 Quantum dot calibration

The wavelength shift of the quantum dots' emission in response to temperature shifts were tested to attempt validation of previously reported data [215, 216]. Emission spectra were recorded with the sample on a heated stage, to measure emission at known temperatures. The emission spectra for the CdTe and CdSe quantum dots were recorded separately, examples of which are presented in Figure 4.14 and 4.15 respectively. A 20 °C to 60 °C temperature range, which easily encapsulates the physiological temperatures of most organisms and sub-cellular organelles, resulted in an overall $\Delta\lambda_{\text{peak}}$ of 8.3 nm in the CdTe quantum dots, with a $\Delta\lambda_{\text{peak}}$ of 3.8 nm in the CdSe quantum dots. There is a linear relationship between temperature and emission peak shift in the 20 to 60 °C range measured in this study. This means that an emission shift of ~ 0.2 nm/°C can be measured with the CdTe quantum dots and ~ 0.1 nm/°C can be measured using CdSe quantum dots. These results are presented in Figure 4.16.

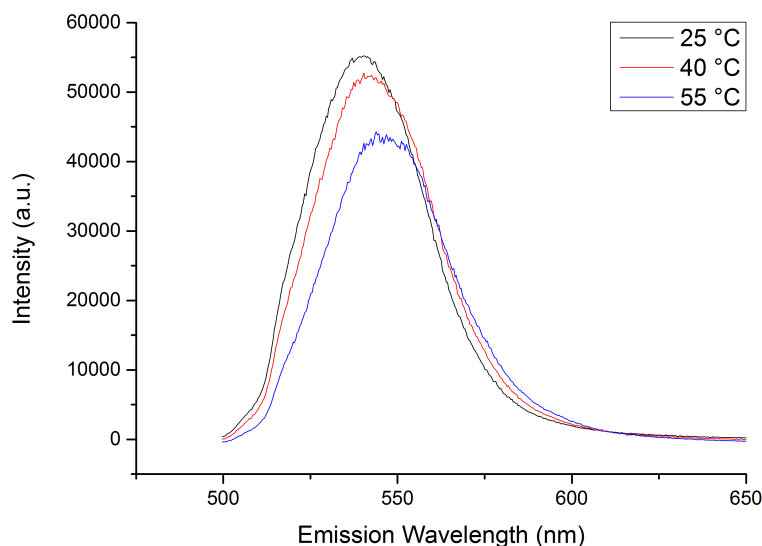


Figure 4.14 – CdTe quantum dot calibration. 2.3 nm CdTe quantum dot emission at 25 °C, 40 °C and 55 °C. This was carried out on the apparatus illustrated in Figure 4.6.

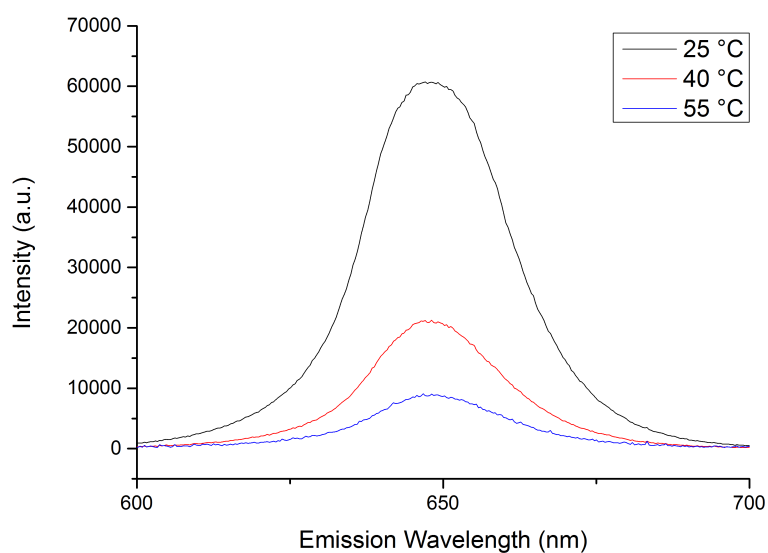


Figure 4.15 – CdSe quantum dot calibration. 6 nm CdSe quantum dot emission at 25 °C, 40 °C and 55 °C. This was carried out on the apparatus illustrated in Figure 4.6.

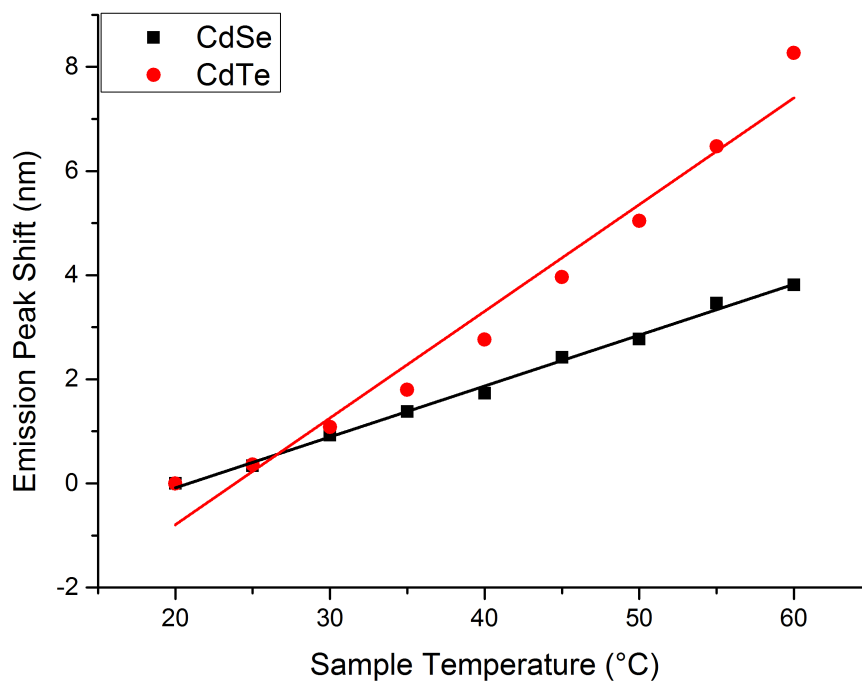


Figure 4.16 – Summary quantum dot calibration. CdTe and CdSe quantum dot emission peak shift from 20 °C to 60 °C. This was performed on the apparatus illustrated in Figure 4.6.

Previous works have reported a wavelength shift of $\sim 0.6 \text{ nm/}^{\circ}\text{C}$ when using these CdTe QDs [233], which is significantly higher than the shift rate of $\sim 0.2 \text{ nm/}^{\circ}\text{C}$ recorded in these experiments. Similarly, prior work with these CdSe QDs noted a wavelength shift rate of $0.16 \text{ nm/}^{\circ}\text{C}$ [232], which is notably higher in shift rate than experienced in this apparatus, $\sim 0.1 \text{ nm/}^{\circ}\text{C}$. The intensity of the emission was noted to decrease with temperature increases. High accuracy measurements of the temperature shift due to the laser power, used in generating optical tweezers, will require accurately recording the optical power at the sample, and as such, we measured the optical power at the source output and at the sample for both the 980 nm and 1064 nm beams.

4.4.2 Laser power measurements

The absorption of light by samples under the microscope, such as in optical tweezing or photoporation apparatus, or within in very small volumes, from nanolitres to picolitres in microfluidics, and the resultant conversion to thermal energy will manifest itself as localised heating in the sample. In order to measure temperature shift as a function of optical power at the sample, we must first measure the optical power that the sample is exposed to.

Microscope objectives are responsible for the largest single source of loss in the optical tweezing system, a loss that was not uniform across the laser sources used. Power measurements taken after the microscope objective were compared to those taken at the laser sources. These are shown in Figure 4.17 (980 nm) and 4.18 (1064 nm). With the x100, 1.25 NA microscope objective in the system, an average loss of 55 % was recorded at $\lambda = 980 \text{ nm}$ and 46 % at $\lambda = 1064 \text{ nm}$. The x40, 0.65 NA configuration resulted in a loss of 26 % at $\lambda = 980 \text{ nm}$ and 28 % at $\lambda = 1064 \text{ nm}$. As these microscope objectives are designed for use within the visible range of the spectrum, losses in the NIR are expected. This is owing to the construction and coatings of the optical elements in these microscope objectives not being intended for use with NIR sources.

The power measurements at sample, recorded here, were used to determine the exposure energy on the sample for nanothermometry work, where the emission from quantum dots was measured under different trapping parameters (wavelength, power, spot size), described in the following section.

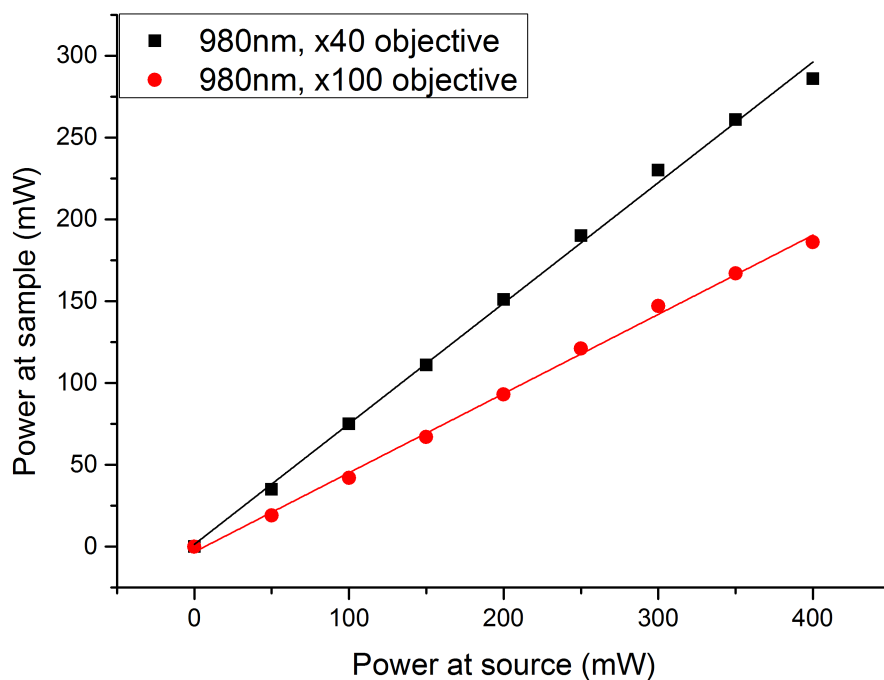


Figure 4.17 – Laser power loss through apparatus, 980 nm. Power recorded using the apparatus illustrated in Figure 4.7, beyond the focus of MO1, where MO1 is either a x40 (0.65 NA) or x100 (1.25 NA) objective. Laser wavelength is $\lambda = 980$ nm.

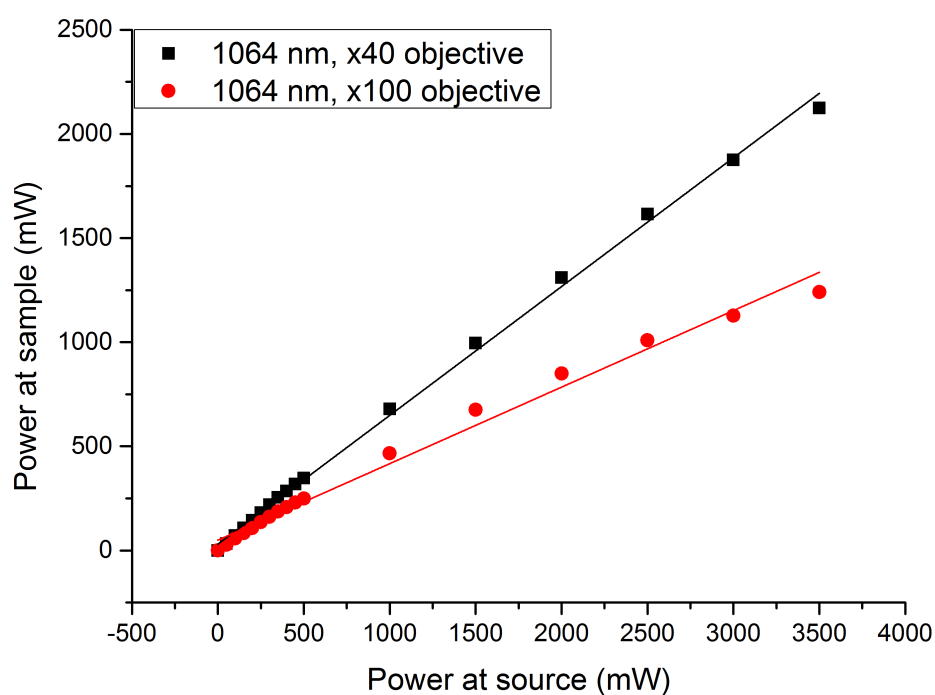


Figure 4.18 – Laser power loss through apparatus, 1064 nm. Power recorded using the apparatus illustrated in Figure 4.7, beyond the focus of MO1, where MO1 is either a x40 (0.65 NA) or x100 (1.25 NA) objective. Laser wavelength $\lambda = 1064$ nm.

4.4.3 Nanothermometry of optical tweezers

To measure the thermal loading produced in a sample by the focused, single beam, optical trap, a sample containing quantum dots was mounted on the optical tweezing and spectroscopy apparatus. Exciting a great number of quantum dots, the spectra from these were recorded for 500 ms and averaged over three readings. All recordings were taken in triplicate.

4.4.3.1 CdSe quantum dots

Optical tweezers were focused into an 800 nM solution of CdSe quantum dots which were excited by a $\lambda = 488$ nm source. The resulting fluorescence emission was recorded using an Ocean Optics USB2000+ ER spectrometer. Optical tweezers were generated using a $\lambda = 1064$ nm laser source, with a 0.65 NA, x40 microscope objective, producing an optical trap with a spot of approximately 3 μm in diameter – using equation (4.1). This is shown in Figure 4.19.

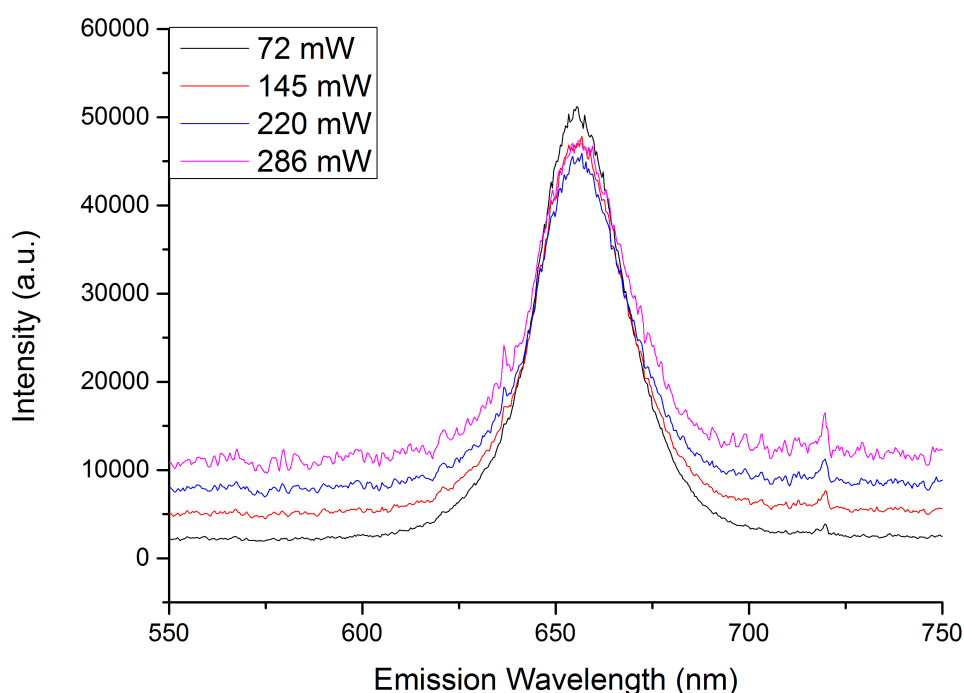


Figure 4.19 – CdSe spectral shift as power of optical tweezing beam increases. Using the apparatus illustrated in Figure 4.7. Optical tweezers generated using $\text{MO1} = 0.65$ NA, x40 and a $\lambda = 1064$ nm source. The emitted fluorescence of the 6 nm CdSe QDs at 72, 145, 220 and 286 mW are presented.

When processed, the peak shift of the CdSe emission wavelength over a range of powers from 0 – 286 mW only registered a shift of 0.34 nm, as this is the resolution limit of the spectrometer, it indicates no significant shift. This implies that temperature changes due to the optical tweezing system may not be inducing a peak emission shift which the spectrometer used here is unable to resolve.

4.4.3.2 CdTe quantum dots

A 20 μ M solution of CdTe QDs was exposed to optical tweezers and the resulting emission spectrum was recorded using the Ocean Optics USB2000+ ER spectrometer. Samples were allowed to reacclimatise to room temperature after each run. Using a $\lambda = 980$ nm laser source, the thermal effects were measured in the approximate focal volume of the optical tweezers, with the spot from a 0.65 NA, x40 microscope objective producing a peak emission shift of 1 nm over 200 mW (Figure 4.20), and a 1.25 NA, x100 microscope objective generating 2 nm at 186 mW (Figure 4.21). Comparatively, using a $\lambda = 1064$ nm laser source, 200 mW of optical tweezing power in the sample generated an emission peak shift of 1.9 nm (Figure 4.22) and 3.2 nm (Figure 4.23), when using the 0.65 NA, x40 and 1.25 NA, x100 microscope objectives, respectively. The peak emission shifts are clearly measurable with the 2.3 nm CdTe QDs, unlike that recorded with the 6 nm CdSe QDs in Figure 4.19. The results are presented in Figure 4.24.

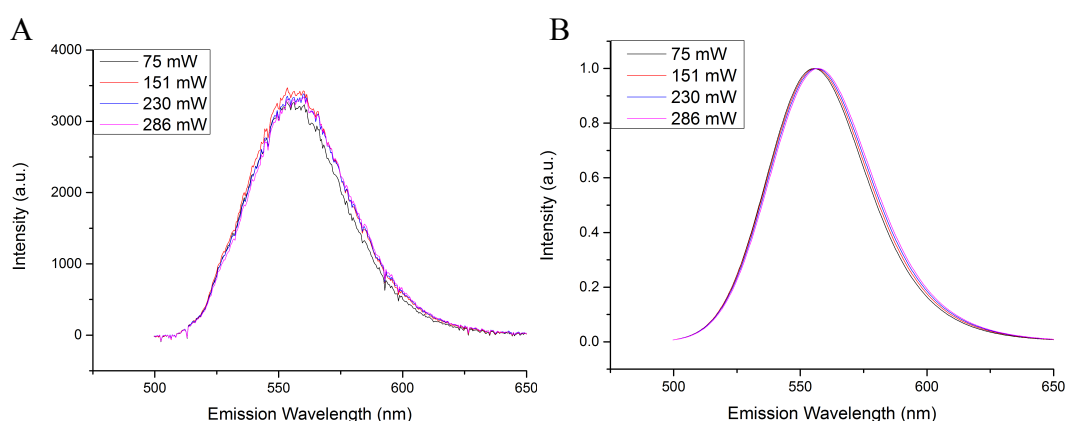


Figure 4.20 – CdTe QDs with 980 nm, x40 microscope objective, optical tweezing. The raw (A) and GausMod fitted (B) λ_{peak} shift of CdTe QDs when exposed to optical tweezers formed with a $\lambda = 980$ nm source and 0.65 NA, x40 microscope objective.

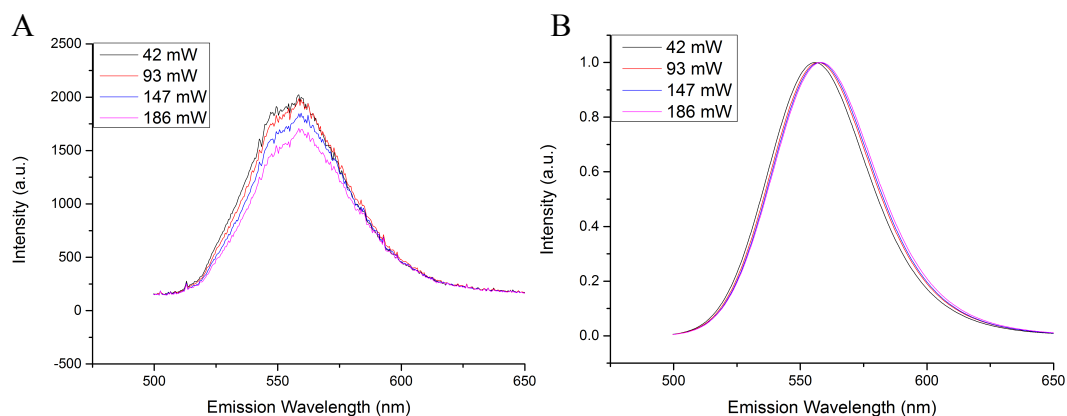


Figure 4.21 – CdTe QDs with 980 nm, x100 microscope objective optical tweezing. The raw (A) and GausMod fitted (B) λ_{peak} shift of CdTe QDs when exposed to optical tweezers formed with a $\lambda = 980$ nm source and 1.25NA, x100 microscope objective.

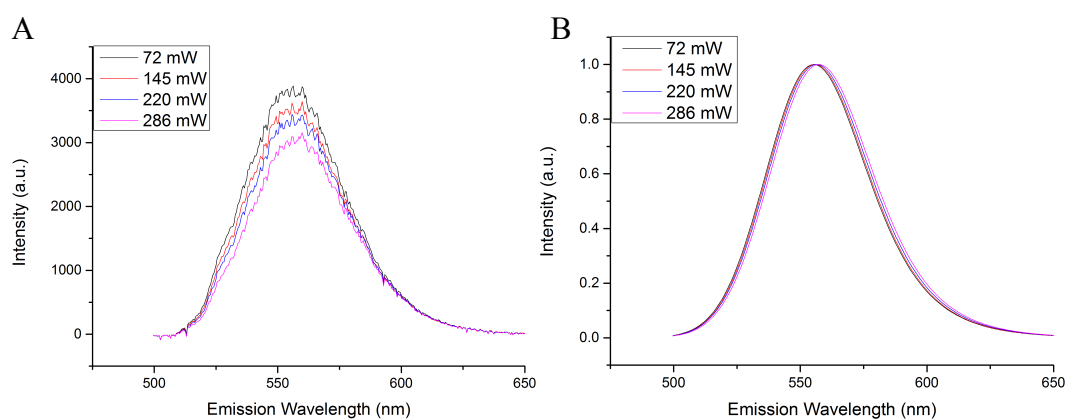


Figure 4.22 – CdTe QDs with 1064 nm, x40 microscope objective optical tweezing. The raw (A) and GausMod fitted (B) λ_{peak} shift of CdTe QDs when exposed to optical tweezers formed with a $\lambda = 1064$ nm source and 0.65 NA, x40 microscope objective.

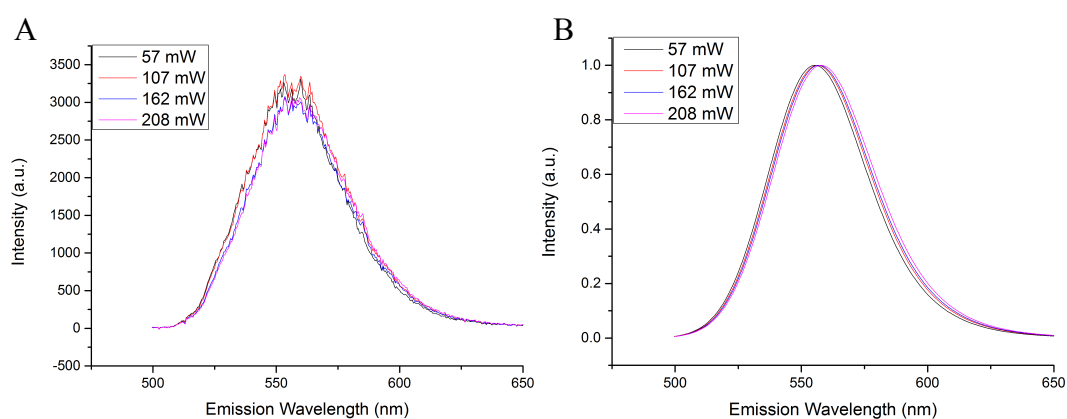


Figure 4.23 – CdTe QDs with 1064 nm, x100 microscope objective optical tweezing. The raw (A) and GausMod fitted (B) λ_{peak} shift of CdTe QDs when exposed to optical tweezers formed with a $\lambda = 1064$ nm source and 1.25NA, x100 microscope objective.

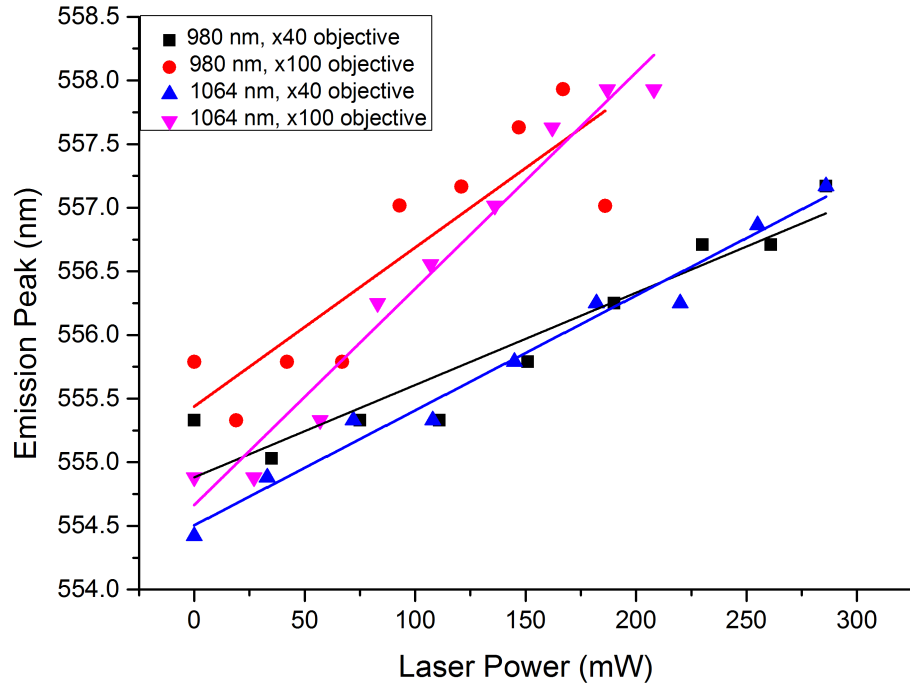


Figure 4.24 – CdTe spectra shift as power of optical tweezing beam increases. The λ_{peak} shift of CdTe QDs when exposed to either $\lambda = 980$ nm or $\lambda = 1064$ nm optical tweezers with x40, 0.65 NA or x100, 1.25 NA objectives, over a range of powers.

Utilizing the results presented in Figure 4.24 and the representative thermal shifts illustrated in Figure 4.16, it is possible to infer the temperature increases induced by optical tweezers generated with $\lambda = 980$ nm and $\lambda = 1064$ nm sources, with x40, 0.65 NA and x100, 1.25 NA microscope objectives. Powers displayed represent the post-microscope objective powers, noted in Figure 4.17 & 4.18.

The peak emission shifts of the CdTe quantum dots were extrapolated to determine the $\Delta\lambda_{\text{peak}} / W$. Using the x40, 0.65 NA MO rates of 5.02 and 9.45 nm $\Delta\lambda_{\text{peak}} / W$ ($\lambda = 980$ nm and $\lambda = 1064$ nm, respectively), were recorded. With the x100, 1.25 NA MO rates of 10.59 and 15.9 nm $\Delta\lambda_{\text{peak}} / W$ ($\lambda = 980$ nm and $\lambda = 1064$ nm, respectively), were recorded. Incorporating the calibration data recorded in Figure 4.16, it was possible to determine the temperature change in degrees Celsius per Watt ($^{\circ}\text{CW}^{-1}$). These results are summarised in Table 4.2. These illustrated an increased $\Delta\lambda_{\text{peak}}$ when using the higher NA microscope objective. Counter to the expected wavelength responses, $\Delta\lambda_{\text{peak}}$ increase from the $\lambda = 980$ nm source was lower than that with the $\lambda = 1064$ nm, with both microscope objectives. This implies a greater rate of heating with the $\lambda = 1064$ nm optical tweezing laser.

Table 4.2 – Summary of CdTe quantum dots in optical tweezers

Microscope Objective	λ_{trap} (nm)	$\Delta\lambda_{\text{peak}} / W$ (nm)	$^{\circ}\text{CW}^{-1}$
x40 0.65 NA	980	5.02	25.10
	1064	9.45	47.25
x100 1.25 NA	980	10.59	52.95
	1064	15.91	79.55

The $\lambda = 1064$ nm laser was capable of significantly higher power (3500 mW) than the $\lambda = 980$ nm laser (400 mW). The higher power ranges of this laser were used to generate an optical trap and the surrounding CdTe fluorescence was then recorded. With the $\lambda = 1064$ nm source the emission shift was recorded as ~ 8.8 nm at a power of 2,125 mW at the sample, with the x40, 0.65 NA microscope objective, and ~ 8.2 nm with a power of 1,241 mW, using the x100, 1.25 NA microscope objective. These higher powers indicated a loss of linear response in regards to the emission peak shift of the CdTe quantum dots, this is presented in Figure 4.25.

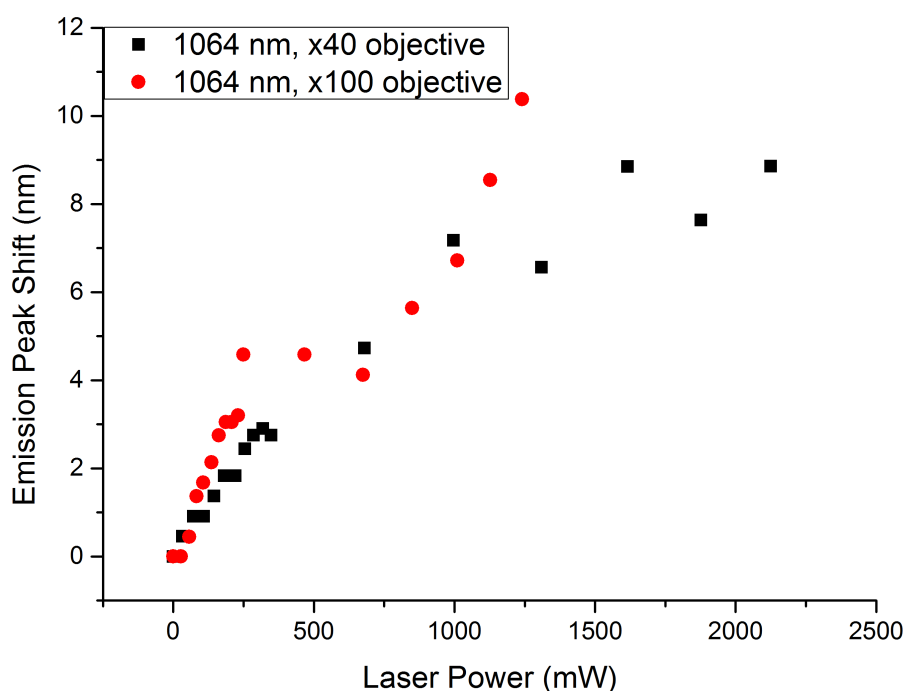


Figure 4.25 – CdTe spectra shift in high power optical tweezing. A comparison of the thermal effects of $\lambda = 1064$ nm optical tweezer with x40, 0.65 NA and x100, 1.25 NA microscope objectives with power at sample of up $> 2,000$ mW. Power on the x axis is the power at sample, $n = 3$.

It is important to note that the thermal diffusivity of the sample medium will result in increased heating across a broader volume of the same, the Heat Affected Zone (HAZ) [240]. This HAZ extends beyond the immediate focus of the optical tweezers, this was measured. Using the planar axis controls on MO2, the $\lambda = 488$ nm excitation beam was actuated in ~ 5 μm steps away from the focus of the optical tweezers. As the actuators did not have a scale, the steps were determined using measurement on the field of view. Measurements were recorded using a source set to 200 mW (both $\lambda = 980$ nm and $\lambda = 1064$ nm lasers), with the x40, 0.65 NA and x100, 1.25 NA microscope objectives in MO1. The resultant thermal dissipation, based on fluorescent shifts, is presented in Figure 4.26.

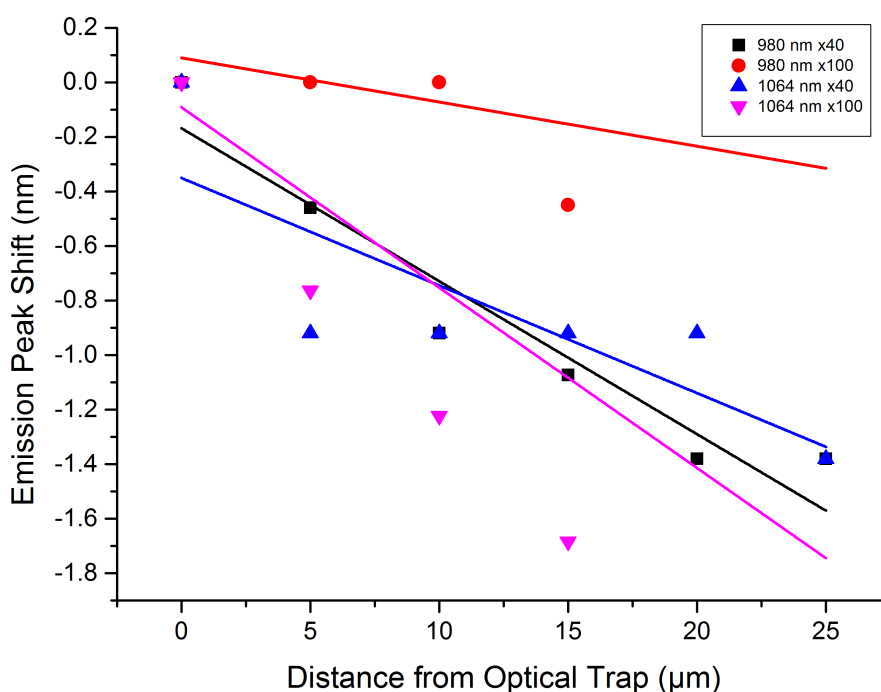


Figure 4.26 – CdTe emission gradient in optical tweezers. The peak of QD emission decreases as readings are recorded at a further distance from the optical tweezers.

The work presented so far in this chapter demonstrated that quantum dot nanocrystals such as CdSe and CdTe might be useful as nanothermometers to measure temperature shift in small volumes in which optical trapping experiments are performed. The CdTe nanocrystals in particular, show a clear shift in the peak emission wavelength of when measured at the site of an optical trap.

The initial calibration setup presented a $\Delta\lambda_{\text{peak}}$ of $\sim 0.2 \text{ nm/}^\circ\text{C}$ and $\sim 0.1 \text{ nm/}^\circ\text{C}$, between 20°C and 60°C , for the CdTe and CdSe quantum dots, respectively. Using known laser powers at the sample, optical tweezers of different wavelengths and spot sizes were tested to determine the thermal loading resulting from those variables. The peak shift of CdTe QDs when using 980 nm and 1064 nm optical tweezing beams, illustrated temperature changes of $52.95^\circ\text{CW}^{-1}$ and $79.55^\circ\text{CW}^{-1}$, respectively, when using a high numerical aperture (1.25 NA) microscope objective. This indicates a $\sim 50\%$ increase in heating when using a 1064 nm source, compared to the 980 nm source. Examples in the literature reported rates of 12°CW^{-1} to 15°CW^{-1} in similar 1064 nm optical tweezing regimes [221, 222], and 56°CW^{-1} to 73°CW^{-1} when using $980 \pm 5 \text{ nm}$ sources [223, 228]. This indicates a difference of $\sim 375\%$ to $\sim 500\%$ in heating rates between these reported optical tweezing regimes. When using an optical tweezer setup with a lower numerical aperture, 0.4 NA, heating rates were notably reduced, CdTe QD wavelength shifts indicating temperature changes of 25.1°CW^{-1} and $47.25^\circ\text{CW}^{-1}$ (980 nm and 1064 nm laser, respectively). This indicated a wavelength dependent difference in heating of approximately 88 %, a higher difference than exhibited by the 1.25 NA microscope objective systems. Results indicate an effect counter to the available literature. To further test the effects, an upgraded system, utilizing a higher resolution spectrometer was built. A broad range of optical tweezing wavelengths provides validation of quantum dots as temperature probes, nanothermometers, for optical tweezers.

4.4.3.3 Improved nanothermometry system

An optical tweezer system with spectroscopy capabilities, based on the system created at Heriot-Watt University (HWU) and described in Figure 4.5, was constructed and operated by collaborators at the Universidad Aut3noma de Madrid (UAM). This system was modified with a higher sensitivity spectrometer than the Ocean Optics spectrometers used in the work at HWU. A high sensitivity Si CCD camera (Synapse, Horiba) was coupled with a monochromator (iH320, Horiba), capable of a 0.06 nm resolution. Several other commonly used optical tweezing wavelengths were investigated. $\lambda = 750 \text{ nm}$, 808 nm, 920 nm, 980 nm and 1090 nm sources were used to produce optical tweezers. These were focused into an aqueous solution containing CdSe quantum dots and were shown to generate shifts in peak emission wavelength of $0.1 \text{ nm/}^\circ\text{C}$. When these peak emission shifts were converted to temperature shifts, levels of heating in the samples was found to vary depending on the coefficient of absorption of water at those wavelengths. Results are shown in Figure 4.27.

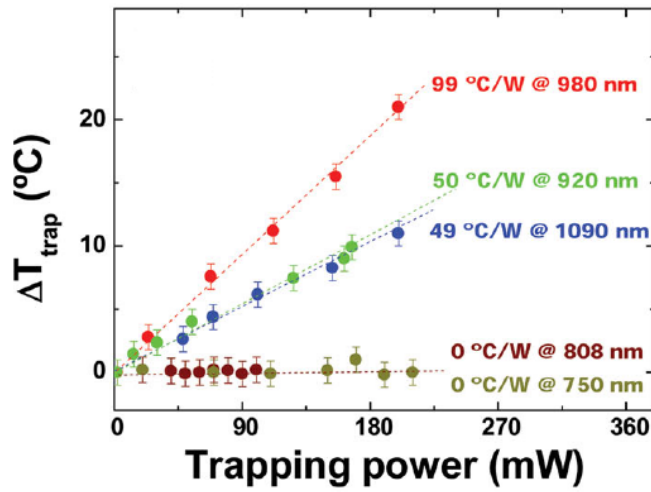


Figure 4.27 – Temperature shift with different optical tweezing wavelengths. Laser sources, from $\lambda = 750$ nm to $\lambda = 1090$ nm, show a range of localised temperature shifts induced by the optical tweezers. Solid dots are experimental data and dashed lines are the best linear fits. The heating rates (β_{trap}) obtained from these fits are shown. Data generated by collaborators at UAM after initial studies at HWU. Taken from Figure 3 (a), Haro, Ramsay et al. (2013) [187].

The CdSe quantum dots used were characterised as exhibiting a temperature dependent peak wavelength shift of $0.1 \text{ nm}/^{\circ}\text{C}$. Heating rates were calculated to be $0 \text{ }^{\circ}\text{C}/\text{W}$ for a trapping wavelength of 750 nm and 808 nm, $49 \text{ }^{\circ}\text{C}/\text{W}$ for 1090 nm, $50 \text{ }^{\circ}\text{C}/\text{W}$ for 920 nm and $99 \text{ }^{\circ}\text{C}/\text{W}$ for 980 nm. These results reported localised heating which, while similar, exceeded that recorded in the experiments at HWU. The only directly comparable trapping wavelength was the 980 nm system. This recorded an approximate heating rate increase that was 87% higher than the HWU experiments and comparable to that expressed in existing literature [223, 228]. The UAM setup utilized a lower numerical aperture microscope object, 0.8 NA compared to the 1.25 NA objective used at HWU. Use of a lower NA objective would be expected to result in reduced heating rates, compared to use of a higher NA objective.

The heating rates of optical tweezers (β_{trap}) of different wavelengths, Figure 4.27, are superimposed on a graph illustrating the wavelength dependent coefficient of absorption in Figure 4.28. These show that the heating rate of an optical trap (β_{trap}) agrees with the curve given by $\alpha_{abs}(\lambda_{trap}) \cdot \ln(\lambda)$, the absorption coefficient of water at the trapping wavelength ($\alpha_{abs}(\lambda_{trap})$) multiplied by the natural logarithm of the trapping wavelength, given as $\ln(\lambda)$.

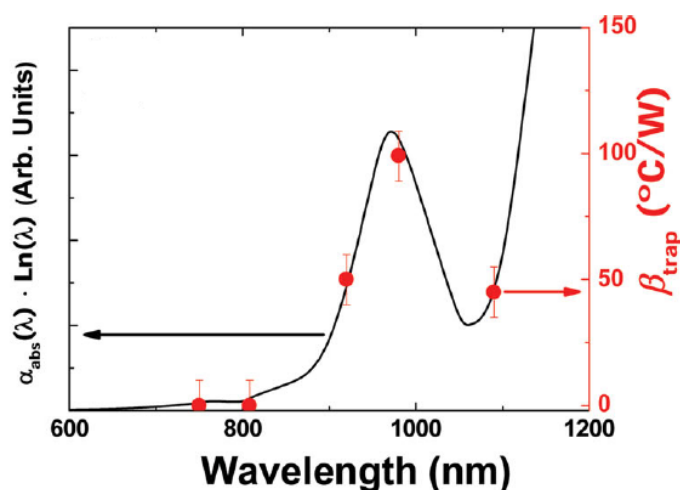


Figure 4.28 – Wavelength dependent heating of water by optical tweezers. Wavelength dependent absorption curve of water, as predicted by Mao *et al.* [4.32] (black), plotted with normalised optical tweezer heating results, β_{trap} (red). Taken from Figure 3 (b), Haro, Ramsay et al. (2013) [187].

This confirms the importance of trapping wavelength optimisation for optical tweezers, to reduce thermal effects. This data also indicates that there is non-negligible heating when using NIR optical tweezers, wavelengths which are generally assumed safe for biological materials in the so-called ‘biological’ or ‘therapeutic’ window. It is then possible to look at wavelengths in the regions with minimal absorption, combined with the exclusion of known phototoxic wavelengths [234], an ideal optical tweezer wavelength is proposed. This is represented in Figure 4.29.

Quantum dots have been shown to exhibit temperature dependent emission characteristics which can be exploited as nanothermometers, in water, for optical tweezers. Given the routine use of optical tweezers in life science applications, the next steps are to determine the functionality of quantum dots as nanothermometers in biological samples. While there is a wealth of literature on the use of quantum dots in biological samples [192 - 196], this typically focuses on a labelling function, where minor changes in the fluorescence profile may not be detected. The temperature dependant wavelength shift of quantum dots is measured in a variety of physiological environments and the toxicity and phagocytosis of these nanoparticles is reviewed.

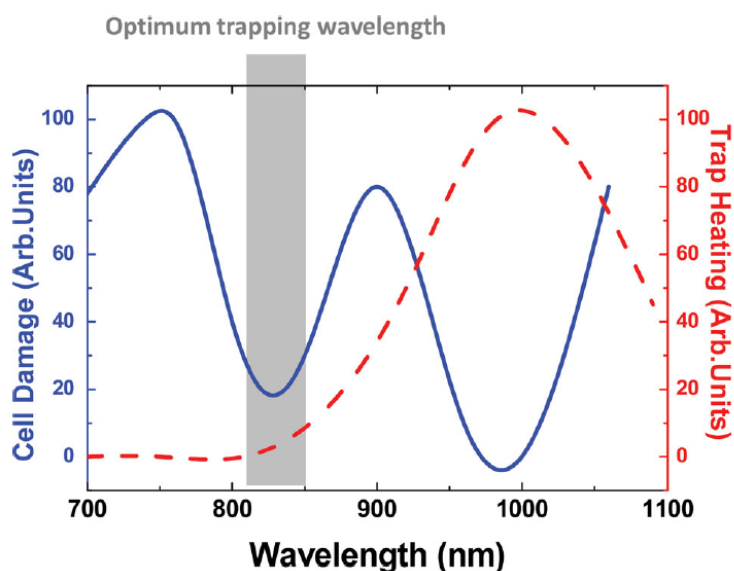


Figure 4.29 Optimal optical tweezer wavelengths. Proposed optimal optical tweezer wavelengths for biological research indicated by shaded area in this plot. Trap heating, assumed to follow the wavelength dependant absorption coefficients of water (red) and wavelength dependent phototoxicity, based upon damage to CHO cells [217] (blue). A region of low phototoxicity and low thermal loading is suggested as the ideal wavelength region for optical tweezing of biological samples to minimise both photothermal and photochemical damage. Taken from Figure 5, Haro, Ramsay et al. (2013) [187].

4.4.4 Nanothermometry in biological environments

The ultimate aim of this body of work is to apply these nanothermometers to biological samples that are optically trapped, without perturbing the biology of the samples being monitored. Therefore, these probes would be used in a range of aqueous environments, intracellular and extracellular. The robustness of these probes must be validated in a range of physiological environments. Quantum dots are tested in a range of PBS concentrations, pH and cell culture mediums, using the apparatus illustrated in Figure 4.4.

4.4.4.1 Phosphate-buffered saline

Phosphate-buffered saline (PBS) is a solution widely used in the handling of cell suspensions. While this does not contain the nutrients essential for cell growth or sustained cell viability, it does provide an isotonic solution for the cell, matching the osmotic pressure of the intracellular environment. Matching tonicity is important for

maintaining cell viability; distilled water that would prove hypertonic, lysing the cell and concentrated ionic solutions would be hypotonic for the cell, also with potentially catastrophic results. A higher PBS concentration was also tested, to record any differing effects in a higher concentration saline solution. Using a heated stage, the emission shift of CdSe quantum dots in 1x PBS and 10x PBS was measured, as illustrated in Figure 4.30, and compared to earlier results in water (Figure 4.16). Again, emission shift was measured from 20 °C to 60 °C and shown in Figure 4.31.

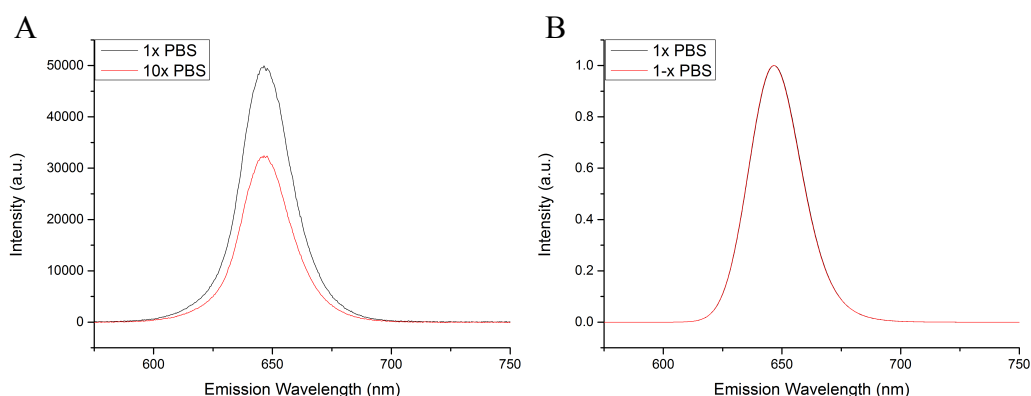


Figure 4.30 – Fluorescence emission of CdSe QDs in PBS. (A) Raw 6 nm CdSe QD emission in 1x and 10x concentrations of PBS, at 25 °C. (B) Fitted curves of 6 nm CdSe QDs in 1x and 10x concentrations of PBS at 25 °C.

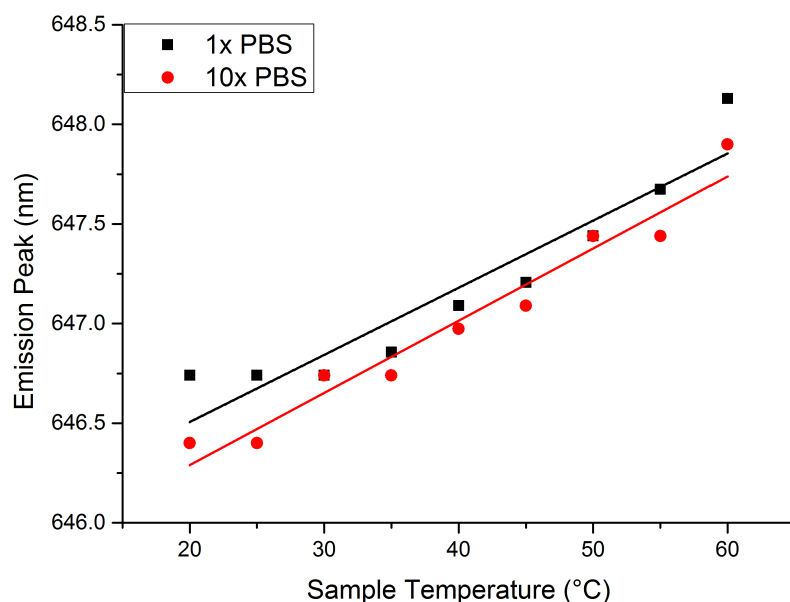


Figure 4.31 – Temperature induced emission shift of CdSe QDs in PBS. CdSe emission in 1x and 10x concentrations of PBS, temperatures ranged from 20 °C to 60 °C.

The 1x and 10x PBS samples exhibited emission shift rates of 0.11 nm/°C and 0.1 nm/°C respectively, there was no significant departure from the emission shift rate of 0.1 nm/°C in the initial dH₂O data (originally presented in Figure 4.16). This indicates that PBS may be used without compromising the efficacy of the CdSe quantum dots.

4.4.4.2 pH

The acidic or basic properties of an environment vary within biological samples. On a cellular level, the pH in the cytosol is slightly alkaline, typically reported to be around pH 7.2. However, the different functional components of the cell have different processes. Lysosomes, for instance, are used to digest materials, using an array of enzymes and an internal pH of ~4.5. Slight changes in pH may have a significant impact on the signalling and reactions of a cell. If quantum dot nanocrystals are to be used in cells as intracellular thermometers, effects of pH variation on CdSe quantum dots must be tested, particularly as these are phagocytosed [193], with the resultant phagosome fusing with an aforementioned, low pH, lysosome [241]. A range of solutions, from pH 3 to pH 11 were produced using a commercially available buffer kit (Sigma), with buffer pH measured prior to use with a pH meter. This range of pH buffers were used to test for changes in CdSe emission shift due to pH of surrounding environment. Each solution contained 800 nM CdSe quantum dots and the emission was measured using the apparatus illustrated in Figure 4.6, an example of the collected spectra is illustrated in Figure 4.32. A full range of stage temperatures from 20 °C to 60 °C, increasing in 5 °C increments were recorded. Measurements were recorded in triplicate. The results are illustrated in Figure 4.33.

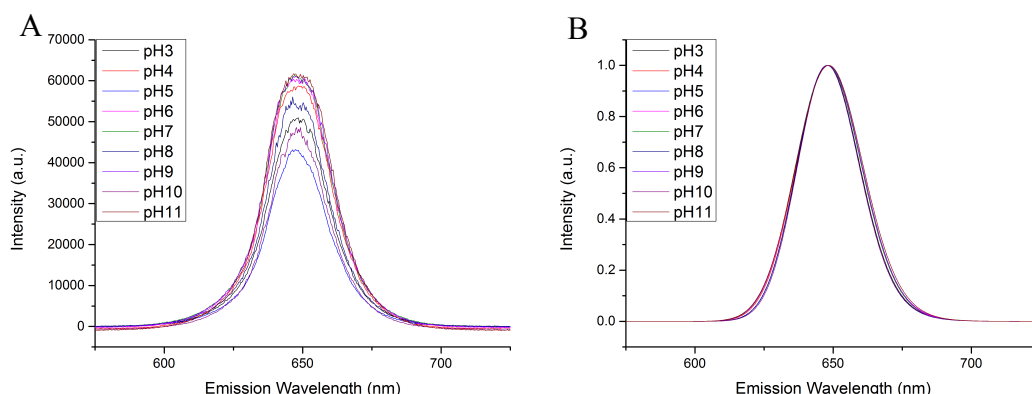


Figure 4.32 – Fluorescence emission of CdSe QDs at various pH levels. (A) Raw 6 nm CdSe QD emission in a range of different pH environments, from pH3 to pH11, at 25 °C. (B) Fitted curves of 6 nm CdSe QD emission in a range of different pH environments, from pH3 to pH11, at 25 °C.

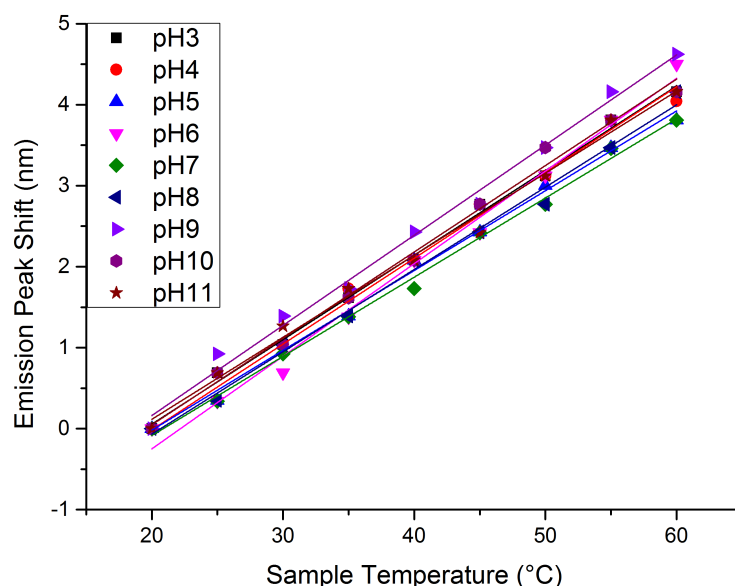


Figure 4.33 – Temperature induced emission shift of CdSe QDs at different pH levels. The fluorescence emission of 6 nm CdSe QDs in a range of different pH environments, with the fluorescence emission peak measured across a range of temperatures, from 20 °C to 60 °C, with the CdSe quantum dots appearing highly consistent between all samples.

The peak emission wavelength shift CdSe quantum dots in a range of solutions, from pH 3 to pH 11, was recorded at 0.095 nm/°C to 0.11 nm/°C. These are summarised in Figure 4.34. Compared to the initial peak emission shift of ~0.1 nm/°C, reported in Figure 4.16, there was no significant deviation in the emission rate of the CdSe QDs in a range of pH buffers. This is a positive indicator of the fluorescence stability of these QDs. This suggests that biological environments, intra- and extracellular, should have no significant impact on the fluorescence properties for nanothermometric purposes.

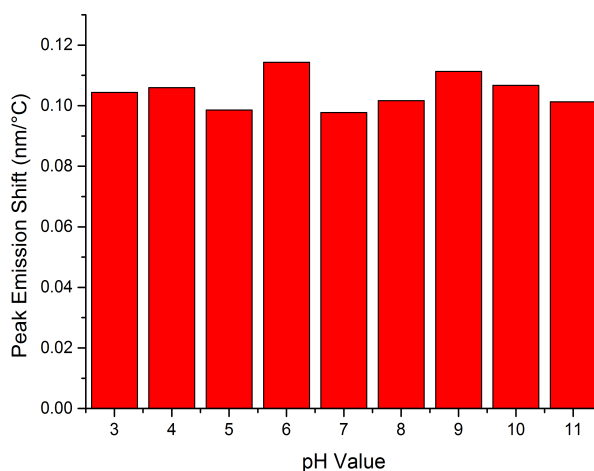


Figure 4.34 – Summary of temperature dependent CdSe emission shift at pH 3 – pH 7. Emission peak of the CdSe quantum dots is highly consistent between all samples.

4.4.4.3 Cell culture media

Cells are grown in a solution that contains a complex mixture of ingredients. There are many culture media in use, catering to the varying physiological requirements of different cell lines. Here, a variety of those growth media are tested. Those tested are routinely found in tissue culture facilities, for common cell lines such as CHO-K1, SAOS-2 and HeLa cells, these were DMEM, F-12 and RPMI. Serum, most commonly FCS, is a supplement generally added to growth media, at varying concentrations, dependent on the cells being cultured. Serum is the blood fraction remaining, following coagulation and removal of blood cells, it is rich in growth factors, such as Epidermal Growth Factor (EGF) and Fibroblast Growth Factor (FGF), and proteins [242], which may bind or interfere with the function of quantum dots. To test for any potential impact of the serum on the quantum dot emission, several DMEM samples were tested, consisting of 0 %, 5 %, 10 % and 20 % serum. The data was recorded in triplicate and the results are presented in Figure 4.35.

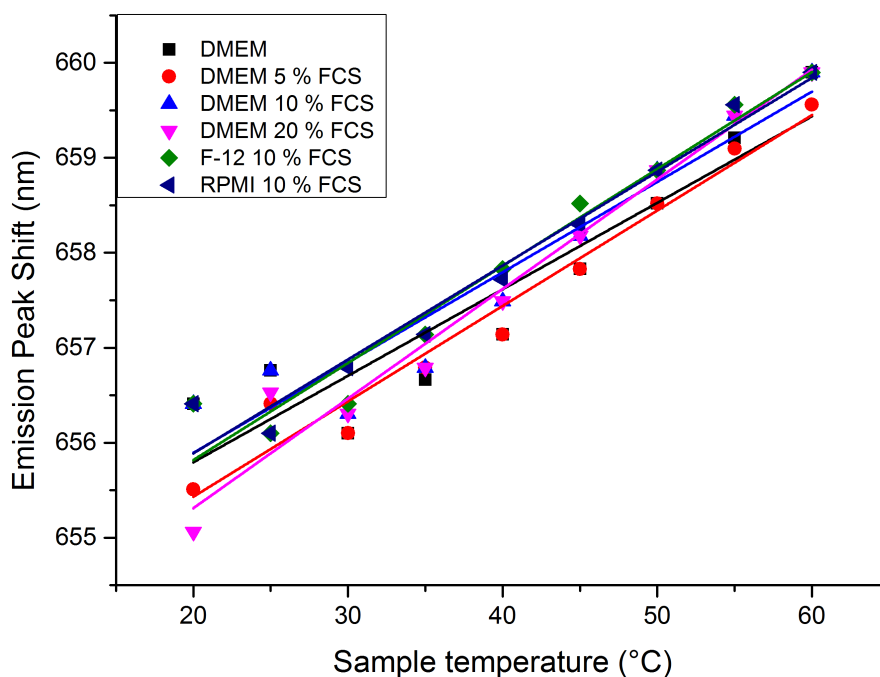


Figure 4.35 – Temperature induced peak emission shift of CdSe QDs in cell media. The fluorescence emission shift of CdSe QDs in a range of cell culture medias between 20 °C and 60 °C.

The emission of CdSe quantum dots was found to be consistent through the tested culture mediums and serum concentration, with emission wavelength shifts of 0.09 nm/ °C to 0.11 nm/°C, as summarised in Figure 4.28. This aligns well with the results recorded with varying PBS concentrations (0.1 – 0.11 nm/°C) and pH values (0.095 – 0.11 nm/ °C), indicating a suitability for use of these quantum dots in a range of biological environments without a loss of temperature sensitive emission shift. While the emission of these quantum dots appears to not be notably affected by biological environments, the effect of these quantum dots on biological cells and environments must also be considered, for example their toxicity to cells.

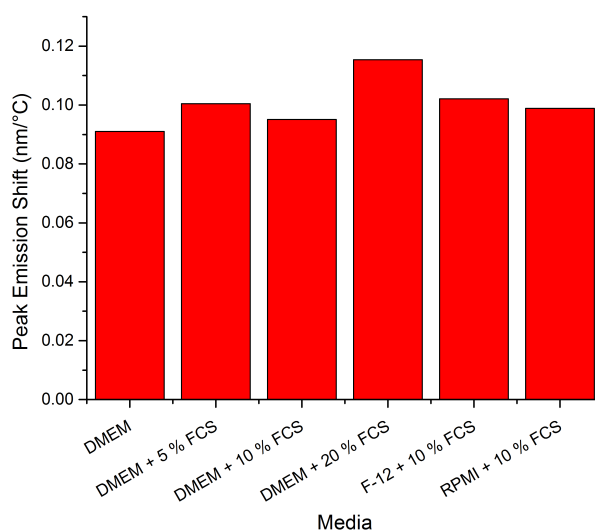


Figure 4.36 – Summary of temperature dependent CdSe emission peaks in cell media. A high degree of consistency is noted in the temperature dependent CdSe emission peak shift measured in a range of common cell culture media.

4.4.5 Toxicity

Continuing with the theme of biological validity, the toxicity of these nanoparticles must be considered. These quantum dots are produced using materials known to be highly toxic and the toxicity is known to often increase as the particle size decreases, as its surface area, per unit volume, increases. Therefore, toxicity studies were carried out on these quantum dots in order to quantify toxic effects, in particular, the membrane integrity and metabolic processes of the cells exposed to different concentrations of quantum dot nanocrystals.

4.4.5.1 CdTe toxicity

The effect of varying quantities of CdTe quantum dots on cell viability and metabolism were recorded. Concentrations of 40 μM to 40 nM of the CdTe quantum dots were used in the growth media, with $\sim 10^4$ macrophage cells (J774) per well. Significant toxicity was recorded at concentrations as low as 800 nM. The results of the LDH assay are shown in Figure 4.37, the resazurin experimental results are presented in Figure 4.38.

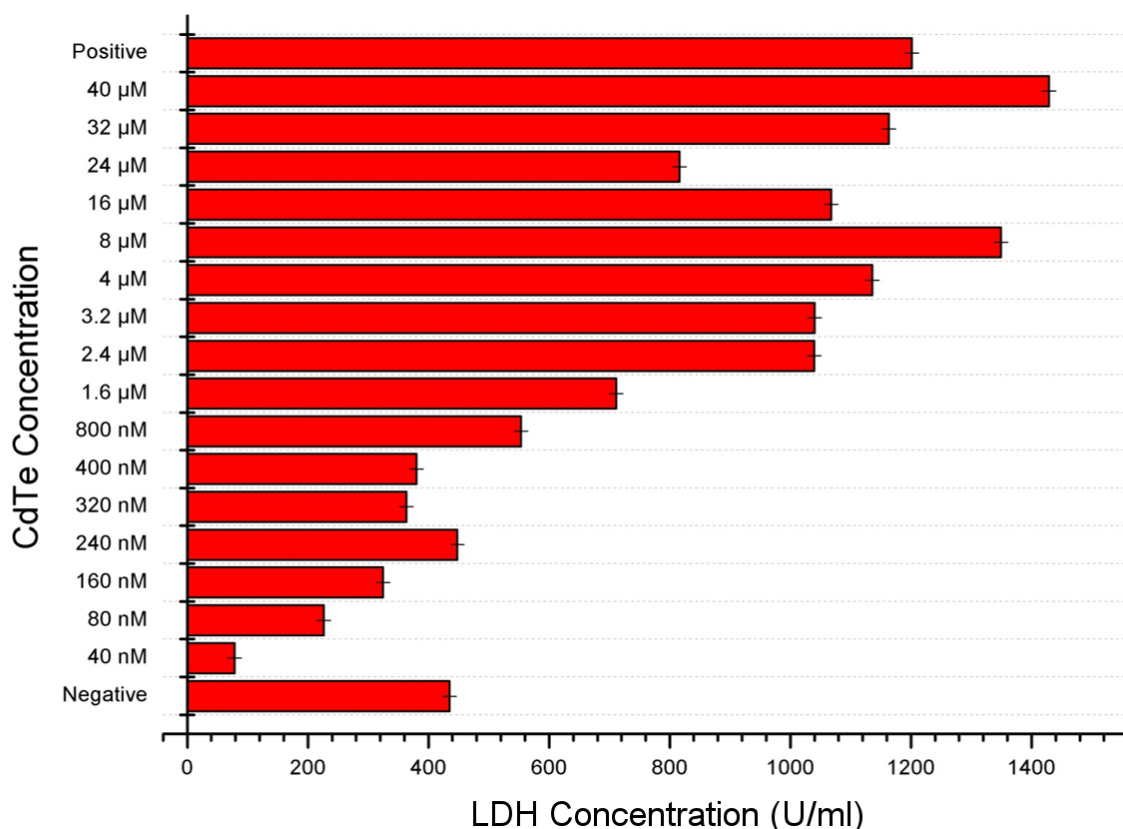


Figure 4.37 LDH assay, CdTe toxicity. Increasing concentration of LHD indicates loss of cell membrane integrity. The negative control denotes an untreated cell population while the positive control has been exposed to Triton X-100. High LDH activity is indicative of cell membrane damage; this is present in all but the lowest concentrations of CdTe quantum dots. Concentrations below 8 μM could not be resolved with the spectrometer in the tweezing apparatus shown in Figure 4.7.

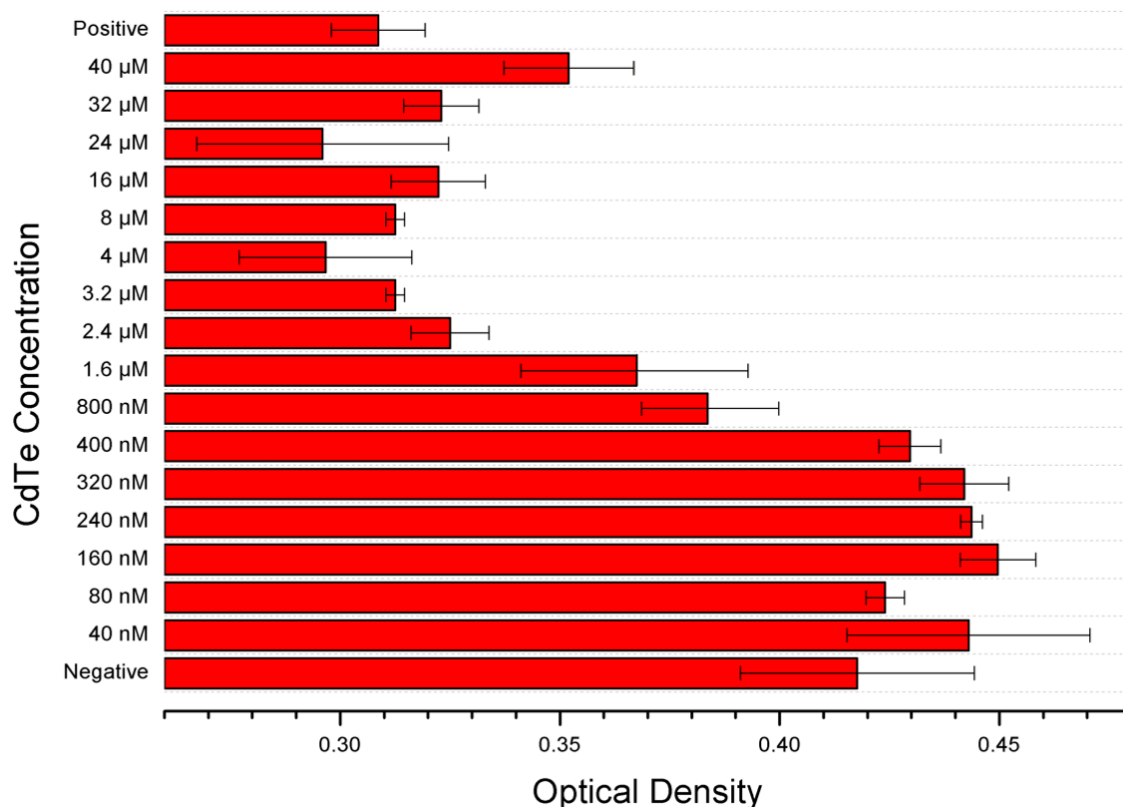


Figure 4.38 Resazurin assay, CdTe toxicity. Decreasing optical density indicates loss in metabolic activity. The negative control denotes an untreated cell population while the positive control has been exposed to Triton X-100. Low fluorescence shows minimal conversion from resazurin (non-fluorescent) to resorufin (fluorescent), indicating low metabolic activity from the cell population, this occurred in all but the lowest concentrations of CdTe quantum dots. Concentrations below 8 μ M could not be resolved with the spectrometer in the tweezing apparatus shown in Figure 4.7.

The results show that the CdTe quantum dots become detrimental to cell metabolism and viability at concentrations between 400 nM and 800 nM, where both data sets illustrated a marked decrease in viability (Figure 4.37) and metabolic activity (Figure 4.38). This poses an issue for use with biological samples in the optical tweezer setup described in this work, which was unable to resolve distinct peaks from CdTe concentrations below 8 μ M. Tweezing experiments were conducted using a concentration of 20 μ M to get sufficient fluorescent signal to spectrometer in order to measure the peak emission wavelength. While biological work may not be suitable for this apparatus, it is still important to view how the cells interact with this quantum dots. This was accomplished using confocal microscopy to generate images of the cells and the position of quantum dots in regards to the cells.

4.4.7 Confocal imaging

Macrophages (J774) incubated with quantum dots were imaged using confocal microscopy to visualise any phagocytosis of the nanoparticles by the cells and to examine the morphology of the cells. The J774 cells were seeded on glass bottomed fluorodishes and allowed to adhere. CdTe (at 4 μM) or CdSe (at 80 nM) were added to the seeded dishes and returned to incubate for 4 hours. Dishes were washed twice with PBS at 37 °C to remove debris and non-internalised particles from the dishes. Images were recorded on a Leica SP5 confocal microscope, using a Leica HXC PL APO CS 63x, 1.4 NA oil immersion microscope objective. Fluorescence was collected using the GFP filter set for CdTe quantum dots and the mCherry filter set for CdSe quantum dots. A composite image overlaying the fluorescence (artificially coloured) on the bright-field was produced. Visible localised fluorescence was recorded from the CdSe samples, showing internalisation of the quantum dots. The imaging of light from individual dots is challenging given our spectrometer, but clusters of CdSe particles, seen in Figure 4.39, may in future be used to indicate the intracellular, localised temperature at specific cellular locations. Combined with optical tweezing, or nanoparticle functionalisation these particles could be manipulated to go to the desired location. No fluorescence was witnessed in the samples incubated with CdTe, likely caused by lack of internalisation by the cell, resulting in the CdTe QDs being washed from the sample during preparation.

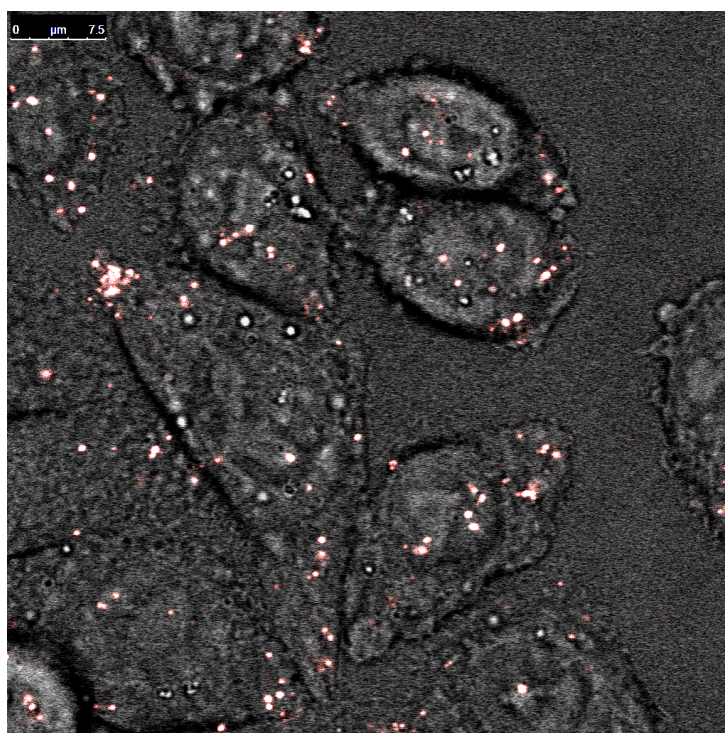


Figure 4.39 CdSe quantum dots in macrophages. Confocal images of J774 macrophages after a 4 hour incubation with 80 nM CdSe quantum dots. Image recorded using a 63x, 1.3 NA microscope objective and mCherry filter set on a Leica SP5.

4.4.8 Optofluidics

The use of quantum dots in the measurement of optically induced heating was not limited to making measurements in samples made from glass coverslips into which a tweezing beam was directed. The technique may be used in any experiment in which the quantum dots can be added if there is an optical window (such as a coverslip thickness piece of glass) in which to excite the luminescence from the quantum dots and collect it. This is demonstrated now, using a lab on a chip device. Using ULI, followed by selective chemical etching, a microfluidic device was produced by Debaditya Choudhury. This consisted of a single sub-surface channel, with a $100\text{ }\mu\text{m}$ by $100\text{ }\mu\text{m}$ cross-section and an integrated waveguide perpendicular to the mid region of this channel. A schematic of the device is shown in Figure 4.40. Measurement of the temperature shift using quantum dots in such a device was carried out in collaboration with Debaditya Choudhury as detailed below. Carbon nanotubes were also added to the microfluidic channel to increase the temperature due to their absorption of the laser light [22].

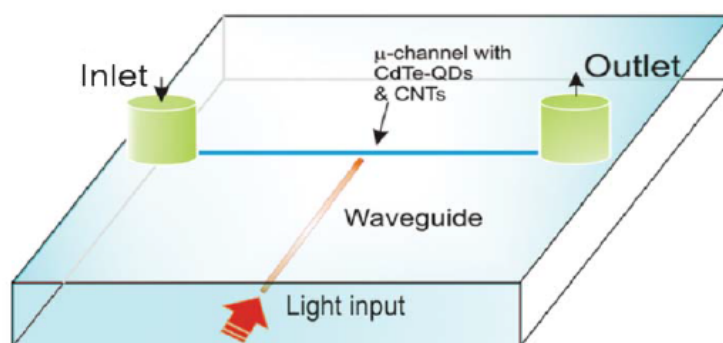


Figure 4.40 – Optofluidic device. Schematic of a simple microfluidic device with integrated waveguide. Taken from Figure 1(a) Choudhury et al. (2012) [22].

Measurements were recorded using a custom confocal microscopy system, illustrated in Figure 4.41. A $\lambda = 1090\text{ nm}$, Yb-doped glass fibre laser was coupled to the waveguide and using a $\lambda = 488\text{ nm}$ excitation source, perpendicular to the surface of the channel, it was possible to measure the emission properties of CdTe quantum dots, with a monochromator, while inducing localised heating from the waveguide source. The wavelength shift indicated a heating rate of $3.1\text{ }^{\circ}\text{CW}^{-1}$. Carbon nanotubes (CNT) were added to the solution at $0.1\text{ }\%$, by mass, to increase the light absorption within the device, increasing the localised heating. The addition of CNTs showed an increase of heating rate at $\lambda = 1090\text{ nm}$ to $160\text{ }^{\circ}\text{CW}^{-1}$.

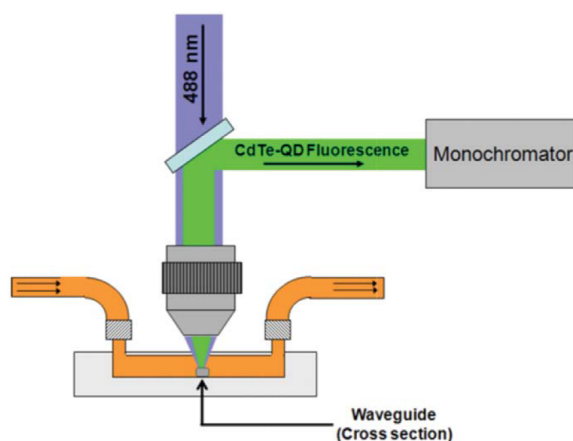


Figure 4.41 – Optofluidic device imaging and spectroscopy. Illustration of the device used for imaging and fluorescence detection. Taken from Figure 2(a) Choudhury et al. (2012) [22].

4.5 Discussion

A shift in peak emission wavelength was recorded in both CdTe and CdSe quantum dots; this shift was seen on both the heated stage and in the localised heating of the optical tweezers. On a heated stage, the rate of emission shift was comparable to the literature for the CdSe quantum dots, however, the CdTe quantum dot calibration indicated a difference in the emission shift recorded in this project, $\sim 0.2 \text{ nm/}^\circ\text{C}$, from that reported in the literature, $\sim 0.6 \text{ nm/}^\circ\text{C}$ [233]. This discrepancy may have been caused due to issues with the CdTe quantum dots, stock sample aggregation was noted, which may indicate why these QDs were not functioning entirely as expected.

When exploited as nanothermometers in an optical tweezing system, a $\lambda = 980 \text{ nm}$ source presented an increase in temperature of $25.1 \text{ }^\circ\text{CW}^{-1}$ to $52.95 \text{ }^\circ\text{CW}^{-1}$ (0.65 NA and 1.25 NA respectively) and a $\lambda = 1064 \text{ nm}$ presented an increase of $47.25 \text{ }^\circ\text{CW}^{-1}$ to $79.55 \text{ }^\circ\text{CW}^{-1}$ (0.65 NA and 1.25 NA respectively). Collaborative work at UAM presented an increased heating rate, of $99 \text{ }^\circ\text{CW}^{-1}$, when using a $\lambda = 980 \text{ nm}$ optical tweezing system. While this is in the same regime as the data gathered at HWU, the UAM system used a lower numerical aperture microscope objective (0.8 NA). This would be expected to place the expected results somewhere between the $25.1 \text{ }^\circ\text{CW}^{-1}$ to $52.95 \text{ }^\circ\text{CW}^{-1}$ found with the work at HWU, however, this was not the case. While the UAM work did not incorporate a $\lambda = 1064 \text{ nm}$ source, the $\lambda = 1090 \text{ nm}$ was expected to yield similar heating

rates. Using the $\lambda = 1064$ nm source optical tweezers, the CdTe QDs exhibited a peak emission shift that represented a shift rate in the temperature of $47.25\text{ }^{\circ}\text{C}\text{W}^{-1}$ to $79.55\text{ }^{\circ}\text{C}\text{W}^{-1}$ (0.65 NA and 1.25 NA respectively), the UAM work presented a rate that fell within this range, with in temperature shift of $49\text{ }^{\circ}\text{C}\text{W}^{-1}$ when using the $\lambda = 1090$ nm (0.8 NA) optical tweezing source. The UAM data presented a higher rate of heating with the 980 nm source, than that which was recorded at HWU, where the 980 nm source, counter to expectations, produced a lower rate of temperature increase than exhibited by the 1064 nm source. We look at potential causes for these discrepancies.

The main concerns regarding the work at HWU could be broken down into three primary factions. Firstly, the resolution of the spectrometer used in these experiments did not appear ideal for the small shifts that were being monitored. This was especially noted when measuring the temperature dependent emission shift of 6 nm CdSe quantum dots induced by optical tweezers (Figure 4.19), while a peak shift was recorded, this was only by a single increment on the spectrometer. The calibration of the CdSe QDs (Figure 4.16) was comparable with that in the literature ($\sim 0.1\text{ nm}/^{\circ}\text{C}$), however, the small temperature shift at lower powered optical tweezer systems would be difficult to resolve with the spectrometer used. This issue was largely addressed with the modified system developed at UAM (Section 4.4.3.3) [187].

Secondly, the $\lambda = 980$ nm source was expected to generate a higher rate of temperature increase than the $\lambda = 1064$ nm source. The modified experimental setup at the UAM did not face this issue and the results published were in food agreement with the theoretical model [187]. This indicates an issue with the system produced at HWU. The most likely cause would be the power levels at sample differing from those initially measured, that power may have been lost owing to a misalignment with the additional beam expanding assembly, which required the use of flip mounts.

Finally, the other potential issue is that the CdTe QDs, while exhibiting a greater temperature related wavelength shift ($\sim 0.2\text{ nm}/^{\circ}\text{C}$), did not exhibit the shift reported in the literature ($\sim 0.6\text{ nm}/^{\circ}\text{C}$). It is possible that this may have been due to inefficiencies with the calibration setup, that it may have not been heating the sample to the desired temperature. However, we believe this to be unlikely owing to the result recorded with the CdSe QDs. Both the CdSe and CdTe quantum dots appeared to largely maintain their emission profile in different media and temperature environments. There is a noted

decrease in fluorescence intensity, which is another way in which to monitor temperature change, however, this is much more susceptible to other variables, as discussed in Section 4.2.5. We noted that the stock solution of CdTe QDs developed a sediment, indicating that there may have been issues with the colloidal solution, it is possible that this degradation may have had a negative impact on the results generated. The work carried out at UAM also overcame this issue, with an improved emission detection system was implemented, using a higher resolution monochromator based system and the CdSe quantum dots.

The toxicity of these particles is a point of concern. With the CdTe QDs appearing highly toxic at concentrations over ~400 - 800 nM. The system designed at HWU did not have the sensitivity to resolve the emission concentrations of QDs lower than 8 μ M, however, it should be possible with a higher sensitivity spectrometer. The resolution and sensitivity of the spectrometer used have been raised as limiting factors in these works. To summarise, a system with higher resolution would allow the finer detection of temperature shift, especially with those particles exhibiting a lower temperature related peak emission shift. Higher sensitivity detection would allow for study using lower concentrations of QDs, which would help overcome viability issues when studying biological samples. While cost limiting, a higher end spectrometer would appear to be the primary improvement to make to the system described in this chapter.

4.6 Conclusions

The use of nanoparticles to measure physical variables is an area that continues to grow and develop. Nanoparticles will continue to generate a keen interest in the biological sciences. A prime goal is to produce quantitative measurements with minimal biological impact. Nanoparticle thermometry, the use of nanothermometers, is a field that has grown extensively in recent years and now there is a wealth of particles being used to measure temperature.

Regarding the initial objective of this work, wavelength optimisation of optical tweezers in an attempt to minimise the thermal load on a sample, we recorded a significant increase in heating rates when using the $\lambda = 1064$ nm optical tweezers, compared to that with the $\lambda = 980$ nm sources, this was counter to the expected outcome. Expanded work carried out by collaborators at UAM indicated broad agreement between the wavelength

dependent absorption coefficients of water and heating induced by optical tweezers over a range of source wavelengths. The potential to apply the temperature dependent emission shift of these QDs to biological work appears sound. There were no significant deviations from the calibration recording when testing these under a range of different cell culture media, PBS concentrations and pH values.

Biophotonics techniques are becoming more widely used. Optical tweezers continue to be one of the cornerstone technologies in the field. However, it is fundamental that these experiments are catered to the biological viability and integrity of the specimens. Here we have seen that temperature can be monitored in optical tweezing systems and optofluidic devices, however, regarding biological viability, the concentration of quantum dots required was an issue in these works. To generate enough light to record a spectrum, with which it was possible to read sub-nanometre changes in emission wavelength, the concentrations were simply too high to apply to cells in our system. The lower concentrations of CdTe and CdSe quantum dots, 4 μ M and 80 nM respectively, used in the pursuit of imaging these particles within cells looks to be damaging, confirming the toxicology assay results, as the adherent cells round up and appear more granular. While work has shown a suggested ideal region of optical tweezing wavelengths, the next goal of these nanothermometers devices should be to show highly localised temperature effects in biological materials, with little to no biological impact and while allowing a rapid measurement to be made.

Chapter 5

Summary

5.1 A close

The intention for this section is to pool a summary of the experimental chapters. Where each experimental chapter tackled a different niche of biophotonic research, this chapter seeks to produce as much of a point of coalescence as is possible. The motivation and techniques that were used throughout this project will be reintroduced, as will the reasoning as to why they were used and the results that were garnered. Some potential routes for future research stemming from this work will then be discussed. This chapter will close on some remarks on the work and experience as a whole.

5.2 Summary of thesis

The work presented in this thesis considered a number of photonic techniques and their applicability to the study of biology, specifically, the study of the single cell. The

single cell, we study for a number of reasons. As the fundamental representation of life it can provide a wealth of knowledge that can be lost on the macroscopic, whole organism level. From fundamental biological knowledge to the pathways of disease, that may start at a cellular level. This is not to discount the importance of biological study at a tissue, whole organism or population level; it is that biology on these different scales requires a different perspective and a different set of tools.

Light manipulation is an immensely powerful tool in the biological sciences. The field of single cell biology owes its founding to the manipulation of light in early microscopes. Microscopy allowing this visualisation of what we could not see with the naked eye. These imaging techniques continued to advance with novel technologies in lens production, light filter and most significantly, the development of the laser. The access to monochromatic, collimated light allowed for significant improvement in fluorescent imaging techniques but importantly, and somewhat underappreciated, the ability to physically manipulate the microscopic world; a paradigm shift from observing to interacting.

Physical manipulation can be interpreted in a number of manners. The most basic concept is the ability to touch, to pick up and to move – a role fulfilled by optical tweezers. These devices were developed from the discovery that laser sources could be used to generate forces that could be employed to manipulate microscopic particles. A tightly focused Gaussian beam will self-centre a spherical particle near the focal volume. This effect is caused by light being refracted as it traverses a change in refractive index in the particle. The resultant change in the momentum of the light, in accordance with Newton's third law, causes a recoil effect upon the sphere. This results in a remarkable stability in the lateral axis. This force, functional in three dimensions, will also result in axial stability, though the particle is held slightly outside the focus due to the additional scattering forces. In many ways, optical tweezers still remain the dominant biophotonic device, at least from a physics laboratory perspective. The other significant form of physical manipulation that this work employed was the ability to induce pore formation in cell membranes, photoporation. A technique that similarly relied on tightly focused laser light, but used ultrafast laser sources to expose a small focal volume to an exceptionally high burst of photonic energy. Significant enough to briefly form a free-electron plasma that generates a short lived submicron compromise in the cell membrane.

Constructing and optimising a device for photoporation, it was observed that this could induce submicron pore formation. Using trypan blue, a stain that cannot cross the cell membrane, it was possible to confirm successful pore formation. The application of raster scanning in place of single shot photoporation allowed for an increased effectiveness in the work presented here, with viability approaching 100 % near optimal power settings. If laser systems with lower peak powers, such as the widely used 80 MHz systems had been available, I believe this would have yielded stronger results still. Implementing a faster shutter would have also drawn this work more in line with the existing literature, and likely generated stronger results in single shot operation. A key benefit of this system is a significantly higher throughput over what is generally presented in the literature. However, this earlier success did not translate to an ability to transfect target cells. While the transfection of HPDE4 cells with *KRAS* may have faced a number of biological uncertainties, with sparse use of the cell line in the literature and *KRAS* potentially causing transfected cells to lose adhesion, these issues would not be shared with the CHO-K1 cell line. It is possible that, while pore formation was occurring, there was insufficient plasmid entering the cell or that unseen processes from the photoporation were hindering the cells.

Looking to other methods of physical manipulation to compromise the cell membrane, optical tweezers were considered. Here the optical confinement of hollow cylindrical structures was studied and first reported. Direct optical tweezing was found to be incredibly weak, even when utilizing multiple beams. An effect caused by the minimum volume of refractive index change from the environment and the lack of refractive index change in the long axis of the hollow cylinder structures. Stronger, though poorly controlled, optical manipulation of the hollow cylinders was possible when optically confining microsphere handles; optical tweezing by proxy. The ability to inject cells in a manner comparable to microinjection appears unlikely with the orientations of cell and microcapillary used in this work. The high flexibility of the cell impedes attempts at piercing the membrane mechanically. Adjustment in orientation or restraining the cell against a rigid structure, perpendicular to direction of the piercing force, as opposed to parallel in this work, would likely be a step closer towards optically driven microinjection, with environmental influences also capable of increasing the permeability of the cell membrane. The next ideal step would be to implement the use of more advanced structures, in place of the microcapillaries or microtubes in this work. This prospect of tailor made, via processes such as two-photon polymerisation, allows for the

optimal design in order to maximise the strength of confinement and therefore the force which may be exerted by an optically trapped particle. This work did, however, find use in the use of optical tweezers and microcapillaries for the applications of isolating cells. With the growing interest in single cell study, this could prove a powerful tool for selecting specific cells of interest.

Significant densities of light are required by these biophotonic techniques that can physically manipulate particles on the microscopic scale. While this localised high energy region is required to generate enough momentum to move a particle or in the generation of free-electron plasma, there are consequences that must be contemplated. One such consequence is the generation of heat as the surrounding environment absorbs some of the light. A particular concern when the biological sensitivity to thermal variance is considered. The pursuit from there is then to evaluate potential mechanisms by which thermal effects can be measured, while minimising the impact of those mechanisms on the effects that are primarily being measured. Conventional temperature measurement techniques are macroscopic or lacking in the resolution required for recording extremely small volumes. This is the realm in which nanothermometers prove the ideal tool, and while a wealth of research is growing around complex lanthanide compounds, the ubiquitous quantum dots were chosen as a suitable probe. The quantum dots in these experiments did remain largely consistent in the exhibited emission shifts. Temperature induced emission peak shifts indicated thermal loading of $47.25\text{ }^{\circ}\text{C}\text{W}^{-1}$ to $79.55\text{ }^{\circ}\text{C}\text{W}^{-1}$ with a 1064 nm source, depending on the microscope objective used, and $25.10\text{ }^{\circ}\text{C}\text{W}^{-1}$ to $52.95\text{ }^{\circ}\text{C}\text{W}^{-1}$ recorded with the 980 nm source, notably lower than expected – when compared to the 1064 nm source. An early concern with this system was the resolution and sensitivity of the spectrometer available. It was unable to resolve finer peak emission wavelength shifts, this was particularly problematic with the CdSe QDs employed in this work, which exhibited a shift of $\sim 0.1\text{ nm}/^{\circ}\text{C}$. This factor was addressed owing to an improved optical setup built by Dr. Daniel Jaque's team at UAM. Implementing a monochromator based system to overcome the issues we had faced with a lower end spectrometer. Using this improved system, a range of optical tweezing wavelengths were tested and an optimised range for safe optical tweezing of biological samples is proposed, based on a combined minima of phototoxicity and photothermal effects at $\sim 810\text{ nm}$ to 850 nm . The concerns regarding sensitivity apply more to the application within functional biological systems, with lower sensitivity, the system constructed here is

limited, requiring concentrations of quantum dots that exhibit significant toxicity to biological samples.

Where the results were certainly mixed, there is no doubt that biophotonics is a large and continually growing field. Novel technological in the physics laboratory will filter into other scientific fields and applications in the life sciences and plentiful. The greatest boundary is not the technology, but the perceived immiscibility of biological and physical study.

5.3 Future work

Where do we go now? Science is a series of rolling questions, typically creating more than it answers. We look to the future with the knowledge and experience of the past, while looking at what sits on the bench in the present.

Moving forward, the objective for photoporation should be towards the transition from physics laboratory to biology laboratory. Be this in the form of commercial or commercial-like products. In this work, a more suitable laser system, with lower peak powers, coupled with a shutter which may operate at a higher speed should improve the outcome of photoporation. As this is for biological work, the samples should be better catered towards, ideally with at least temperature and CO₂ regulation. This would allow the samples to be maintained outside of an incubator for greater periods of time and further minimise the stress on the samples. Applications in cancer research will continue to be exploited where possible, the significant societal impact and funding will drive this forward. *KRAS* is widely studied and will continue to be so, especially while viewed as a major component in pancreatic cancer.

Optical tweezers for confining hollow cylinders remains an interesting prospect, with some potential biological applications, such as cellular isolation and optical tweezing by proxy. The future work here could focus on two central factors. First, the production of consistent micro scale hollow cylinders is key for this research. ULI remains an interesting prospect with the potential for a greater control on the dimensions of the cylinders being produced. Two-photon polymerisation techniques are also growing in use, offering a great range of potential object shapes and structure. Secondly, the adaptation of optical tweezers. There is a host of techniques that allow for controlled

generation of multiple optical tweezers. Incorporating a spatial light modulator based system could provide a broader range of optical trap shapes and configurations, allowing further optimisation in confinement strength to be carried out. The exploitation of such technologies could significantly increase the confinement efficiency of the hollow cylindrical structures.

Nanothermometry is a small but thriving area of research. There are many materials and methods of measuring temperature that have been reported. Moving forward, for biological projects the focus must be on the sensitivity of equipment recording these particles. Significant reduction in the quantity of additional particles, ideally to the point of single particle detection, would minimise toxicity effects. Tracking the emission properties of particles conjugated to antibodies, for surface binding, could present a method of thermal detection in close proximity to the cell, while minimising toxic effect. It would also be interesting to implement a highly sensitive system that could track temperature effects in a photoporation system.

5.4 Closing remarks

Positive, conformational results are always the most desirable outcome. However, science does not always provide the results we expect. Negative results do not typically present in the literature. This in itself does not invalidate the research itself and adds to the field in its own way, introducing more questions and, at the very least, saving researchers from repeating the same mistakes. This work provided a mixture.

Photoporation is routinely limited to the best-available system, while early works presented a range of techniques, increasingly, it has focused in use of Ti:Sapph laser operating at 80 MHz. It was not possible to perform the body of work presented here with such a system. However, it does present two modalities which are now known to be poor sources or such a system. Opportunities to employ alternative biophotonics techniques in approach to transfection are also introduced.

Optical tweezers had not previously been reported as capable of manipulating hollow cylindrical structures. While this generated a degree of initial results, it also highlighted the issue in producing these structures with a high degree of consistency, a must with any applications for which they are required. Rudimentary multiple optical trap generation

with the use of a fixed grating assisted in illustrating some of the issues presented by the optical confinement of the hollow cylindrical structures. The effects of the high energy densities introduced by optical tweezers are also explored.

Heat induced by optical tweezers has been discussed numerous times within the literature. Here, nanoparticles – quantum dots – are employed to act as nano-scale temperature probes. As a technique, there was a significant level of promise, and in this instance, it was possible to see this system advanced by collaborators, during the process of this research. Showing a functional method by which to directly measure changes in temperature, induced by optical tweezers, presenting an optimised recommendation for bio-optimal optical tweezers.

Multidisciplinary research opens novel avenues into research bodies, it is a natural expansion of the collaboration we all seek in research. Biophotonics is no different in this regard and, as a field, it is open to contributions from scientists from practically any field. It presents an exciting opportunity, for those within it, and the potential it holds for advancing the human condition.

Appendix A – Publications

A.1 – Quantum Dot-Based Thermal Spectroscopy and Imaging of Optically Trapped Microspheres and Single Cells

Haro-Gonzalez, P., Ramsay, W. T., Maestro, L. M., Rosal, B., Santacruz-Gomez, K., Cruz, M. C. I., Sanz-Rodriguez, S., Bettinelli, M., Choudhury, D., Kar, A. J., Sole, J. G., Jaque, D. & Paterson, L. “Quantum dot-based thermal spectroscopy and imaging of optically trapped microspheres and single cells” *Small* **9(12)**, 2162-2170 (2013).

DOI: 10.1002/sml.201201740

Quantum Dot-Based Thermal Spectroscopy and Imaging of Optically Trapped Microspheres and Single Cells

Patricia Haro-González, William T. Ramsay, Laura Martinez Maestro, Blanca del Rosal, Karla Santacruz-Gomez, Maria del Carmen Iglesias-de la Cruz, Francisco Sanz-Rodríguez, Jing Yuang Choo, Paloma Rodriguez Sevilla, Marco Bettinelli, Debaditya Choudhury, Ajoy K. Kar, José García Solé, Daniel Jaque, and Lynn Paterson*

Laser-induced thermal effects in optically trapped microspheres and single cells are investigated by quantum dot luminescence thermometry. Thermal spectroscopy has revealed a non-localized temperature distribution around the trap that extends over tens of micrometers, in agreement with previous theoretical models besides identifying water absorption as the most important heating source. The experimental results of thermal loading at a variety of wavelengths reveal that an optimum trapping wavelength exists for biological applications close to 820 nm. This is corroborated by a simultaneous analysis of the spectral dependence of cellular heating and damage in human lymphocytes during optical trapping. This quantum dot luminescence thermometry demonstrates that optical trapping with 820 nm laser radiation produces minimum intracellular heating, well below the cytotoxic level (43 °C), thus, avoiding cell damage.

1. Introduction

Optical traps or optical tweezers are now well established as some of the most versatile tools for microscopic particle manipulation,^[1] with numerous applications over a wide range

of fields, ranging from material studies for the determination of the mechanical properties of bio-polymers^[2] to single cell manipulation.^[3] These non-contact manipulation techniques are also very suitable to move biological cells away from

W. T. Ramsay,^[+] D. Choudhury, Dr. L. Paterson
Scottish Universities Physics Alliance (SUPA)
Institute of Biological Chemistry
Biophysics and Bioengineering
School of Engineering & Physical Sciences
Heriot Watt University
Edinburgh EH14 4AS, Midlothian, Scotland
E-mail: L.Paterson@hw.ac.uk

Prof. A. K. Kar
Scottish Universities Physics Alliance (SUPA)
Institute of Photonic and Quantum Sciences
School of Engineering & Physical Sciences
Heriot Watt University
Edinburgh EH14 4AS, Midlothian, Scotland
Dr. P. Haro-González,^[+] Prof. M. Bettinelli
Laboratorio di Chimica dello Stato Solido
DB, Università di Verona and INSTM
UdR Verona, Ca' Vignal, Strada Le Grazie 15, I-37134 Verona, Italy

DOI: 10.1002/sml.201201740

L. M. Maestro, B. del Rosal
Dr. M. C. Iglesias-de la Cruz, Dr. F. Sanz-Rodríguez
J. Y. Choo, P. R. Sevilla, Prof. J. García Solé,
Dr. D. Jaque
Fluorescence Imaging Group
Departamento de Física de Materiales
C-IV, Universidad Autónoma de Madrid C/Francisco Tomás y Valiente 7,
Madrid, 28049, Spain

K. Santacruz-Gomez
Centro de Investigación en Materiales Avanzados
CIMAV, Departamento de Física
Universidad de Sonora
A.P 1626 Hermosillo, Sonora, México
K. Santacruz-Gomez
Departamento de Física
Universidad de Sonora
Blvd. Luis Encinas y Rosales s/n, C.P. 83000,
Hermosillo, Sonora, México

[+] These authors contributed equally to this work.



interfering substrates in order to acquire low background Raman spectra from biological cells^[4] and to study the interactions between individual cells.^[5] Optical trapping of micrometric objects relies on the use of tightly focused laser beams with high numerical aperture optics so that laser spots with dimensions close to the diffraction limit are achieved. Laser wavelengths are chosen in the near infrared as this is the biological window for optical trapping where absorption of the light by both water and components of the biological specimen is at a minimum.^[5] Typically, to generate the necessary optical forces of tens of pico Newtons, laser powers of the order of few hundreds of milliwatts are required.^[1d] Since typical diffraction limited laser spot sizes in optical trapping experiments are of the order of micrometers, these laser powers lead to laser densities at the optical trap as large as several MW/cm². Even using 'safe' near infrared beams, with such large excitation densities any residual absorption, associated either to the trapped micro object or to the surrounding medium, can lead to non-negligible thermal loadings resulting in temperature increments at the trap position.^[6]

For most applications, the presence of such temperature increments is detrimental to the experiment. In the case of biological applications such as single cell manipulation, moderate temperature increments of less than 5 °C could modify the biochemistry, the molecular dynamics and the function of essential molecular machinery of the living cell.^[7] If the laser induced temperature increments are severe, then the specimen temperature is likely to be driven above the cytotoxic level of 43 °C, promoting apoptosis or necrosis.^[8] Temperature is also a critical parameter when using optical traps for the study of the mechanical properties of micro-systems such as DNA and other macromolecules.^[1d,9] In these cases, temperature increments in the surroundings of the optical trap can affect the mechanical properties of the system under investigation, leading to systematic errors in the determination of the intrinsic elastic properties. Furthermore, laser induced trap heating can also drastically affect the trapping dynamics itself since at moderate and elevated temperatures, radiation pressure is not the only mechanism causing local forces. In these regimes, other forces such as those originating from temperature induced pressure differences could also play a relevant role, leading to the appearance of the so-called photo-thermal trapping.^[6a,6b,6d] Therefore, the exact knowledge of the laser induced temperature increment in optical traps is required in order to establish the optimum working range that ensures minimum thermal damage of living specimens in addition to enabling the correct interpretation of results from experiments involving optical manipulation of micro-objects.

Due to its intrinsic interest, it is possible to find in the literature numerous works dealing with laser induced thermal loading of optical traps. Liu^[6a] and co-workers were pioneers of these studies. They employed micrometer-sized spherical liposome vesicles constituted by phospholipid bilayer membranes labeled with Laurdan that showed a characteristic temperature dependent luminescence. When the vesicles were optically trapped, the analysis of their luminescence was used to determine the trap temperature. They employed a 1.06 µm laser beam focused by a 1.3 NA objective to trap the

luminescent vesicles within a 170 µm thick micro chamber. Under these experimental conditions, the laser induced trap heating was found to be close to 15 °C/W for laser powers up to 300 mW. Quite a different heating rate of 70 °C/W was later reported by Celliers et al.^[6d] by using very similar experimental conditions (170 micrometers thick chamber and 1.25 NA focusing objective) but a quite different trapping wavelength, 985 nm (±10 nm) instead of 1.06 µm. In this case trap temperature was determined by interferometric techniques that take advantage of the temperature induced refractive index change of water. Some years later Peterman et al.^[6b] who analyzed the variation of the frequency of the Brownian motion of an optically trapped microsphere, also found a laser induced heating rate close to 15 °C/W. In this case the trapping wavelength and microscope objective NA were 1.064 µm and 1.3, respectively and the trapped microsphere was in an aqueous solution, located in a chamber with unspecified thickness. They concluded that the 15 °C/W heating rate is mainly due to the residual absorption of the solvent surrounding the microspheres but also slightly influenced by the presence of the trapped microsphere. The laser induced thermal loading at the focus of tightly focused laser beams in liquids has been also studied with the purpose of achieving temperature control in dual beam optical tweezers. Mao et al.^[6c] found that a tightly focused 975 nm laser beam causes an on-focus thermal loading close to 60 °C/W as obtained from the study of laser induced modifications in the medium viscosity. Finally, Ramser et al.^[10] concluded, from the analysis of Raman spectra of optically trapped cells, that when the laser trapping wavelength lies within the 488–568 nm spectral range, where water absorption is below 0.1 cm⁻¹, the laser induced heating rate is further reduced. The large discrepancies between the already reported laser induced heating rates, obtained under different experimental conditions, can be understood by recalling the simple model proposed by Mao et al.^[6c] They state that the laser induced heating in an optical trap (ΔT_{trap}) depends on the absorption coefficient of liquid medium at the laser wavelength ($\alpha_{abs}(\lambda_{trap})$), the laser power (P_l), the chamber thickness (D), the thermal diffusivity of the liquid medium (K) and the laser spot radius (W_l):

$$\Delta T_{trap} = \frac{\alpha_{abs}(\lambda_{trap}) \cdot P_l}{2 \cdot \pi \cdot K} \cdot \ln \left[\frac{D}{W_l} \right] \quad (1)$$

For a fixed focusing objective, the laser spot radius is given by $W_l = \frac{0.6 \cdot \lambda_{trap}}{NA}$ where NA is the numerical aperture of the focusing objective. Thus, according to expression (1) the heating rate of an optical trap, β_{trap} , defined by the temperature increment divided by the laser power, i.e. $\beta_{trap} = \frac{\Delta T_{trap}}{P_l}$, can be written as:

$$\beta_{trap} = \frac{\Delta T_{trap}}{P_l} = \frac{\alpha_{abs}(\lambda_{trap})}{2 \cdot \pi \cdot K} \cdot \ln \left[\frac{D \cdot NA}{0.6 \cdot \lambda_{trap}} \right] \quad (2)$$

From expression (2) it is clear that one of the most relevant parameters determining the thermal loading of optical traps is the laser wavelength. Thus, an appropriate choice of λ_{trap} would minimize the laser-induced thermal loading effects.

For the particular case of optical manipulation of living cells, the wavelengths that result in minimum thermal loading of the aqueous environment would not necessarily be the optimum trapping wavelengths, since other processes such as photochemical reactions could also play a role.^[11] In these cases, it is necessary to take into account scattering and, importantly, to avoid damage to the specimen. Therefore, the optimum trapping wavelength should simultaneously provide a minimum thermal loading of the environment that surrounds the cell whilst preserving cell viability. To determine an optimum trapping wavelength, both the heating spectrum and the photo-damage spectrum of the particular cell type to be trapped, need to be known very accurately.

It is important to note that, due to the thermal diffusivity of the medium, the laser-induced temperature increment induced in the optical trap is not only restricted to the laser focus but it spreads out leading to the creation of a Heat Affected Zone (HAZ) in the surroundings of the trap.^[12] The extension and magnitude of this HAZ could play a major role in numerous applications of Optical Traps where the trapped particle is used to manipulate a system located in the proximities of the laser focus e.g. an *in vitro* model of a micro-environment consisting of many different closely packed cell types, extracellular matrix molecules and secreted molecules in the growth media. Previous models concluded that the temperature in the surroundings of the trap follows a logarithmic decay with the distance r to the laser focus; i.e. $\Delta T(r) = A - B \cdot \ln(r)$.^[6c] Indeed, even for optical trapping experiments involving tightly focused laser beams (spot sizes below 1 μm) HAZs extending for hundreds of micrometers have been postulated.^[6d]

In this work we systematically investigated the laser induced thermal loading of optically trapped micrometric polymer beads by using quantum dot luminescence thermometry (QDLT). QDLT is based on the temperature induced spectral shift of the characteristic luminescence band of QDs.^[13] This temperature induced spectral shift follows a linear relation with temperature so that it can be used as a temperature indicator providing a constant thermal sensitivity over a wide temperature range.^[14] QDs are dispersed into an aqueous solution containing micrometer-sized polymer microsphere. A double-beam fluorescence confocal microscope allows for simultaneous trapping of a polymer microsphere and thermal sensing and imaging through the detection and analysis of the QD luminescence at the laser focus and surroundings. Laser-induced thermal loading of polymer microsphere optically trapped by using five different wavelengths has been investigated. Results are compared to previous models^[6c] and the relative weight of the different contributions to the total thermal loading is discussed.

Secondly, the incorporation of QDs in living cells (human lymphocytes) via endocytosis has provided a non-invasive way for intracellular thermal sensing during single cell optical manipulation. The spectral dependence of the intracellular temperature increment during single cell optical manipulation and its effects on cell health has been investigated. Results have been used to elucidate the existence of an optimum trapping wavelength simultaneously leading to a minimum thermal loading and laser damage in optically trapped single cells.

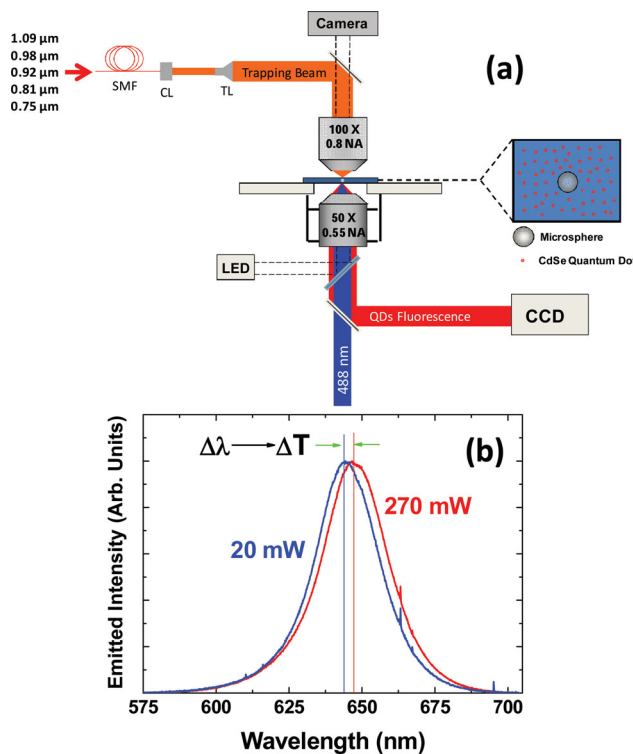


Figure 1. (a) Schematic diagram of the experimental set-up, double beam confocal microscope, used for thermal sensing and imaging of optical traps. (b) Emission spectra of CdSe-QDs as obtained from the trap position for two different trapping powers (20 and 270 mW). Trapping wavelength was 980 nm. Note the clear spectral red-shift caused by the laser-induced trap heating. From this spectral shift the trap temperature was calculated.

2. Results and Discussion

2.1. Thermal Spectroscopy of Optically Trapped Microspheres

Figure 1(a) schematically shows the double beam fluorescence microscope used in this work. The upper section of the microscope allows for multi-wavelength trapping of 3 μm diameter polymer microspheres (polystyrene spheres, Cat. no. 17134, Polysciences, Eppenheim, Germany). The bottom section provides thermal sensing at the optical trap by spectrally analyzing the fluorescence generated by CdSe-QDs (Cat. no. Q21721MP, Invitrogen Inc.) that have been suspended in the aqueous solution containing the optically trapped microspheres (**Figure 2(a)**). A Transmission Electron Microscope (TEM) image of the CdSe-QDs used in this work is shown in **Figure 2(b)**. The CdSe-QDs have been found to be, on average, 14 nm in length and 6 nm wide with a dispersion of 2.4 and 0.6 nm, respectively (see the size histograms in **Figure 2(d),(e)**). The random distribution of CdSe-QDs around the microspheres is evidenced. The mixed solution containing both CdSe-QDs and microspheres (**Figure 2(c)**) showed a very stable colloidal behavior with no evidence of precipitation over several months. We use CdSe-QDs for nano-thermometry as they have been recently proposed^[14,15] as reliable thermal probes based on the characteristic temperature-induced red shift of its luminescence band. The

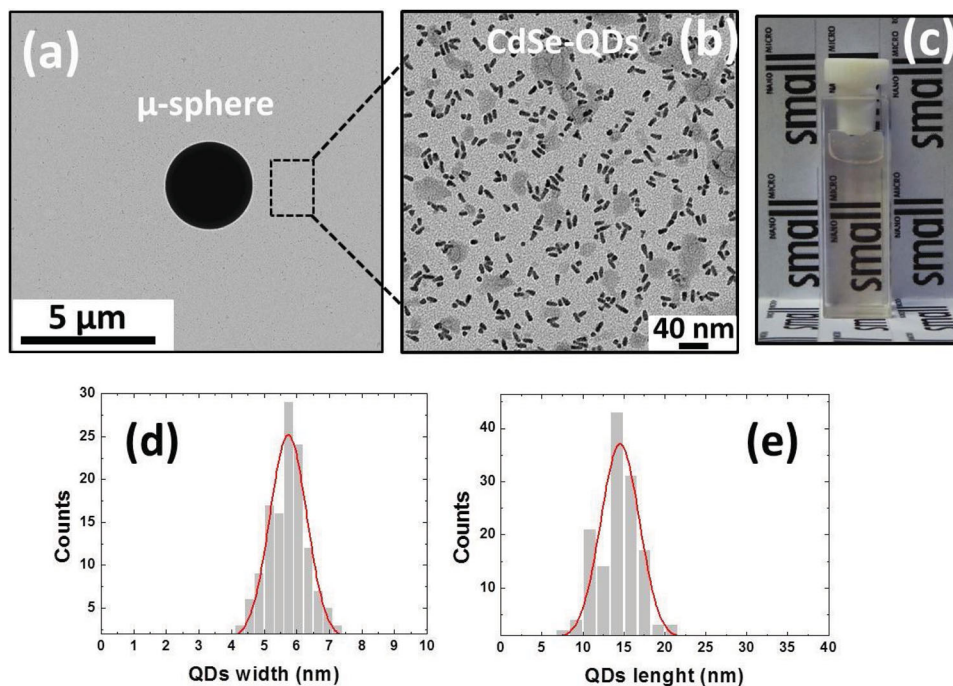


Figure 2. (a) Low magnification transmission electron micrograph of a single polymer microsphere. (b) High-magnification transmission electron micrograph as obtained from the surroundings of a polymer microsphere. (c) Optical image of the mixed aqueous solution containing polymer microspheres and CdSe quantum dots. (d,e) Size distribution of the CdSe-QDs.

QD emission peak wavelength shifts linearly towards longer wavelengths with temperature at a rate of 0.1 nm/K. Thus, from the determination of luminescence peak, it is possible to acquire an accurate thermal reading. Figure 1(b) illustrates the working principle of QD thermometry. It shows two typical fluorescence spectra as obtained when the CdSe-QD excitation beam was focused at the optical trap. In this case the trapping wavelength was 980 nm. The spectrum in blue was obtained when the minimum laser power of 20 mW was used to trap the microsphere. On the other hand, the spectrum in red was obtained when the trapping power was set to 270 mW. From the comparison of both spectra it is clear that the increment in the trapping laser power caused a noticeable spectral red-shift in the CdSe-QD luminescence. This confirms a remarkable localized heating at the focus of the optical

trap. From the observed spectral shift of 2.3 nm the temperature increment induced by laser radiation in the optical trap can be estimated to be 23 °C.^[13a,16] At this point it should be noted that, since one photon absorption of CdSe-QDs in the 700–1100 nm range is negligible and the 488 nm laser power used for CdSe-QD excitation is kept below 3 mW, the contribution of CdSe-QDs to the overall trap heating must be neglected. Therefore, the CdSe-QDs behave as non-heating nano-thermometers.

Figure 3(a) shows the laser-induced temperature increments at trap position as a function of the trapping power obtained for five different trapping wavelengths within the 700–1100 nm range. Linear temperature dependence is obtained for all five trapping wavelengths under study. This is, indeed, in agreement with expression (1) and unequivocally indicates

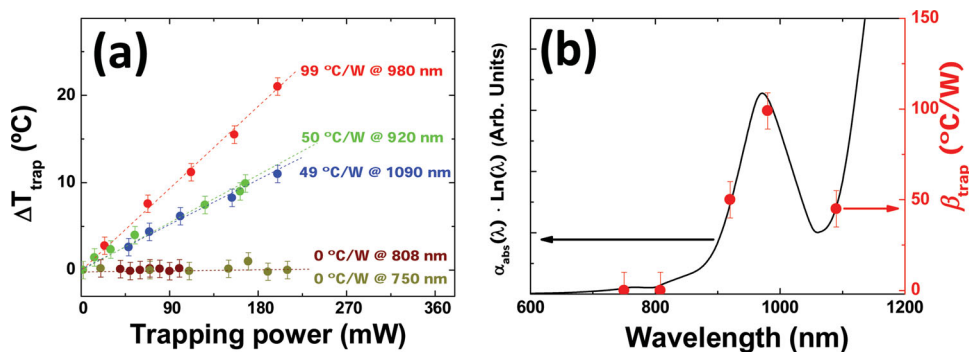


Figure 3. (a) Laser-induced temperature increment at the laser trap as a function of the trapping power for all the trapping wavelengths used in this work. Solid dots are experimental data and dashed lines are the best linear fits. The heating rates obtained from these fits are included. (b) Heating rates (β_{trap}) obtained from (a) as a function of the trapping wavelength (dots). Solid line represents the wavelength dependence of the heating rate predicted by the model of Mao et al.^[6c] (that is given by the wavelength dependence of the $\alpha_{\text{abs}}(\lambda_{\text{trap}}) \cdot \ln[\lambda_{\text{trap}}]$ term).

that the effect of other processes (such a bubble formation or creation of convection curves) can be neglected, at least for the trapping powers used in this work. From Figure 3(a) it is also evident that the heating rate of the optical trap, β_{trap} , is strongly dependent on the particular trapping wavelength. Note that the maximum heating of 99 °C/W was achieved when a trapping wavelength of 980 nm was used and vanished when trapping wavelengths were set to 808 nm and 750 nm. According to expression (2) the heating rate should vary with the trapping wavelength following the $\alpha_{\text{abs}}(\lambda_{\text{trap}}) \cdot \ln[\lambda_{\text{trap}}]$ trend, where $\alpha_{\text{abs}}(\lambda_{\text{trap}})$ refers to the absorption coefficient at trap wavelength of the liquid medium (water in our case). Figure 3(b) includes the β_{trap} values obtained from the experimental data of Figure 3(a) alongside the wavelength dependence of the $\alpha_{\text{abs}}(\lambda_{\text{trap}}) \cdot \ln[\lambda_{\text{trap}}]$ term (calculated by using the wavelength dependence of water absorption coefficient reported by Palmer *et al.*).^[17] Thus, a good agreement is observed between experimental data and the model proposed by Mao *et al.*^[6c] Indeed, the experimentally obtained β_{trap} values have been found to follow the wavelength dependence of the water absorption coefficient, dominant term in the $\alpha_{\text{abs}}(\lambda_{\text{trap}}) \cdot \ln[\lambda_{\text{trap}}]$ product, peaking at 980 nm where water absorption has a maximum. This is also in agreement with Peterman *et al.*^[6b] who concluded that thermal loading of laser traps was mainly caused by the solvent absorption.

The magnitude and extension of the heat affected zone (HAZ) has been investigated in order to understand how neighbouring, untrapped particles may be affected. Figure 4(a) shows the spatial variation of temperature in the surroundings of an optical trap. For the acquisition of this thermal image the bottom microscope objective used for excitation and collection of the CdSeQD luminescence (see Figure 1(a)) was mounted onto an XY piezoelectric stage (PI Hera, Physik Instrumente Inc) so that the CdSe-QD excitation spot could be scanned in the surroundings of the optical trap. In this case the polymer microsphere was optically trapped with a 400 mW, 1090 nm laser beam that was tightly focused by the top microscope objective (50× long working distance, 0.5 NA objective) into a 200 µm thick microchannel (Ibidi Inc). The

thermal image denotes a relevant temperature increment at the position of the optically trapped polymer microsphere. It is important to note here that, although a maximum temperature increment is produced at the trap's position, it is clear that heating is spread over tens of micrometers. From the thermal image of Figure 4(a) we have estimated the HAZ extension, here defined as the distance at which temperature increment is half that induced at the trap's position, to be close to 40 µm. Thus, although the laser beam is focused down to a spot size below 2 µm, heat diffusion through the medium spreads the laser-induced thermal loading over several tens of micrometers. According to previously proposed models,^[5c] the temperature increment produced by a tightly focused laser beam at a distance r with respect to laser focus, $\Delta T(r)$, can be written as:

$$\Delta T(r) = A - B \cdot \ln(r) \quad (3)$$

where A and B are constants that depend on a variety of factors such as chamber geometry, thermal diffusivity of the medium, laser spot size amongst others. In order to verify the consistency of our thermal image with previous models, Figure 4(b) shows a thermal profile (temperature versus distance from the trap) obtained along the dashed line included in Figure 4(a). It is evidenced that, for distances larger than laser spot size (i.e. for $r \gg w_i$) temperature decreases linearly with respect to $\ln(r)$, in agreement with expression (3).

2.2. Quantum Dot-Based Thermometry in Optically Trapped Living Cells

Results described in Section 2.1 are not only important for the elucidation of the heating mechanism in optical traps but are also of critical relevance for the optimization of single-cell manipulation experiments. When a living cell is illuminated by a tightly focused laser beam photochemical and/or photo-thermal process may take place due the absorption, rather than transmission or scattering of photons by the cell, leading to irreversible damage (necrosis, apoptosis or a loss of genetic integrity).^[18]

Photochemical damage is traditionally associated with laser-induced intracellular generation of free radicals, which can give rise to oxidative damage. Several studies have investigated the wavelength dependence of laser-induced photochemical damage in living cells. Liang *et al.*^[19] investigated how laser irradiation with different wavelengths modified the cell cloning efficiency of Chinese Hamster Ovary (CHO) cells. Based on their results, the photochemical damage spectrum that is shown in Figure 5 was proposed, revealing minimum photochemical damage for laser wavelengths close to 820 or 980 nm. The presence of such 'damage minima' was later confirmed by different studies on a great variety of living systems such as

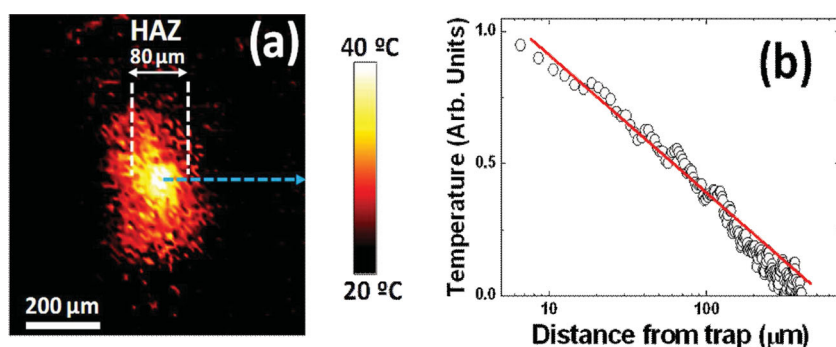


Figure 4. (a) Temperature distribution in the surroundings of an optically trapped polymer microsphere. The trapping conditions were 400 mW of laser power at 1.09 µm. Laser beam was focused down to a 1.3 µm spot. Vertical dashed lines represent the HAZ limits, where temperature increment is half that achieved at trap's position. (b) Temperature profile obtained along the horizontal scan line indicated by the dashed arrow in (a). Dots are the experimental data and solid line is a guide for the eyes to indicate the linear relation between temperature and the logarithm of distance.

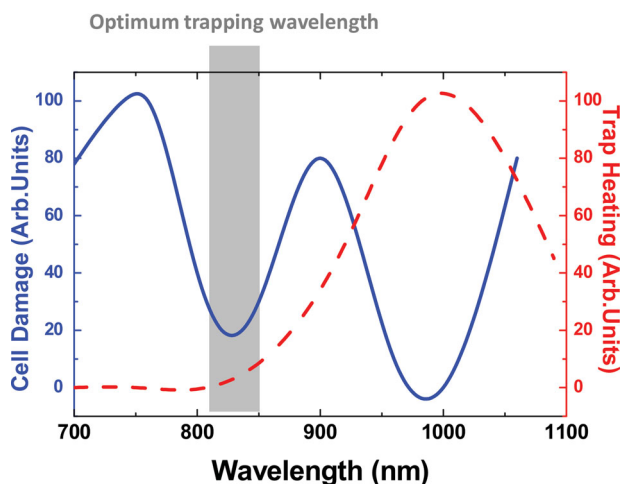


Figure 5. Solid line represents the wavelength dependence of the laser-induced cell damage as obtained from the analysis of the cloning efficiency of Chinese Hamster Ovary cells after optical trapping.^[19] Dashed line is the wavelength dependence of the laser-induced thermal loading of an optical trap assumed to be given by the absorption spectrum of water. The possible existence of an optimum spectral range for optical trapping of single cells is schematically indicated.

E. coli bacteria, *C. elegans* and mitotic rat kangaroo (PtK2) cells.^[11c,11d,11h] Thus, in a first order approximation, the photochemical damage spectrum proposed initially by Liang et al.^[19] for CHO cells can be assumed as universal. Photothermal damage takes place when, due to absorption, laser induced thermal loading drives the intracellular temperature up to the cytotoxic level ($>43^{\circ}\text{C}$).^[20] At such temperatures irreversible protein denaturation takes place and the cell will die either by programmed cell death or immediately, due to trauma. If we reasonably assume that both the surrounding medium and the cell itself are primarily composed of water, the universal solvent for biological cells and extracellular liquid, then the spectrum of the laser-induced photothermal damage would be given by water absorption whose spectrum is also included in Figure 5.

From the inspection of Figure 5 it is clear that simultaneous minimization of photochemical and photothermal damage is expected to occur for trapping wavelengths around 820 nm. Our next study compares the effect of optical trapping at 820 nm and at 980 nm on mammalian cells by monitoring both cell damage to optically trapped lymphocytes and the intracellular temperature increase within individual, trapped cells. CdSe-QDs were incubated with human lymphocytes and upon internalization by the cell acted as intracellular fluorescent nano-thermometers. Optical trapping of single lymphocytes containing CdSe-QDs was achieved with the same

experimental set-up as that used for microsphere trapping (Figure 1). Single lymphocyte optical trapping is evidenced in Figure 6(a), which shows a series of optical images of lymphocytes in suspension, with the central lymphocyte optically trapped and the surrounding lymphocytes being translated in the XY plane (perpendicular to the beam propagation axis). Trapping forces were found to be independent of laser wavelength and estimated to be close to 70 pN, for the maximum laser powers used in this study (≈ 300 mW). From the spectral analysis of the CdSe-QDs' luminescence we were able to monitor, in real time, the intracellular temperature of optically trapped lymphocytes. Figure 6(b) shows the measured intracellular temperature increment as a function of the laser trapping power for both 820 and 980 nm laser wavelengths. The intracellular heating rates were found to be 3 and $60^{\circ}\text{C}/\text{W}$ for 820 and 980 nm, respectively. Thus, intracellular QDLT revealed that tuning the trapping wavelength from 980 nm to 820 nm has led to a 20 fold intracellular thermal loading reduction. Indeed, this ratio is in good agreement with that estimated from Figure 3 which considers water absorption as the only heating source. Therefore, it supports our assumption that optical absorption of trapped cells and surroundings is mainly due to water and validates the photothermal damage spectrum proposed in Figure 5. According to Figure 5, this remarkable difference in the laser induced thermal loading between 820 nm and 980 nm is achieved while the two wavelengths produce similar low levels of photochemical damage, manifested in the better ability of irradiated cells to form colonies.^[11b,f] Therefore, in a first order approximation, if differential cell damage is observed during 820 and 980 nm optical trapping this should be related to photothermal damage.

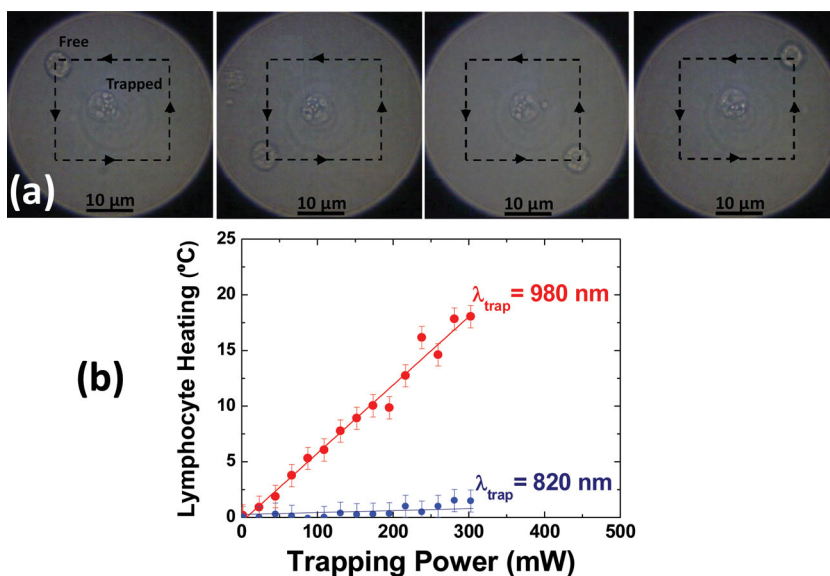


Figure 6. (a) A series of optical transmission images of a solution containing human lymphocytes in the presence of a tightly focused 980 nm laser beam that optically traps a single lymphocyte. Non-trapped (free) lymphocytes can be translated by applying different fluxes (indicated by arrows and dashed lines). (b) Intracellular temperature increment produced in the trapped lymphocyte as a function of the trapping laser power as obtained for two different trapping wavelengths (820 and 980 nm). Dots are experimental data and lines are best linear fits.

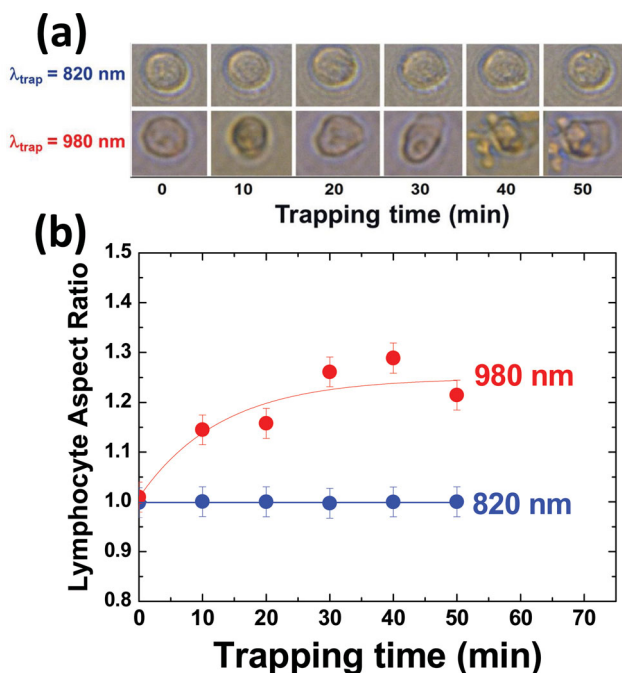


Figure 7. (a) Optical transmission images of a single trapped lymphocyte as obtained for different trapping durations. Results obtained for 980 and 820 nm laser trapping wavelengths are included. (b) Time evolution of lymphocyte's aspect ratio during 820 and 980 nm optical trapping. Dots are experimental data and solid lines are guides for the eyes.

Some forms of cell damage (membrane rupture, lysis, blebbing) can be monitored under the microscope in real time by analyzing the cellular morphology.^[11f,21] In the particular case of spherically shaped human lymphocytes a convenient assay is to measure the change in a cell's circularity. This can be numerically evaluated as an increase in their aspect ratio and used as an indicator of cell viability. **Figure 7** (a) shows a series of optical transmission images of human lymphocytes being trapped by 820 and 980 nm laser beams. Optical images were all obtained for the same laser trapping power (300 mW) and correspond to different trapping durations. From the analysis of these optical images the time evolution of lymphocyte aspect ratio was evaluated. Results are included in Figure 7(b). While for 820 nm trapping, the aspect ratio remains unchanged, for 980 nm trapping the lymphocyte aspect ratio has increased by almost 20% after 50 minutes. This remarkable cell deformation, due in part to blebbing and membrane leakage, unequivocally reveals the presence of relevant cell damage. According to our previous arguments, this damage has a photothermal origin. Indeed, intracellular QDLT of optically trapped lymphocytes revealed that 980 nm trapping wavelength causes intracellular temperature increments close to 20 °C (see Figure 6(b)). Experiments were conducted at 22 ± 1 °C (room temperature), therefore during 980 nm trapping the intracellular temperature would be close to 42 °C, i.e. close to the cytotoxic level. In contrast, for 820 nm trapping no cell damage, as measured by change in aspect ratio, was observed. We attribute this to the postulated absence of photochemical damage in addition to weak laser induced cell

heating; less than 4 °C, according to results provided by QD based intracellular thermometry (see Figure 6(b)).

This minimal heating keeps the lymphocyte well below the cytotoxic level, ensuring minimum cell damage.

3. Conclusion

In summary, laser induced thermal effects in optically traps containing single trapped microspheres and living cells have been studied by quantum dot luminescence thermometry. The influence of the trapping wavelength on the trap temperature has been systematically investigated. It has been found that the thermal loading of the trap follows the absorption spectrum of the medium which is water. Maximum heating has been found for a trapping wavelength of 980 nm. In contrast, negligible heating was found when the trapping wavelength is below 800 nm where water absorption vanishes. The thermal image of an optical trap has also been reported, from which the extension of the Heat Affected Zone has been estimated. It has been found that, although maximum heating is produced at the trap position, heat spreads out several tens of micrometers due to the medium diffusivity. Both the wavelength dependence and spatial extension of laser induced thermal loading in optical traps have been found to be in excellent agreement with previously proposed theoretical models.

When the wavelength dependence of thermal loading in optical traps is combined with the photochemical damage spectrum of living cells, it is concluded that an optimum trapping wavelength (820 nm) should exist for biological applications. This fact has been experimentally corroborated from the experimental evaluation of the laser damage induced in optically trapped human lymphocytes. Results have shown that when the optical trapping wavelength is set to 820 nm, intracellular heating is minimum, keeping the lymphocyte temperature well below the cytotoxic level and avoiding laser-induced damage. This is at variance with the results obtained during 980 nm optical trapping that show relevant cell damage during optical trapping due to the laser-induced cell heating up to the cytotoxic level.

Results included in this work reveal CdSe-QDs as versatile, efficient and accurate nano-thermometers for real time temperature monitoring of the local environment surrounding optically trapped micro-sized objects and single living cells.

4. Experimental Section

Materials: The polymer microspheres used in this work were provided by Polysciences Inc. They were monodisperse, uniform polystyrene microspheres 3 μm in diameter with a nominal diameter of 3 μm (at. no. 17134, Polysciences, Eppenheim, Germany). Figure 2(a) shows a TEM image of a single microsphere. They were dispersed in distilled water with a concentration as low as 0.02 $\mu\text{g/mL}$. The use of such low concentration was required to avoid multi-particle trapping when using high trapping powers. For the purpose of thermal sensing, CdSe-QDs (Cat. no. Q21721MP,

Invitrogen Inc) were added to the solution resulting in a final QD concentration as low as $1 \times 10^9 \text{ cm}^{-3}$. CdSe-QDs were randomly distributed around the microspheres, as can be observed in Figure 2(b). The CdSe-QDs used in this work were 14 nm length and 6 nm width as seen in Figure 2(d),(e), leading to a broadband luminescence centered at around 655 nm. The luminescence peak wavelength shifts linearly towards longer wavelengths with temperature at a rate of 0.1 nm/K. The aqueous solution containing both the CdSe-QDs and polymer microspheres, shown in Figure 2(c), displayed a very stable colloidal behavior without any evidence of precipitation over several months.

On-Focus Thermal Sensing during Optical Trapping: The aqueous solution containing both the CdSe-QDs and polymer microsphere was placed within a 130 μm thick micro chamber constituted by two microscope slides separated by a thin vinyl sticker making a circular well of 4 mm in diameter. The micro-chamber was placed in a double beam microscope as is schematically shown in Figure 1. Four different laser sources were used for optical trapping. Two single-mode fiber coupled diode lasers working at 980 and 808 nm, a 1090 nm Ytterbium doped fiber laser coupled to a single mode fiber and a Ti:Sapphire laser also coupled to a single mode fiber and operating at 920 and 750 nm. The laser radiation coming out from the corresponding single-mode fiber (SMF) was collimated by a fiber-port (Thorlabs PAF-X-7-B, CL in Figure 1(a)). The collimated beam was expanded by using a 2X beam expander (Thorlabs BE02M, TL in Figure 1(a)) resulting in a 2 mm beam diameter. This matches the back aperture of the 100X long working distance microscope objective of 0.8 NA that was used to focus the trapping beam into micro-chamber. Microsphere trapping was evident when the trapping laser power exceeded 20 mW, for all the trapping wavelengths used in this work. CdSe-QD luminescence excitation was provided by a 488 nm air cooled Argon laser counter propagating to the trapping beam. The 488 nm radiation was focused into the micro-chamber with a second microscope objective (50X, 0.55 NA). This second objective was perfectly aligned with respect to the trapping wavelength so that both the trapping and 488 nm spots were spatially overlapping. The 488 nm laser power reaching the micro-chamber was below 3 mW so that the thermal effects associated with this radiation could be neglected. The fluorescence generated by the CdSe-QDs was collected by the same objective used for 488 nm laser focusing. After passing through different filters and apertures this luminescence was spectrally analyzed by a high resolution spectrometer. For imaging purposes, the micro-chamber was illuminated by a white-light source (LED in Figure 1(a)) that was focused by the 50X microscope objective. The transmitted white light was collected by the 100X microscope objective and formed and image onto a CCD camera. Several filters were used to block both trapping and 488 nm radiation so that the trapped microsphere was monitored continuously. We have performed several thermal sensing and imaging experiments of optical traps by using different QD concentrations in the mixed solution. We found no changes at all in the final heating curves obtained. Nevertheless, it should be pointed out that when the QD concentration was set to be below 10^8 cm^{-3} , the QD luminescence spectrum was very weak and the consequent noise prevented an accurate determination of the peak wavelength and, hence, of the temperature. Otherwise, when using QD concentrations in the 10^8 – 10^{10} cm^{-3} range, the heating rates and images of optical traps were found to be independent on the QD concentration.

Thermal Imaging of an Optical Trap: The experimental set-up depicted in Figure 1(a) was slightly modified. The 50X microscope objective used for excitation/collection of the CdSe-QD luminescence was mounted onto a 1 nm resolution XY motorized stage (PI Hera. Physik Instrumente Inc). This motorized stage allowed us to scan the 488 nm excitation spot in the surroundings of the optical trap. From the spectral analysis of the point-by-point emission spectra we were able to determine the 2D temperature distribution in the surroundings of the optical trap. Optical trapping experiments were conducted room temperature (22 °C).

Lymphocyte Preparation: For single-cell optical trapping experiments we used Jurkat cells (clone E6.1), a commercially available human T lymphocyte cell line from the American Type Culture Collection (ATCC), kindly provided by Drs V. Calvo and M. Izquierdo. Freshly cultured suspensions of these cells were maintained in RPMI 1640 medium supplemented with 10% fetal calf serum (FCS), 1% (v/v) penicillin/streptomycin (10 000 IU/mL/10 000 g/mL), and 2 mM L-glutamine (complete medium) in an incubator with humidified 95% air, 5% CO₂ atmosphere at 37 °C. All reagents were purchased from Fisher Scientific (Massachusetts, USA). For experiments, an aliquot of 100 μL of fresh, exponentially growing lymphocytes (cell density of $1 \times 10^6 \text{ cells/mL}$) were taken and subsequently diluted 1/5 with complete medium. Immediately afterwards 50 μL of this diluted suspension was placed on a microscopy chamber (Ibidi, Germany).

Acknowledgements

This work was supported by the Universidad Autónoma de Madrid and Comunidad Autónoma de Madrid (Project S2009/MAT-1756), by the Spanish Ministerio de Educacion y Ciencia (MAT2010-16161 and MAT2010-21270-C04-02), Malta Consolider-Ingenio 2010 (CSD2007-0045), by the Caja Madrid Foundation and by Fondazione Cariverona, project Verona Nanomedicine Initiative and by fundacion Dr. Manuel Morales and Banco Santander and CEAL-UAM through the UAM-NUS cooperation project. We thank Drs Victor Calvo and Manuel Izquierdo, from the Biochemistry Department (UAM) for kindly provide us with the Jurkat cell line. WTR is supported by UK Engineering and Physical Sciences Research Council (EPSRC) and DC is supported by Heriot Watt University Life Science Interface Theme Scholarship. Authors thank Antonio Benayas for helpful discussion and experimental help.

- [1] a) A. Ashkin, J. M. Dziedzic, T. Yamane, *Nature* **1987**, 330, 769; b) A. Ashkin, J. M. Dziedzic, *Science* **1987**, 235, 1517; c) K. Svoboda, S. M. Block, *Annu. Rev. Biophys. Biomol. Struct.* **1994**, 23, 247; d) S. Hormeno, J. R. Arias-Gonzalez, *Biol. Cell.* **2006**, 98, 679; e) D. J. Stevenson, F. Gunn-Moore, K. Dholakia, *J. Biomed. Opt.* **2010**, 15, 041503; f) M. Gu, J.-B. Haumonte, Y. Micaeu, J. W. M. Chon, X. Gan, *Appl. Phys. Lett.* **2004**, 84, 4236.
- [2] a) K. Wang, E. Schonbrun, P. Steinvurzel, K. B. Crozier, *Nat. Commun.* **2011**, 2; b) W. H. Wright, G. J. Sonek, M. W. Berns, *Appl. Opt.* **1994**, 33, 1735; c) H. Maruyama, T. Fukuda, F. Arai, *Microfluidics Nanofluidics* **2009**, 6, 383.
- [3] a) R. D. Snook, T. J. Harvey, E. Correia Faria, P. Gardner, *Integr. Biol.* **2009**, 1, 43; b) Y. Wu, K. Liu, K. Song, S. Pan, *Appl. Biochem.*

- Biotechnol.* **2011**, *165*, 485; c) K. Ramser, W. Wenseleers, S. Dewilde, S. Van Doorslaer, L. Moens, *Spectrosc.-Int. J.* **2008**, *22*, 287; d) A. Bankapur, E. Zachariah, S. Chidangil, M. Valiathan, D. Mathur, *PLoS One* **2010**, *5*, e10427.
- [4] C. Xie, J. Mace, M. A. Dinno, Y. Q. Li, W. Tang, R. J. Newton, P. J. Gemperline, *Anal. Chem.* **2005**, *77*, 4390.
- [5] K. Dholakia, P. Reece, M. Gu, *Chem. Soc. Rev.* **2008**, *37*, 42.
- [6] a) Y. Liu, D. K. Cheng, G. J. Sonek, M. W. Berns, C. F. Chapman, B. J. Tromberg, *Biophys. J.* **1995**, *68*, 2137; b) E. J. Peterman, F. Gittes, C. F. Schmidt, *Biophys. J.* **2003**, *84*, 1308; c) H. Mao, J. R. Arias-Gonzalez, S. B. Smith, I. Tinoco, Jr., C. Bustamante, *Biophys. J.* **2005**, *89*, 1308; d) P. M. Celliers, J. Conia, *Appl. Opt.* **2000**, *39*, 3396.
- [7] a) F. Wetzel, S. Ronicke, K. Muller, M. Gyger, D. Rose, M. Zink, J. Kas, *Eur. Biophys. J.* **2011**, *40*, 1109; b) J. J. Foo, K. K. Liu, V. Chan, *Ann. Biomed. Eng.* **2003**, *31*, 354.
- [8] a) W. Fiers, R. Beyaert, W. Declercq, P. Vandenabeele, *Oncogene* **1999**, *18*, 7719; b) G. Majno, I. Joris, *Am. J. Pathol.* **1995**, *146*, 3.
- [9] M. Righini, P. Ghenuche, S. Cherukulappurath, V. Myroshnychenko, F. J. Garcia de Abajo, R. Quidant, *Nano Lett.* **2009**, *9*, 3387.
- [10] K. Ramser, K. Logg, M. Goksoy, J. Enger, M. Kall, D. Hanstorp, *J. Biomed. Opt.* **2004**, *9*, 593.
- [11] a) S. P. Gross, *Methods Enzymol.* **2003**, *361*, 162; b) H. Liang, K. T. Vu, P. Krishnan, T. C. Trang, D. Shin, S. Kimel, M. W. Berns, *Biophys. J.* **1996**, *70*, 1529; c) K. C. Neuman, E. H. Chadd, G. F. Liou, K. Bergman, S. M. Block, *Biophys. J.* **1999**, *77*, 2856; d) G. Leitz, E. Fallman, S. Tuck, O. Axner, *Biophys. J.* **2002**, *82*, 2224; e) Y. J. Pang, R. Gordon, *Nano Lett.* **2012**, *12*, 402; f) H. Liang, K. T. Vu, T. C. Trang, D. Shin, Y. E. Lee, D. C. Nguyen, B. Tromberg, M. W. Berns, *Lasers Surgery Med.* **1997**, *21*, 159; g) M. E. Fallat, Y. Siow, A. M. Belker, J. K. Boyd, S. Yoffe, D. T. MacLaughlin, *Human Reproduction* **1996**, *11*, 2165; h) I. A. Vorobjev, L. Hong, W. H. Wright, M. W. Berns, *Biophys. J.* **1993**, *64*, 533.
- [12] I. Krasnikov, A. Seteikin, I. Bernhardt, *J. Biophotonics* **2011**, *4*, 206.
- [13] a) D. Jaque, F. Vetrone, *Nanoscale* **2012**, *4*, 4301; b) C. D. S. Brites, P. P. Lima, N. J. O. Silva, A. Millan, V. S. Amaral, F. Palacio, L. D. Carlos, *Nanoscale* **2012**, *4*, 4799; c) C. D. S. Brites, P. P. Lima, N. J. O. Silva, A. Millan, V. S. Amaral, F. Palacio, L. D. Carlos, *New J. Chem.* **2011**, *35*, 1177.
- [14] L. M. Maestro, C. Jacinto, U. R. Silva, F. Vetrone, J. A. Capobianco, D. Jaque, J. G. Sole, *Small* **2011**, *7*, 1774.
- [15] D. Choudhury, D. Jaque, A. Rodenas, W. T. Ramsay, L. Paterson, A. K. Kar, *Lab Chip* **2012**, *12*, 2414.
- [16] L. M. Maestro, E. M. Rodriguez, F. S. Rodriguez, M. C. I. la Cruz, A. Juarranz, R. Naccache, F. Vetrone, D. Jaque, J. A. Capobianco, J. G. Sole, *Nano Lett.* **2010**, *10*, 5109.
- [17] K. F. Palmer, *J. Opt. Soc. Am.* **1973**, *63*, 475.
- [18] R. S. Hotchkiss, A. Strasser, J. E. McDunn, P. E. Swanson, *New Engl. J. Med.* **2009**, *361*, 1570.
- [19] Y. G. Liu, G. J. Sonek, C. F. Chapman, B. J. Tromberg, P. Patrizio, Y. Tadir, M. W. Berns, *P. Soc. Photo-Opt. Ins.* **1995**, *2391*, 484.
- [20] V. K. Singh, S. Biswas, C. M. Pandey, S. S. Agarwal, *Pathobiology* **1996**, *64*, 150.
- [21] a) K. J. Chalut, K. Kulangara, M. G. Giacomelli, A. Wax, K. W. Leong, *Soft Matter* **2010**, *6*, 1675; b) S. Y. Chen, M. Z. Zhao, G. Wu, C. Y. Yao, J. W. Zhang, *Comput. Math Method Med.* **2012**, *2012*, 101536; c) B. D. Chithrani, A. A. Ghazani, W. C. W. Chan, *Nano Lett.* **2006**, *6*, 662.

Received: July 23, 2012
 Revised: November 15, 2012
 Published online:

A.2 – Quantum dot enabled thermal imaging of optofluidic devices

Choudhury, D., Jaque, D., Rodenas, A., Ramsay, W. T., Paterson, L. & Kar, A. J.
“Quantum dot enabled thermal imaging of optofluidic devices” *Lab Chip* **12(13)**, 2414-2420 (2012).

DOI: 10.1039/C2LC40181A

Quantum dot enabled thermal imaging of optofluidic devices

Debaditya Choudhury,^{*a} Daniel Jaque,^b Airan Rodenas,^a William T. Ramsay,^a Lynn Paterson^a and Ajoy K. Kar^a

Received 20th February 2012, Accepted 12th March 2012

DOI: 10.1039/c2lc40181a

Quantum dot thermal imaging has been used to analyse the chromatic dependence of laser-induced thermal effects inside optofluidic devices with monolithically integrated near-infrared waveguides. We demonstrate how microchannel optical local heating plays an important role, which cannot be disregarded within the context of on-chip optical cell manipulation. We also report on the thermal imaging of locally illuminated microchannels when filled with nano-heating particles such as carbon nanotubes.

1. Introduction

Temperature is one of the key physical factors governing the fundamental chemical reactions that occur within a live cell. Small changes in temperature can affect intra-cellular dynamics and could also modify the cell's metabolic activity, making it unviable.^{1,2} This fact underlies the recent advancements achieved in applying the exceptional optical, thermal and electrical properties of nanoscale materials for therapeutic, imaging and diagnostic biomedical applications.^{3,4} Surface functionalized fluorescent semiconductor nanocrystals (Quantum Dots) have far reaching potential as biological probes due to their unprecedented photostability and high sensitivity over long time scales.^{4,5} The other rapidly emerging class of biologically significant nanoscale materials are carbon nanotubes (CNT), which absorb energy in the “tissue-transparent” near-infrared (NIR) spectrum and are a promising tool for targeted cell hyperthermia.³ Recent advances in ultrafast laser inscription (ULI) techniques have enabled the creation of optofluidic microenvironments that can be tailored to mimic *in vivo* conditions. A rigorous understanding of the temperature distribution created in microchannels would also enable the evaluation of additional forces that may arise due to the presence of non-negligible thermal gradients such as those leading to photothermal trapping.^{6,7} In this paper, we demonstrate the use of these nanomaterials as probes for temperature sensing as well as effectors which act as nano-heaters to understand temperature distribution in microchannels within optofluidic microenvironments. Quantum dots (QD) are used to accurately determine the magnitude, spatial distribution and spectral dependence of laser-induced temperature increments within an optofluidic-integrated chip. This study elucidates how the light-induced thermal

loading of microchannels is affected by the presence or absence of absorbing particles (CNT) within the fluid.

The small dimensions of microchannels introduce complications in the accurate determination of their internal temperature. The reduced dimensions of the optically pumped volumes make the use of traditional “contact” methods of temperature measurement futile.⁸ The requirement of “remote thermal sensing” can be realized by recently emerging optical techniques. These are based on the incorporation, within the fluid, of luminescent particles whose luminescence is strongly dependent on temperature in terms of spectral shape, intensity or lifetime.^{9,10} Thus, with the help of confocal microscopy, the detailed analysis of the fluid spectral features will provide intra-channel thermal sensing and imaging. The use of fluorescent nanoparticles will also lead to high spatial resolutions significantly improving those achievable by the use of micro-thermocouples. Previous works have reported high-resolution thermal images of fluids using organic compounds such as rhodamine and its derivatives, based on the large temperature-induced variations of their fluorescence intensity and lifetime. The fluorescent compounds were incorporated into the fluid either in the form of a colloidal suspension¹¹ or by encapsulating within a micro-droplet.¹² These approaches provide 1–2 °C thermal resolution with micron-scale spatial resolution and are capable of thermal imaging in microfluidic environments involving optical traps.^{13–15} Despite these excellent results, the use of organic compounds has several drawbacks such as photo-deterioration and low molar absorption coefficient. Both could, in principle, be overcome by the use of CdTe semiconductor quantum dots (CdTe-QDs).¹⁶ Their characteristic fluorescence band that is tunable by QD size,¹⁷ has also very recently been shown to possess an outstanding thermal sensitivity.¹⁸ In particular, for the brightest CdTe-QDs of around 3.8 nm in diameter, the thermal-induced spectral shift is close to 0.35 nm °C^{−1}, allowing for temperature resolutions well below 0.5 °C, beating those achieved by other QDs such as CdSe-QDs.¹⁹ In respect to the previously used organic compounds, CdTe-QDs show superior photo-stability, larger molar absorption coefficients,

^aSUPA, School of Engineering & Physical Sciences, Heriot-Watt University, Edinburgh, UK. E-mail: A.K.Kar@hw.ac.uk

^bFluorescence Imaging Group, Departamento de Física de Materiales, Facultad de Ciencias, Universidad Autónoma de Madrid, 28049, Madrid, Spain. E-mail: daniel.jaque@uam.es

better thermal stability and improved fluorescence quantum yield in the NIR.¹⁶ In addition, CdTe-QDs show a larger two-photon absorption cross-section in such a way that thermal sensing could be achieved under optical excitation within the so-called “biological window” (700 nm–900 nm).^{20–24} This, indeed, ensures large penetration depths within the microchannel while minimising the possible presence of auto-fluorescence of the fluid and the thermal loading induced during the thermal imaging procedure. Regardless of these expected benefits, CdTe-QD based fluorescent thermometry has not yet been applied to the study of laser-excited optofluidics.

In this work, we have incorporated CdTe-QDs within an optofluidic device consisting of a microchannel locally illuminated by an adjacent buried waveguide. The laser-induced local heating of the fluid within the microchannel has been determined from the analysis of the spectral position of the CdTe-QDs fluorescence band. To begin with, the validity of CdTe-QDs nano-thermometers was checked by measuring the multi-wavelength laser-induced thermal loading of a water-filled microchannel. Results were compared to those predicted by simple theoretical models for laser-induced heating in optical traps.²⁵ Subsequently, QD based fluorescence thermometry was applied to determine how laser-induced optofluidic thermal loading is affected by the presence of absorbing particles such as CNTs within the fluid. By analysing the experimental data within the frame of simple theoretical models, we were able to estimate the fraction of the absorption coefficient of CNTs that can be attributed to heat generation. Furthermore, scanning confocal fluorescence imaging was then used to provide the first (to best of our knowledge) two dimensional thermal image of a laser-excited optofluidic device containing absorbing nanoparticles, which are essentially very advanced nano-heaters.

2. Materials and methods

2.1 Optofluidic device

The monolithic device with a microchannel and an optical waveguide was fabricated using the process of ULI followed by selective chemical etching. This technique involves the focusing of femtosecond laser pulses in bulk transparent materials which, depending upon the pulse energy regime, leads to local modification of the material's refractive index as well as enhanced chemical etching selectivity. This allows the simultaneous fabrication of optical waveguides and microchannels with 3D design freedom²⁶ leading to the fabrication of micro cell-stretchers,²⁷ sorters²⁸ and optofluidic sensors.²⁹ Inscription of the device was performed using 460 fs pulses at 1047 nm from a variable repetition rate, commercial Yb-doped master oscillator power amplifier (IMRA America FCPA μ Jewel), with the repetition rate set at 500 kHz. The pulses were focused using a 0.4 NA ($\times 20$) aspheric lens inside a fused silica substrate (Corning 7980, UVFS) that was translated through the laser focus using high precision Aerotech A3200 multi-axis air-bearing stages. As illustrated in Fig. 1a, the device consists of an optical waveguide designed perpendicular to a 5 mm long embedded microchannel with a cross-section of $100\ \mu\text{m} \times 100\ \mu\text{m}$ that is interfaced with cylindrical inlet and outlet ports, each with an outer diameter of 1 mm. The waveguide was inscribed using the multiscan technique,³⁰ with each laser scan offset by $0.4\ \mu\text{m}$,

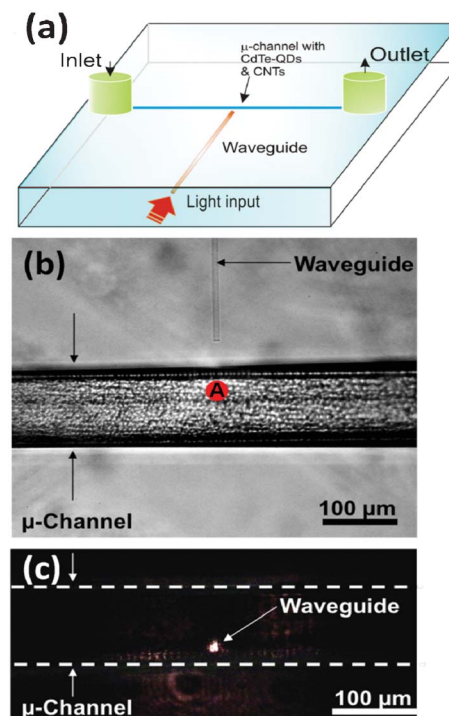


Fig. 1 a) Schematic representation of the thermometry device showing the microchannel and optical waveguide arrangement. b) Top view optical transmission image of the ultrafast laser inscribed device. The $100\ \mu\text{m}$ wide channel as well as the buried waveguide are indicated. Marked point (A) corresponds to the intra-channel location where maximum laser-induced heating was observed and where “single-point” thermal measurements were performed. c) Side view of the ultrafast laser inscribed device when a 633 nm laser was coupled into the buried waveguide. Focal plane was set to be the channel wall nearest to the waveguide.

constructing a geometrical cross-section of $8\ \mu\text{m} \times 8\ \mu\text{m}$. The fluidic components were inscribed using 650 nJ linearly polarized pulses and a translation speed of $4\ \text{mm s}^{-1}$, while the waveguide was inscribed using 290 nJ circularly polarized pulses at $2\ \text{mm s}^{-1}$. The inscribed device was subsequently etched for 5 h using hydrofluoric acid at 5% dilution in deionised water. Post etch, the waveguide was polished back to reveal the facet, which was then bonded to a single-channel fibre array (Opteron Co.) using UV curable epoxy (Norland NOA-61) to form a robust, reusable device. Fig. 1b shows the bright-field optical transmission micrograph of the etched microchannel and optical waveguide that form the device. Fig. 1c shows the side-view of the microchannel with the buried waveguide when light from a 633 nm laser was coupled to it while aligning the fibre-array.

2.2 Confocal fluorescence thermal imaging

For the purpose of thermal imaging and sensing, the optofluidic device was filled with an aqueous solution of CdTe-QDs at a concentration of 0.3% by mass. Once filled, the microchannel was blocked at both ends so there was no flow in the microchannel containing the QD solution. The CdTe-QDs, provided by Plasmachem Inc., were 3.8 nm in diameter and had been surface functionalised using thiocarboxylic acid in such a way that the sulphur binds to Cd in CdTe and $-\text{COOH}$ groups are formed surrounding the QDs. As already mentioned,

CdTe-QDs have recently been proposed as very sensitive fluorescent nano-thermometers based on their characteristic temperature-induced spectral shift so that thermal reading is achieved from the accurate determination of the fluorescence peak position.¹⁸ Thermal sensitivity as well as brightness depends on the dot size. The dot size used in this work (3.8 nm) was chosen since it provides a good compromise between these two characteristics.^{19,31} For thermal sensing and imaging we used a custom-built confocal fluorescence microscope, which is schematically drawn in Fig. 2a. The optofluidic device was placed on a 10 nm resolution XY motorized stage (PI Hera). A 488 nm beam provided by a CW Argon laser was focused into the microchannel by using a 50× long working distance microscope objective with a numerical aperture of 0.55. The CdTe-QD fluorescence generated from the 488 nm focal point was collected by the same microscope objective and, after passing through appropriate filters and confocal apertures, was analysed spectroscopically by a CCD attached to a high-resolution spectrometer. Integration time for spectrum acquisition was, in all cases, 1 s. The axial and lateral resolutions of our confocal fluorescence system have been estimated to be 3.6 μm and 0.6 μm, respectively. Fig. 2b shows a typical CdTe-QD emission spectrum obtained in our confocal microscope when the 488 nm beam was focused inside the microchannel. In this figure, we indicate the location of the emission peak as well as the relation between its spectral position and the QD temperature increment with respect to room temperature

(25 °C).¹⁸ Finally, the local heating produced by the presence of absorbing nano-centres in the solution has been evaluated by incorporating, into the aqueous solution of CdTe-QDs, single-wall carbon nanotubes provided by Sigma Aldrich Ltd. with a concentration of 0.1% by mass.

During thermal imaging, laser-induced thermal gradients were generated by coupling into the buried waveguide either a 980 nm or 1090 nm laser radiation provided by a diode laser or a Yb-doped glass fibre laser, respectively. In both cases, the maximum power launched into the optofluidic device was close to 600 mW. Pump power was, in both cases, controlled through the laser drive current.

3. Results and discussion

3.1 Influence of pump wavelength on the optofluidic thermal loading

One of the most promising applications of optofluidic devices is the achievement of intra-channel optical trapping. Due to the non-vanishing absorption coefficients of water in the NIR, optical trapping in an aqueous environment is accompanied by laser-induced local heating.^{32,33} A theoretical prediction, assuming a cylindrical geometry for heat generation and dissipation, predicts that the laser-induced temperature increment at focus, ΔT , in a liquid can be written as:²⁵

$$\Delta T = (P_{\text{in}} \cdot \alpha_{\text{abs}} / 2\pi K) \cdot \ln(D/w) \quad (1)$$

where P_{in} is the laser power reaching the liquid, α_{abs} is the absorption coefficient of the liquid at the laser wavelength, K is the thermal conductivity of the liquid, D is the shortest dimension of the micro-chamber containing the liquid along the light path, and w is the laser beam waist. The absorption coefficient (α_{ext}) is given by $\alpha_{\text{ext}} = \alpha_{\text{sct}} + \alpha_{\text{abs}}$, where α_{sct} is the scattering coefficient. For the case of distilled water, where light scattering can be neglected, we can assume $\alpha_{\text{ext}} = \alpha_{\text{sct}} + \alpha_{\text{abs}} \approx \alpha_{\text{abs}}$. The absorption coefficient of distilled water is shown in Fig. 3 (a). It is evident that the use of trapping wavelengths above 800 nm will be accompanied by some local heating and this has been widely reported in the literature.^{11,32–35} In this section, we will take advantage of this effect to explore the ability of QD based thermometry for the determination of laser-induced local heating effects in optofluidics.

The launched laser light travels through a length of optical fibre, the single-channel fibre array and finally the buried ULI waveguide before reaching the microchannel. Due to coupling mismatch between the single-channel fibre array and the waveguide, the net laser power reaching the microchannel (P_{in}) could differ by a large extent from the initial laser power launched into the system (P_{laser}). In order to determine the actual ratio between P_{in} and P_{laser} we first measured the 1090 nm laser-induced heating rate with respect to P_{laser} . We obtained a heating rate of $\Delta T / \Delta P_{\text{laser}}$ (1090 nm) = 3.1 °C W⁻¹. This value can be compared to the 1090 nm laser-induced heating rate (with respect to P_{in}) predicted by eqn (1) and experimentally corroborated by Ebert *et al.*:¹¹ $\Delta T / \Delta P_{\text{in}}$ (1090 nm) \approx 12 °C W⁻¹. Comparing both magnitudes, we can extract the ratio $P_{\text{in}} / P_{\text{laser}} \approx$ 0.25. Once this ratio is known

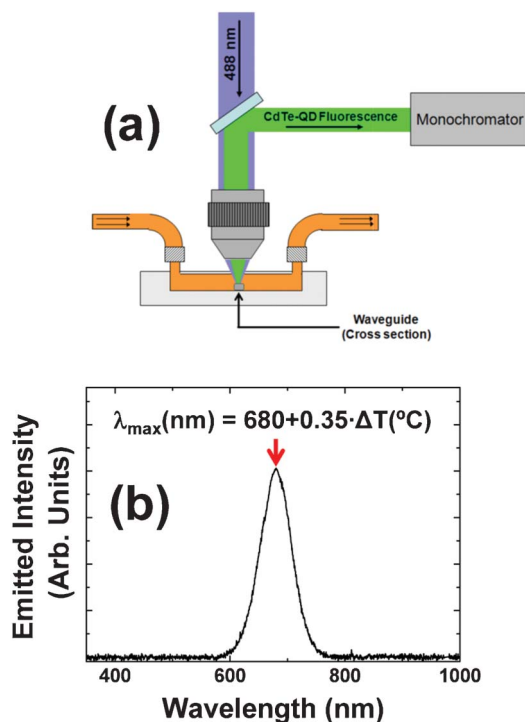


Fig. 2 a) Schematic diagram of the confocal microscope used for fluorescence thermal sensing and imaging in the optofluidic device. b) Typical intra-channel CdTe-QD emission spectrum obtained in our experimental set-up. The location of the peak wavelength and its relation with temperature change (with respect to 25 °C) is indicated.

it is possible to analyse heating rates with respect to the laser power reaching the microchannel.

In order to check the efficacy of the QD based thermometry as well as the validity of the laser power calibration procedure, we have investigated the laser-induced local heating produced when the microchannel is optically excited at 980 nm. At this wavelength, as can be observed in Fig. 3 (a), the water absorption coefficient peak reaches 0.5 cm^{-1} , more than twice the absorption coefficient at 1090 nm. Therefore, a larger local heating is expected under 980 nm excitation. Fig. 3(b) shows the microchannel temperature measured at the closest point to the waveguide indicated by point A in Fig. 1b. It is evident that the microchannel temperature increases linearly with the laser power, in agreement with eqn (1).²⁵ From the data included in Fig. 3(b) we have estimated a heating rate of $\Delta T/\Delta P_{\text{in}}$ at 980 nm $\approx 55 \text{ }^{\circ}\text{C W}^{-1}$. This value can be compared to the one theoretically calculated by using eqn (1) that yields $\Delta T/\Delta P_{\text{in}}$ (980 nm) = $45 \text{ }^{\circ}\text{C W}^{-1}$,²⁵ therefore there is a reasonable agreement between experimental data and theoretical predictions. The laser-induced heating rate at 980 nm obtained here can also be compared, within a first order approximation, to that previously reported by Mao *et al.* in an optical tweezers system.²⁵ They found a 980 nm laser-induced heating rate of $56 \text{ }^{\circ}\text{C W}^{-1}$ that is, indeed, in excellent agreement with our experimental results.

The results described in this section clearly confirm CdTe-QD thermometry as a valid approach for fluorescence thermal imaging of optofluidic devices. This fact suggests its use for thermal imaging of laser-excited optofluidics containing absorbing centres, as demonstrated in Section 3.2.

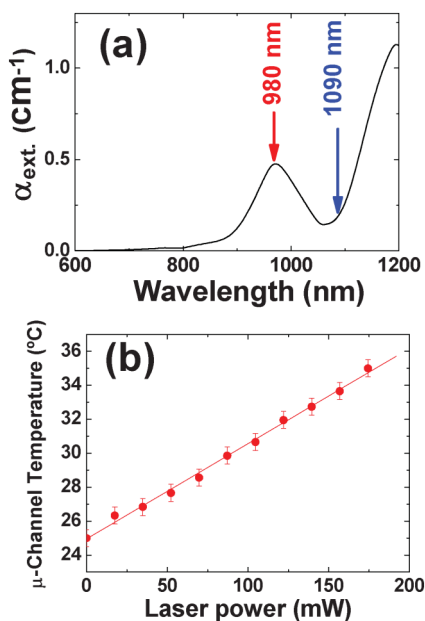


Fig. 3 a) Room temperature absorption spectrum of distilled water in the 800–1200 nm range. Arrows indicate the absorption coefficients for the two laser wavelengths used in this work (980 and 1090 nm). b) Local temperature as measured at point A within the microchannel (see Fig. 1 (b)) as a function of 980 nm laser power reaching the microchannel.

3.2 Thermal loading of an optofluidic device containing absorbing nanoparticles

Although laser-induced heating is usually regarded as an undesirable effect, in many applications laser-induced heating is a desirable effect that should be maximised. This is the case, as indicated earlier, of light-induced cell hyperthermia. In this case, controlled heating of a trapped cell is required for targeted cell death or for the study of the thermal dependence of cell properties such as elasticity, growth and division rates and membrane stability.

One approach to achieve this controlled cellular hyperthermia consists of the inclusion of heat-absorbing nanoparticles in the fluid containing the cells. CNTs are known to induce relevant heating when optically illuminated in the infrared, therefore acting as nano-heaters.^{35–38} Nevertheless, to the best of our knowledge, the magnitude and spatial distribution of the laser-induced temperature variations induced by CNTs in an optofluidic device is still unknown. For that purpose, an aqueous solution of both CdTe-QDs and CNTs (0.3 and 0.1% by mass, respectively) was injected into our optofluidic device. The absorption spectrum of the CdTe-QDs and CNT solution is shown in Fig. 4a. The absorption spectrum of an aqueous solution of CdTe-QDs (0.3% by mass) is also included for the sake of comparison. As can be observed, the presence of CNTs increases the optical absorption of the solution, in agreement with previous works on CNTs, reporting a broad absorption band extending from the visible to the infrared.^{36–38} In particular, the presence of CNTs increases the absorption coefficient at 1090 nm from $0.21 \text{ up to } 5.3 \text{ cm}^{-1}$ *i.e.* almost by

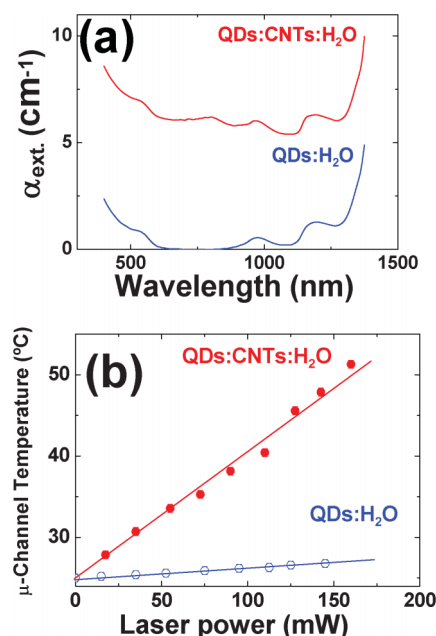


Fig. 4 a) Room temperature absorption spectrum of an aqueous solution containing CdTe-QDs in the presence and absence of CNTs in distilled water. b) Local temperature at point A (see Fig. 1(b)) as a function of 1090 nm laser delivered power when the microchannel was filled with a solution containing CNTs. Data obtained for the same solution in the absence of CNTs is also included for the sake of comparison.

a factor of 20. This increment is attributed to the non-vanishing absorption of CNTs in this spectral range as well as to the light scattering induced by CNTs. Thus, the 1090 nm laser-induced thermal loading of the optofluidic device is expected to be significantly enhanced due to the presence of CNTs. This is, indeed, what we have observed. Fig. 4b shows the microchannel temperature measured at the closest point to the waveguide indicated by point A in Fig. 1b, in the presence and absence of CNTs. In both cases a linear relation has been obtained, as predicted by eqn (1). In the presence of CNTs the heating rate has been found to be as large as $\Delta T/\Delta P_{\text{laser}}$ (1090 nm, CNT) = $160\text{ }^{\circ}\text{C W}^{-1}$, *i.e.* more than 10 times the heating rate found in pure water (without CNTs). From the experimentally determined heating rate and taking advantage of eqn (1) it is possible to estimate the absorption coefficient of CNTs at 1090 nm. We have obtained α_{abs} (1090 nm, CNT) $\approx 2.4\text{ cm}^{-1}$. When compared to the absorption coefficient at this wavelength (α_{ext} (1090 nm, CNT) $\approx 5.8\text{ cm}^{-1}$) this reveals a noticeable scattering contribution to the absorption coefficient of CNT at this wavelength. Indeed, scattering accounts for more than 50% of the optical absorption of CNTs at 1090 nm. Appreciable relative scattering contributions to the absorption coefficient have been also observed for other heating nanoparticles such as gold nano-rods of large aspect ratios.³⁹ Thus, from data included in Fig. 4b it is evident that CNTs could induce intra-channel temperatures well in excess of those required for targeted cell hyperthermia (above $45\text{ }^{\circ}\text{C}$), even by using moderate 1090 nm laser powers of 150 mW.

As mentioned before, for practical applications it is vital to know the maximum induced thermal heating of the optofluidic device as well as its spatial distribution. This requires the acquisition of thermal images of the microchannel in the presence of the laser radiation. Such thermal imaging is also possible with the aforementioned QD based thermometry. For that purpose we scanned the optofluidic device by varying the 488 nm focus spot within the microchannel. For each point, the spectral position of CdTe-QDs emission peak was determined so that a fluorescence image of the microchannel was obtained in terms of emission shift. The fluorescence image was then translated into temperature units by taking into account the temperature coefficient of the CdTe-QDs fluorescence band ($0.35\text{ nm }^{\circ}\text{C}^{-1}$, in our case). This enabled us to obtain thermal images as shown in Fig. 5a, showing the spatial temperature variation induced in the microchannel filled with the CdTe-QD and CNT solution, when 38 mW of 1090 nm radiation was launched into the microchannel. Fig. 5a reveals how the temperature reaches a maximum where the intra-channel photon density peaks along the propagation path of the laser radiation delivered by the waveguide. From this thermal image it is possible to estimate the heat-affected zone. Fig. 5b shows the microchannel temperature profile obtained along the dashed line indicated in the thermal image of Fig. 5a. This profile shows that although the 1090 nm laser beam is expected to be well localized within the microchannel, the temperature variation extends over tens of microns, due to the presence of heat diffusion processes. In addition to the determination of the heat-affected zone, the temperature profile included in Fig. 5 also reflects the thermal and spatial resolution achieved using this on-chip thermometry method. It is important to note that temperature oscillations

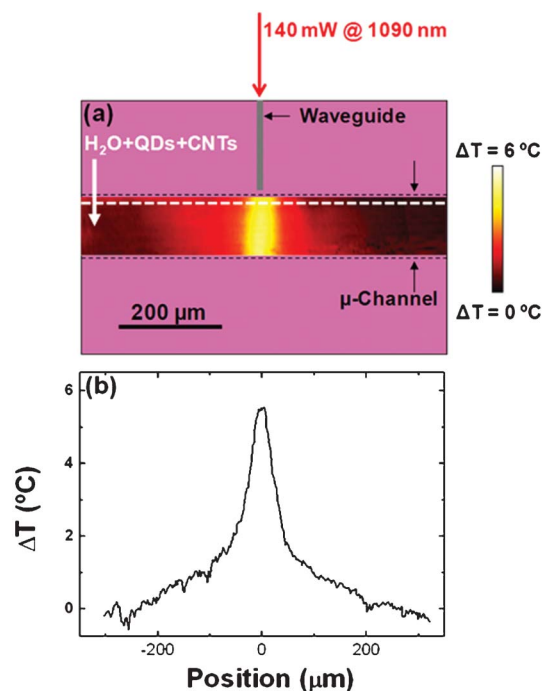


Fig. 5 a) Thermal image of a microchannel filled with an aqueous solution of CdTe-QDs and CNTs when optically excited at 1090 nm. The laser power reaching the microchannel was 38 mW. b) Thermal profile obtained along the horizontal scan-path indicated by the dashed line in part a.

attributed to noise *i.e.* thermal uncertainty is well below $0.2\text{ }^{\circ}\text{C}$, constituting an outstanding thermal sensitivity.

The outstanding sensitivity of CdTe-QDs can be used to monitor weak variations of temperature along the microchannel, such as those produced along the beam propagation path. The absorption coefficient of the CNT solution at 1090 nm is 5.8 cm^{-1} (see Fig. 4a). In accordance with the Beer–Lambert law, this should result in the reduction of about 5% in the beam intensity along its path across the $100\text{ }\mu\text{m}$ wide microchannel. This in turn, would lead to a small ($\approx 5\%$) reduction in the on-axis temperature. Fig. 6 shows the variation of temperature

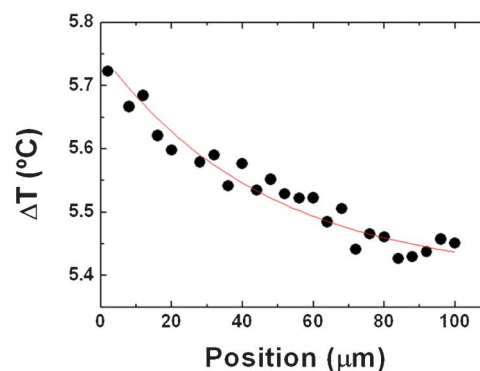


Fig. 6 Temperature variation along the 1090 nm laser beam path as obtained from Fig. 5a. Dots are experimental data and the solid line is a guide for the eyes. Positions $x = 0$ and $100\text{ }\mu\text{m}$ correspond to the input and output faces of the microchannel along the beam path, respectively for a 1090 nm laser power of 38 mW.

along the laser beam path within the microchannel obtained from the thermal image of Fig. 5a. The position $x = 0$ refers to the input face of the microchannel whereas the position $x = 100\ \mu\text{m}$ corresponds to the output face. As expected, the temperature decreases monotonously along the beam path. The total temperature reduction across the microchannel is close to 4%, in good agreement with the estimation made on the basis of the Beer–Lambert law.

4. Conclusion

QD thermometry has been applied to obtain high-resolution spatio-thermal images of the phenomenon of increased thermal loading within an optofluidic device due to the presence of absorbing nanoparticles such as carbon nanotubes. This work incorporates the powerful techniques of ultrafast laser inscription and semiconductor quantum dot thermometry allowing the creation of a non-intrusive temperature sensor platform for laser-excited, optofluidic microenvironments.

Acknowledgements

Debaditya Choudhury is funded by a Heriot-Watt University Life Science Interface Theme Scholarship. William T. Ramsay acknowledges funding from the UK Engineering and Physical Sciences Research Council (EPSRC). Airan Rodenas acknowledges financial support from the Spanish Ministerio de Educación under the Programa de Movilidad de Recursos Humanos del Plan Nacional de I+D+I 2008/2011 for abroad postdoctoral researchers. The authors wish to acknowledge EPSRC (grant number EP/G030227/1) for the IMRA FCPA μJewel femtosecond laser MOPA system. The authors also wish to acknowledge Kevin Prior for facilitating the HF etching capabilities of the group and Peter Heron for prompt technical support. Daniel Jaque thanks Caja Madrid Foundation for the Exchange Scholarship and MICIIN for financial support through project 2010-16161.

References

- 1 R. I. Morimoto, Cells in stress: transcriptional activation of heat shock genes, *Science*, 1993, **259**, 1409–1410.
- 2 F. Wetzel, S. Ronicke, K. Muller and M. Gyger, Single cell viability and impact of heating by laser absorption, *Eur. Biophys. J.*, 2011, **40**, 1109–1114.
- 3 K. Kostarelos, A. Bianco and M. Prato, Promises, facts and challenges for carbon nanotubes in imaging and therapeutics, *Nat. Nanotechnol.*, 2009, **4**, 627–633.
- 4 I. L. Medintz, H. T. Uyeda, E. R. Goldman and H. Mattoussi, Quantum dot bioconjugates for imaging, labelling and sensing, *Nat. Mater.*, 2005, **4**, 435–446.
- 5 R. Hardman, A Toxicologic Review of Quantum Dots: Toxicity Depends on Physicochemical and Environmental Factors., *Environ. Health Perspect.*, 2006, **114**, 165–172.
- 6 H. R. Jiang, H. Wada, N. Yoshinaga and M. Sano, Manipulation of Colloids by a Nonequilibrium Depletion Force in a Temperature Gradient, *Phys. Rev. Lett.*, 2009, **102**, 208301–208305.
- 7 H. Xin, X. Li and B. Li, Massive photothermal trapping and migration of particles by a tapered optical fiber, *Opt. Express*, 2011, **19**, 17065–17074.
- 8 J. Lee and N. A. Kotov, Thermometer design at the nanoscale, *Nano Today*, 2007, **2**, 48–51.
- 9 C. D. S. Brites, P. P. Lima, N. J. O. Silva, A. Millan, V. S. Amaral, F. Palacio and L. D. Carlos, Lanthanide-based luminescent molecular thermometers, *New J. Chem.*, 2011, **35**, 1177–1183.
- 10 C. D. S. Brites, P. P. Lima, N. J. O. Silva, A. Millan, V. S. Amaral, F. Palacio and L. D. Carlos, A Luminescent Molecular Thermometer for Long-Term Absolute Temperature Measurements at the Nanoscale, *Adv. Mater.*, 2010, **22**, 4499–4504.
- 11 S. Ebert, K. Travis, B. Lincoln and J. Guck, Fluorescence ratio thermometry in a microfluidic dual-beam laser trap., *Opt. Express*, 2007, **15**, 15493–15499.
- 12 M. A. Bennet, P. R. Richardson, J. Arlt, A. McCarthy, G. S. Buller and A. C. Jones, Optically trapped microsensors for microfluidic temperature measurement by fluorescence lifetime imaging microscopy, *Lab Chip*, 2011, **11**, 3821–3828.
- 13 E. M. Graham, K. Iwai, S. Uchiyama, A. Prasanna de Silva, S. W. Magennis and A. C. Jones, Quantitative mapping of aqueous microfluidic temperature with sub-degree resolution using fluorescence lifetime imaging microscopy, *Lab Chip*, 2010, **10**, 1267–1273.
- 14 S. W. Magennis, E. M. Graham and A. C. Jones, Quantitative Spatial Mapping of Mixing in Microfluidic Systems, *Angew. Chem., Int. Ed.*, 2005, **44**, 6512–6516.
- 15 R. K. P. Benninger, Y. Koc, O. Hofmann, J. Requejo-Isidro, M. A. A. Neil, P. M. W. French and A. J. deMello, Quantitative 3D Mapping of Fluidic Temperatures within Microchannel Networks Using Fluorescence Lifetime Imaging, *Anal. Chem.*, 2006, **78**, 2272–2278.
- 16 U. Resch-Genger, M. Grabolle, S. Cavaliere-Jaricot, R. Nitschke and T. Nann, Quantum dots versus organic dyes as fluorescent labels, *Nat. Methods*, 2008, **5**, 763–775.
- 17 Y. Masumoto and K. Sonobe, Size-dependent energy levels of CdTe quantum dots, *Phys. Rev. B: Condens. Matter*, 1997, **56**, 9734–9737.
- 18 L. M. Maestro, C. Jacinto, U. R. Silva, F. Vetrone, J. A. Capobianco, D. Jaque and J. Garcia Sole, CdTe Quantum Dots as Nanothermometers: Towards Highly Sensitive Thermal Imaging, *Small*, 2011, **7**, 1774–1778.
- 19 L. M. Maestro, E. M. Rodriguez, F. Sanz-Rodriguez, M. C. Iglesias-de la Cruz, A. Juarranz, R. Naccache, F. Vetrone, D. Jaque, J. A. Capobianco and J. Garcia Sole, CdSe Quantum Dots for Two-Photon Fluorescence Thermal Imaging, *Nano Lett.*, 2010, **10**, 5109–5115.
- 20 D. R. Larson, W. R. Zipfel, R. M. Williams, S. W. Clark, M. P. Bruchez, F. W. Wise and W. W. Webb, Water-Soluble Quantum Dots for Multiphoton Fluorescence Imaging *in Vivo*, *Science*, 2003, **300**, 1434–1436.
- 21 K. König, Multiphoton microscopy in life sciences., *J. Microsc.*, 2000, **200**, 83–104.
- 22 V. Venugopalan, N. S. Nishioka and B. B. Mikic, Thermodynamic response of soft biological tissues to pulsed infrared-laser irradiation, *Biophys. J.*, 1996, **70**, 2981–2993.
- 23 M. K. So, C. Xu, A. M. Loening, S. S. Gambhir and J. Rao, Self-illuminating quantum dot conjugates for *in vivo* imaging, *Nat. Biotechnol.*, 2006, **24**, 339–343.
- 24 L. M. Maestro, J. E. Ramirez-Hernandez, N. Bogdan, J. A. Capobianco, F. Vetrone, J. Garcia Sole and D. Jaque, Deep tissue bio-imaging using two-photon excited CdTe fluorescent quantum dots working within the biological window, *Nanoscale*, 2012, **4**, 298–302.
- 25 H. Mao, J. R. Arias-Gonzalez, S. B. Smith Jr., I. Tinoco and C. Bustamante, Temperature Control Methods in a Laser Tweezers System, *Biophys. J.*, 2005, **89**, 1308–1316.
- 26 M. Kim, D. J. Hwang, H. Jeon, K. Hiromatsu and C. P. Grigoropoulos, Single cell detection using a glass-based optofluidic device fabricated by femtosecond laser pulses, *Lab Chip*, 2009, **9**, 311–318.
- 27 N. Bellini, K. C. Vishnubhatla, F. Bragheri, L. Ferrara, P. Minzioni, R. Ramponi, I. Christiani and R. Osellame, Femtosecond laser fabricated monolithic chip for optical trapping and stretching of single cells, *Opt. Express*, 2010, **18**, 4679–4688.
- 28 D. Choudhury, W. T. Ramsay, R. Kiss, N. A. Willoughby, L. Paterson and A. K. Kar, A 3D mammalian cell separator biochip, *Lab Chip*, 2012, **12**, 948–953.
- 29 V. Maselli, J. R. Grenier, S. Ho and P. R. Herman, Femtosecond laser written optofluidic sensor: Bragg grating waveguide evanescent probing of microfluidic channel, *Opt. Express*, 2009, **17**, 11719–11729.
- 30 N. D. Psaila, R. R. Thomson, H. T. Bookey, N. Chiodo, S. Shen and R. Osellame, Er:Yb-Doped Oxyfluoride Silicate Glass Waveguide Laser Fabricated Using Ultrafast Laser Inscription, *IEEE Photonics Technol. Lett.*, 2008, **20**, 126–128.

- 31 L. M. Maestro, C. Jacinto, U. Rocha, M. C. Iglesias-de la Cruz, F. Sans-Rodriguez, A. Juarranz, J. Garcia Sole and D. Jaque, Optimum quantum dot size for highly efficient fluorescence bioimaging, *J. Appl. Phys.*, 2012, **111**, 023513.
- 32 E. J. G. Peterman, F. Gittes and C. F. Schmidt, Laser-Induced Heating in Optical Traps., *Biophys. J.*, 2003, **84**, 1308–1316.
- 33 Y. Liu, D. K. Cheng, G. J. Sonek, M. W. Berns, C. F. Chapman and B. J. Tromberg, Evidence for localized cell heating induced by infrared optical tweezers, *Biophys. J.*, 1995, **68**, 2137–2144.
- 34 P. M. Celliers and J. Conia, Measurement of Localized Heating in the Focus of an Optical Trap, *Appl. Opt.*, 2000, **39**, 3396–3407.
- 35 C. Iancu and L. Mocan, Advances in cancer therapy through the use of carbon nanotube-mediated hyperthermia, *Int. J. Nanomed.*, 2011, **6**, 1675–1684.
- 36 J. R. Whitney, S. Sarkar, J. Zhang, T. Do, T. Young, M. K. Manson, T. A. Campbell, A. A. Poretzky, C. M. Rouleau, K. L. More, D. B. Geohegan, C. G. Rylander, H. C. Dorn and M. N. Rylander, Single walled carbon nanohorns as photothermal cancer agents, *Lasers Surg. Med.*, 2011, **43**, 43–51.
- 37 F. Zhou, D. Xing, Z. Ou, B. Wu, D. E. Resasco and W. R. Chen, Cancer photothermal therapy in the near-infrared region by using single-walled carbon nanotubes, *J. Biomed. Opt.*, 2009, **14**, 021009.
- 38 Z. M. Markovic, L. M. Harhaji-Trajkovic, B. M. Todorovic-Markovic, D. P. Kepic, K. M. Arsikin, S. P. Jovanovic, A. C. Pantovic, M. D. Dramicanin and V. S. Trajkovic, In vitro comparison of the photothermal anticancer activity of graphene nanoparticles and carbon nanotubes, *Biomaterials*, 2011, **32**, 1121–1129.
- 39 P. K. Jain, K. S. Lee, I. H. El-Sayed and M. A. El-Sayed, Calculated Absorption and Scattering Properties of Gold Nanoparticles of Different Size, Shape, and Composition: Applications in Biological Imaging and Biomedicine, *J. Phys. Chem. B*, 2006, **110**, 7238–7248.

A.3 – A 3D mammalian cell separator biochip

Choudhury, D., Ramsay, W. T., Kiss, R., Willoughby, N. A., Paterson, L. & Kar, A. K.
“A 3D mammalian cell separator biochip” *Lab Chip* **12(5)**, 948-953 (2012).

DOI: 10.1039/C2LC20939J

A 3D mammalian cell separator biochip†

Debaditya Choudhury,^{*a} William T. Ramsay,^a Robert Kiss,^b Nicholas A. Willoughby,^b Lynn Paterson^a and Ajoy K. Kar^a

Received 27th September 2011, Accepted 3rd January 2012

DOI: 10.1039/c2lc20939j

The dissimilar cytoskeletal architecture in diverse cell types induces a difference in their deformability that presents a viable approach to separate cells in a non-invasive manner. We report on the design and fabrication of a robust and scalable device capable of separating a heterogeneous population of cells with variable degree of deformability into enriched populations with deformability above a certain threshold. The three dimensional device was fabricated in fused silica by femtosecond laser direct writing combined with selective chemical etching. The separator device was evaluated using promyelocytic HL60 cells. Using flow rates as large as $167 \mu\text{L min}^{-1}$, throughputs of up to 2800 cells min^{-1} were achieved at the device output. A fluorescence-activated cell sorting (FACS) viability analysis on the cells revealed 81% of the population maintain cellular integrity after passage through the device.

1. Introduction

The human anatomy consists of a large number of hierarchical networks that are essentially microfluidic in nature. Unlike conventional macroscopic cell culture and manipulation environments, Lab-on-Chip (LOC) devices offer the unique opportunity to mimic *in vivo* biological systems onto closely resembling *in vitro* microfluidic environments. Miniaturized LOC systems have been reported to offer several advantages including precise control and monitoring of the microenvironment, reduced analysis times, smaller reagent volumes, reduced chemical waste and lowered diagnosis costs. In this respect, recent years have seen the emergence of several microfabricated fluidic systems based on photo and soft lithographic techniques.^{1–7} In particular, microfluidic systems capable of sorting both bulk and single cells have been reported by different methods including mechanically controlled hydrodynamic flow switching,⁸ micro-component enabled hydrodynamic flow switching,⁹ electrophoretic/electro-osmotic methods,¹⁰ magnetic,¹¹ optical¹² and size based methods.^{13,14}

In this paper, we report on the fabrication and demonstration of a 3D, pressure-driven, cell manipulation device that is embedded in fused silica using direct femtosecond laser writing followed by selective wet etching. The device is capable of sorting a heterogeneous population of cells with varied levels of

deformability into enriched populations of cells with uniform deformability. Laser writing and selective etching parameters are investigated in order to achieve embedded microchannels with preserved post-etch aspect ratios. As proof of principle, human promyelocytic leukemia cells (HL60) are used to demonstrate that cells can pass through narrow, sub-surface channels fabricated by the aforementioned technique. In addition, the feasibility of the device in delivering a viable population of cells is investigated by collecting the cells at the device output and analysing their integrity using a commercial flow cytometer.

Fused silica was chosen as the substrate material for this work due to several advantages, such as high optical quality, robustness, biological compatibility, thermal stability, a wide transmission window and fully controllable photo-induced selective etching rates by varying irradiation parameters such as energy, translation speed and even polarisation state of writing pulses. It is also known that regions in fused silica modified using femtosecond laser pulses exhibit chemical etching rates sensitive to the polarisation of the pulses.¹⁵ The pulse polarisation can be tailored to write sub-surface structures which can then be etched to obtain microchannels with significant difference in aspect ratio. While single channel optofluidic devices have been successfully demonstrated in the recent past,^{16,17} a monolithic multichannel device fabricated using this property has not been reported so far.

2. Design and fabrication

2.1 Design considerations and working principle

The proposed sorting mechanism relies on the dissimilarities in cytoskeletal architecture that exist in different cell types. The cytoskeleton of most cells is primarily composed of proteins

^aSUPA, Department of Physics, School of Engineering & Physical Sciences, Heriot-Watt University, Edinburgh, EH14 4AS, Scotland. E-mail: dc119@hw.ac.uk

^bDepartment of Chemical Engineering, School of Engineering & Physical Sciences, Heriot-Watt University, Edinburgh, EH14 4AS, Scotland

† Electronic supplementary information (ESI) available. See DOI: 10.1039/c2lc20939j

which can be thought of as scaffolding that provides shape and structure to the cells. Difference in the cytoskeletal network between various cell types manifests as a discernible variation in cell elasticity.¹⁸ Thus, cells with sparse cytoskeletal architecture are softer than cells with a relatively denser network of proteins making up the cytoskeleton.

A network of appropriately designed microchannels enabling accurate pressure driven flow control provides a method to exploit any difference in cell deformability without the use of external forces such as magnetic or electric fields. As shown in Fig. 1, we present a ‘proof of principle’ design for the device consisting of a T-junction formed by two microchannels with one inlet port and two outlet ports.

At the junction, these microchannels are linked together by narrow constrictions forming a filter region. If a heterogeneous population of cells is inserted into the device through the inlet and a pressure gradient is maintained across the constrictions, the softer cells will be able to deform and navigate their way through these constrictions into outlet 1 of the device, provided the cross-section of the constrictions is narrower than the average size of a cell. The more rigid cells will be unable to deform enough to travel through the constrictions and can be collected at outlet 2.

2.2 Device fabrication

The rapidly evolving technique of femtosecond laser direct writing and subsequent wet etching in bulk transparent dielectrics allows unprecedented 3D design freedom¹⁹ with high spatial resolution,²⁰ making it a powerful tool for microfluidic and micro-optic applications. Furthermore, there is no requirement to seal the top surface of microfluidic devices when compared to photo and soft lithographic microfabricated devices. The technique involves the irradiation of bulk substrate

material using focused, sub-bandgap femtosecond laser pulses leading to enhanced chemical etching selectivity.²¹ In recent years, novel applications have been successfully demonstrated using femtosecond laser direct writing in the fields of integrated optics,²² optofluidic LOC devices¹⁷ and micromechanical systems.²³

The device was written using 460 fs pulses at a repetition rate of 500 kHz from a commercial Yb-doped master oscillator power amplifier laser system (IMRA America FCPA μ Jewel D400) at 1047 nm, focused inside a fused silica substrate (Corning 7980, UV Grade) using a 0.4 NA (x20) aspheric objective lens. Accurate translation of the substrate through the laser focus was controlled using Aerotech Automation 3200 multi-axis air bearing stages. We applied the polarisation sensitive wet etching property of fused silica and fabricated the device in separate components in order to preserve their post etch aspect ratio. Each component was written using optimum laser writing parameters to achieve controlled etch rates. Optimising the parameters allowed us to achieve etching rate selectivity one order of magnitude higher than those reported by Hnatovsky *et al.*¹⁴ The details of the optimisation process will be communicated separately.

Optical micrographs of various components of the device before and after the etching process are shown in Fig. 2(a)–(c).

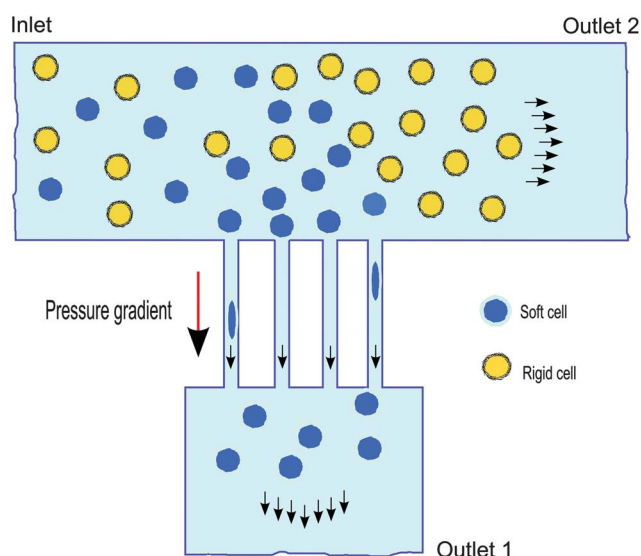


Fig. 1 Schematic showing the working mechanism of the device. A pressure gradient applied between the two microchannels allows the relatively softer cells to squeeze through the constrictions to be collected at outlet 1.

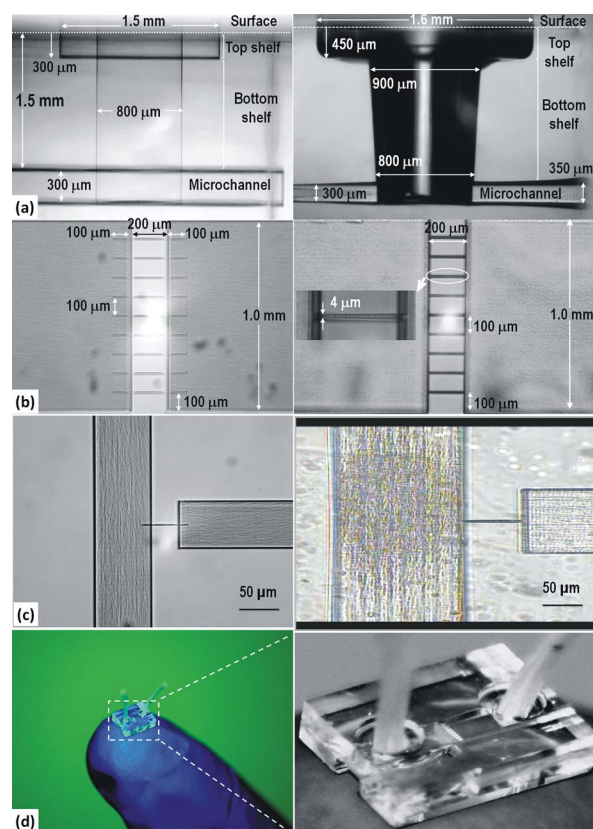


Fig. 2 (a–c) Optical micrographs showing the components of the device before etching (left) and after etching (right) with HF at 13.3% (v/v) dilution for 4.5 h. (a) The inlet system viewed side-on. (b) Top view of the constriction array. (c) Top view of the T-junction. (d) The device on a fingertip with a magnified view shown alongside.

The inlet ports shown in Fig. 2a have been designed in a concentric cylindrical pattern with an outer diameter of 1.5 mm, inner diameter of 750 μm and a depth of 1.6 mm. They were written using circularly polarised 650 nJ pulses at a translation speed of 4 mm s^{-1} . Fig. 2b and 2c show the microchannels with constrictions that have been fabricated in a straight and T-junction arrangement respectively. The channels with a cross-section of 1 mm \times 300 μm in Fig. 2b were fabricated using 650 nJ pulses at 2 mm s^{-1} . The microchannels forming the 'T' in Fig. 2c have been designed with a cross-section of 100 μm \times 100 μm and were also written using 650 nJ pulses at a translation speed of 2 mm s^{-1} . The electric field vector of the laser pulses was maintained perpendicular to the translation direction at all times in order to ensure appropriate etching selectivity of the laser written microchannels. The constrictions were written using a single laser scan at the junction of the two microchannels using 270 nJ pulses at a translation speed of 0.1 mm s^{-1} . In order to minimize unwanted mechanical forces on the cell by forcing them to remain deformed for an extended period of time, the maximum length of the constrictions is set to 200 μm . As imaging is to be performed from the bottom surface of the substrate, the network of channels were fabricated at a depth of 400 μm . Chip-to-world interfacing is achieved by linking the input and output arms of the device to cylindrical inlet ports which can be directly accommodated without the need of external adapters. Platinum cured silicone tubing (VWR) with an outer diameter of 640 μm and inner diameter of 300 μm can be directly inserted into the ports as shown in Fig. 2d.

The fused silica substrate with the laser written structures was subsequently etched in an ultrasonic bath using hydrofluoric acid (HF) at 5% aqueous dilution for 11 h. The long etch time at 5% dilution can be attributed to the fact that access to the laser modified structures gets increasingly difficult as the etch profile ingresses deeper into the substrate. This issue was addressed by increasing the concentration to 13.3% (aq.), which subsequently reduced the etch time to 4.5 h without compromising the aspect ratio of the laser written structures. It was observed that optimum selection of the length of the microchannels is critical to ensure that etchant arrives at the constriction from all routes at approximately the same time in order to avoid over etching the structures.

Once etched, the device was rinsed in an ultrasonic cleaner using deionised water followed by acetone and IPA for 30 min to remove any residual traces of HF inside the microchannels. A second sacrificial etched device was ground back and polished in order to reveal the cross-section of the constriction. It was found that the constriction was slightly elongated along one axis. As shown in Fig. 3b, the longer axis was measured to be 8 μm and the shorter axis 4 μm .

3. Device performance

We investigated the throughput of the device and subsequently, the viability and size distribution of cells within the population which have travelled through the constrictions. A T-junction device with a single constriction as shown in Fig. 2c and Fig. 3a was used to examine if the femtosecond laser direct writing and selective etching method produced an optimally sized

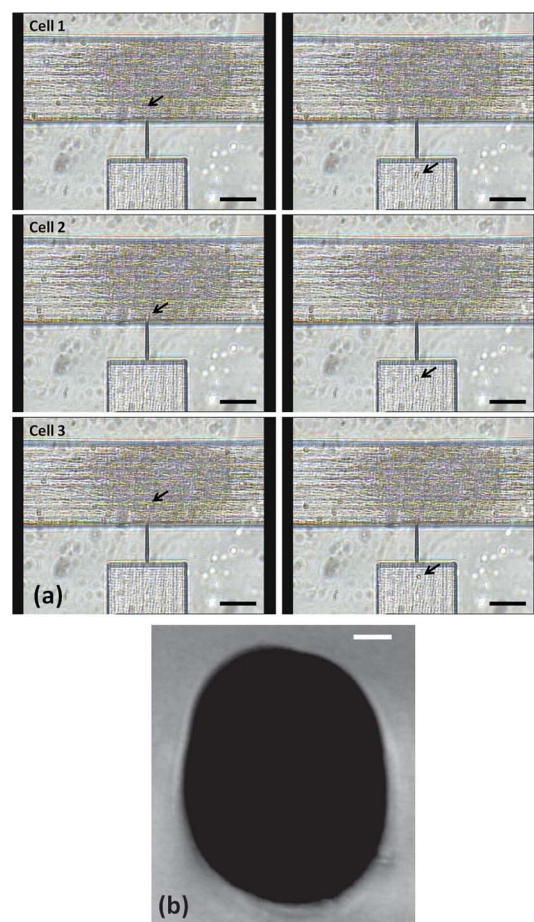


Fig. 3 Optical micrographs of the single constriction T-junction device. (a) The HL60 cells can be clearly seen after they pass through the constriction (see supplementary material). Scale bar - 50 μm (b) Cross-sectional view of a constriction. Scale bar represents 1 μm .

constriction for cells to squeeze through and exit from in an unaltered state. Human promyelocytic leukemia (HL60) cells were chosen since they need simple maintenance *in vitro* and grow as single-cell suspension cultures without the tendency to clump or adhere to plastic or glass and are also known to possess a somewhat elastic cytoskeleton that is not uniform within a population.²⁴ Sample injection into the microchannels and flow rates were controlled by using a microfluidic syringe infusion pump (WPI, SP100i). Sample collection reservoirs were placed at the outlet ports of the device, which was then placed on an inverted microscope platform (Olympus IX series). The microchannels were initially flushed using phosphate-buffered saline (PBS) in order to remove any residual water in them. The device showed lag free response to external changes in flow rates ranging from 1.67 μL to 1 mL min^{-1} , indicating that the chip-to-world interfacing is leak free and able to withstand high fluid pressures.

The HL60 cells cultured in DMEM (Invitrogen) growth media supplemented with 20% fetal bovine serum (FBS), 2mM glutamine and 100 units of Penicillin and 100 μg of streptomycin per mL were injected into the T-junction device through the inlet port at a constant flow rate of 0.5 mL min^{-1} . Prior to this, a sample of the cells from the same suspension was used to

measure the cell size under a microscope, using 3 μm diameter microspheres as a control. The average size of healthy looking cells was obtained to be $11.7 \mu\text{m} \pm 1.1 \mu\text{m}$ with a standard deviation of 1.09 for 25 cells. The output microchannel for outlet 1 was maintained at a lower pressure using an open ended syringe. Importantly, the constriction was found to be of optimum cross section to enable deformation of the cells during transit. Fig. 3a shows snapshot images where the cells can be seen entering the constriction and then in the output microchannel travelling towards outlet 1 after passing through the constriction.

The results indicate the possibility of separating a heterogeneous population of cells with varying degrees of elasticity into enriched populations of cells with elasticity above a certain threshold using a monolithic device fabricated by fs-laser direct writing. However, such an application would only be useful for practical purposes if the populations of cells at the output reservoirs are not damaged by the process of passage through narrow constrictions. In order to analyse if this is the case and also to obtain a high throughput, the design was consequently multiplexed into a straight channel device with an array of constrictions as shown in Fig. 2b. The microchannel dimensions were increased to $1000 \mu\text{m} \times 300 \mu\text{m} \times 3100 \mu\text{m}$. A two dimensional array of 18 constrictions, each of length 200 μm and width 4 μm was fabricated in the device. The cell viability assessment was performed on the output population of the device using a commercial fluorescence activated cell cytometer (BD FACSCaliburTM).

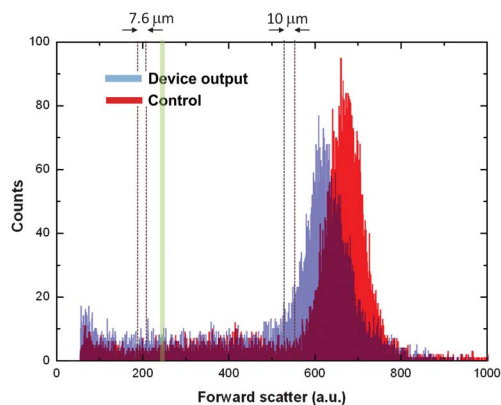


Fig. 4 Forward scatter histogram plots obtained from the fluorescence activated cell sorter (FACS) live/dead analysis, showing the position of live cells. Data from the sample that passed through the device is plotted in blue. The control data is plotted in red. The overlaid plots reveal that the healthy population in the control lies between forward scatter values of ~ 550 and ~ 800 and makes up 78.6% of the total number of events detected. In the device output, this population lies between forward scatter values of ~ 480 and ~ 780 and constitutes 64.3% of the total events. A relative drop in maximum counts is observed in the device output. A shift towards lower forward scatter is also observed in the distribution of the device output indicating a reduction in average size of the viable cells. A corresponding increase in the device output is observed in sub-200 values representing debris from fragmented cells. The vertical dashed bands represent the size of 7.6 μm and 10 μm microspheres that have been used for size calibration. The green vertical band represents the microchannel size of 8 μm .

Prior to introducing cells into the device, they were stained with the BDTM cell viability kit consisting of Thiazole Orange (TO) and Propidium Iodide (PI). A constant flow rate of 167 $\mu\text{L min}^{-1}$ was used to deliver the stained HL60 cell sample through the device. A comparative FACS analysis was then carried out using a control sample of stained HL60 cells which were not sent through the device. Fig. 4 shows a comparison of the forward scatter results, representing cell volume, obtained in both control and sample cases and Fig. 5 shows the respective dot plots showing forward scatter *versus* side scatter (granularity). The fluorescence plots showing TO and PI content for this data is included as supplementary information.

A size calibration was performed in order to compare the relation of the viable cell size distribution with the constriction size. Microspheres of known size (7.6 μm and 10 μm) were introduced into the FACS and their forward scatter position noted, as shown in Fig. 4 and Fig. 5a–5b. The relative position of the constriction size is also indicated. The number of total gated events (30 000) in the device output was kept equal to that of the control.

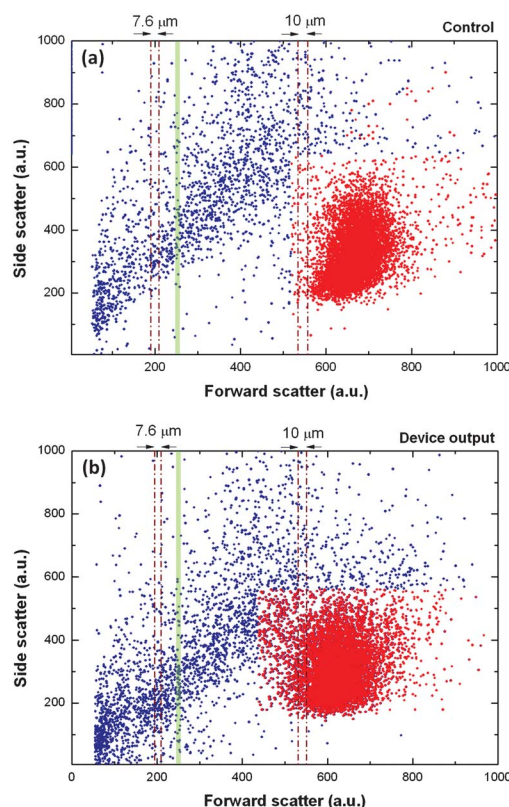


Fig. 5 Dot plots showing variation of side scatter (SSC) against forward scatter (FSC) after the FACS live/dead analysis. Red dots represent cells stained with Thiazole Orange (TO) (representing all cellular material) while blue dots represent cells that took up Propidium Iodide (PI) (representing dead and injured cells). (a) Dot plot of side scatter against forward scatter of the control. (b) Dot plot of side scatter against forward scatter of the device output. The fluorescence FACS plots for this data is included as supplementary information. The vertical dashed bands represent the size of 7.6 μm and 10 μm microspheres that were run through the FACS for size calibration. The green band represents the microchannel size of 8 μm .

The healthy cells in the FACS histogram (Fig. 4) and dot plots (Fig. 5) correspond to the events in the fluorescence plots (see supplementary information) that show high TO content but low PI content (R1) (viable cells). In Fig. 5a, these cells are represented by a dense population of cells with x parameter values between ~ 550 and ~ 800 as marked by the red gated region in Fig. 5. These cells, comprising of 78.6% of the total gated events in the control (Fig. 5a) are almost certainly healthy due to high TO content, low PI content, large volume and low levels of granularity and therefore this population forms our region of interest. In terms of size, this population also agrees with the measured cell size of $11.7 \mu\text{m} \pm 1.1 \mu\text{m}$. In comparison, the data obtained from the stained HL60 cells after being sent through the device revealed 64.3% of the total gated events to be within the region of interest. In addition, compared to the control, a slight increase in counts is observed in the device output data at low levels of forward scatter (<200). These events also showed low levels of both TO and PI in the fluorescence plots (see supplementary information). This indicates an increase in the number of objects much smaller than the average size of healthy cells and is attributed to large cells being damaged during their travel through a constriction, in addition to some small viable cells. Thus, in Fig. 4 and Fig. 5a–5b all forward scatter objects with a value <200 can be considered as debris. This region is gated (R3) in the fluorescence plot and showed an increase from 1.9% in the control to 7.8% in the device output.

As shown in Fig. 4, this is complemented by a lowering of the maximum counts in the device output when compared to the control indicating a reduction in the number of healthy cells. A shift towards lower forward scatter is also observed in the distribution of the device output, indicating that the average size of viable cells is smaller when compared to the control. Furthermore, a number of cells in the control with larger size as shown in Fig. 5 were found to be absent in the population of cells which had travelled through the device. This observation indicates a potential size selectivity application of the constriction array. The minimum PI threshold in region R2 was selected at a slightly higher value than the maximum PI fluorescence in R1. The region R2 consists of dead and injured cells and makes up 19.5% in the control which rises to 27.9% in the device output. Events in R2 showing high TO as well as high PI content are attributed to large cells whose membrane has been compromised. It is clear from Fig. 5a and 5b that a large fraction of cells had to deform to go through the constrictions.

The passage of a single cell through a constriction is depicted in Fig. 6. The cell has a diameter of $\sim 12 \mu\text{m}$ and can be seen to deform as it travels through a constriction with $4 \mu\text{m} \times 8 \mu\text{m}$ cross-section and a length of $200 \mu\text{m}$. We estimate that around 150 cells per minute travelled through a single constriction, as a total of about 30 000 cells passed through the 18 constriction array in 11 min, with 81% of the collected cells viable. The results indicate that a small population of cells does suffer damage and disruption of cellular integrity after passing through the constrictions, as expected. However, majority of the healthy population remain viable after travelling through the device and can potentially be grown in culture. This result is promising for cellular diagnostic, therapeutic and point of care applications.

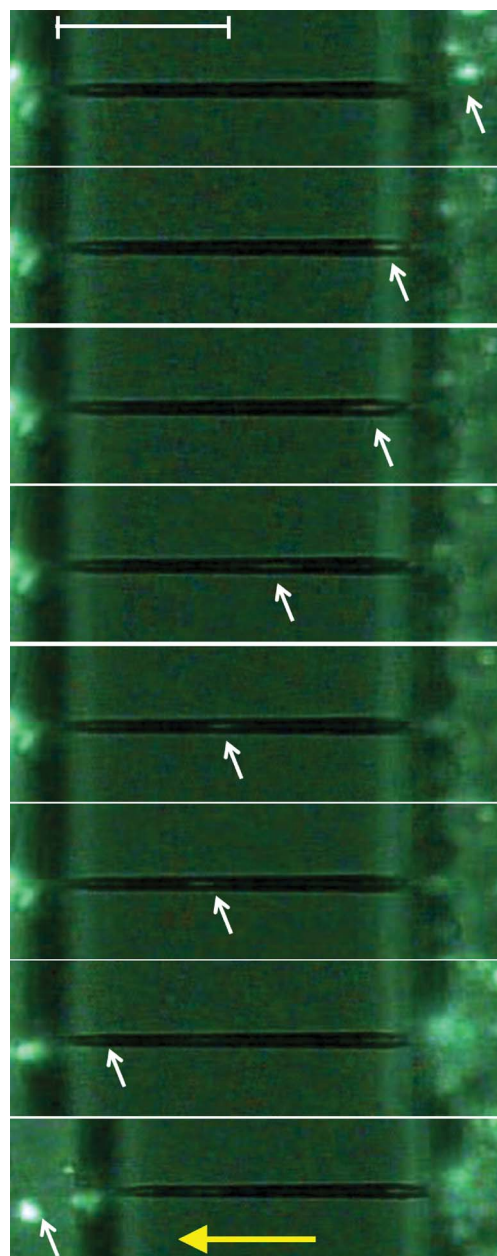


Fig. 6 Fluorescence images showing the deformation of a single cell as it travels through the constriction in the multi-constriction device. The scale bar represents $100 \mu\text{m}$. The white arrows show the position of the cells. The yellow arrow indicates flow direction.

4. Conclusions

The work presented here introduces a proof-of-principle femto-second laser written device capable of sorting cells and collecting viable cell populations. In addition, the possibility of creating etched structures embedded in fused silica with large differences in aspect ratio is demonstrated for the first time.

The technique of femtosecond laser direct writing also presents the prospect of creating low loss optical waveguides in dielectric substrates. We are also investigating ways to optimise the device into a high-throughput, cell separator platform which includes looking into the design of novel geometries. The future version of

this reported device is envisioned to be a high throughput optofluidic biochip offering cytometric capability with potential applications in cancer research, regenerative medicine, affinity biosensing, cell migration, immunology and studying stress response behaviour at cellular level.

Acknowledgements

The authors wish to acknowledge the Bioprocessing Research Industry Club (BBSRC) for facilitating this research and EPSRC (grant number EP/G030227/1) for the IMRA FCPA μ Jewel femtosecond laser MOPA system. The authors also wish to acknowledge Kevin Prior for facilitating the HF etching capabilities of the group and Peter Heron for prompt technical support. DC gratefully acknowledges funding from the Heriot-Watt Life Sciences Interface theme. WTR acknowledges funding from EPSRC.

Notes and references

- 1 G. M. Whitesides, *Nature*, 2006, **442**, 368–373.
- 2 M. A. Unger, H.-P. Chou, T. Thorsen, A. Scherer and S. R. Quake, *Science*, 2000, **288**, 113–116.
- 3 J. P. Urbanski, W. Thies, C. Rhodes, S. Amarasinghe and T. Thorsen, *Lab Chip*, 2006, **6**, 96–104.
- 4 P. S. Dittrich and A. Manz, *Nat. Rev. Drug Discovery*, 2006, **5**, 210–218.
- 5 A. Tourovskaia, X. Figueroa-Masot and A. Folch, *Lab Chip*, 2005, **5**, 14–19.
- 6 S. K. Sia and G. M. Whitesides, *Electrophoresis*, 2003, **24**, 3563–3576.
- 7 F. Lautenschlager, S. Paschke, S. Schinkinger, A. Bruel, M. Beil and J. Guck, *Proc. Natl. Acad. Sci. U. S. A.*, 2009, **106**, 15696–15701.
- 8 A. Wolff, I. R. Perch-Nielsen, U. D. Larsen, P. Friis, G. Goranovic, C. R. Poulsen, J. P. Kutter and P. Tellemann, *Lab Chip*, 2003, **3**, 22–27.
- 9 A. Y. Fu, H.-P. Chou, C. Spence, F. H. Arnold and S. R. Quake, *Anal. Chem.*, 2002, **74**, 2451–2457.
- 10 A. Y. Fu, C. Spence, A. Scherer, F. H. Arnold and S. R. Quake, *Nat. Biotechnol.*, 1999, **17**, 1109–1111.
- 11 M. Berger, J. Castelino, R. Huang, M. Shah and R. H. Austin, *Electrophoresis*, 2001, **22**, 3883–3892.
- 12 M. P. MacDonald, G. C. Spalding and K. Dholakia, *Nature*, 2003, **426**, 421–424.
- 13 M. Yamada, M. Nakashima and M. Seki, *Anal. Chem.*, 2004, **76**, 5465–5471.
- 14 M. Yamada and M. Seki, *Anal. Chem.*, 2006, **78**, 1357–1362.
- 15 C. Hnatovsky, R. S. Taylor, E. Simova, V. R. Bhardwaj, D. M. Rayner and P. B. Corkum, *Opt. Lett.*, 2005, **30**, 1867–1869.
- 16 M. Kim, D. J. Hwang, H. Jeon, K. Hiromatsu and C. P. Grigoropoulos, *Lab Chip*, 2009, **9**, 311–318.
- 17 N. Bellini, K. C. Vishnubhatla, F. Bragheri, L. Ferrara, P. Minzioni, R. Ramponi, I. Cristiani and R. Osellame, *Opt. Express*, 2010, **18**, 4679–4688.
- 18 H. Schillers, M. Wälte, K. Urbanova and H. Oberleithner, *Biophys. J.*, 2010, **99**, 3639–3646.
- 19 R. R. Gattass and E. Mazur, *Nat. Photonics*, 2008, **2**, 219–225.
- 20 R. M. Vazquez, R. Osellame, D. Nolli, C. Dongre, H. van den Vlekert, R. Ramponi, M. Pollnau and G. Cerullo, *Lab Chip*, 2009, **9**, 91–96.
- 21 A. Marcinkevicius, S. Juodkazis, M. Watanabe, M. Miwa, S. Matsuo, H. Misawa and J. Nishii, *Opt. Lett.*, 2001, **26**, 277–279.
- 22 R. Osellame, V. Maselli, R. M. Vazquez, R. Ramponi and G. Cerullo, *Appl. Phys. Lett.*, 2007, **90**, 231118.
- 23 Y. Bellouard, A. Said and P. Bado, *Opt. Express*, 2005, **13**, 6635–6644.
- 24 T. G. Kuznetsova, M. N. Starodubtseva, N. I. Yegorenkov, S. A. Chizhik and R. I. Zhdanov, *Micron*, 2007, **38**, 824–833.

A.4 – Triple beam optical trap for microsyringe construction

Ramsay, W. T., Bechu, M., Quinones, V. A. B., Mei, Y., Schmidt, O. G. & Paterson, L.
“Triple beam optical trap for microsyringe construction” *Proc. SPIE 8097 Optical Trapping and Optical Micromanipulation VIII*, 809708 (2011).

DOI: 10.1117/12.893667

Triple beam optical trap for microsyringe construction

William T. Ramsay, Muriel Bechu, Vladimir A. Bolanos Quinones^a, Yongfeng Mei^{ab},
Oliver G. Schmidt^a and Lynn Paterson^{*}.

Scottish Universities Physics Alliance, School of Engineering and Physical Sciences,
Heriot-Watt University, Edinburgh, EH14 4AS, UK.

^a Institute for Integrative Nanosciences, IFW Dresden, Helmholtzstr. 20, 01069 Dresden, Germany.

ABSTRACT

A limited range of instruments are available which allow the controlled injection of sub-picolitre volumes; microfluidic devices and commercially produced mechanical microinjection systems accounting for the majority. We present an optically controlled microsyringe capable of dispensing femtolitres of liquid. Triple beam optical tweezers are used to manipulate hollow glass microneedles and also polymer microspheres which were used as ‘handles’ to assist the manipulation of microneedles and ‘plungers’ to dispense liquid from the microneedle.

Standard optical tweezers were used with the addition of a Ronchi ruling (250 lines per inch) mounted in the image relay telescope. The diffraction pattern generated by the Ronchi ruling produced three optical traps in the sample chamber. Trap spacing was controlled by translating the ruling along the axis of beam propagation within the image relay telescope.

Utilizing the three-beam trap, it was possible to manipulate pulled, borosilicate capillaries (5-150µm in length, 1-10µm in diameter) both perpendicular and parallel to the axis of the capillary. Rolled SiO/SiO₂ microtubes (4µm diameter, 50µm long) were also manipulated, however in this case polymer microspheres were used as ‘handles’. In both cases the microneedles did not align vertically along the propagation axis; an advantage over using a single beam optical trap. Tweezing a microsphere within a microneedle dispenses femtolitres of liquid from the needle. The force exerted on microneedles is calculated to be in the order of picoNewtons so may have applications where femtolitre volumes must be controllably delivered beyond a barrier, such as single cell microinjection.

Keywords: optical tweezers, diffraction, microneedles, microtubes, microcapillaries, microinjection, microsyringe
Ronchi ruling, lab-on-a-chip, microfluidics

1. INTRODUCTION

Optical tweezers, or a single beam optical trap, first demonstrated in the seminal paper by Ashkin¹ are used in the biological sciences to manipulate microscopic particles which have volumes of sub- to hundreds of femtolitres; for instance a 1µm diameter sphere, similar in volume to a bacterium, of around half a femtolitre, or a small mammalian cell which has a volume of around 200fl. It follows that the manipulation of particles with these dimensions within a confined space such as a hollow cylinder, which has the same inner diameter as the particle diameter, may be used to displace similarly small volumes. The ability to control of volumes of liquid in the femtolitre scale enables even microfluidic, lab-on-a-chip experiments to be miniaturised.

In this paper, we present a method for manipulating microneedles, and microspheres within the microneedles, creating an-optically controlled microsyringe with the potential to controllably dispense femtolitres of material. Our

^b Present address: Department of Materials Science, Fudan University, Handan Road 220, Shanghai 200433, China.

^{*} email L.Paterson@hw.ac.uk

approach uses a dynamic, linear, triple beam trap created by placing a Ronchi ruling in the vicinity of the focus within the image relay telescope in an optical tweezers setup.

1.2 Optical trapping of non-spherical particles

The majority of optical trapping experiments and theoretical simulations use spherical particles. This is because trapping of spherical particles is stable and the forces acting on a sphere can be modelled relatively easily due to well-established, accurate theory for symmetrical systems. However, throughout the last 20 years non-spherical particles have also been optically manipulated^{2,3} and a range of methods have been developed to produce different shapes and patterns of optical traps: methods such as using higher order laser modes⁴, interference of trapping beams⁵ and spatial light modulators⁶. As these technologies become more widely used, interest in modelling the optical trapping forces and torques on particles with less than spherical symmetry⁷, in particular cylindrical particles (microrods)⁸⁻¹², has also grown. Trapping techniques have also been adapted to specifically trap and manipulate microrods^{5,13-17}. However, to the best of our knowledge the optical manipulation of microneedles (or hollow microrods) has not been reported and this paper describes the first demonstration of such manipulations. We also consider the force exerted by the optical trap on the microneedle as it is dragged parallel to its long axis and manipulate a microsphere within a microneedle, which acts as a plunger within the optically assembled microsyringe, capable of dispensing femtolitre volumes.

1.2 Ronchi Rulings in optical tweezers

We have used a linear triple beam trap to manipulate microneedles and also microspheres within the microneedles. The triple beam trap was generated by placing a Ronchi ruling at the focal position within the image relay telescope of an optical tweezers setup. Ronchi rulings have been used previously in optical trapping experiments where an image of the grating (alternating bright and dark lines) is typically projected onto the plane where manipulation is to take place, not the pattern of diffracted beams. Garces-Chaves *et al.* use the image of a Ronchi ruling on an interface between a glass prism and water in evanescent field trapping to show a passive accumulation, guiding and trapping of thousands of particles, within linear fringe structures, over a macroscopic area¹⁸, however active manipulation is not possible due to the lack of a strong axial force. A standard optical tweezer setup can be used to project a reduced image of a Ronchi ruling at the focal plane of the microscope objective by placing the Ronchi at the back focal plane of the microscope objective¹⁵. Colloidal particles can be trapped within the bright fringes and actively manipulated by translating the Ronchi in a direction perpendicular to the rulings. More efficient axial trapping in linear fringes is achieved using interferometric tweezers^{13,15}, due to the negligible change in intensity distribution of the pattern over the Rayleigh range and the resulting, stronger, axial force.

The experiments described above generate a reduced image of the pattern of lines on the grating into the sample chamber where tweezing takes place. In this work, described below, we image the diffraction pattern, creating three optical traps in a line, whose separation can be adjusted by simply translating the Ronchi ruling along the axis of beam propagation.

2. EXPERIMENTAL METHOD

2.1 Optical trap

The experimental set up for the single beam and the three beam trap is depicted in figure 1. The output beam from a Nd:YAG laser (Ventus, Laser Quantum, Photonic Solutions) operating at 1064nm was directed upwards (M1) and then directed horizontally (M2) into a Keplerian telescope. The collimated output from the 1:1 telescope (L1 and L2) is then directed downwards by a dichroic mirror (DC) (Y1-1037-45UNP, CVI) into the back aperture of a x40 microscope objective (MO) with a NA of 0.65 (M40X, Newport). The beam is focused into a sample chamber, which is placed on an adapted translation stage (M-562-XYZ, Newport). White light from an LED is used to illuminate the sample from below and a CCD camera (WAT 250D, Watec, Altered Images) is placed behind the microscope objective at a distance of 160mm. The camera is connected to a laptop via a video capture card (UTV2820, Techgear) so that images and movies of tweezing can be recorded.

To transform this single beam set up into a triple beam trap, a binary Ronchi ruling (R) (B56-596, Edmund Optics) of 250 lines per inch (50 μ m period) was placed in the beam path. It was positioned in the vicinity of the focus of

the telescope within the image relay system of the setup, perpendicular to the optical axis. The objective lens projected a reduced image of the three diffracted beams at its front focal plane where the particles were situated within the sample chamber. The position of the ruling within the telescope to give an ideal structure of optical traps in the sample chamber was not known *a priori*. The ruling was mounted in a holder (STK01, Thor labs) and translated back and forth along the beam propagation direction by hand, to achieve the desired separation of optical traps.

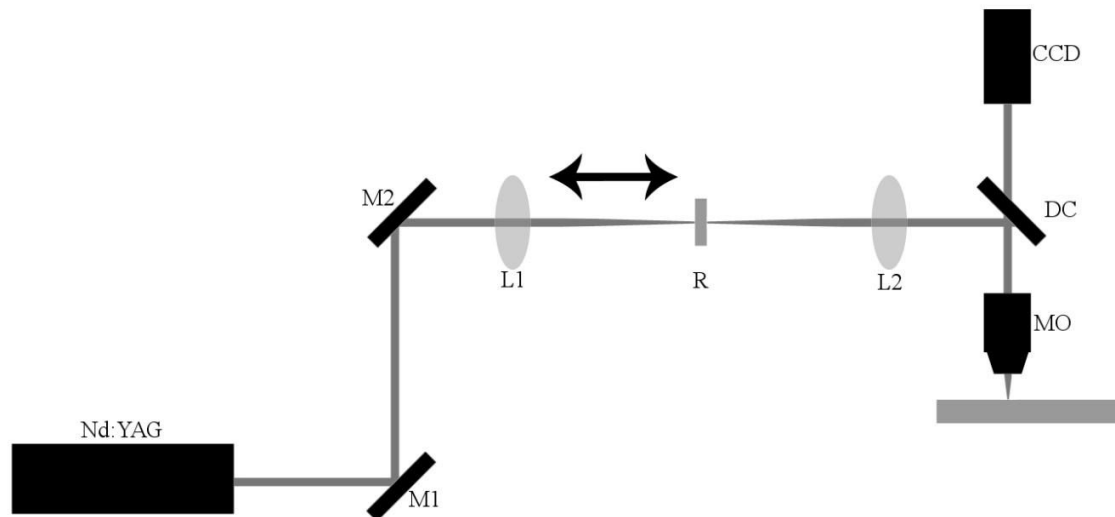


Figure 1. Experimental setup for the triple beam optical trap. The Ronchi ruling, R, is translated between the focus of the image relay telescope towards L1.

2.2. Quantification of trap spacing

The separation of the outer, first order traps from the central, zeroth order trap within the sample chamber was measured with respect to the distance that the Ronchi ruling was translated as shown in figure 2 in the results and discussion section. The distance between the optical traps was measured by trapping 3 μ m microspheres in each of the three traps. An image of the trapped particles for each position of the Ronchi was analysed by counting the number of pixels between the centres of the three trapped spheres and converting this to micrometers. This was repeated three times for each data point. The position of the Ronchi ruling was measured by eye with a steel ruler.

2.3. Sample preparation

Two types of microneedles have been used in these experiments; rolled up microneedles^{19,20} and pulled borosilicate capillaries. The fabrication of rolled up microneedles is described by Huang *et al.*¹⁹. Borosilicate capillaries (ID 0.5mm, OD 1.0mm, BF-100-50-10, Sutter Instruments) were pulled using a micropipette puller (P-97, Sutter Instruments) using a temperature of 289 (RAMP), a pull of 30, velocity of 120 and delay of 200. Needles from 15mm in length, 4-10 μ m in inner diameter and 6-14 μ m in outer diameter were produced and these pulled capillaries were shortened to a length of 60-10 μ m by simply dicing with a scalpel blade in deionised water. Trapped microspheres were either 3 μ m diameter latex spheres (17134, Polysciences) or 7 μ m polystyrene spheres (64100, Polysciences).

20 μ l of these microneedles plus microspheres in water were pipetted into a vinyl sample chamber on a microscope slide then a cover slip was placed on top. The sample was placed on the stage which was translated in x, y and z. A motion controller (Z825B, Thor labs) was used so that the sample could be moved at a constant velocity in a direction orthogonal to the propagation axis of the beam to simulate a fluid flow.

2.4. Measuring trapping velocity

The maximum velocity that a single, trapped microsphere could be moved was measured in order to calculate the trapping force of the three individual traps within the triple beam pattern compared to a single beam optical trap. A sample of diluted $3\mu\text{m}$ spheres (0.1% stock in water) was prepared on a microscope slide as described in the previous section. The motion controller (Z825B, Thor Labs) was programmed to move the sample 2mm in the x direction, at a constant velocity and return to the original position. The program was set to repeat this cycle with increasing velocities from 0.05mm s^{-1} to 0.5mm s^{-1} at increments of 0.01mm s^{-1} . This process was used for powers ranging from 50mW to 100mW (in 10mW increments) with each set repeated three times. The maximum velocity attained before the sphere dropped from the optical trap was recorded and used to calculate the viscous drag force using Stokes' law.

3. RESULTS AND DISCUSSION

3.1. Control of the triple beam trap

Placing a Ronchi ruling at the vicinity of the beam focus within the image relay telescope in the optical system created the triple beam trap. The resulting diffraction pattern containing the zeroth order and two first order beams were directed through the microscope objective into the sample chamber where trapping took place. Separation between the zeroth order beam and the two first order beams was controlled by translating the Ronchi ruling within the image relay telescope along the axis of beam propagation. The distance between traps in the sample chamber, controlled by varying the position of the Ronchi, are shown in figure 2.

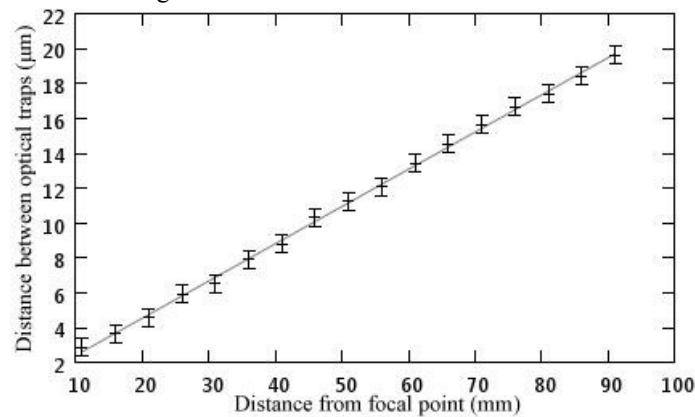


Figure 2. Distance between the zeroth order and first order traps as the position of the Ronchi ruling within the image relay telescope is changed.

Microspheres can be manipulated simultaneously in all three traps in both x and y directions by translating the sample stage. They can also be moved, as shown in figure 3, by translating the Ronchi ruling such that the particle trapped in the zeroth order beam remains stationary and those particles trapped in the peripheral beams move away from the central beam. It can be seen from figure 2 that moving the Ronchi a distance of 20mm away from the focus within the image relay telescope results in the outer, first order traps moving a distance of $5\mu\text{m}$ away from the central trap.



Figure 3. Sequence of images manipulating three microspheres in x by translating the Ronchi ruling in the tweezers setup. Frame A: three $3\mu\text{m}$ spheres are separated by $3.5\mu\text{m}$ each. Frame B: the Ronchi is translated 40 mm and the separation between the traps and hence the particles increases to $12\mu\text{m}$. Frame C: the Ronchi is translated a further 30mm towards L1 resulting in a final separation of $18\mu\text{m}$ between the particles.

3.2. Optical tweezing of microspheres in triple beam trap

As a force calibration method we calculate the viscous drag on the trapped spheres that is exerted by a fluid flow. The viscous force that a fluid of viscosity η exerts on a spherical particle of radius r , moving with a velocity v is described by Stokes' law

$$F_{Stokes} = 6\pi\eta rv \quad (1.1)$$

The maximum force that a single beam optical trap can exert on a spherical particle can be calculated if the maximum velocity with which the optically trapped particle can be moved is measured and if the viscosity of the medium and the particle radius is known, by equating F_{trap} with F_{Stokes} . The force that can be exerted onto 3 μ m diameter, polymer spheres by each beam in the triple beam trap has been calculated in this way, as well as by a single beam trap with an equal power to the triple beam trap, for comparison. The tweezing was performed in water, which has a viscosity of 10^{-3} Nsm^{-2} , and maximum tweezing velocity measurements (critical velocity) in the x direction were made three times each on 3 μ m microspheres, at powers from 50mW to 100mW (10mW increments), measured at the back aperture of the microscope objective lens. The critical velocity results were used to calculate the trap force following Stokes' Law (equation 1.1) and results are presented in figure 4.

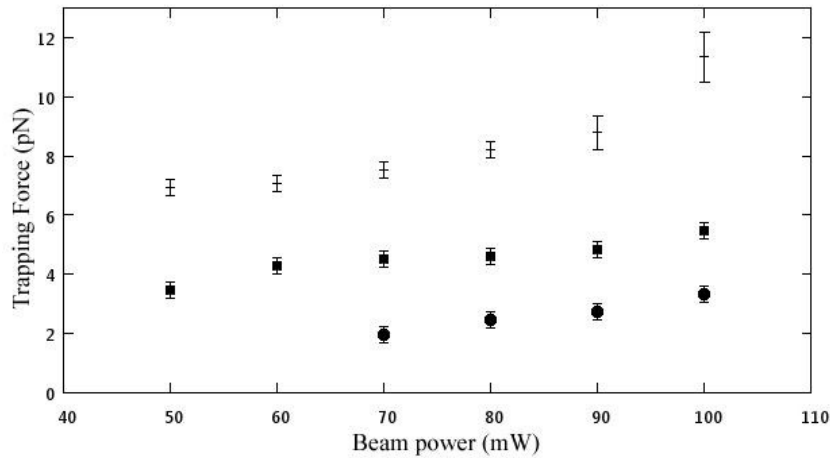


Figure 4. Forces experienced by 3 μ m spheres in a single beam optical trap with beam powers of 50-100mW (dashes). Also shown are the trapping forces on spheres in the 0th order of the triple beam trap (squares) and the 1st order of the triple beam trap (circles) with the total power of the triple beam pattern of 50 to 100mW. (Powers were measured at the objective back aperture).

Using equation 1.1, and our measurements for critical velocity, it was calculated that the single beam optical tweezer with a power of 100mW (at the back aperture of the objective) exerts a force of 11.3pN (± 0.85 pN) on a 3 μ m diameter sphere. In a triple beam trap of equal total power (100mW), the zeroth order spot, the central trap in the triple beam trap exerts a force of 5.5pN (± 0.3 pN) on a 3 μ m sphere. The first order spots of the same pattern exert a force of 3.3pN (± 0.3 pN) on a 3 μ m diameter sphere.

3.3. Optical manipulation of microneedles

Two types of microneedle have been used in these optical trapping experiments as detailed above: rolled up SiO/SiO₂ microneedles and pulled borosilicate capillaries. In the first case a single beam trap was used to manipulate the needles. Neither type could be tweezed perpendicular to the microneedle's long axis with a single beam trap. However, both types could be rotated in the x-y plane by continuously moving the trap near the end of a microneedle in a direction perpendicular to its long axis. This behaviour is shown in figure 5 where a single beam trap is continuously moved in a direction perpendicular to the long axis of the needle. The needle follows the beam and hence rotates.

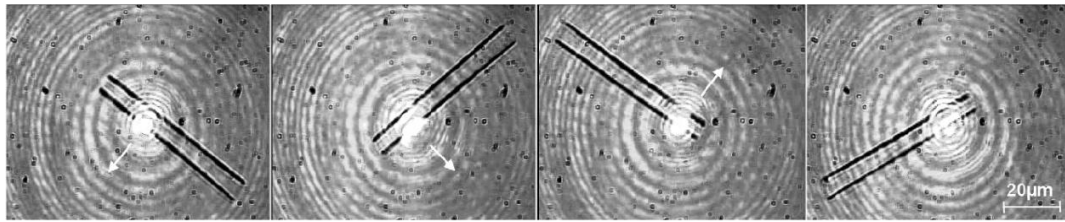


Figure 5. A rolled up SiO/SiO₂ microneedle, 63μm in length, rotated by moving a single beam trap.

A major parameter that affects trapping efficiency is the refractive index contrast between the trapped particle and the surrounding medium. It follows that microneedles with the same outer diameter but larger inner diameter will be less efficiently trapped than a microneedle with thicker walls. This is indeed what we observed as pulled borosilicate capillaries, with a thicker wall than the rolled up capillaries, could be moved in this way using lower power of less than 100mW.

Trapping of rolled up microneedles in a direction perpendicular to its long axis was possible. Figure 6 shows the microneedle being dragged into the triple beam trap. The microneedle is trapped with its long axis out of alignment with the triple beam trap. In all cases the microneedle was oriented with one side trapped by the +1 order trap and the other side of the needle held in the -1 order trap and this alignment can be seen in the third frame of figure 6.



Figure 6. A rolled up microneedle is attracted by the triple beam, trapping pattern. The first frame shows the microneedle at the position from where it started to move towards the traps. The time between the first and second frame is 20s. From the second to third frame the time is only 7s. (40x magnification) (Laser power was 490mW)

It was not possible to move the rolled up microneedles in a direction parallel to their long axis using a single or triple beam trap. To achieve this movement, which is crucial if microneedles are to be used for microinjection though some sort of barrier, we make use of microsphere handles. Figure 7 shows the translation of a microneedle almost parallel to its long axis using a 7μm sphere as a handle with which to push the needle. Microspheres with a slightly larger diameter than the outer diameter of the microneedle were chosen for this purpose.



Figure 7. A 7μm diameter sphere is trapped in the zeroth order trap and is used as a handle to push a rolled up microneedle parallel to its long axis. In this case two 7μm spheres have stuck together and four 3μm spheres are stuck in the capillary. The arrow points to a reference particle in the sample.

In contrast, a single beam trap can drag a pulled borosilicate capillary parallel to its long axis. This is achieved in an inverted optical tweezers system by positioning the beam at one end of the capillary and moving it away from the capillary in the direction parallel to its long axis, such that the capillary follows. This is shown in figure 8 where a capillary of length 150 μm and width 9 μm is dragged across a sample at a velocity of 7 μms^{-1} ($\pm 1\mu\text{ms}^{-1}$). Higher velocities were not possible due to increased scattering force as power was increased, resulting in the capillaries aligning in the direction of beam propagation.

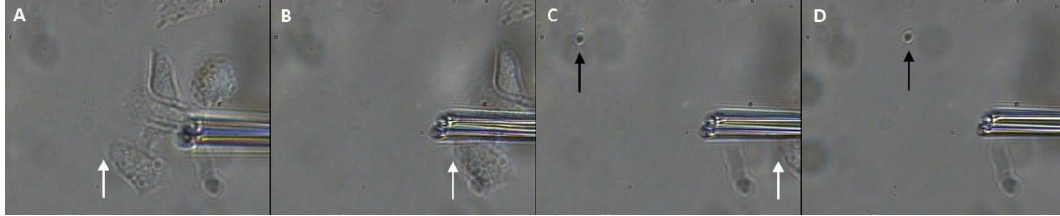


Figure 8. A pulled borosilicate capillary is dragged, using a single beam trap, across a sample. The arrow shows a reference point in the sample.

3.4. Force exerted by microneedles

Stokes' law is only valid for spherical objects with a very low Reynolds number such as colloidal microspheres. It is useful however, to calculate the force that an optically trapped microneedle can exert. There is no analytical expression for the viscous drag force on a solid or hollow cylinder, but there are several approaches for approximating this such as the numerical beads on a shell model²¹ or the experimental solution measuring the drag coefficient for a solid cylinder in an unbounded fluid^{22,23}. We have used the method developed by Hunt *et al*²⁴ as it takes into account a surface close to the cylindrical particle and parallel to the cylinder's axis. Both types of microneedle are in water and are situated at the bottom of the sample chamber. Optical trapping of the microneedles in this work does not lift them a significant distance off the bottom of the sample chamber. The drag force parallel to the microneedle's axis can be calculated from

$$F_{drag} = C_{\parallel} \eta L v \quad (1.2)$$

where η is the viscosity of the liquid, L is the length of the microtubule, v is the terminal velocity of translation of the microneedle through the liquid and C_{\parallel} is the dimensionless drag coefficient for the motion parallel to the microneedle's long axis. The drag coefficient depends on the height of the microneedle above the surface of the sample chamber and is given by

$$C_{\parallel} = 2\pi / \cosh^{-1}(h/r) \quad (1.3)$$

where h is the distance between the sample chamber surface and the central axis of the microneedle and r is the radius of the microneedle. Equations 1.2 and 1.3 apply to solid cylinders, but in this work we are using hollow microtubes. We approximate our hollow microtubes to solid cylinders because we neglect the liquid flow within our microneedles due to their small diameter. We are able to neglect volumetric flux because it is proportional to r^4 according to the Hagen-Poiseuille law so it is decreased by a factor of 16 if the radius is halved. Additionally, friction forces, thought to be due to the electro viscous effect, are predominant in microtubes with small diameter²⁵. Therefore, the fluid inside the microneedle acts as a resistance to the approaching fluid, making the hollow cylinder effectively a solid cylinder to which equation 1.2 can be applied.

Applying equations 1.2 and 1.3 to our data, in which a pulled borosilicate capillary of 150 μm length and 9 μm width was dragged with a velocity of 7 μms^{-1} ($\pm 1\mu\text{ms}^{-1}$) through water parallel to its long axis, give us a force of 10pN ($\pm 1\text{pN}$) on this cylindrical particle.

3.5. Optical construction and control of microsyringe

Microspheres were used both as a handle to push the microneedle in the direction parallel to its long axis (figure 7) and as a plunger inside the microneedle, as shown in figure 9. A microsphere plunger ($3\mu\text{m}$ diameter sphere) is trapped in one of the first order traps and manoeuvred into a rolled up microneedle. The microsphere can be moved along the length of the microneedle, either by translating the sample stage with respect to the beam (as is shown here) or by translating the Ronchi ruling such that any sphere trapped in either of the first order traps will be moved.

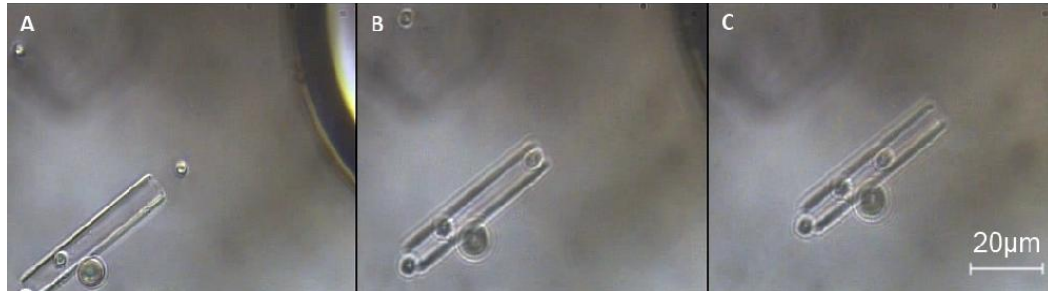


Figure 9. A $3\mu\text{m}$ diameter sphere is trapped in one of the first order traps and manoeuvred into a stationary, rolled up microneedle.

Both the translation of a microneedle parallel to its long axis and the manipulation of microspheres within the microneedle results in the realization of an all-optically controlled microsyringe. This is achieved here by pushing a rolled up SiO/SiO_2 tube, of internal diameter just over $3\mu\text{m}$, with an optically trapped $7\mu\text{m}$ polymer sphere held in the zeroth order trap of the triple beam pattern. A $3\mu\text{m}$ diameter sphere is held by one of the first order traps within the needle. The needle and its handle can be held stationary whilst the Ronchi ruling is moved in the beam path as shown in figure 1. This leads to the $3\mu\text{m}$ sphere being moved along the inside of the needle, whilst maintaining the stationary position of the $7\mu\text{m}$ sphere handle and the needle, dispensing material inside the needle.

4. CONCLUSION

We have demonstrated concepts with which to realise an all-optically controlled microsyringe. A triple beam trap was used to manipulate the needles, microsphere handles and microsphere plungers of the device. Placing a Ronchi ruling within the image relay telescope of the optical tweezers system generated a diffraction pattern. The zeroth order beam and the weaker +1 and -1 orders of the diffraction pattern were imaged into a sample chamber and used as a triple beam trap. A microsphere handle, trapped in the zeroth order spot, was used to translate a SiO/SiO_2 microneedle parallel to its long axis. A microsphere plunger was trapped in the first order spot and was moved with respect to the handle by translation of the Ronchi ruling. We also found that a single beam trap could be used to drag a pulled borosilicate microneedle parallel to its long axis with a trap force of 10pN .

An all-optical microsyringe such as this enables the control of sub to hundreds of femtolitres with applications in lab-in-a-chip and lab-in-a-cell technologies, such as injecting single cells and precisely controlling delivery of reagents to chemical reactions.

Acknowledgements

WTR thanks the Engineering and Physical Sciences Research Council (UK) for funding.

5. REFERENCES

- [1] Ashkin, A., Dziedzic, J. M., et al., "Observation of a single-beam gradient force optical trap for dielectric particles." *Optics Letters* 11(5), 288-290 (1986).
- [2] Higurashi, E., Tanaka, H., et al., "Optically induced rotation of anisotropic micro-objects fabricated by surface micromachining." *Applied Physics Letters* 64(17), 2209-2210 (1994).
- [3] Galajda, P. and Ormos, P., "Rotors produced and driven in laser tweezers with reversed direction of rotation." *Applied Physics Letters* 80(24), 4653-4655 (2002).
- [4] Sato, S., M. Ishigure, et al., "Optical trapping and rotational manipulation of microscopic particles and biological cells using higher-order mode Nd:YAG laser beams." *Electronics Letters* 27(20), 1831-1832 (1991).
- [5] Paterson, L., MacDonald, M. P., et al., "Controlled rotation of optically trapped microscopic particles." *Science* 292(5518), 912-914 (2001).
- [6] Hayasaki, Y., Itoh, M., Yatagai, T. and Nishida, N., "Nonmechanical Optical Manipulation of Microparticle Using Spatial Light Modulator." *Optical Review* 6(1), 24-27 (1999).
- [7] Ling, L., Zhou, F., et al., "Optical forces on arbitrary shaped particles in optical tweezers." *Journal of Applied Physics* 108, 073110 (2010).
- [8] Gauthier, R. C., "Theoretical investigation of the optical trapping force and torque on cylindrical micro-objects." *Journal of the Optical Society of America B* 14(12), 3323-3333 (1997).
- [9] Gauthier, R. C., Ashman, R. C., et al., "Experimental confirmation of the optical trapping properties of cylindrical objects." *Applied Optics* 38(22), 4861-4869 (1999).
- [10] Matstre, D. and Vincent, P., "Making photonic crystals using trapping and binding optical forces on particles." *Journal of Optics A* 8(12), 1059-1066 (2006).
- [11] Simpson, S. H. and Hanna, S., "Holographic optical trapping of microrods and nanowires." *Journal of the Optical Society of America A* 27(6), 1255-1264 (2010).
- [12] Simpson, S. H. and Hanna, S., "Optical trapping of microrods: variation with size and refractive index." *Journal of the Optical Society of America A* 28(5), 850-858 (2011).
- [13] MacDonald, M. P., Paterson, L., et al., "Trapping and manipulation of low-index particles in a two-dimensional interferometric optical trap." *Optics Letters* 26(12), 863-865 (2001).
- [14] Yu, T., Cheong, F., et al., "The manipulation and assembly of CuO nanorods with line optical tweezers." *Nanotechnology* 15, 1732-1736 (2004).
- [15] Chiou, A. E., Wang, W., et al., "Interferometric optical tweezers." *Optics Communications* 133, 7-10 (1997).
- [16] Phillips, D. B., Carberry, D. M., et al., "Optimizing the optical trapping stiffness of holographically trapped microrods using high speed video tracking." *Journal of Optics* 13, 044023 (2011).
- [17] Bonin, K. D., B. Kourmanov, et al., "Light torque nanocontrol, nanorotors and nanorockers." *Optics Express* 10(19), 984-989 (2002).
- [18] Garcés-Chavez, V., Dholakia, K., et al., "Extended-area optically induced organisation of microparticles on a surface." *Applied Physics Letters* 86(3), 031106 (2005).
- [19] Huang, G., Mei, Y., et al., "Rolled-up transparent microtubes as two-dimensionally confined culture scaffolds of individual yeast cells." *Lab on a Chip* 9(2), 263-268 (2009).
- [20] Mönch, I., Schumann, J., et al., "Multifunctional nanomembranes self-assembled into compact rolled-up sensor-actuator devices." *Smart Materials and Structures* 20, 085016 (2011).
- [21] Roger, R. and Weidman, P., "Axisymmetric Stokes drag on hollow cylinders: Computation and comparison with experiment." *European Journal of Mechanics B-Fluids* 17(2), 187-203 (1998).
- [22] Tirado, M. M. and de la Torre, J. G., "Translational friction coefficients of rigid, symmetric top macromolecules - application to circular-cylinders." *Journal of Chemical Physics* 71(6), 2581-2587 (1979).
- [23] Reece, P. J., Toe, W. J., et al., "Characterisation of semiconductor nanowires using optical tweezers." *Nanoletters* 11(6), 2375-2381 (2011).
- [24] Hunt, A. J., F. Gittes, et al., "The force exerted by a single kinesin molecule against a viscous load." *Biophysical Journal* 67(2), 766-781 (1994).
- [25] Ren, L., Li, D., et al., "Interfacial electrokinetic effects on liquid flow in microchannels." *International Journal of Heat and Mass Transfer* 44(16), 3125-3134 (2001).

References

- [1] Robert Hooke “Micrographica” *Royal Society*. (1665).
- [2] Schmid, A. *et al.* “Chemical and biological single cell analysis” *Curr. Opin. Biotechnol.* **21(1)**, 12-20 (2010).
- [3] Wang, D. & Bodovitz, S. “Single cell analysis: the new frontier in ‘omics’” *Trends Biotechnol.* **28(6)**, 281-290 (2010).
- [4] Hogan, R. P. & Kenny, L. C. “SACreview ‘omic’ technologies: genomics, transcriptomics, proteomics and metabolomics” *Obstet Gynecol* **13**, 189-195 (2011).
- [5] Ritchie, M. D. *et al.* “Methods of integrating data to uncover genotype-phenotype interactions” *Nature Rev. Genet.* **16(2)**, 85-97 (2015).
- [6] Gehlenborg, N. *et al.* “Visualization of omics data for systems biology” *Nat. Methods.* **7(3)**, S56-S68 (2010).
- [7] Lui, B. *et al.* “Micro-separation toward systems biology” *J. Chromatogr. A* **1106(1)**, 19-28 (2006).
- [8] Weber, B. L. “Cancer genomics” *Cancer Cell* **1(1)**, 37-47 (2002).
- [9] Velculescu, V. E. *et al.* “Analysing uncharted transcriptomes with SAGE” *Trends Genet.* **16(10)**, 423-425 (2000).
- [10] Wang, Z. *et al.* “RNA-Seq: a revolutionary tool for transcriptomics” *Nature Rev. Genet.* **10(1)**, 57-63 (2009).
- [11] Jaitin, D. A. *et al.* “Massively Parallel Single-Cell RNA-Seq for Marker-Free Decomposition of Tissues into Cell Types” *Science* **343(6172)**, 776-779 (2014).

- [12] Dopazo, J. "Genomics and transcriptomics in drug discovery" *Drug Discov. Today* **19(2)**, 126-132 (2014).
- [13] Vitzthum, F. *et al.* "Proteomics: From Basic Research to Diagnostic Application. A Review of Requirements & Needs" *J. Proteome Res.* **4(4)**, 1086-1097 (2005).
- [14] Whitesides, G. M. "The origins and the future of microfluidics" *Nature* **442**, 368-373 (2006).
- [15] Franke, T. A. & Wixforth, A. "Microfluidics for miniaturized laboratories on a chip" *Chemphyschem.* **9**, 2140-2156 (2008).
- [16] Rios, A. *et al.* "Miniaturization through lab-on-a-chip: Utopia or reality for routine laboratories? A review" *Anal. Chim. Acta* **740**, 1-11 (2012).
- [17] Andersson, H. & van der Berg, A. "Microtechnologies and nanotechnologies for single-cell analysis" *Curr. Opin. Biotechnol.* **15(1)**, 44-49 (2004).
- [18] Wadsworth, M. H. *et al.* "Marrying microfluidics and microwells for parallel, high-throughput single-cell genomics" *Genome Biol.* **16(129)**, (2015).
- [19] Yin, H. & Marshall, D. "Microfluidics for single cell analysis" *Curr. Opin. Biotechnol.* **23(1)**, 110-119 (2012).
- [20] Lecault, V. *et al.* "Microfluidic single cell analysis: from promise to practice" *Curr. Opin. Chem. Biol.* **16(3-4)**, 381-390 (2012).
- [21] Legally, E. T. *et al.* "Single-Molecule DNA Amplification and Analysis in an integrated microfluidic device" *Anal. Chem* **73(3)**, 565-570 (2001).
- [22] Choudhury, D. *et al.* "Quantum dot enabled thermal imaging of optofluidic devices" *Lab Chip.* **12**, 2414-2420 (2012).

- [23] Choudhury, D. *et al.* "A 3D mammalian cell separator biochip" *Lab Chip* **12**, 948-953 (2012).
- [24] Myers, F. B. & Lee, L. P. "Innovations in optical microfluidic technologies for point-of-care diagnostics" *Lab Chip* **8(12)**, 2015-2031 (2008).
- [25] Martinez, A. W. *et al.* "Diagnostics for the developing world: microfluidic paper-based analytical devices" *Anal. Chem.* **82**, 3-10 (2010).
- [26] Savile Bradbury "The Evolution of the Microscope" *Pergamon Press*. (1967).
- [27] Hecht, E. "Optics" 2nd Edition, USA, Addison-Wesley (1987).
- [28] Newton, I. "Opticks: or a treatise of the Reflections, Refractions, Inflections and Colours of Light" 4th Edition, London, William Innys (1730).
- [29] Bessis, M. *et al.* "Cytophysiologie-irradiation des organites cellulaires a laide dun laser a rubis" *Comp. Rend. Acad. Sci.* **255**, 1010 (1962).
- [30] Dolmans, D. E. G. J. *et al.* "Photodynamic therapy for cancer" *Nat. Rev. Cancer* **3**, 380-387 (2003).
- [31] Brancalion, L. & Moseley, H. "Laser and Non-laser Light Sources for Photodynamic Therapy" *Lasers Med. Sci.* **17**, 173-187 (2002).
- [32] Winter, P. W. & Shroff, H. "Faster fluorescence microscopy: advances in high speed biological imaging" *Curr. Opin. Chem. Biol.* **20**, 46-53 (2014).
- [33] Santi, P. A. "Light Sheet Fluorescence Microscopy: A Review" *J. Histochem. Cytochem.* **59(2)**, 129-138 (2011).
- [34] Kovarik, M. L. & Jacobson, S. C. "Nanofluidics in Lab-on-a-Chip Devices" *Anal. Chem.* **81(17)**, 7133-7140 (2009).

- [35] Cancer Research UK Annual Report 2015/16. “https://www.cancerresearchuk.org/sites/default/files/cruk_annual_report_and_accounts_201516.pdf” (Accessed 05/03/2017).
- [36] Moore, N. M. *et al.* “Physical Sciences-Oncology Centers: Bridging Engineers and Oncologists for a New Perspective on Fighting Cancer” *Cell. Mol. Bioeng.* **3(4)**, 334-336 (2010).
- [37] Stevenson, D. J. *et al.* “Single cell optical transfection” *J. R. Soc. Interface* **7**, 863-871 (2010).
- [38] Evan, G. I. & Vousden, K. H. “Proliferation, cell cycle and apoptosis in cancer” *Nature* **411(6835)**, 342-48 (2001).
- [39] Office for National Statistics “Mortality statistics: Deaths registered in England and Wales”
- [40] General Register Office for Scotland “Vital events reference tables”
- [41] Northern Ireland Statistics and Research Agency “Registrar General Annual Reports”
- [42] Ahmad, A. S. *et al.* “Trends in the lifetime risk of developing cancer in Great Britain: comparison of risk for those born from 1930 to 1960” *Br. J. Cancer* **112(5)**, 943-947 (2015).
- [43] Hanahan, D. & Weinberg, A. “The hallmarks of cancer” *Cell* **100(1)**, 57-70 (2000).
- [44] Hanahan, D. & Weinberg, A. “Hallmarks of cancer: the next generation” *Cell* **144(5)**, 646-674 (2011).
- [45] Surget, S. *et al.* “Uncovering the role of p53 splice variants in human malignancy: a clinical perspective” *Onco. Targets. Ther.* **7**, 57-68 (2013).

- [46] Levine, A. J. *et al.* "The p53 tumour suppressor gene" *Nature* **351(6326)**, 453-456 (1991).
- [47] Hollstein, M. *et al.* "p53 mutations in human cancers" *Science* **253(5015)**, 49-53 (1991).
- [48] Siegel R. L. *et al.* "Cancer statistics, 2016" *CA: Cancer J. Clin.* **66(1)**, 7-30 (2016).
- [49] Radulovich, N. *et al.* "Human pancreatic duct epithelial cell model for *KRAS* transformation" *Methods Enzymol.* **439**, 1-13 (2008).
- [50] Bardeesy, N. & DePinho, R. A. "Pancreatic cancer biology and genetics" *Nat. Rev. Cancer* **2(12)**, 897-909 (2002).
- [51] Maitra, A. *et al.* "Molecular pathogenesis of pancreatic cancer" *Best Pract. Res. Cl. Gas.* **20(2)**, 211-226 (2006).
- [52] Murtaugh, L. C. & Leach S. D. "A case of mistaken identity? Noductal origins of pancreatic "ductal" cancers" *Cancer Cell* **11(3)**, 211-213 (2007).
- [53] Cancer Research UK "<http://www.cancerresearchuk.org/health-professional/cancer-statistics/statistics-by-cancer-type/pancreatic-cancer/survival>" (Accessed 01/09/2015)
- [54] Deramaudt, T. & Rustgi, A.K. "Mutant KRAS in the initiation of pancreatic cancer" *Biochim. Biophys. Acta* **1756(2)**, 97-101 (2005).
- [55] Ellis, C. A. & Clark, G. "The importance of being K-Ras" *Cell Signal.* **12(7)**, 425-434 (2000).
- [56] Weyden, L. & Adams, D. J. "The Ras-association domain family (RASSF) members and their role in human tumorigenesis" *Biochim. Biophys. Acta* **1776(1)**, 58-85 (2007).

- [57] Buday, L. & Downward, J. “Many face of Ras activation” *Biochim. Biophys. Acta* **1286(2)**, 178-187 (2008).
- [58] Cully, M. & Downward, J. “SnapShot: Ras signaling” *Cell* **133(7)**, 1292 (2008).
- [59] Rajalingam, K. *et al.* “Ras oncogenes and their downstream targets” *Biochim. Biophys. Acta* **1773(8)**, 1177-1195 (2007).
- [60] Feig, L. A. “Cell signalling: Life or death decisions of Ras proteins” *Curr. Biol.* **12(7)**, R259-R261 (2002).
- [61] Eser, S. *et al.* “Oncogenic KRAS signalling in pancreatic cancer” *Br. J. Cancer* **111**, 817-822 (2014).
- [62] Friday, B. B. & Adjei, A. A. “K-ras as a target for cancer therapy” *Biochim. Biophys. Acta* **1756(2)**, 127-144 (2005).
- [63] Collins, M. A. *et al.* “Oncogenic Kras is required for both the initiation and maintenance of pancreatic cancer in mice” *J. Clin. Invest.* **122(2)**, 639-653 (2012).
- [64] Hingorani, S. R. *et al.* “Preinvasive and invasive ductal pancreatic cancer and its early detection in the mouse” *Cancer Cell* **4(6)**, 437-450 (2003).
- [65] Li, C. *et al.* “Identification of pancreatic cancer stem cells” *Cancer Res.* **67(3)**, 1030-1037 (2007).
- [66] Naldini, L. *et al.* “*In Vivo* gene delivery and stable transduction of nondividing cells by a lentiviral vector” *Science* **272(5259)**, 263-267 (1996).
- [67] Felgner, P. L. *et al.* “Lipofection: A highly efficient, lipid-mediated DNA-transfection procedure” *Proc. Natl. Acad. Sci.* **84**, 7413-7417 (1987).
- [68] Kingston, R. E. *et al.* “Calcium phosphate transfection” *Curr. Protoc. Mol. Biol.* **9**, S63 (2013).

- [69] Mehier-Humbert, S. & Guy, R. H. "Physical methods for gene transfer: Improving the kinetics of gene delivery into cells" *Adv. Drug Deliv. Rev.* **57**, 733-753 (2005).
- [70] Nakagawa, Y. *et al.* "Production of knockout mice by DNA microinjection of various CRISPR/Cas9 vectors into freeze-thawed fertilized oocytes" *BMC Biotechnology* **15**, 33 (2015).
- [71] McKnight, T. E. *et al.* "Tracking gene expression after DNA delivery using spatially indexed nanofiber arrays" *Nano Lett.* **4(7)**, 1213-1219 (2004).
- [72] Matthews, K. E. & Keating, A. "Gene therapy with physical methods of gene transfer" *Transfus. Sci.* **17(1)**, 29-34 (1996).
- [73] Iida, A. *et al.* "Gene delivery into cultured plant cells by DNA-coated gold particles accelerated by a pneumatic particle gun" *Theor. Appl. Genet.* **80(6)**, 813-816 (1990).
- [74] Finer, J. J. *et al.* "Development of the particle inflow gun for DNA delivery to plant cells" *Plant Cell Rep.* **11(7)**, 323-328 (1992).
- [75] Sharei, A. *et al.* "A vector-free microfluidic platform for intracellular delivery" *Proc. Natl. Acad. Sci. U.S.A.* **110(6)**, 2082-2087 (2012).
- [76] Bessis, M & Ter-Pogossian, M. M. "Micropuncture of cells by means of a laser beam" *Annals of the New York Academy of Sciences* **122**, 689-694 (1965).
- [77] Tsukakoshi, M. *et al.* "A novel method of DNA transfection by laser microbeam cell surgery" *Appl. Phys. B* **35**, 135-140 (1984).
- [78] Spence D. E. *et al.* "60-fsec pulse generation from a self-mode-locked Ti: sapphire laser" *Opt. Lett.* **16(1)**, 42-44 (1991).

- [79] Tao, W. *et al.* "Direct gene transfer into human cultured cells facilitated by laser micropuncture of the cell membrane" *Proc. Natl. Acad.* **84(12)**, 4180-4184 (1987).
- [80] Tirlapur, U. K. & König, K. "Targeted transfection by femtosecond laser" *Nature* **418**, 290-291 (2002).
- [81] Antkowiak, M. *et al.* "Femtosecond optical transfection of individual mammalian cells" *Nat. Protoc.* **8(6)**, 1216-1233 (2013).
- [82] Mohanty, S. K. *et al.* "Laser-assisted microinjection into targeted animal cells" *Biotechnol. Lett.* **25**, 895-899 (2003).
- [83] Brown, C. T. *et al.* "Enhanced operation of femtosecond lasers and application in cell transfection" *J. Biophoton.* **1(3)**, 183-199 (2008).
- [84] Lei, M. *et al.* "Femtosecond laser-assisted microinjection into living neurons" *J. Neurosci. Methods* **174**, 215-218 (2008).
- [85] Antkowiak, M. *et al.* "Towards gene therapy based on femtosecond optical transfection" *Proc. SPIE* **8427**, 84270R (2012).
- [86] Wehner, M. *et al.* "Laser-mediated perforation of plant cells" *Proc. SPIE* **6632**, 66321W (2007).
- [87] Mitchell, C. A. *et al.* "Femtosecond optoinjection of intact tobacco BY-2 cells using a reconfigurable photoporation platform" *PLoS ONE* **8(11)**, e79235 (2013).
- [88] Tsampoula, X. *et al.* "Fibre based cellular transfection" *Opt. Express* **16(21)**, 17007-17013 (2008).
- [89] He, H. *et al.* "Targeted photoporation and transfection in human HepG2 cells by a fibre femtosecond laser at 1554 nm" *Opt. Lett.* **33(24)**, 2961-2963 (2008).

- [90] Praveen, B. B. *et al.* "Enhancement and optimization of plasmid expression in femtosecond optical transfection" *J. Biophoton.* **4(4)**, 229-235 (2011).
- [91] Stevenson, D. *et al.* "Femtosecond optical transfection of cells: viability and efficiency" *Opt. Express* **14(16)**, 7125-7133
- [92] Tsampoula, X. *et al.* "Femtosecond cellular transfection using a nondiffracting light beam" *Appl. Phys. Lett.* **91**, 053902 (2007).
- [93] Paterson, L. *et al.* "Photoporation and cell transfection using a violet diode laser" *Opt. Express* **13(2)**, 595-600 (2005).
- [94] Pirolo, A. *et al.* "Indocyanine green-assisted diode-laser optoporation of plant cells" *Proc SPIE* **2928**, 176-179 (1996).
- [95] Palumbo, G. *et al.* "Targeted gene transfer in eucaryotic cells by dye-assisted laser optoporation" *J. Photochem. Bhotobiol. B* **36**, 41-46 (1996).
- [96] Xiong, R. *et al.* "Comparison of gold nanoparticle mediated photoporation: Vapor nanobubbles outperform direct heating for delivering macromolecules in live cells" *ACS Nano* **8(6)**, 6288-6296 (2014).
- [97] Bhattacharyya, K. *et al.* "Optically absorbing nanoparticle mediated cell membrane permeablization" *Opt. Lett.* **37(21)**, 4474-4476 (2012).
- [98] Sipos, B. *et al.* "A comprehensive characterization of pancreatic ductal carcinoma cell lines: towards the establishment of an in vitro research platform" *Virchows Arch.* **442**, 444-452 (2003).
- [99] Ouyang, H. *et al.* "Immortal Human Pancreatic Duct Epithelial Cell Lines with Near Normal Genotype and Phenotype" *Methods Enzymol.* **157(5)**, 1623-1631 (2000).
- [100] Radulovich, N. *et al.* "Human Pancreatic Duct Epithelial Cell Model for KRAS Transformation" *Methods Enzymol.* **439**, 1-13 (2008).

- [101] Leung L. *et al.* “Loss of Canonical Smad4 Signaling Promotes KRAS Driven Malignant Transformation of Human Pancreatic Duct Epithelial Cells and Metastasis” *PLos ONE*. **9(7)**, e84366 (2013).
- [102] Li L. H. *et al.* “Apoptosis induced by DNA uptake limits transfection efficiency.” *Anal. Chem.* **72**, 1342-1347 (2000).
- [103] Souhayer J. S. *et al.* “Characterization of Cellular Optoporation with Distance” *Exp. Cell. Res.* **253(2)**, 541-550 (1999).
- [104] Marchington, R. F. *et al.* “Optical injection of mammalian cells using a microfluidic platform” *Biomed. Opt. Express* **1(2)**, 527-536 (2010).
- [105] Ashkin, A. “Acceleration and trapping of particles by radiation pressure” *Phys. Rev. Lett.* **24(4)**, 156-159 (1970).
- [106] Ashkin, A. *et al.* “Observation of a single-beam gradient force optical trap for dielectric particles” *Opt. Lett.* **11(5)**, 288-290 (1986).
- [107] Ashkin, A. *et al.* “Optical trapping and manipulation of single cells using infrared laser beams” *Nature* **330(6150)**, 769-771 (1987).
- [108] Ramser, K. & Hanstorp, D. “Optical manipulation for single-cell studies” *J. Biophoton.* **3(4)**, 187-206 (2010).
- [109] Uchida, M. “Whole-cell manipulation by optical trapping” *Curr. Biol.* **5(4)**, 380-382 (1995).
- [110] Svoboda, K. & Block S. M. “Biological applications of optical forces” *Annu. Rev. Biophys. Biomol. Struct.* **23**, 247-285 (1994).
- [111] Bonin, K. D. *et al.* “Light torque nanocontrol, nanomotors and nanorockers” *Opt. Express* **10(19)**, 984-989 (2002).

- [112] Ashkin, A. & Dziedzic, J. M. "Internal cell manipulation using infrared laser traps" *Proc. Natl. Acad. Sci.* **86**, 7914-7918 (1989).
- [113] Wang, M. D. *et al.* "Stretching DNA with optical tweezers" *Biophys. J.* **72**, 1335-1346 (1997).
- [114] Molloy, J. E. & Padgett, M. J. "Lights, action: optical tweezers" *Contemp. Phys.* **43(4)**, 241-258 (2002).
- [115] Nieminen, T. A. *et al.* "Physics of optical tweezers" *Method. Cell. Biol.* **82**, 207-236 (2007).
- [116] Ricárdez-Vargas, I. *et al.* "Hollow spheres as individual movable micromirrors in optical tweezers" *Opt. Express* **13(3)**, 968-976 (2005).
- [117] Sato, S. *et al.* "Optical trapping and rotational manipulation of microscopic particles and biological cells using higher-order mode Nd:YAG laser beams" *Electron. Lett.* **251**, 1831-1832 (2002).
- [118] Casaburi, A. *et al.* "Two- and three-beam interferometric optical tweezers" *Opt. Commun.* **251**, 393-404 (2005).
- [119] Grier, D. G. "A revolution in optical manipulation" *Nature* **424**, 810-816 (2003).
- [120] Gauthier, R. C. *et al.* "Experimental confirmation of the optical trapping properties of cylindrical objects" *Appl. Opt.* **38(22)**, 4861-4869 (1999).
- [121] Gauthier, R. C. "Theoretical investigation of the optical trapping force and torque on cylindrical micro-objects" *J. Opt. Soc. Am. B* **14(12)**, 3323-3333 (1997).
- [122] Matstre, D. & Vincent, P. "Making photonic crystals sing trapping and binding optical forces on particles" *J. Opt. A* **8(12)**, 1059-1066 (2006).

- [123] Simpson, S. H. & Hanna, S. “Holographic optical trapping of microrods and nanowires” *J. Opt. Soc. Am. A* **27(6)**, 1255-1264 (2010).
- [124] Philips, D. B. *et al.* “Optimizing the optical trapping stiffness of holographically trapped microrods using high speed video tracking” *J. Opt* **13**, 044023 (2011).
- [125] Villangca, M. J. *et al.* “Light-driven micro-tool equipped with a syringe function” *light Sci. Appl.* **5**, e16148 (2016).
- [126] Philips, D. B. *et al.* “An optically actuated surface scanning probe” *Opt. Express* **20(28)**, 29679-29693 (2012).
- [127] Ramsay, W. T. *et al.* “Triple beam optical trap for microsyringe construction” *Proc. SPIE 8097 Optical Trapping and Optical Micromanipulation VIII*, 809708 (2011).
- [128] Cuerrier, C. M. *et al.* “Single cell transfection using plasmid decorated AFM probes” *Biochem. Biophys. Res. Commun.* **355(3)**, 632-636 (2007).
- [129] Angle, M. R. *et al.* “Penetration of cell membranes and synthetic lipid bilayers by nanoprobe” *Biophys. J.* **107(9)**, 2091-2100 (2014).
- [130] Quinn, P.J. “Effects of temperature on cell membranes” *Symp. Soc. Exp. Biol.* **42**, 237-258 (1988).
- [131] Xie, Y. *et al.* “A Force Control Approach to a Robot-assisted Cell Microinjection System” *Int. J. Robot. Res.* **29(9)**, 1222-1232 (2010).
- [132] Roger, R. P. & Weidman, P. D. “Axisymmetric stokes drag on hollow cylinders: Computation and comparison with experiment” *Eur. J. Mech. B. Fluids* **17(2)**, 187-203 (1998).
- [133] Hunt, A. J. *et al.* “The force exerted by a single kinesin molecule against a viscous load” *Biophys. J.* **67(2)**, 766-781 (1994).

- [134] Tam, J. M. *et al.* “An imaging fiber-based optical tweezer array for microparticle array assembly” *Appl. Phys. Lett.* **84**, 4289-4291 (2004).
- [135] Visscher, K. *et al.* “Construction of multi-beam optical traps with nanometer-resolution position sensing” *IEEE J. Sel. Top. Quantum Electron.* **2(4)**, 1066-1076 (1996).
- [136] MacDonald, M. P. *et al.* “Trapping and manipulation of low-index particles in a two-dimensional interferometric optical trap” *Appl. Phys. Lett.* **26(12)**, 863-865 (2001).
- [137] Chiou, A. E. *et al.* “Interferometric optical tweezers” *Opt. Commun.* **133**, 7-10 (1997).
- [138] Dufresne, E. R. *et al.* “Computer-generated holographic tweezer arrays” *Rev. Sci. Instrum.* **72**, 1810-1816 (2001).
- [139] Bowman, R. W. *et al.* “iTweezers: optical manipulation controlled by an Apple iPad” *J. Opt.* **13(4)**, 044002 (2011).
- [140] Barber, M. A. “A technique for the inoculation of bacteria and other substances into living cells” *J. Infect. Dis.* **8**, 348-360 (1911).
- [141] Korzh, V. & Strähle, U. “Marshall Barber and the century of microinjection: from cloning of bacteria to cloning of everything” *Differentiation* **70**, 221-226 (2002).
- [142] Zhang, Y. & Yu, L. “Single-cell microinjection technology in cell biology” *BioEssays* **30**, 606-610 (2008).
- [143] Marh, J. *et al.* “Hyperactive self-inactivating *piggyback* for transposase-enhanced pronuclear microinjection transgenesis” *Proc. Natl. Acad. Sci. U.S.A.* **109(47)**, 19184-19189 (2012).

- [144] Viigipuu, K. & Kallio, P. "Microinjection of living adherent cells by using a semi-automatic microinjection system" *Altern Lab Anim.* **32(4)**, 417-423 (2004).
- [145] Hamaguchi, Y. & Hiramoto Y. "Activation of sea urchin eggs by microinjection of calcium buffers" *Exp. Cell Res.* **134(1)**, 171-179 (1981).
- [146] Knoblauch, M. *et al.* "A galinstan expansion femtosyringe for microinjection of eukaryotic organelles and prokaryotes" *Nat. Biotechnol.* **17**, 906-909 (1999).
- [147] Onishi, A. *et al.* "Pig cloning by microinjection of fetal fibroblast nuclei" *Science* **289(5482)**, 1188-1190 (2000).
- [148] Harbers, K. *et al.* "Microinjection of cloned retroviral genomes into mouse zygotes: integration and expression in the animal" *Nature* **293(5822)**, 540-542 (1981).
- [149] Penman, D. J. *et al.* "*Factors affecting survival and integration following microinjection of DNA into rainbow trout eggs*" *Aquaculture* **1(4)**, 35-50 (1990).
- [150] Neuhaus, G. *et al.* "Transgenic rapeseed plants obtained by the microinjection of DNA into microspore-derived embryoids" *Theor. Appl. Genet.* **75(1)**, 30-36 (1987).
- [151] Schnorf, M. *et al.* "An improved approach for transformation of plant cells by microinjection: molecular and genetic analysis" *Transgenic Res.* **1(1)**, 22-30 (1991).
- [152] Perry, A. C. F. *et al.* "Mammalian transgenesis by intracytoplasmic sperm injection" *Science* **284(5417)**, 1180-1183 (1999).
- [153] Ma, H. *et al.* "Correction of a pathogenic gene mutation in human embryos" *Nature* **548(7668)**, 413-419 (2017).

- [154] Huang, G. *et al.* “Rolled-up transparent microtubes as two-dimensionally confined culture scaffolds of individual yeast cells” *Lab Chip* **9**, 263-268 (2009).
- [155] Choudhury, D. *et al.* “Ultrafast laser inscription: perspectives on future integrated applications” *Laser Photon. Rev.* **8(6)**, 827-846 (2014).
- [156] Choudhury, D. “Femtosecond laser microfabricated devices for biophotonic applications” (doctoral thesis) Heriot-Watt University, Edinburgh (2013).
- [157] Yokokawa, M. *et al.* “Mechanical properties of plasma membrane and nuclear envelope measured by scanning probe microscope” *J. Microsc.* **232(1)**, 82-90 (2007).
- [158] Keloth, A. *et al.* “Ultrafast laser inscribed devices for cell manipulation” *Optics in the Life Sciences Congress* OtW2E.3 (2017).
- [159] Berger, N.A. & Weber, G. “Description of a permeable eukaryotic cell system to study agents affecting DNA synthesis: demonstration that cytembena is a direct inhibitor of replicative DNA synthesis” *J. Natl. Cancer Inst.* **58(4)**, 1167-1169 (1977).
- [160] Vaara, M. “Agents that increase the permeability of the outer membrane” *Microbiol. Rev.* **56(3)**, 395-411 (1992).
- [161] Radi, H. A. & Rasmussen, J. O. “Principles of Physics” 2nd Edition, USA, Springer (2013).
- [162] König, K. *et al.* “Cell damage in near-infrared multimode optical traps as a result of multiphoton absorption” *Opt. Lett.* **21(14)**, 1090-1092 (1996).
- [163] Khalil, A. A. *et al.* “Heat shock proteins in oncology: Diagnostic biomarkers or therapeutic targets?” *Biochim. Biophys. Acta* **1816(2)**, 89-104 (2011).

- [164] Welch W. J. "Mammalian Stress Response: Cell Physiology, Structure / Function of Stress Proteins, and Implications for Medicine and Disease" *Physiol. Rev.* **72(4)**, 1063-1081 (1992).
- [165] Wytenback, A. *et al.* "Effects of heat shock, heat shock protein 40 (HDJ-2), and proteasome inhibition on protein aggregation in cellular models of Huntington's disease" *Proc. Natl. Acad. Sci. U.S.A.* **97(6)**, 2898-2903 (2000).
- [166] Hsu, A. *et al.* "Regulation of Aging and Age-Related Disease by DAF-16 and Heat-Shock Factor" *Science* **300(5622)**, 1142-1145 (2003).
- [167] Neckers, L. & Percy, I. S. "Heat shock protein 90" *Curr. Opin. Oncol.* **15(6)**, 419-424 (2003).
- [168] Ciocca, D. R. *et al.* "Heat Shock Protein hsp70 in Patients With Axillary Lymph Node-Negative Breast Cancer: Prognostic Implications" *J. Natl. Cancer Inst.* **85(7)**, 570-574 (1993).
- [169] Aghdassi A. *et al.* "Heat Shock Protein 70 Increases Tumorigenicity and Inhibits Apoptosis in Pancreatic Adenocarcinoma" *Cancer Res.* **67(2)**, 616-625 (2007).
- [170] Snoeckx, L. H. E. H. *et al.* "Heat Shock Proteins and Cardiovascular Pathophysiology" *Laser Photon. Rev.* **81(4)**, 1461-1497 (2014).
- [171] Gao, Y. & Bando, Y. "Nanotechnology: Carbon nanothermometers containing gallium." *Nature* **415**, 599 (2002).
- [172] Brites, C. D. S. *et al.* "Thermometry at the nanoscale" *Nanoscale* **4**, 4799-4829 (2012).
- [173] Cui, J. B. *et al.* "Noncontact temperature measurements of diamond by Raman scattering spectroscopy" *J. Appl. Phys.* **83(12)**, 7929-7933 (1998).

- [174] Kuball, M. *et al.* “Measurement of Temperature in Active High-Power AlGaIn / GaIn HFTEs Using Raman Spectroscopy” *IEEE Electron Device Lett.* **23(1)**, 7-9 (2002).
- [175] Jaque, D. & Vetrone, F. “Luminescence Nanothermometry” *Nanoscale* **4(15)**, 4301-4326 (2012).
- [176] Patterson, G. H. & Piston, D. W. “Photobleaching in Two-Photon Excitation Microscopy” *Biophys. J.* **78(4)**, 2159-2162 (2000).
- [177] Bastiaens, P. I. H. & Squire, A. “Fluorescence lifetime imaging microscopy: spatial resolution of biochemical processes in the cell” *Trends Cell Biol* **9**, 48-52 (1999).
- [178] Zhao, B. *et al.* “Surface-Directed Liquid Flow Inside Microchannels” *Science* **291(5506)**, 1023-1026 (2001).
- [179] Kirill, K. *et al.* “Red-Emitting Rhodamine Dyes for Fluorescence Microscopy and Nanoscopy” *Chem. Eur. J.* **16**, 158-166 (2010).
- [180] Johnson, L. V. *et al.* “Localization of mitochondria in living cells with rhodamine 123” *Proc. Natl. Acad. Sci. U.S.A.* **77(2)**, 990-994 (1980).
- [181] Kaprelyants, A. S. & Kell, A. B. “Rapid assessment of bacterial viability and vitality by rhodamine 123 and flow cytometry” *J. Appl. Microbiol.* **72(5)**, 410-422 (1992).
- [182] Woods, G. L. & Walker, D. W. “Detection of Infection or Infectious Agents by Use of Cytologic and Histologic Stains” *Clin. Microbiol. Rev.* **9(3)**, 382-404 (1996).
- [183] Chauhan, V. M. *et al.* “Thermo-optical characterization of fluorescent rhodamine B based temperature-sensitive nanosensors using a CMOS MEMS micro-hotplate” *Sens. Actuator B-Chem.* **192**, 126-133 (2014).

- [184] Cui, Y. *et al.* “A ratiometric and colorimetric luminescent thermometer over a wide temperature range based on a lanthanide coordination polymer” *Chem. Commun.* **50**, 719-721 (2014).
- [185] Cui, Y. *et al.* “A Luminescent Mixed-Lanthanide Metal-Organic Framework Thermometer” *J. Am. Chem. Soc.* **134**, 3979-3982 (2012).
- [186] Bailey, R. E. *et al.* “Quantum dots in biology and medicine” *Physica E.* **25**, 1-12 (2004).
- [187] Haro-González, P., Ramsay, W. T. *et al.* “Quantum-dot based thermal spectroscopy and imaging of optically trapped microspheres and single cells” *Small* **9(12)**, 2162-2170 (2013).
- [188] Kilmon, V. I. *et al.* “Optical Gain and Stimulated Emission in Nanocrystal Quantum Dots” *Science* **290**, 314-317 (2000).
- [189] Norris, D. J. & Bawendi, M. G. “Measurement and assignment of the size-dependent optical spectrum in CdSe quantum dots” *Phys. Rev. B.* **53**, 16338-16346 (1996).
- [190] Efros, A. L. & Rosen, M. “The Electronic Structure of Semiconductor Nanocrystals” *Annu. Rev. Mater. Sci.* **30**, 475-521 (2000).
- [191] Yoffe, A. D. “Semiconductor quantum dots and related systems: Electronic, optical, luminescence and related properties of low dimensional systems” *Adv. Phys.* **50**, 1-208 (2001).
- [192] Bruchez, M. *et al.* “Semiconductor Nanocrystals as Fluorescent Biological Labels” *Science* **281(5385)**, 2013-2016 (1998).
- [193] Chan, W. C. W. & Nie, S. *et al.* “Quantum Dot Bioconjugates for Ultrasensitive Nonisotopic Detection” *Science* **281(5385)**, 2016-2018 (1998).

- [194] Parak, W. J. *et al.* "Labelling of cells with quantum dots" *Nanotechnology* **16**, R9-R25 (2005).
- [195] Goldman, E. R. *et al.* "Conjugation of Luminescent Quantum Dots with Antibodies using an Engineered Adaptor Protein To Provide New Reagents for Fluoroimmunoassays" *Anal. Chem.* **74(4)**, 841-847 (2002).
- [196] Probst, C. E. *et al.* "Quantum dots as a platform for nanoparticle drug delivery vehicle design" *Adv. Drug Deliv. Rev.* **65(5)**, 703-718 (2013).
- [197] O'Donnell, K. P. & Chen, X. "Temperature dependence of semiconductor band gaps" *Appl. Phys. Lett.* **58**, 2924-2926 (1991).
- [198] Walker, G. W. *et al.* "Quantum-dot optical temperature probes" *Appl. Phys. Lett.* **83**, 3555-3557 (2003).
- [199] Li, S. *et al.* "Single Quantum Dots as Local Temperature Markers" *Nano Lett.* **7(10)**, 3102-3105 (2007).
- [200] Albers, A. E. *et al.* "Dual-Emitting Quantum Dot/Quantum Rod-Based Nanothermometers with Enhanced Response and Sensitivity in Live Cells" *J. Am. Chem. Soc.* **134**, 9565-9568 (2012).
- [201] Yang, J. *et al.* "Quantum Dot Nano Thermometers Reveal Heterogeneous Local Thermogenesis in Living Cells" *ACS Nano* **5(6)**, 5067-5071 (2011).
- [202] Maestro, L. M. *et al.* "Quantum Dot Thermometry Evaluation of Geometry Dependent Heating Efficiency in Gold Nanoparticles" *Langmuir* **30**, 1650-1658 (2014).
- [203] Maestro, L. M. *et al.* "CdSe Quantum Dots for Two-Photon Fluorescence Thermal Imaging" *Nano Lett.* **10**, 5109-5115 (2010).
- [204] Yue, Y. & Wang, X. "Nanoscale thermal probing" *Nano Rev* **3**, 11586 (2012).

- [205] Maestro, L. M. *et al.* “CdTe Quantum Dots as Nanothermometers: Towards Highly Sensitive Thermal Imaging” *Small*. **7(13)**, 1774-1778 (2011).
- [206] Kalytchuk, S. *et al.* “Temperature-Dependent Exciton and Trap-Related Photoluminescence of CdTe Quantum Dots Embedded in a NaCl Matrix: Implication in Thermometry” *Small*. **12(4)**, 466-476 (2016).
- [207] Haro-González, P. *et al.* “High-Sensitivity Fluorescence Lifetime Thermal Sensing Based on CdTe Quantum Dots” *Small*. **8(17)**, 2652-2658 (2012).
- [208] Bagheri, A. *et al.* “Lanthanide-Doped Upconversion Nanoparticles: Emerging Intelligent Light-Activated Drug Delivery Systems” *Adv. Sci.* **3(7)**, 1500437 (2016).
- [209] Aulin, Y. V. *et al.* “Photochemical upconversion in metal-based octaethyl porphyrin-diphenylanthracene systems” *RSC Adv.* **5**, 107896-107903 (2015).
- [210] Vetrone, F. *et al.* “Temperature Sensing Using Fluorescent Nanothermometers” *ACS Nano* **4(6)**, 3254-3258 (2010).
- [211] Flick, D. F. *et al.* “Toxic effects of cadmium: A review” *Environ. Res.* **4(2)**, 71-85 (1971).
- [212] Yong, K. *et al.* “Nanotoxicity assessment of quantum dots: from cellular to primate studies” *Chem. Soc. Rev.* **42**, 1236-1250 (2013).
- [213] Clift, M. J. D. *et al.* “The uptake and intracellular fate of a series of different surface coated quantum dots in vitro” *Toxicology* **286**, 58-68 (2011).
- [214] Wang, L. *et al.* “Toxicity of CdSe Nanoparticles in Caco-2 Cell Cultures” *J. Nanobiotechnol.* **6(11)**, 10.1186/1477-3155-6-11 (2005).
- [215] Kirchner, C. *et al.* “Cytotoxicity of Colloidal CdSe and CdSe/ZnS Nanoparticles” *Nano. Lett.* **5(2)**, 331-338 (2005).

- [216] Cho, S. J. *et al.* “Long-Term Exposure to CdTe Quantum Dots Causes Functional Impairments in Live Cells” *Langmuir* **23(4)**, 1974-1980 (2007).
- [217] Lovrić, J. *et al.* “Differences in subcellular distribution and toxicity of green and red emitting CdTe quantum dots” *J. Mol. Med.* **83**, 377-385 (2005).
- [218] Dholakia, K. *et al.* “Optical Manipulation” *Chem. Soc. Rev.* **37**, 42-55 (2008).
- [219] Godley, B. F. *et al.* “Blue Light Induces Mitochondrial DNA Damage and Free Radical Production in Epithelial Cells” *J. Biol. Chem.* **280(22)**, 21061-21066 (2005).
- [220] Kielbassa, C. *et al.* “Wavelength dependence of oxidative DNA damage induced by UV and visible light” *Carcinogenesis* **18(4)**, 811-816 (1997).
- [221] Liu, Y. *et al.* “Evidence for localized cell heating induced by infrared optical tweezers” *Biophys. J.* **68**, 2137-2144 (1995).
- [222] Peterman, E. J. G. *et al.* “Laser-induced heating in optical traps” *Biophys. J.* **84(2)**, 1308-1316 (2003).
- [223] Celliers, P. M. & Conia, J. “Measurement of localized heating in the focus of an optical trap” *Appl. Opt.* **39(19)**, 3396-3407 (2000).
- [225] Wetzel, F. *et al.* “Single cell viability and impact of heating by laser absorption” *Eur. Biophys. J.* **40**, 1109-1114 (2011).
- [225] Foo, J. J. *et al.* “Thermal effect on a viscously deformed liposome in a Laser trap” *Ann. Biomed. Eng.* **31(3)**, 354-362 (2013).
- [226] Fiers, W. *et al.* “More than one way to die: apoptosis, necrosis and reactive oxygen damage” *Oncogene* **18**, 7719-7730 (1999).
- [227] Majno, G. & Joris, I. “Apoptosis, oncosis, and necrosis. An overview of cell death” *Am. J. Pathol.* **146(1)**, 3-15 (1995).

- [228] Mao, H. *et al.* “Temperature Control Methods in a Laser Tweezers System” *Biophys. J.* **89**(2), 1308-1316 (2005).
- [229] Gosse, C. *et al.* “Molecular probes for thermometry in microfluidic devices” *Top. Appl. Phys.* **118**, 301-341 (2009).
- [230] Kairdolf, B. A. *et al.* “Semiconductor Quantum Dots for Bioimaging and Biodiagnostic Applications” *Annu. Rev. Anal. Chem.* **6**, 143-162 (2013).
- [231] Michalet, X. *et al.* “Quantum Dots for Live Cells, in Vivo Imaging, and Diagnostics” *Science* **307**(5709), 538-544 (2005).
- [232] Maestro, L. M. *et al.* “CdSe Quantum Dots for Two-Photon Fluorescence Thermal Imaging” *Nano. Lett.* **10**(12), 5109-5115 (2010).
- [233] Maestro, L. M. *et al.* “CdTe Quantum Dots as Nanothermometers: Towards Highly Sensitive Thermal Imaging” *Small* **7**(13), 1774-1778 (2011).
- [234] Liang, H. *et al.* “Wavelength dependence of cell cloning efficiency after optical trapping” *Biophys. J.* **70**(3), 1529-1533 (1996).
- [235] Curcio, J. A. & Petty, C. C. “The Near Infrared Absorption Spectrum of Liquid Water” *J. Opt. Soc. Am.* **41**(5), 531-558 (1951).
- [236] Arai, S. *et al.* “Mitochondria-targeted fluorescent thermometer monitors intracellular temperature gradient” *Chem. Commun.* **51**, 8044-8047 (2015).
- [237] Stone, V. *et al.* “Development of in vitro systems for nanotoxicology: methodological considerations” *Crit. Rev. Toxicol.* **39**(7), 613-626 (2009).
- [238] Romoser, A. *et al.* “Mitigation of Quantum Dot Cytotoxicity by Microencapsulation” *PLoS ONE* **6**(7), e22079 (2011).

- [239] Lovrić, J. *et al.* “Unmodified Cadmium Telluride Quantum Dots Induce Reactive Oxygen Species Formation Leading to Multiple Organelle Damage and cell Death” *Chem. Biol.* **12**, 1227-1234 (2005).
- [240] Rosal, B. D. *et al.* “Heat in optical tweezers” *Proc. SPIE* **8810**, 88102A (2013).
- [241] Aderem, A. & Underhill, D. M. “Mechanisms of Phagocytosis in Macrophages” *Annu. Rev. Immunol.* **17**, 593-623 (1999).
- [242] Gospodarowicz, D. & Moran, J. S. “Growth factors in mammalian cell culture” *Annu. Rev. Biochem.* **45(1)**, 531-558 (1976).